2-2016

Analysis and simulation of small scale microwave interferometer experiments on non-ideal explosives

David E. Kittell
Purdue University

Graduate School Form
30 Updated 12/26/2015

PURDUE UNIVERSITY
GRADUATE SCHOOL
Thesis/Dissertation Acceptance

This is to certify that the thesis/dissertation prepared

By David Erik Kittell

Entitled

ANALYSIS AND SIMULATION OF SMALL SCALE MICROWAVE INTERFEROMETER EXPERIMENTS ON NON-IDEAL EXPLOSIVES

For the degree of Doctor of Philosophy

Is approved by the final examining committee:

Steven F. Son Chair	Lori J. Groven
Sally Bane	
Cole Yarrington	
Weinong Chen	

To the best of my knowledge and as understood by the student in the Thesis/Dissertation Agreement, Publication Delay, and Certification Disclaimer (Graduate School Form 32), this thesis/dissertation adheres to the provisions of Purdue University's "Policy of Integrity in Research" and the use of copyright material.

Approved by Major Professor(s): Steven F. Son

Approved by: Anil Bajaj 02/04/2016

Head of the Departmental Graduate Program Date

ANALYSIS AND SIMULATION OF SMALL SCALE MICROWAVE INTERFEROMETER EXPERIMENTS ON NON-IDEAL EXPLOSIVES

A Dissertation

Submitted to the Faculty

of

Purdue University

by

David E. Kittell

In Partial Fulfillment of the

Requirements for the Degree

of

Doctor of Philosophy

May 2016

Purdue University

West Lafayette, Indiana

To Mom and Dad.

ACKNOWLEDGMENTS

I am forever indebted to many different people for their encouragement and support of my Ph.D. research. Earning a Ph.D. is a long journey, and most graduate students will at some point experience feelings of frustration and loneliness trying to push forward on their results. These feelings happen because we forget the bigger picture - all research is really an endeavor to improve society in some meaningful way. Therefore, I am all the more thankful for the people who made a positive impact during my time in graduate school in tangible and intangible ways.

First and foremost, I would like to thank my advisor Steven Son and committee member Lori Groven for their guidance, vision, and expertise in the field of energetic materials. These two people were instrumental in completing the work, and they also introduced me to the small community of researchers in the field (for which I am grateful). I truly believe that my dissertation is standing on the shoulders of giants because of the dedication and hard work that these two people invested into their own careers, and are now paying forward.

Another person who mentored me through the process is Cole Yarrington, a current staff member at Sandia National Laboratories and former Ph.D. student from our research group. Cole arranged for me to participate in the student intern program (SIP) at Sandia, which has been an on-going partnership for the last three years. Under the mentorship of Cole and other members of the technical staff, I learned how to run increasingly complex CTH simulations on the Cray supercomputers. I would also like to thank my manager, Tony Geller, for the opportunity to work at Sandia, and access to some of the computational resources to finish my own Ph.D. research.

Throughout my time at Purdue, many students and staff helped me to complete this work. Sometimes, the goals and deadlines seemed impossible; yet these people worked tirelessly to make the impossible happen. Although much space could be

devoted to recalling all of the different stories, two of the most significant contributions to the work were made by fellow students Jesus Mares and Nick Cummock. My first Ph.D. publication on wavelet analysis took a full year of editing with Jesus; yet that paper is the one of which I am most proud. The second acknowledgment is that when I returned to Purdue in the fall of 2015, I was confronted with the challenge of collecting and analyzing an entirely new data set before the end of December. Nick helped me to meticulously prepare sixteen explosive charges over the course of two weeks, and then we tested them in a single day (a record never to be equaled).

Finally, I would like to thank my parents and relatives for the love and support that I received to finish the degree. Over the years in graduate school, I tended to think less of the accomplishment - especially watching all of my friends back home moving on with their lives. But as an only child, I am the first in the family to be attaining a Ph.D. degree and to all of us this achievement is significant. I hope to use it in order to make a positive impact on society and to pay forward the knowledge that I have gained. I believe that Tuncer "Tunch" Kuzay and R. B. Stewart would be proud as well, though sadly both have passed away. My prayer is that this work has not become self-serving, as we are all living in a world much bigger than any of us. I am thankful for the grace of God in my life to make it thus far.

This material is based upon work supported by the U.S. Department of Homeland Security, Science and Technology Directorate, Office of University Programs, under Grant Award No. 2013-ST-061-ED0001. The views and conclusions contained in this document are those of the author and should not be interpreted as necessarily representing the official policies, either expressed or implied, of the U.S. Department of Homeland Security.

TABLE OF CONTENTS

Page

LIST OF TABLES

Table Page

LIST OF FIGURES

Figure Page

ABBREVIATIONS

ANFO	ammonium nitrate plus fuel oil
ANUR	ammonium nitrate plus urea
AP	ammonium perchlorate
ARB	Arrhenius reactive burn
BP	ball powder (double-base explosive)
CJ	Chapman-Jouguet
CTPB	carboxyl-terminated polybutadiene
CTH	shock physics hydrocode owned by Sandia National Laboratories
CWT	continuous wavelet transform
DDT	deflagration-to-detonation transition
EBW	exploding bridge-wire
EGDN	ethylene glycol dinitrate
EOS	equation-of-state
FFT	fast Fourier transform
GWT	Gabor wavelet transform
HE	high explosive
HME	homemade explosive
HMX	cyclotetramethylene-tetranitramine
HNS	hexanitrostilbene
HTPB	hydroxyl-terminated polybutadiene
HVRB	history variable reactive burn
IED	improvised explosive device
IGRB	ignition and growth reactive burn
JWL	Jones-Wilkins-Lee
LASL	Los Alamos Scientific Laboratory

LANL	Los Alamos National Laboratory
LLNL	Lawrence Livermore National Laboratory
MI	microwave interferometry
PB	polybutadiene
PBAA	polybutadiene acrylic acid
PBX	plastic-bonded explosive
PDC	piston driven compaction
PDV	photonic Doppler velocimetry
PETN	pentaerythritol tetranitrate
PMMA	polymethylmethacrylate
PS	polystyrene
PTFE	polytetrafluoroethylene
PU	polyurethane
PVC	polyvinyl chloride *or* experimental geometry I.D.
RDX	cyclotrimethylene-trinitramine
SDT	shock-to-detonation transition
SM	experimental geometry I.D.
SNR	signal-to-noise ratio
STFT	short-time Fourier transform
TATB	triaminotrinitrobenzene
TE	transverse electric
TEM	transverse electric and magnetic
THK	experimental geometry I.D.
THN	experimental geometry I.D.
TMD	theoretical maximum density
TNT	trinitrotoluene
VISAR	velocity interferometer system for any reflector
ZND	Zel'dovich-von Neumann-Döring

NOMENCLATURE

α	thermal expansion coefficient
c	material sound speed
c_v	specific heat
e	specific internal energy
f	frequency
Fc	center frequency
Fs	sampling frequency
$\mathcal{G}$	fundamental derivative
Gs	Gabor wavelet shaping factor
Γ	Grüneisen parameter
K_S	isentropic bulk modulus ($= \rho c^2$)
K_T	isothermal bulk modulus
λ	wavelength *or* extent of reaction
$\dot{m}''$	mass flux
μ	compression or stain
ϕ	reference function
p	pressure
$\psi(t)$	mother wavelet
ρ	density
v	specific volume
s	specific entropy
T	temperature
θ	phase angle

ABSTRACT

Kittell, David E. PhD, Purdue University, May 2016. Analysis and Simulation of Small Scale Microwave Interferometer Experiments on Non-Ideal Explosives. Major Professor: Steven F. Son, School of Mechanical Engineering.

Small scale experiments for non-ideal and homemade explosives (HMEs) were investigated, analyzed, and subsequently modeled in an attempt to develop more predictive capabilities for the threat assessment of improvised explosive devices (IEDs), as well as to provide new analysis capabilities for other investigators in the field. Non-ideal explosives and HMEs are challenging to characterize because of the nearly limitless parameter space (e.g. sample composition, density, particle morphology, etc.) which gives rise to a broad range of explosive sensitivity and performance. Large scale tests, such as rate stick and gap tests, are not feasible for characterizing every HME of interest due to limitations in time and cost. These small scale experiments utilize a 35 GHz microwave interferometer to measure the instantaneous shock and failing detonation wave velocities in explosives. Only those explosives which are transparent to the microwave radiation are evaluated, including ammonium nitrate plus fuel oil (ANFO). It is shown here for the first time that the small scale measurements may be related to large scale sensitivity and performance for a large enough sample size and level of confinement.

Specifically, four different experimental configurations were explored that require only 1-5 g of material. By varying the charge diameter, as well as the thickness and sound speed of the confining material, the failure rate and shock front curvature of an overdriven failing detonation may be tailored. The detailed experimental data is also highly repeatable, provided that the initial sample density is uniform and consistent from test to test. Results from the MI data also reveal the existence of an inflexion

point in velocity, which is thought to be related to the measurements obtained from larger rate sticks.

The different MI experiments were subsequently modeled in 2d as well as 3d using the shock physics hydrocode CTH. An ignition and growth reactive burn (IGRB) model was developed for non-ideal explosives, and shown to be relevant to capturing the behavior of some of the overdriven failing detonation waves. Many simplifying assumptions were made, so that the MI data might possibly be used for model calibration and validation. It was determined that an intermediate level of confinement utilizing low sound speed polyvinyl chloride (PVC) is most relevant for fitting the IGRB model constants, which were then used to predict the other MI experiments with partial success.

Overall, the CTH simulations provide much more information than what is available from the MI measurements alone. These simulations were used to investigate pressure waves in the explosive and confiner materials, and to show that the reactive waves are likely transitioning from supersonic to subsonic deflagration, where thermal effects, compaction behavior, and material strength are important. Consequently, these simulations are not able to match the weaker confinement and smaller diameter experiments over the full duration of the tests. The calibrated IGRB model was then used to make several predictions for shock sensitivity, changes to the initial density, and other large scale tests. Future work is suggested to validate these predictions and to improve the model development. Overall, the high level of integration between experimental and modeling efforts shown in this work is critical to better understand HMEs and to design new small scale experiments.

1. INTRODUCTION

1.1 Motivation

At the present time, there exists a need for greater understanding of homemade explosives (HMEs). One critical observation is that the number of different chemical and physical formulations available to potential terrorists is rapidly increasing, while detailed experimental data on these materials is severely lacking. In order to more adequately assess the behavior and performance of a wide range of HMEs, new and novel characterization experiments must be developed. Moreover, it is critical that these experiments are supported by modeling for interpretation of the results. However, the advancement of experimental and modeling efforts is confronted by two significant challenges: (1) the feasibility of testing a wide variety of materials with limitations on time and cost, and (2) the accuracy of previously-accepted model approximations under less ideal (e.g. small scale) conditions. Nevertheless, it is necessary to continue to investigate an integrated experimental and modeling approach in order to respond to the growing threat of HMEs.

A single experiment would most likely be ineffective, as different methodologies will be required for various HMEs depending on their combustion behavior. For example, different physical mechanisms are relevant to the combustion of 'low' and 'high' explosives. Low explosives are slower burning, and are used to produce high velocity fragments with heavy or light confinement. High explosives undergo a fast burning supersonic combustion process, and usually require no confinement to produce a strong blast wave. The blast wave from a high explosive has the greater potential for fatalities and damage to surrounding buildings; yet it may also require a more sophisticated blasting cap or detonator to be initiated. The effect of an initiator

on a HME could possibly be simulated using a reactive burn model, and it is this possibility which motives much of the present work.

Two recent examples of domestic terrorist attacks which illustrate the differences in low and high explosives are the Boston Marathon bombing in 2013, and the Oklahoma City bombing in 1995, respectively. In the former attack, two stainless steel pressure cookers were filled with low explosive gun powder and ball bearings. The explosions killed 3 people and injured an estimated 264 others; most of the damage was due to high velocity shrapnel. In this scenario, a desirable predictive capability may be to assess the potential range and velocity of the fragments based on combustion properties. In contrast to the Boston Marathon bombing, the Oklahoma City bombing was perpetrated using a high explosive consisting of ammonium nitrate, diesel fuel, and nitromethane to much greater effect: the attack killed 168 people and injured more than 600 others. In this case, a desirable predictive capability might include an estimation of the TNT equivalent of the bomb, detonation velocity, and the initiation behavior (which may also effect the yield of the bomb).

Overall, new methodologies are needed to study these types of HMEs, as most established tests for explosives are prohibitive for investigations over a wide parameter space. Historically, these established tests were designed and performed on a handful of explosives critical to the operation of certain explosive devices. For example, the calibration of an equation-of-state or reactive burn model may involve methods which require: (1) large sample sizes >100 g for rate stick, cylinder, and wedge tests, (2) a high degree of complexity including embedded material gages, or (3) a specific use form of the explosive that is either cast or machined. Unfortunately, it is not feasible due to time and cost to apply these complex and large-scale experiments to every HME of interest.

Moreover, many HMEs fall into a further classification known as non-ideal explosives. A non-ideal explosive deviates from the classical theory of detonation, as only a fraction of the available chemical energy goes into raising the pressure of the detonation wave. For example, two-part mixtures (also known as binary explosives)

are not combined at the molecular level, and the reaction tends to be incomplete over the time scales of a shock wave. Large critical diameters are associated with non-ideal explosives, so that a steady detonation wave will not be observed below a certain sample size. Hence, current work to develop new methodologies based on small scale experiments must take into consideration the potential for observing detonation failure.

It is hoped that some method may be found wherein the detonability of a broad range of HMEs is assessed via small scale experiments. To this end, microwave interferometry (MI) is proposed here as a non-intrusive diagnostic capable of measuring transient reactive wave phenomena in small diameter (<1 cm) explosive charges. Various confinement and initiation conditions may be studied with minimal increase to the time and complexity of testing. Large quantities of detailed experimental data may then be quickly obtained, and coupled directly to the modeling effort of HMEs. This kind of transient, reactive wave propagation data also provides a rich data set for model validation, and supports the larger effort to enable more predictive capabilities for assessing the threat of HMEs. However, the scalability of the small scale data and the applicability of a reactive burn model to simulate these types of experiments is largely unknown. The success of this work depends on answering these research questions with experimental and computational investigations into a baseline non-ideal explosive. Future applications of the work may include higher fidelity simulations of improvised explosive devices (IEDs), as well as new analysis capabilities for explosive-related accident investigations.

1.2 Scope

The scope of the work is broad, and encompasses many different disciplines. One field of study which underlies much of the work is that of energetic materials. An informal definition of the field includes explosives, as well as other materials with the capability of self-sustained exothermic chemical reactions (e.g. solid propellants,

roadside flares, and thermites). The field of energetic materials is itself multidisciplinary, requiring some knowledge of chemistry, heat transfer, mass diffusion, and fluid dynamics - a majority of these disciplines fall within the scope of mechanical engineering. Two major branches exist for combustion processes, as either subsonic deflagration or supersonic detonation waves. Deflagation waves are self-sustaining with sufficient heat feedback, whereas detonation waves are sustained by the high pressures associated with a shock wave.

Another field of study within the scope of the work is that of microwave interferometry (MI). This field, too, is quite broad having been developed in the early 1950's in parallel with radar. The applications of MI are widespread, and may be found across different types of measurements, including: propellant regression rates, plasma densities, remote sensing applications, and also the explosives measurements considered in the present work. MI may be described as an electromagnetic analogue to an optical Michelson interferometer, and it is used in conjunction with explosives to make non-intrusive, time-resolved measurements of the velocity of shock or detonation waves.

In order to extract high-quality velocity data from the MI technique, several advanced digital signal processing methods are needed. This is also within the scope of the work; some of these techniques subsequently require an understanding of spectral decomposition, Fourier transforms, and time-frequency analysis. Time-frequency analysis is especially useful for low quality MI signals, which are known to occur for a variety of reasons, most notably non-ideal instrumentation and signal conditioning. Nonetheless, these advanced techniques are still important for a greater understanding of the data analysis, and calibrating some explosive material properties.

The last major area covered in the scope of the work is that of numerical simulation and modeling. This area may be further subdivided between explosives modeling, and the computer codes which are used to implement these models. In this work, a hydrocode is used to simulate the experimental MI results. All hydrocodes share some aspects of structural dynamics and wave propagation codes, although neither

one is a more accurate description. In these types of simulations, fluid-like behavior is assumed when the associated shock and detonation pressures are much higher than the material yield strength. Overall, many assumptions go into the computer codes and explosive models, and these are active areas for research within the larger scientific community.

1.3 Organization

The remaining chapters have been organized with an emphasis on topic area to improve the flow and readability of the work. Chapter 2 is a literature review of the MI technique; it is structured to provide a broad survey of relevant information, rather than going deeper into the technical content. This chapter includes a background and history for the MI technique in addition to the literature review.

Chapter 3 is the experimental methods section. This chapter includes an overview of the experimental apparatus, sample preparation, and data collection for the small scale MI tests. Some aspects of pressing explosives are discussed which affect the variation in density between samples. In addition, procedural notes are documented which appear to increase the likelihood for achieving high quality MI output signals.

Chapter 4 is the data analysis section, which covers MI theory, equations, and four different methods which may be used to analyze the MI signals. Additional equations are provided for an error analysis, considering both the measurement error and random sample variation. Dynamic wavelength calibration is also discussed, which was used to determine the dielectric properties of the test explosives.

Chapter 5 covers the development of an ignition and growth reactive burn model for a baseline ammonium nitrate fuel oil (ANFO) non-ideal explosive. The chapter begins by describing all of the model sub-components, and then establishing each one in greater detail. Attention is placed on the assumptions made, and also the unknown model parameters. The chapter ends with a discussion of the model implementation in the CTH hydrocode, followed by model calibration and validation.

Chapter 6 discusses some improvements made to the Mie-Grüneisen equation of state (EOS), using a physically-based Einstein oscillator model for the specific heat. This work is soon to be published in a journal article, and addresses some of the challenging of temperature predictions when simulating heterogeneous explosives. The chapter ends with a simulation of pore collapse and predictions of a dynamic hot spot temperature distribution. This type of modeling approach could be used to describe sub-grid phenomena that the ignition and growth model is currently incapable of capturing.

Chapter 7 contains the results section, beginning with the small scale MI experiments, companion simulations, and ending with some predictions of large scale experiments using the calibrated model. Implications of the model predictions are discussed, and future work is identified to provide additional validation of the model. The dissertation ends with Chapter 8, which summarizes the major conclusions of the work.

Data processing and analysis calculations relevant to the work may be found in Appendix A through C. This includes time-frequency results (i.e. spectrograms and scalograms) corresponding to the sample calculations in Chapter 4. A summary of material properties, error analysis, and the MI output signals may be found in Appendix C. Two of the most important codes that were developed for the work are given in Appendix D and E for the CTH input deck and FORTRAN post processing code, respectively. Last, the slides presented in an oral defense of the work may be found in Appendix F.

2. MICROWAVE INTERFEROMETRY

Microwave interferometry (MI) is an established technique for measuring shock and detonation velocities in explosives. Compared to other photographic and chronographic methods of testing, MI is a unique, non-intrusive diagnostic with high temporal resolution. MI operates by transmitting microwave signals through transparent media (which may be any unreacted explosive with low loss), and then observing the reflections from locations of interest. These reflections occur at dielectric discontinuities, which may be varying in both time and space. The phenomena which have been observed to produce suitable reflecting planes include: detonation waves [1], highly ionized gases or plasmas [2, 3], compaction waves [4], and free surfaces [5], to name a few examples. Detonation waves may be nearly perfect reflectors as a result of the strongly ionized detonation products just behind the leading shock wave [6].

2.1 Background

The implementation of a MI system for detonation velocity measurements has been accomplished in a variety of ways, as depicted in Fig. 2.1. The free-field configuration shown in Fig. 2.1(a) offers the most flexibility for testing different size charges; however, multiple modes of microwave propagation and off-axis reflection from the detonation products render most of the data analysis techniques inaccurate [7]. It was not until recent work utilizing either a horn/axicon arrangement [8] or a high-directivity horn antenna [9] that this method was seriously considered. Instead, an explosive-filled waveguide may be used to allow only the lowest transverse electric (TE) mode to be propagated, which does place some restrictions the maximum charge diameter. Explosive-filled waveguides have been embedded into the center of larger diameter charges (semi-intrusive) as shown in Fig. 2.1(b), or tested

at relatively small (<1 cm) diameters with varying levels of confinement as shown in Fig. 2.1(c). Finally, some unconfined charges have been tested at larger diameters with the use of a waveguide mode selector as shown in Fig. 2.1(d); however, difficulties in performing the analysis are reported to occur near charge diameters of 5 cm and greater [10].

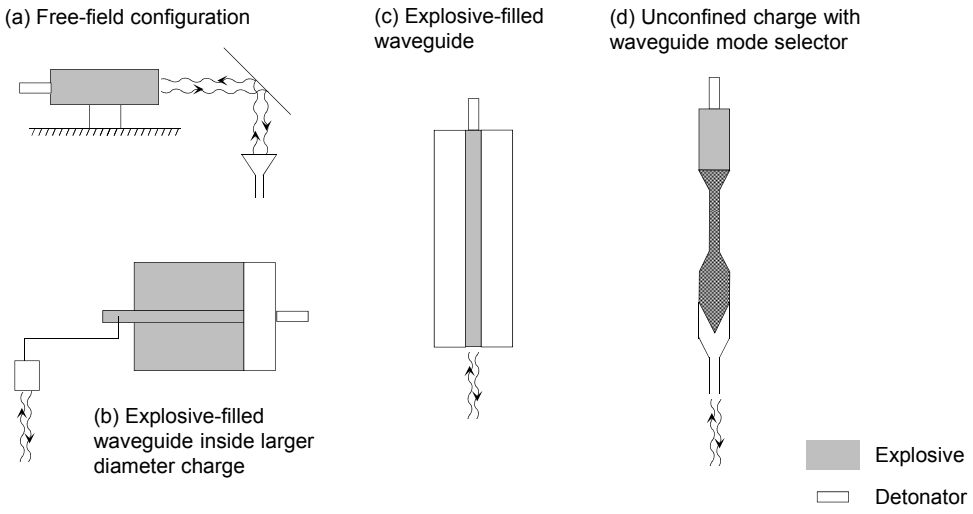

Figure 2.1. Different implementations of MI systems used for measuring detonation velocity.

The output from modern MI systems may be understood as the sum of two reflected waves. One of the reflected waves originates from the MI transmission line, and is of constant phase. The other reflected wave is from inside the explosive, and undergoes a 2π phase shift for each displacement of the moving surface by exactly one half wavelength. The phase measurement is used to infer the relative position and velocity of the phenomena. Less extractable information is contained in the amplitude of the MI signal; however, under ideal conditions it is possible to determine an amplitude reflection coefficient [4]. The preceding description of MI is based on an understanding of phase advancement, and is used exclusively in the dissertation; however, early MI systems (which resembled the operation of radar) were sometimes

interpreted in terms of the Doppler shift in frequency produced by the velocity, v, of the detonation front [10]. The Doppler frequency shift, f_d, is given by,

$$f_d = 2vf_0/c' \tag{2.1}$$

where f_0 is the microwave frequency and c' is the velocity of propagation of the microwaves within the unreacted explosive. These different interpretations came about due to the MI circuitry used; modern MI systems incorporate a network analyzer or quadrature mixer, whereas older MI systems occasionally used a type of beat frequency detector to measure the Doppler shift frequency directly.

A literature review with historical context is provided for the development of MI as it applies to energetic materials (i.e. explosives and propellants) from World War II until the present day. Some of the work reviewed contained very good background information and is worth mentioning: Stanton, Venturini, and Dietzel (1985) [11] for a review of MI applied to explosives; Aničin *et al.* (1986) [12] for a review of explosive and propellant work, in an attempt to understand the source of microwave reflections; Zarko, Vdovin, and Perov (2000) [13] for modern advancements in propellant research; and Bel'skii *et al.* (2011) [14] for a summary of work conducted through the Russian Federal Nuclear Center-Institute of Experimental Physics. There are, at times, overlap between MI applied to explosives, propellants, shock waves, and gaseous detonations. Much care was taken to exhaust the literature on explosives and propellants, while providing additional context from the other applications when appropriate.

2.2 Literature Review

The 1940's: The origins of MI may be traced back to the development of radio navigation just prior to World War II. A low power system for guiding airplanes on landing was adapted by the Germans during the war to direct bomber flights over England. These beams were operated in the high frequency (HF) to very high frequency (VHF) bands of the radio spectrum. The deployment of these navigational

Table 2.1. IEEE standard radar-frequency letter band nomenclature.

Band Designation	**Frequency Range**	**Wavelength**
HF	3-30 MHz	dekameter
VHF	30-300 MHz	meter
UHF	300-1000 MHz	
L	1-2 GHz	decimeter
S	2-4 GHz	
C	4-8 GHz	
X	8-12 GHz	centimeter
K_u	12-18 GHz	
K	18-27 GHz	
K_a	27-40 GHz	
V	40-75 GHz	millimeter
W	75-110 GHz	

systems (e.g. Knickbein, X-Gerät, and Wonton), and the countermeasures taken by England occurred during the so-called "Battle of the Beams" as chronicled by Jones [15]. During this time, klystron oscillators were developed to amplify radio waves into even higher frequency bands (refer to Table 2.1), which greatly benefited the advancement of radar as well as long distance communications. Using radar, it was possible to remotely determine the velocity of a moving projectile, and this influenced much of the design of MI systems into the late 1940's and early 1950's. Researchers from multiple countries also began the construction of Michelson-type interferometers using the klystron oscillators as a microwave source; see for example the development history given by Froom (1952) [5].

The 1950's: The first documented studies of MI applied to explosives were performed by Lochte-Holtgreven and Koch in Germany during World War II [16].

However, this report was not available until it was published in the proceedings of the French Academy of Sciences by Koch (1953) [17]. The original work consisted of a klystron source operating at 2.0 GHz, which transmitted and reflected microwave radiation through the air via an antenna (see Fig. 2.1(a)). Koch was able to observe a detonation wave in a 1:1 mixture of TNT and RDX, and measured a detonation velocity of 7994 m/s with 3.5% error. In this configuration, microwaves were reflected off the ionized detonation products, and the experiments resembled the operation of radar.

Meanwhile, similar free-field experiments were reported by Cook, Doran, and Morris (1955) [18] in the U.S. using a klystron source operating at 9.4 GHz with a horn antenna. Their test samples were unconfined cylinders cast out of four explosives: TNT, 50/50 Pentolite, 50/50 Amatol, and 80/20 Tritonal. They observed detonation velocities with as much as 6% error compared to ionization pin results. The charge diameters also varied between 5 and 20 cm, and it was observed that the larger diameters obscured the fringe patterns recorded. The researchers concluded (correctly) that the explosive charges act as dielectric wave guides, with multiple modes of propagation at the larger diameters. Farrands and Cawsey (1955) [7] in Australia immediately criticized the work of Cook *et al.*, suggesting that the results were further obscured by multiple sources of reflection; i.e. both the detonation wave and the ionized detonation products expanding laterally from the sides of the charge.

The original MI study by Farrands and Cawsey (1955) [7], later expanded by Cawsey, Farrands, and Thomas (1958) [1], used a klystron oscillator at 34.5 GHz and an explosive-filled waveguide (see Fig. 2.1(c)) to observe granulated tetryl. Only the lowest TE mode was propagated at 34.5 GHz, which dramatically improved the fringe pattern and simplified analysis. Furthermore, Cawsey *et al.* determined the measurement error associated with MI to lie between 1-2% based on parameter estimation. In summary of the sources of error, a 1% uncertainty in density was shown to propagate a 1.5% uncertainty into velocity (which corresponds to approx. 0.5% uncertainty in tube diameter); also, a 0.5% uncertainty in the explosive dielectric constant

was shown to propagate a 0.7% uncertainty into velocity. To facilitate an accurate analysis of the MI signals, dielectric constants were measured at 34.5 GHz for tetryl, TNT, PETN, and RDX-based explosives for nine packing densities from 0.9 to 1.7 g/cm^3. Overall, the error calculations led the authors to believe the main advantage of MI was not the ability to measure velocity with greater accuracy; rather, it was the set of new opportunities to observe detonation phenomena including variations in velocity due to density, effects of diameter and confinement, contact transmission, and instabilities in the detonation front.

In summary of the MI study conducted by Cawsey *et al.* [1], the MI waveguide consisted of brass tubing 15.2 mm outer diameter, 3.86 mm inside diameter, 50.8 mm long, with the tetryl pressed inside to a density between 1.3 and 1.6 g/cm^3. The velocity data showed a linear increase with increasing density, and provided evidence of a diameter effect, as all measured values were less than the infinite diameter velocity. Additional experiments were performed to measure density gradients due to the pressing, as well as growth to detonation from about 1 km/s to 6.5 km/s; these later studies were achieved by placing a small air gap between the lead azide initiator and tetryl column. A slightly modified theory of growth from Eyring (1945) [19] was then applied to the transient velocity profiles to determine a reaction zone length of 0.4 mm and activation energy of 2 kcal/mole, as fitting parameters.

The work of Koch [17], Cook *et al.* [18], and Cawsey *et al.* [1], is almost exclusively cited when reviewing the origins of the MI technique; however, Boyd and Fagan (1955) [20] described a MI system in the 2nd International Detonation Symposium, being used at LASL on a regular basis. Specifically, a klystron oscillator at 9.3 GHz was used to send microwaves through a rectangular waveguide and then transmitted into a flexible coaxial cable. The cable was terminated into a probe attached directly to an explosive-filled waveguide, as shown in Fig. 2.1(b). The authors had machined a small, cylindrical bore out of a larger diameter explosive charge, and fitted the explosive-filled waveguide into the center axis. Although the technique is semi-intrusive, the waveguide was formed out of two layers of 0.5 mil foil and inserted with

silicone grease to ensure good contact; these foil layers did not significantly interfere with the measured run distance to detonation, and no limitations were placed on the charge diameter. The conclusions of Boyd and Fagan are also similar to Cawsey and Farrands [7]; namely, that the accuracy of the technique is limited between 1-2%, and MI holds an advantage over other measurement techniques when the detonation velocity is non-steady.

Finally, the first documented study of MI applied to the measurement of a shock wave velocity was reported by Hey, Pinson, and Smith (1957) in the U.K. [2]. A klystron oscillator at 5.0 GHz was attached to a steel shock tube having cross section 5.4 cm^2 and filled with argon. The high pressure section was filled with hydrogen near 30 Atm, and the resulting shock wave was observed to decay from approximately Mach 10 to Mach 8 over a 12 meter long section.

The 1960's: The only substantial reports of MI applied to explosives were made by Johnson (1965) [10, 21, 22] working for the Rohm and Haas Co. at the Redstone Arsenal in the U.S. These studies used X-band and K-band frequencies transmitted through an expendable polystyrene (PS) dielectric waveguide to investigate shock initiation near the 50% card gap level. The explosives consisted of Composition C-4, ammonium perchlorate (AP), and Pentolite, with charge diameters between 2.5 to 5 cm, and weak confinement (cardboard and glass), or no confinement at all (explosive pellets). The experimental configuration is shown in Fig. 2.1(d), and permitted larger charge diameters than the explosive-filled waveguides used by Cawsey *et al.* [1]; however, problems launching a pure mode into the test samples limited the maximum diameters near 5 cm. The work was significant in that detailed growth to detonation measurements were made near the large scale initiating shock pressures; the MI results were also confirmed by simultaneous streak camera photographs and witness plate dents to provide validation of the technique.

The first measurements on gaseous detonations were made in the 1960's by Edwards, Job, and Lawrence (1962) [23], following a similar experimental technique

to Hey *et al.* [2]. The research was motivated by the study of marginal detonation waves, and employed a supersonic detonation tube, 15 m long and 5 cm dia., with premixed hydrogen and oxygen at the stoichiometric ratio. The results of the work include steady velocity measurements slightly below the predicted value, as well as intermittent and periodic instabilities near a low pressure limit of 40 kPa.

Although MI had matured somewhat for explosives by the end of the 1960's, new investigations with solid propellants began to appear; these studies of MI applied to propellant burning rate measurements presided over the literature for the next two decades. During this time, solid rocket motors were developed for intercontinental ballistic missiles (ICBM) and later the Space Shuttle Solid Rocket Boosters (SRBs). Significant technical challenges in the propellant community were understanding rapid depressurization and acoustic instabilities, so new measurement techniques were needed to investigate transient burn rate data; hence, many of the initial reports applying MI to propellant burn rates were classified. One of the first documented studies was made by Johnson (1962) working for Giannini Controls Corp. [24], which contained time-resolved strand thickness and burning rate measurements. The report discussed current problems associated with burn rate measurements, and demonstrated the applicability of MI with increased sensitivity from the inclusion of a magic tee coupler. A similar report was made by Jenks *et al.* (1963) [25] using a 10 GHz microwave source frequency.

Another contribution to MI burn rate measurements was that of Cole (1965) [26] using a K-band 24.0 GHz klystron oscillator. Cole, as well as Johnson [10, 21, 22], worked for the Rohm and Haas Co. and collaborated on the development of MI techniques for explosives and propellants. The work of Cole is interesting in that propellant regression rates were investigated using a self-pressurizing closed bomb, for pressures up to 1.4 GPa. The MI technique was needed in order to simplify the design of the bomb, and resolve the transient regression rates under increasing pressure. This work was motivated by understanding the malfunctions of rocket motors, and bridging the gap between deflagration and detonation regimes; ultimately, a non-aluminized

25%PBAA/75%AP propellant was chosen for study due to the absorption of the MI radiation in some aluminized samples. Initial results were promising, yet some error was introduced as the dynamic pressurization affected the material dielectric properties.

Later MI studies with propellants used increasingly higher frequency bands for greater spatial resolution. These examples include a paper by Dean and Green (1967) [27], which demonstrate two applications of near field experiments. The authors report using a 37.5 GHz klystron source and a microwave horn to make either burn rate or porosity measurements through an optical port on a solid rocket motor. The paper was extended in a technical note by Green (1968) from the Rocket Propulsion Establishment in the U.K. [28]. A preliminary and final report were also made by Wood (1968,1970) [29, 30], working under a NASA grant at the Virginia Polytechnic Institute. Wood conducted experiments on a BF 117 propellant, using a 30 GHz klystron source with a microwave horn and phase-correcting lens. At this time, the source of the microwave reflections in propellants was not well understood; Wood was probably the first to express doubt in the source of the reflections as the propellant flame zone.

The MI studies previously described for propellants did not achieve continuous measurement of the regression rate; analysis was essentially based on a peak picking technique. A progression towards higher frequency bands (from about 10 to 30 GHz) could only decrease the material wavelength and increase spatial resolution so far. By the end of the 1960's, Shelton (1967) [31] at the Jet Propulsion Laboratory had pioneered a high-resolution, fast response microwave network analyzer for increased spatial resolution. The experimental apparatus of Shelton was acquired by Strand [32–37], who continued to improve the technique into the early 1980's.

The 1970's: Advancement of the MI technique applied to solid propellants continued to receive much attention in the literature throughout the 1970's. With the development of new microwave circuitry, including the network analyzer and other

digital analyzers, lower X-band and K-band frequencies were able to achieve greater spatial resolution than higher frequency MI systems relying on a simple peak picking analysis. A technical report by Schuemann *et al.* (1971) [38] from Hercules Inc., Allegany Ballistics Laboratory, considered multiple MI layouts with a 9.6 GHz solid-state microwave source and on-line computer for data processing. Burn rate measurements were reported for three different propellants (FMA, KAA-114, and a fluorocarbon), and the source of the microwave reflection was assumed to be the highly ionized propellant flame. A paper by Gittins *et al.* (1972) [39] reports quasi-stationary burn rates in a rocket motor with acoustic mode instabilities; Gould and Penny (1973) [40] used MI with a T-burner and KT-rocket motor configurations, and measured steady and oscillatory regression rates for the propellant ANB-3066. Most of the early rocket motor work assumed the source of the reflections to be the luminous propellant flame.

Over the course of time, Shelton moved from the Jet Propulsion Laboratory to the Georgia Institute of Technology; he took the design for a continuous phase measurement system based on the microwave network analyzer and a propellant filled waveguide. Shelton was the principal investigator in a report by Alkidas *et al.* (1974) [41], which utilized a 9.13 GHz source frequency to measure burning rates of a carboxyl-terminated polybutadiene/ammonium perchlorate (CTPB/AP) composite solid propellant during steady state, as well as rapid depressurization. The accuracy of the transient measurements was demonstrated to be $\pm 10\%$ in burning rate, for depressurization rates up to 17.5 MPa/sec. The report was also noteworthy for completely abandoning the idea of microwave reflection by a highly ionized, almost metallic propellant flame.

Oscillatory combustion and rapid depressurization were of significant interest during this time, and Strand *et al.* (1972) [32] determined that a spatial resolution of 10 μm or better was needed to define the regression rate curve. Using the apparatus left by Shelton at the Jet Propulsion Laboratory, Strand and co-workers performed measurements on four different propellants (with the formulations 20/80 PU/AP, 17/83 HTPB/AP, 25/75 CTPB/AP, and 25/73/2 CTPB/AP/Al) in a combustion

bomb fitted with a burst diaphragm, and also a T-burner assembly. These results were subsequently published in a journal article (1974) [33], although the authors were suspicious of two of their findings: values of the regression rate were slightly negative for the highest depressurization rates tested, and oscillatory regression rates in the T-burner were one to five or more times the measured mean rate. The authors concluded that flame ionization effects introduced some errors.

Afterward, Strand and McNamara (1976,1978) [34,35] applied their MI apparatus to an L^*-burner to focus on the low-frequency bulk mode response, rather than the higher frequency T-burner and rapid depressurization experiments. These results were more promising than the original work; the authors retracted previous concerns over flame ionization effects, instead siding with Alkidas *et al.* (1974) [41] that the reflections were not influenced by the flame plasma as much as previously thought. The anomalous results in original work by Strand *et al.* [32, 33] were probably due to inadequate frequency resolution of the microwave signals.

Although the original MI system used by Strand had a purported spatial resolution of 10 μm, it was later deemed incapable of measuring unsteady regression rates (quasisteady only). A second generation system was then developed by Strand *et al.* (1979,1980) [36, 37] to have a phase resolution of 10 millidegrees, or equivalently a spatial resolution of about 0.2 μm. The modified design included a custom phase shift measurement system, as well as pressure and burner modulation system to reduce vibrations; overall, these vibrations limited measurements of the propellant response function below $\sim$1 kHz. The real component of the pressure-coupled response function was measured for three propellants (A-13, ANB-3066, and UTP 19360), and compared favorably to data from T-burner and rotating valve methods. By the end of the decade, Russell (1979) [42] had developed a similar MI system for propellant measurements, and presented a detailed model for the burn region.

No substantial work was reported again for solid explosives until the mid-1980's. Nonetheless, it is worth mentioning that Edwards and co-workers continued their research at University College of Wales investigating gaseous detonations with MI. For

example, Edwards *et al.* (1970) [43] applied MI to investigate marginal detonation waves in a stoichiometric mixture of hydrogen-oxygen diluted with argon. Another study by Edwards *et al.* (1974) [44] was made using the detonation tube for galloping detonation waves; the gaseous mixture of $C_3H_8+5O_2+ION_2$ and initial pressure were selected to match previous work using discrete pressure probes. Edwards *et al.* (1976) [45] also used MI to measure the shock front of spherical detonation waves, initiated in stoichiometric mixtures of propane-oxygen contained in plastic balloons. Edwards and Morgan (1977) [46] returned to investigations of detonation wave instabilities inside their detonation tube with propane-oxygen and hydrogen-oxygen systems diluted with oxygen, nitrogen, or argon. Finally, Edwards *et al.* (1978) applied MI to study the initiation behavior of spherical detonation waves in oxyacetylene; supercritical and critical waves were obtained by varying the energy of an exploding bridge wire initiator. Additional references for MI applied to gaseous detonations may be found by cross-referencing these papers.

The 1980's: The major achievement of the 1970's was the development of MI systems with greater spatial resolution for low-speed deflagration; these advancements were now extended to measurements of detonation waves in solid explosives. McCall, Bongianni, and Gilbert (1985) [47] at Los Alamos National Laboratory were the first to report a continuous MI measurement system applicable to the detonation regime. Their system utilized a 1 W, 8 GHz Impatt oscillator fed to a quadrature mixer with two-channel output. Microcoaxial or stripline cables were used to conduct the MI signal into the interior or along the outside of an explosive charge; the technique did not rely on an explosive-filled waveguide so that any charge diameter or geometry could be tested.

The minimum spatial resolution of the MI system used by McCall *et al.* was reported to be 0.2 mm, which is larger than the 0.2 μm resolution achieved by Strand *et al.* (1980) [37]; this observation does not imply an inferior system, since the resolution of the MI technique depends on the magnitude of the velocity measurement

and tuning of the system. A "mousetrap" experiment was then conducted for a 25.4 mm thick by 241 mm dia. layer of the explosive PBX-9404. The MI results compared favorably to simultaneous streak camera, wire pin, and foil pin data, showing that the shock trajectory measurement was as good as or possibly better than the other techniques.

Another report by Stanton, Venturini, and Dietzel (1985) [11] at Sandia National Laboratories describes improved resolution of the MI technique for explosive-filled waveguides. The authors explored tuning methods to minimize phase distortion, inclusion of a quadrature mixer, and different source frequencies in the X-band (10.6 GHz), K_a-band (35 GHz), and W-band (91 GHz) in order to improve spatial resolution. The final system utilized a Gunn diode microwave source at 10.6 GHz, two-channel quadrature output signals, and a rectangular or circular waveguide. Measurements were made for the explosives PBX-9404, Composition C-4, HMX, and a low density PETN/glass micro-balloon mixture with an explosive plane wave generator to initiate the charges.

Four different types of experiments were demonstrated by Stanton *et al.* [11] using their MI system, including: steady detonation, detonation transfer, deflagration-to-detonation transition (DDT), and gap tests. Of note, the measured detonation velocity for PBX-9404 was determined to be 2% above the literature value, due to some uncertainty in the dielectric constant. Also, the detonation transfer experiment is particularly relevant to the present work, as it corresponds to an overdriven detonation; the glass micro-balloons were used to sensitize the low density PETN to achieve a steady detonation instead of immediate failure. The DDT experiments in granular HMX paved the way for future studies at Los Alamos (see for example Ref. [48]), and the gap tests were a preliminary indication that run distance to detonation might be measured with MI for shock initiation studies.

The next year, Aničin *et al.* (1986) [12] published a review paper of the MI technique with an emphasis on propellant combustion. The authors used their survey of the literature to challenge the accepted theory for the source of the microwave

reflections (i.e. the highly-ionized plasma in the reaction zone of propellants and explosives). Some experiments were performed using a 35 GHz microwave source and transmission horn with a polyurethane (PU) propellant; the results indicated no significant reflections as the propellant flame passed through the focal point of the microwaves. The authors concluded that the dielectric discontinuity at the solid-gas interface, and not the reaction zone, was the source of the reflections for all MI measurements. This claim, which disregarded the role of flame plasma conductivity, prompted a later response by Krall, Glancy, and Sandusky (1993) [4, 6]. Aničin was only partially correct; some reaction zones in propellants correspond to a lossy dielectric, whereas other well-formed plasmas in detonations make for excellent reflective surfaces.

Outside of the review paper by Aničin, few additional propellant studies were reported. For example, Wood *et al.* (1983) [49] presented results for a 37.5 GHz MI system, to show improved spatial resolution over lower frequencies with the peak picking technique. O'Brien *et al.* (1983) [50] investigated the possibility for multiple reflections from material interfaces and the propellant-combustion zone interface, and simulated some burn rate measurements with a numerical model. Waesche and O'Brien (1987) [51] reviewed three non-intrusive measurement techniques (x-ray video, ultrasonics, and MI) for burn rate measurements in nozzleless motors. Of the three techniques, it was concluded that only MI has a theoretical error much less than 1% and useful for further study.

The 1990's: Following the development of higher resolution MI systems for explosives, investigations of transient shock and detonation phenomena were made in greater detail. Glancy and Krall (1990) [16], working at the Naval Surface Warfare Center, built a MI system based on the circuitry of Stanton *et al.* [11]. They used the technique to investigate some aspects of the shock-to-detonation transition (SDT) and deflagraion-to-detonation transition (DDT) in porous energetic materials. The

microwave source frequency was 8.2 to 12.4 GHz (X-band), and an explosive-filled rectangular brass waveguide 10.2 mm by 22.9 mm was used in most of the tests.

Glancy and Krall verified their MI system by measuring a steady detonation velocity in a porous bed of 73.0% TMD class D HMX. The following study consisted of two HMX beds on either side of a section of 59.4% TMD NaCl, in order to attenuate the leading shock pressure and promote SDT in the second HMX section. Of note, the authors observed strong microwave reflections in the non-reacting NaCl; however, they were unsure whether this was due to ionization or compaction. Additional experiments were run to help determine the source of the reflections, including: explosively driven shock waves in inert powders (60% TMD Teflon 7C and 30% aluminized melamine), a modified gap test with a double-base ball powder (BP), and a piston driven compaction (PDC) apparatus to measure the compaction waves in samples of melamine.

Krall, Glancy, and Sandusky (1993) [4, 6] responded to the criticism of Aničin *et al.* [12] over the source of the microwave reflections. Two papers examined unreacting and reacting porous media with the PDC apparatus. For an inert porous bed consisting of 65% TMD melamine, relatively low speed impacts ∼200 m/s were sufficient to observe partially reflecting compaction waves (which supported only some of the criticism by Aničin). The portion of the MI signal not reflected by the compaction wave was completely reflected by the metal piston face of the PDC apparatus. Hence, the quadrature output signals contained a high-frequency low-amplitude oscillation corresponding to the compaction wave, and a low-frequency high-amplitude oscillation corresponding to the displacement of the piston. These two frequencies may be analyzed to infer a particle and wave velocity, which introduced the intriguing new possibility for Hugoniot measurements with the MI technique.

In a second paper by Glancy *et al.* [6], the PDC apparatus was used to investigate reactive wave build up in a porous ∼60% TMD bed of a double-based ball powder (BP). The initial behavior produced MI reflections similar to the ones observed in non-reacting media. However, as the reactions increased, the piston reflection vanished

indicating that all of the incident radiation was either absorbed or reflected by the reaction zone. The MI amplitude corresponding to the reacting wave was low, until rapid growth to detonation occurred. From these results, it was proposed that hot spots create locally ionized regions behind the leading compression wave. These hot spots are isolated (lossy) and may grow to become interconnected (reflective); the effect of hot spots was simulated by adding ∼400 μm dia. Al particles to the 434 μm dia. BP at a volume fraction of 5, 10, and 15%. Dielectric measurements of these materials in a cylindrical resonator at 9 GHz allowed the authors to extract a plot of hot spot evolution over time from the PDC data. Thus, ionization was shown to play a primary role in reflecting the MI signal during the build-up to detonation; this result was contradictory to the conclusion of Aničin *et al.* [12].

Meanwhile, Luther, Vesser, and Warthen (1991) [52] at Los Alamos National Laboratory developed an X-band microwave interferometer to directly measure particle and shock velocities, as well as the dielectric constant of the shocked material; this work was similar to that of Glancy and Krall in 1990 [16]. Preliminary data was reported for shock-particle velocities over a pressure range of 4 to 30 GPa, with future plans to increase the shock pressure up to 60 GPa, and the microwave source frequency up to the K-band.

Warthen and Luther (1994) [8,53] improved the design of their original system by incorporating a 24-GHz Gunn diode oscillator; one novelty is that the Gunn diode was obtained from a garage door opener, and the complete system was simple, lightweight, inexpensive, and compact in the K-band frequency range (coined 'SLICK' by the authors). Several experiments were performed using SLICK, including some shock-particle velocity measurements of Teflon/grout; this filling was used in holes dug during Nevada Test Site experiments to measure ground shocks. The SLICK measurements for Teflon/grout were shown to agree with data from the Marsh Handbook [54], and supported the use of the Gladstone-Dale model for index of refraction calculations.

Other experiments using SLICK included some free-field detonation measurements with 10.16 cm dia., 5.08 cm long cylinders of PBX-9501. These measurements were made possible with a microwave horn and Teflon axicon, and were probably the first successful free-field experiments since Cook *et al.* in 1955 [18]. The SLICK apparatus was also used to investigate DDT in granular HMX samples that were contained in a circular brass waveguide and initiated with a pyrofuse. Studies of piston-driven DDT in HMX using the MI technique were also continued at Los Alamos (see for example Burnside *et al.* (1997) [48]).

Propellant regression rate measurements using MI appeared in the literature as well. Foss, Roby, and O'Brien (1993) [55] showed preliminary results for a dual-frequency measurement system, with two simultaneous frequencies operating at 9.15 GHz and 10.33 GHz. A motorized reflector moving at 0.44 cm/s was used to simulate the propellant burning surface, and the results indicated some potential for error reduction. Later, Bozic, Blagojevic, and Aničin (1997) [56] at Belgrade University in Yugoslavia developed an experimental propellant burning motor and custom MI system utilizing a 35 GHz Gunn oscillator and horn antenna. The configuration is similar to a cross-flow experiment, allowing for larger propellant samples and wide pressure variations; the chamber conditions were designed to better represent the environment inside a solid rocket motor than a traditional Crawford bomb used for propellant strand burns. Three double-base propellants and three PVC/AP/Al propellants were characterized over the pressure range 2 to 20 MPa, as well as different initial temperatures.

Following the success of their reflection-type MI system and experimental rocket motor, Bozic, Blagojevic, and Aničin (1998) [57] built a second experimental motor for use with a stand-off (or transmission) MI system. Two microwave viewing ports allowed the radiation to be incident on a sample propellant grain; interpretation of the results was more complex as both MI reflection and transmission phenomena were present. Only the transmission of the MI signal was relevant to measuring propellant grain thickness. The theory and data analysis software were verified by a simulated

grain burn, using a moving cone with similar dielectric properties as the propellant samples. Nominal and erosive burning conditions were explored for three formulations of a PVC/AP/Al propellant.

Elsewhere, A master's thesis by J. Lee (1992) [58] describes the development of a coaxial MI system for gaseous detonation measurements. By inclusion of a thin wire along the center of a detonation tube, the dominant mode of propagation becomes the transverse electric and magnetic (TEM) mode instead of the TE mode. Consequently, the electromagnetic waves behave similar to plane waves in free space, and some restrictions are lifted from the geometry of the detonation tubes.

The 2000's: From the turn of the century until closer to 2010, publications on the MI technique mostly appeared in the Russian literature. A lack of documented studies in the U.S. could possibly indicate some maturation of the field. Zarko, Vdovin, and Perov (2000) [13] gave a brief literature review of propellant measurements, and classified all of the previous techniques into one of three categories (free-field, propellant-filled waveguide, or slab configurations with a horn-lens antenna). The authors then built a custom MI system using a 139.8 GHz Gunn oscillator in the centimeter wavelength; this system was tested with different double-base and composite PB/AP and AP/PMMA/Al propellants. Although the higher frequency greatly improved spatial resolution, the smaller wavelength was on the same length scale as the burning surface roughness and sample heterogeneities, leading to distortion of the output signal. A full list of the potential sources for error and suggestions for future MI systems were discussed.

Multiple investigations of shock and detonation phenomena were also performed at the Institute of Experimental Gas Dynamics and Physics of Explosion (IEGDPE) of the Russian Federal Nuclear Center-Institute of Experimental Physics (RFNC-VNIIEF) [14]. A common 93.7 GHz single-channel MI system was used in each of the studies. Following the work of Krall *et al.* [4], Rodionov *et al.* (2005) [59] made successful shock-particle velocity measurements for porous PTFE. Kanakov *et al.*

(2007) [60] developed a more comprehensive theory for multimode interferometry; of which shock-particle velocity calculations are one example.

Bogdanov *et al.* (2007) [61] (and later Bel'skii *et al.* (2011) [14]) report for the first time MI measurements of explosively driven aluminum flyer plates. This type of experiment is widely accepted for calibrating an explosives product equation-of-state (EOS); however, when using MI the authors found that it is also possible to measure the highly ionized air shock in front of the flyer plate. As proof of their claim, the explosive experiments were repeated in rarefied air and helium, in order to change the shock pressure for which ionization occurs. The MI results were compared to simultaneous optical VISAR data; the velocity curves matched only when no significant ionization was present.

Many of the shock and detonation measurements by Russian investigators appeared in foreign conference papers; Kanakov *et al.*(2008) [62] published some of these results in a journal paper. A wide survey of different experiments were reported, including: a pendulum test for system calibration, explosive acceleration of a 2.2 mm thick steel plate by TNT, sympathetic detonation of explosive rods resulting in multimode propagation, and a shock-particle velocity measurement for plastic fluor (accurate to the Hugoniot curve determined in other work).

Finally, Rodionov *et al.*(2009) [63] applied MI to determine the run distance to detonation for a SDT event with plastic bonded HMX and TATB explosives. The plastic-bonded HMX charges were 60 mm dia. by 20 mm long, and the plastic-bonded TATB charges were 90 mm dia. by 40 mm long; both charges were pressed to a density of $\sim$1.89 g/cm^3 and initiated with variable pressures up to 24 GPa (controlled by the gap thickness of an aluminum or copper plate). This work was significant as the first documented study leading to quantitative shock initiation measurements (i.e. Pop-plot data) with MI. A summary of the Russian experiments may be found in a review paper by Bel'skii *et al.*(2011) [14], including some additional results e.g. a shock-particle Hugoniot for benzene, structural dynamics measurements for explosive confining chambers, and acceleration of explosively driven projectiles.

The 2010's: New and on-going research in the U.S. suggests a possible revival of the MI technique. Rae *et al.* (2011) [9] at Los Alamos National Laboratories describe a free-field 34 GHz MI system utilizing a high directivity horn antenna, which was used to measure shock and detonation velocities inside 25.4 mm dia. cylinders of PBX-9501. This was not the first modern free-field apparatus (see for example Refs. [8, 53] from 1994); however, the high quality of the MI signal allowed the authors to observe shock front breakout and subsequent run to detonation when an aluminum shock attenuator was placed in the samples.

Besides the work at Los Alamos, most current research seeks to leverage the MI measurements in new and novel ways, rather than improve the circuitry or spatial resolution. Tringe and co-workers at the Lawrence Livermore National Laboratory are investigating DDT and SDT phenomena in greater detail. Tringe *et al.* (2014) [64] were the first to simulate transient MI data for low-density HMX powder and Composition B using an Ignition and Growth reactive flow model. Kittell *et al.* (2014) were able to compare MI data for velocity measurements in low density TATB with thermochemical equilibrium calculations; some preliminary work on modeling SDT was also discussed. Janesheski *et al.* (2014) [65] published transient overdriven detonation failure data for some non-ideal explosives, that might possibly be useful for calibration and validation of explosives models.

Finally, some work was performed to address the low-quality MI signals inherent to some detonation phenomena and explosives of interest. Kittell *et al.* (2014) discuss new time-frequency analysis techniques based on a continuous wavelet transform (CWT) to achieve a more robust data analysis. Kittell *et al.* (2015) also give a comparison of previous analysis techniques for both high and low quality MI signals; a fully automated Gabor wavelet transform was found to be most effective for the different MI signals studied, using a Gabor wavelet shaping factor of 4.

3. EXPERIMENTAL METHODS

3.1 Experimental Apparatus

The experimental apparatus is similar to the ones used in previous work by Janesheski *et al.* [65] and Kittell *et al.* [66–68]. A description may be found in Ref. [68], reproduced here with permission from the editors: a 35 GHz signal was generated using a custom microwave interferometer and transmitted to the test article through a solid 0.635 cm dia. polytetrafluoroethylene (PTFE) waveguide. A quadrature mixer was used to produce two-channel output 90° out of phase, and was recorded at 2.5 GHz using a Tektronix DPO4034 digital phosphor oscilloscope. The MI output was de-sampled to 100 MHz for data analysis, and the highest frequency content of the output signal was below 4 MHz. Timing of the experiment was based on first light observed by fiber optics: a M34L02 Thorlab patch cable with a 600 μm core diameter transmitted light to a DET10A Thorlab photodetector with a 1 ns rise time. The detonation event was contained inside a thick-walled steel box; a schematic of the experiment is shown in Fig. 3.1. Triple shielded Pasternack coaxial cables (PN: PE-P195) were used to transmit the MI output and fiber optic signal to the Tektronix oscilloscope, located in a separate control room.

High explosives were pressed into four different charge configurations as summarized in Table 3.1 and shown Fig. 3.2. The charge configurations were selected based on preliminary work, in an attempt to tailor the behavior of the failing overdriven detonation waves. Confiner materials consisted of 304 stainless steel and polyvinyl chloride (PVC); the I.D. of each confiner was either 6.52 or 11.28 mm, and the length of the charges was 10.16 cm. Machining tolerances in diameter were requested to be $\pm$0.05 mm. A Teledyne Risi, Inc., RP-502 exploding bridge-wire (EBW) detonator was used to initiate a detonation in a booster explosive, which transitioned into the

test article. The booster consisted of PRIMASHEET® 1000 (Ensign Bickford), and the test article consisted of a stoichiometric mixture of Kinepouch™ (Orica Mining Services) and diesel fuel, as discussed below and in Sec. 5.2.1. Material properties of the explosives including density and permittivity may be found in Appendix C.

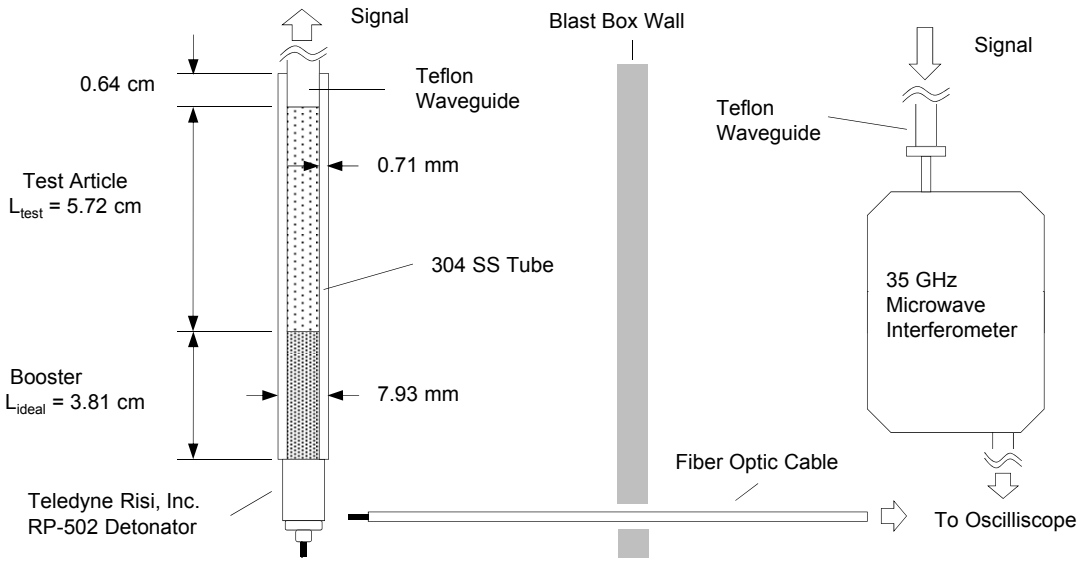

Figure 3.1. Schematic drawing of the microwave interferometer and small diameter stainless steel test article (not to scale). Reproduced with permission from Ref. [68].

Figure 3.2. Picture of all assembled charges and a detonator holder (left), and side-by-side comparison of the different charge configurations (right) for THK, PVC, THN, and SM in descending size.

Table 3.1. Summary of the charge configurations and their abbreviations used throughout the work.

Abbr.	**I.D.**	**Confiner Material**	**Thickness**	m_{Sample}	$m_{Booster}$
	(mm)		**(mm)**	**(g)**	**(g)**
SM	6.52	304 Stainless Steel	0.7	1.55	1.86
THN	11.28	304 Stainless Steel	0.7	4.67	5.59
PVC	11.28	304 Stainless Steel	0.7	4.67	5.59
		PVC outer layer	19.1	4.67	5.59
THK	11.28	304 Stainless Steel	32.5	4.67	5.59

3.2 Sample Preparation

The Kinepouch™ explosive was dried in a convection oven at 60 °C for 24 hours prior to use, and then mixed with 5.32 wt.% diesel fuel for 8 minutes at 80% intensity on a Resodyn (Butte, MT) Lab RAM acoustic mixer. The explosive was mixed in batch sizes of 100 g and was given the name of ANFO KP-1, i.e. Kinepouch™ ammonium nitrate plus fuel oil mixed using formula No. 1. The baseline ANFO KP-1 and PRIMASHEET® 1000 booster explosives were incrementally pressed into the different charges with a Carver 25 ton press, with the following procedures.

A common set of Nylon™ and PVC shims were used to achieve nominal pressing increments of 9.53 mm, with incremental L/D ratios near 1.5 and 0.8 for the smaller (6.52 mm) and larger (11.28 mm) diameter charges, respectively. Pressing was done to a stop, maintaining a low hydraulic line pressure less than 1 MPa. An interactive spreadsheet was used to manage the pressing, which required mass and length measurements after each increment. These measurements allowed for on-the-fly density estimation, as well as mass corrections in order to achieve the target bulk density. Without these on-the-fly corrections, the target density is usually missed in one of two ways: (1) the booster explosive relaxes over time to a density near 1.44 g/cm^3,

compressing the ANFO KP-1 above it, and (2) the location of the interface between explosives cannot be measured after the first increment of the ANFO KP-1 explosive has been pressed. Additional precautions included pressing the booster explosive 24 hours prior to the test explosive. In this work, the target density was 1.44 g/cm^3 for PRIMASHEET® 1000, and 0.826 g/cm^3 for ANFO KP-1 corresponding to 50% of the theoretical maximum density (TMD).

3.3 Testing Notes

Several observations were made during the testing, which appear to affect the MI output signal quality. These observations are documented here for the reproducibility of the work, and to inform future researchers of the techniques. The observed MI signal quality may be low for a number of different reasons (see for example Ref. [68]); only two of these effects may be mitigated in the experiments. These effects include the presence of an electromagnetic impulse (EMP) originating from the EBW detonator, and losses in the PTFE waveguide.

Because of some dissipative losses, the PTFE waveguide should be kept as short as possible. Usually, the MI is positioned on top of the blast chamber, minimizing the distance to the explosive charge while providing just enough shielding so that the system is not damaged by high velocity fragments (see Fig. 3.3). It is best to attach the waveguide with a friction fit, as excess tape, glue, etc. may act as an antenna on the waveguide and increase signal losses. A custom PTFE insert was made for the port on the blast chamber as shown in Fig. 3.3; this should be the only piece in contact with the waveguide in addition to the MI and explosive sample. Some taper should be cut into the waveguide as it enters the rectangular cross-section tubing of the MI system; no taper is needed fitting the larger 11.28 mm diameter charges when using the PTFE charge adapter piece (visible in Fig. 3.2).

Mitigating the EMP from the EBW detonator is more complicated; however some basic guidelines are provided. Only the highest quality shielded coaxial cables (e.g.

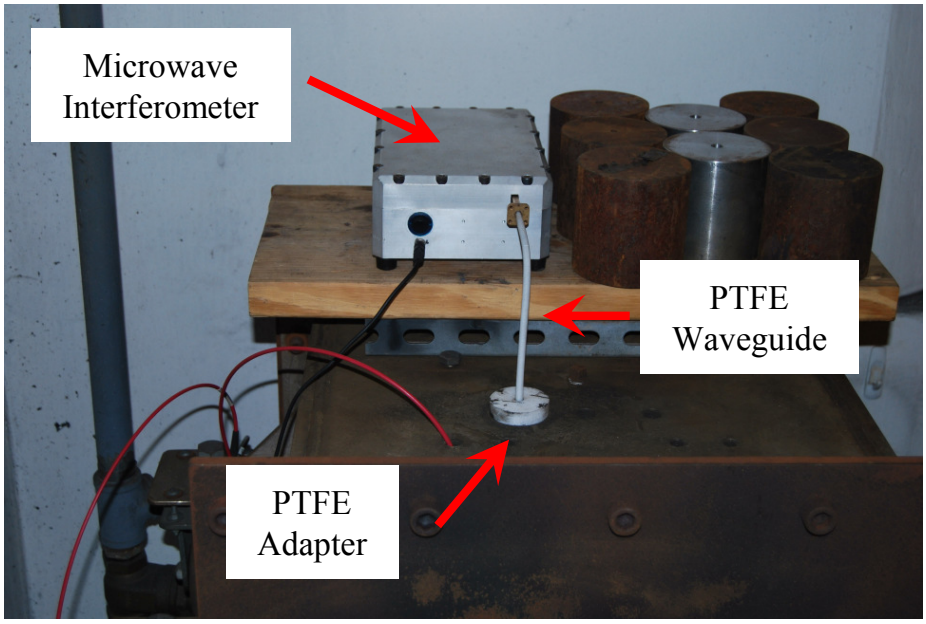

Figure 3.3. Location of MI system and shortened PTFE waveguide for best results.

Pasternack PN: PE-P195) are recommended to transmit the MI signals to the oscilloscope. In addition, the CDU lead lines should be shielded, kept as short as possible, and physically separate from the coaxial cables (routed through different ports between the test cell and control room). The shielding in the CDU leads may deteriorate with use and should be inspected often. Longer wires with less shielding always produce a more significant EMP in the MI data.

One additional technique that appears to mitigate some of the influence of the EMP is the length and placement of the EBW leads. The firing circuit should consist primarily of twisted pair shielded wires; the EBW leads are shorted (after the charge is installed in the blast chamber) as shown in Fig. 3.4. Electrical tape is used to cover any exposed metal showing in the leads, and the entire firing circuit should be inspected for pinched wires. A final step is to place external steel shielding over the remainder of the EBW leads, as shown in Fig. 3.5. In this way, the bare EBW leads are sandwiched between the blast chamber and the steel plates. These guidelines do not guarantee that the EMP will disappear from the MI signal; rather, these

techniques have evolved as best practice which appear to increase the likelihood for acquiring higher quality MI data.

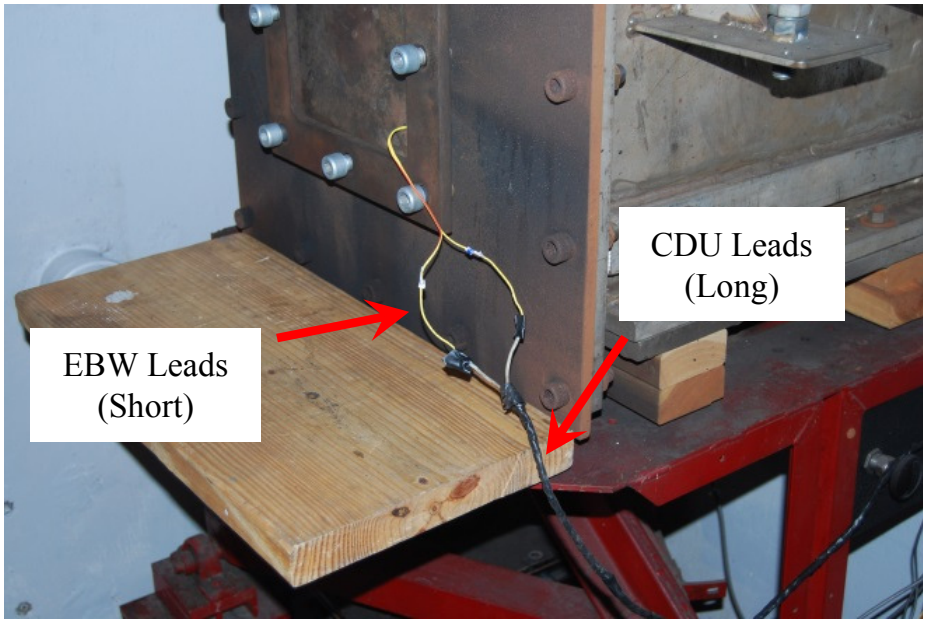

Figure 3.4. Appropriate length of shortened EBW leads for best results.

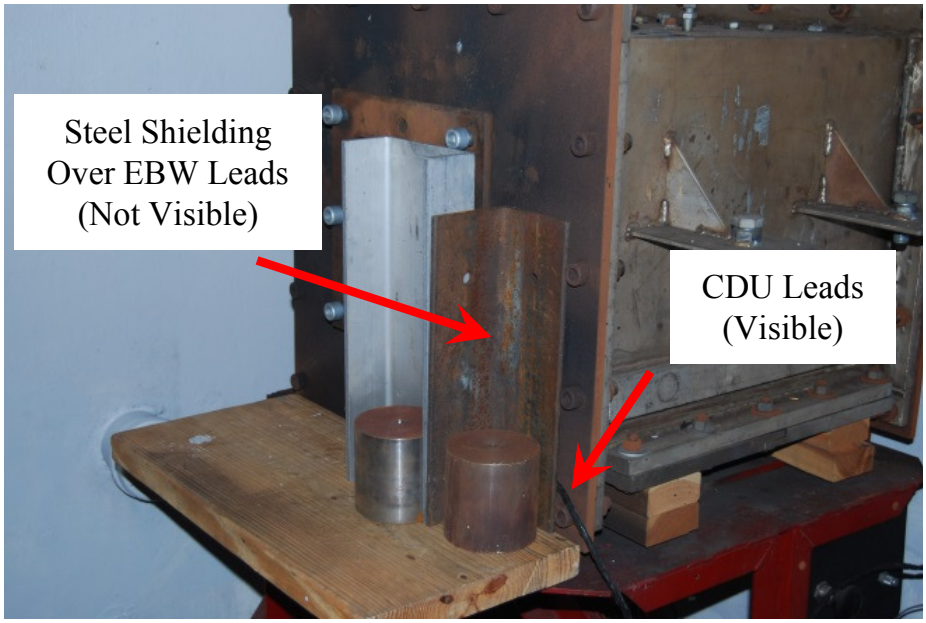

Figure 3.5. External steel shielding of EBW leads for best results.

4. DATA ANALYSIS

4.1 Theory

Previous work [4, 6, 16] has established that microwave reflections in explosives occur due to dielectric discontinuities from shock and compaction waves, as well as highly ionized detonation products. Three different scenarios for microwave reflections utilizing a hollow or explosive-filled waveguide are shown in Fig. 4.1. For the hollow waveguide with a piston reflector, an interference signal is produced as the sum of two reflected waves. One of these reflected waves is from the MI transmission line and is of constant phase; the other is reflected from the moving surface and goes through a phase shift of 2π for each displacement of the moving surface by exactly one half wavelength. When the reflector is moving with a uniform velocity, an interference pattern is observed with a constant frequency.

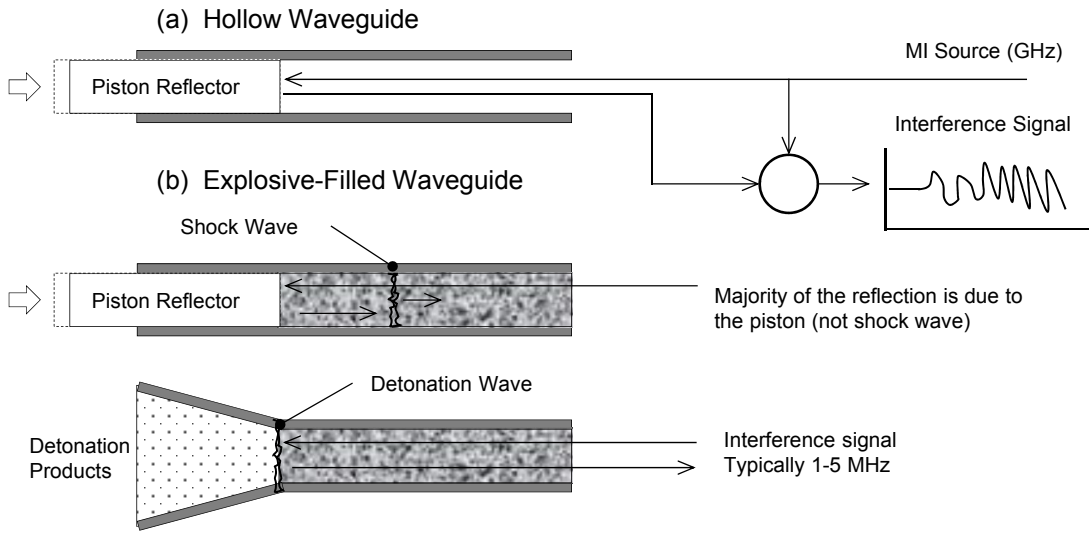

Figure 4.1. Possible moving reflectors in waveguides for the MI analysis.

When the hollow waveguide is filled with an inert material transparent to the microwave radiation, shock and compaction waves change the dielectric constant only slightly to create a partial reflector. If a piston is used to support the compression wave that is also a reflective surface, it may be able to produce a stronger amplitude reflection than the one from the leading wave. In this case, two frequencies are observed in the interference pattern: one for the piston and one for the shock wave.

A strong reflection is caused by a detonation wave and is depicted at the bottom of Fig. 4.1. Because of detonation speeds on the order of a few km/s, and the dielectric properties of most explosives, the output signal frequency content is usually between 1-5 MHz. The strong reflection of the microwaves is due to the highly ionized detonation products [6] so that the detonation front appears as a thin metallic sheet. However, during a shock to detonation transition (SDT) or deflagration to detonation transition (DDT), intermediate reaction with lower electron density may cause the microwaves to be absorbed in the reaction zone. Consequently, for SDT and DDT there may be a sudden jump in signal amplitude as the strength of reflection increases from the coalescence of a detonation wave.

Any MI output signal may be converted into a velocity-displacement curve through an exact knowledge of the wavelength inside the waveguide (λ_g). For steady detonation velocities and high-quality signals, a simple peak picking analysis technique is relatively straightforward to apply; however, when the detonation velocity is varying with time and the signal quality is low or very poor, more advanced analysis techniques are needed. Some of the more advanced techniques are discussed in Sec. 4.3.

4.2 Equations

Beginning with an overview of dielectric material property calculations, all dielectric materials are defined by a complex permittivity,

$$\epsilon = \epsilon' - j\epsilon'', \tag{4.1}$$

where the real component is normalized by the permittivity of free space ϵ_0,

$$\epsilon_r = \epsilon'/\epsilon_0, \tag{4.2}$$

and ϵ_r is the relative permittivity or dielectric constant, sometimes denoted K. The dielectric constant is a measure of the material's ability to store electric field energy and is a function of the frequency of the external field. In a two-component system, it may be estimated according to the Landau-Lifshitz/Looyenga (LLL) mixture equation [4],

$$\epsilon_r{}^{1/3}\,(mix) = \left(\epsilon_{r_A}{}^{1/3} - \epsilon_{r_B}{}^{1/3}\right) V_A + \epsilon_{r_B}{}^{1/3}, \tag{4.3}$$

where V_A is the volume fraction occupied by material A. To account for porosity in a single component system, component B may be taken as air with $\epsilon_{r_B} = 1$. In this case, a reasonable approximation to determine the dielectric constant of a porous crystalline material is,

$$\epsilon_r{}^{1/3} \approx \left(\epsilon_{r,TMD}{}^{1/3} - 1\right) \frac{\rho_0}{\rho_{TMD}} + 1, \tag{4.4}$$

where ρ_0 is the porous density and ρ_{TMD} is the theoretical maximum density.

Now, the wavelength inside the explosive filled waveguide may be calculated according to [1]

$$\lambda_g = \lambda_0 / \left[\epsilon_r - (\lambda_0/\lambda_c)^2\right]^{1/2}, \tag{4.5}$$

where λ_g is the wavelength inside the waveguide, λ_0 is the free-space wavelength, and λ_c is the cut-off wavelength for the empty waveguide ($\lambda_c = 3.413R$ for a tube of radius R). This is the wavelength needed for all velocity calculations, and is a function of the microwave frequency, f_0, as well as the sample diameter.

When designing new experiments, it is possible to determine a range of sample diameters suitable for testing at a particular microwave frequency, f_0, and dielectric constant, ϵ_r. The constraint is given by [1]

$$\frac{c}{3.413R\sqrt{\epsilon_r}} \leq f \leq \frac{c}{2.613R\sqrt{\epsilon_r}}, \tag{4.6}$$

where c is the speed of light in a vacuum and R is the radius of the waveguide. The lower bound corresponds to the lowest TE mode which can propagate through

a waveguide of radius R, and the upper bound with the next highest mode of propagation.

The complex part of the permittivity in Eq. (4.1) is related to dissipative or heating effects as source radiation passes through the material. Like the dielectric constant, it is also a function of the frequency of the radiation; often, it is reported by the loss tangent as

$$tan\,(\delta) = \epsilon''/\epsilon'. \tag{4.7}$$

Cawsey [1] finds that a loss tangent of $tan\,(\delta) = 0.03$ shows an exponentially growing set of fringes inconvenient over a sample length of 5 cm. Many explosives exist with loss tangents considerably less than 0.03, and this datum should be used when considering a new material for the MI technique. A loss tangent larger than 0.03 will not make for a good dielectric waveguide filler material.

Inside the waveguide, the dominant transverse electric (TE) mode of microwave propagation has the associated wave impedance

$$Z\,(TE) = \frac{\eta_0}{\left[\epsilon_r - (\lambda_0/\lambda_c)^2\right]^{1/2}} = \left(\frac{\eta_0}{\lambda_0}\right)\lambda_g, \tag{4.8}$$

where η_0 is the free-space impedance defined by the permeability, μ_0, and permittivity, ϵ_0, of free-space via $\eta_0 = \sqrt{\mu_0/\epsilon_0}$. The impedance may be used to extract information from the amplitude of the MI signal according to the amplitude reflection coefficient,

$$\Gamma = \frac{Z_1 - Z_2}{Z_1 + Z_2} = \frac{\lambda_{g_1} - \lambda_{g_2}}{\lambda_{g_1} + \lambda_{g_2}}, \tag{4.9}$$

where the subscripts 1 and 2 denote the material before and after the location of the reflection, respectively. If the amplitude reflection coefficient has been calibrated to a known peak-to-peak output voltage, additional information may be determined such as the wavelength behind a shock wave. Krall *et al.* [4] have used this technique to estimate the density immediately behind a shock wave in melamine; Glancy *et al.* [6] extended the technique for the shock-to-detonation transition (SDT) to calculate a quantity thought to be related to the percent of reacted material.

Having developed the necessary equations to solve for λ_g, an analysis of the non-reacting case in Fig. 4.1 is discussed first. Once both of the interference signal frequencies have been determined, the leading shock velocity is calculated as [4]

$$U_s = \frac{\lambda_{g1}}{2} f_1, \tag{4.10}$$

where U_s is the shock or compaction wave velocity, λ_{g1} is the wavelength of the uncompressed explosive, and f_1 is the higher frequency associated with the wave motion. When a second frequency, f_2, is determined from a supporting piston, particle velocity is calculated as [4]

$$u_p = \frac{U_s}{\lambda_{g1}} \left(\lambda_{g1} - \lambda_{g2}\right) + \frac{\lambda_{g2}}{2} f_2, \tag{4.11}$$

where state 2 is located just behind the leading shock wave.

Detonation velocity measurements are simplified by the observation of a single dominant frequency in the MI output signal. A fundamental velocity-frequency relationship is given as [4],

$$v\left(t\right) = \frac{\lambda_g}{2} f\left(t\right) \tag{4.12}$$

where $v\left(t\right)$ is the time-varying velocity of the detonation wave, $f\left(t\right)$ is the time-varying frequency content of the MI output signal, and λ_g is the material wavelength as defined by Eq. (4.5).

4.3 Analysis Techniques

Four different analysis techniques are used to analyze the two-channel MI output, consisting of discrete peak-picking, phase unwrapping (i.e. quadrature analysis), and two time-frequency analysis methods using either a short-time Fourier transform (STFT) or a continuous wavelet transform (CWT). These analysis techniques are derived in Sec. 4.3.1 through 4.3.5, and compared in Sec. 4.4. The comparison is made based on experimental data consisting of transient detonation phenomena observed in triaminotrinitrobenzene (TATB) and ammonium nitrate plus urea (ANUR) explosives, representing high and low quality signals, respectively.

Much of the work in Sec. 4.3 and 4.4 has been reproduced from D. E. Kittell, J. O. Mares, and S. F. Son, "Using time-frequency analysis to determine time-resolved detonation velocity with microwave interferometry," Review of Scientific Instruments, volume 86, issue 4 (2015) with kind permission from the editors. In addition, the calculations were implemented in MATLAB R2013b using functions from the Wavelet Toolbox™ and WaveLab 850 from Stanford University. For this work, several custom codes were also packaged into a digital signal processing folder (named 'DSP'); when this folder is added to the current MATLAB path, it may be accessed via the command 'aboutdsp.' These codes include high-level routines for STFT, CWT, spectral decomposition, filtering, sampling, and efficient numerical derivatives, among other operations.

A common set of data analysis procedures was identified for each technique, and is summarized here for organization. The pre-treatment of the signal consisted of a low-pass filter to eliminate high-frequency noise, and the signal was cropped from the initiation of the booster to the end of the test article. A scaled time variable, $\hat{t}$, was introduced to account for the discontinuous jump in velocity at $t = 0$; it is defined by the piecewise equation,

$$\hat{t} = \begin{cases} (2/\lambda_1)\, t & : t \leq 0 \\ (2/\lambda_2)\, t & : t > 0 \end{cases}, \tag{4.13}$$

where λ_1 and λ_2 correspond to the material wavelength of the booster and test article, respectively. Eq. (4.13) was used to eliminate the material wavelength from the velocity equations, as the time-varying frequency content of the signal is proportional to velocity with a scale factor of unity in the $\hat{t}$-domain. The MI signal in the $\hat{t}$-domain was re-sampled to a common sampling rate limited by the equation,

$$V_S = \frac{1}{2} F_S \times min\left(\lambda_1, \lambda_2\right), \tag{4.14}$$

where F_S is the original sampling frequency and V_S is the maximum achievable sampling rate over the entire scaled time signal.

4.3.1 Peak Picking Analysis

Peak-picking is a discrete method to determine the average detonation velocity at a finite number of points. This method is unbiased from signal filtering, provided the filtering operations do not interfere with the identification of local maxima and minima in time. The analysis is derived from the fundamental velocity-frequency relationship [4],

$$v\left(t\right) = \frac{\lambda_k}{2} f\left(t\right), \tag{4.15}$$

where $f\left(t\right)$ is the time-varying frequency content of the MI signal, and λ_k is the calibrated material wavelength corresponding to an explosive, k, in a multi-material system ($k > 1$). The material wavelength is dependent on microwave frequency, sample diameter, and permittivity as discussed in Sec. 4.2. To calculate velocity from the MI output, each advance in phase of the signal by 2π corresponds to the advance of the moving reflector by $\lambda_k/2$ and the time between consecutive peaks. Thus, an average time-velocity series may be constructed between the ith and ith+1 peaks as

$$\left(\frac{t_{i+1} + t_i}{2}, \frac{\lambda_k/2}{t_{i+1} - t_i}\right), \tag{4.16}$$

which is a discretization of Eq. (4.15). The resolution of this method could be improved using time points from minima, maxima, and zero crossings; however, the most reliable calculations are made between similar features (e.g. peak-to-peak). A simple automated routine was used to identify the local minima and maxima, and the discrete velocity calculations are presented in Sec. 4.4.

A shock trajectory, or t-x diagram may also be constructed via the recursion relationship,

$$x_{i+1} = x_i + \lambda_k/2, \tag{4.17}$$

where the position is known at each time step, t_i. The series x_i should be averaged at the center of each interval in order to be directly combined with Eq. (4.16) and obtain a position-velocity curve.

4.3.2 Quadrature Analysis

Quadrature analysis, or phase unwrapping, provides greater spatial resolution than discrete peak-picking. The objective of this analysis is to calculate a phase angle from the two-channel MI output using circularized Lissajous curves; however, the MI signals must be filtered, normalized, and transformed. Initially, low-pass filters are used to eliminate most of the high frequency noise from the signal. For time-varying signals, especially those corresponding to significant variation in velocity (e.g. detonation failure), filters are applied in multiple sections for a range of frequencies. The resulting signals are then spliced together and filtered to eliminate higher frequency noise. A linear map is then used to normalize the microwave signals between extrema to the interval $[-1, 1]$.

After normalization, the Lissajous curves lie on an ellipse and will introduce measurement error. The correction of this quadrature fringe measurement error is discussed in detail in previous work [69]. Here, the equation of an ellipse is written in terms of the phase angle, θ, as

$$\vec{f}(\theta) = \vec{Z} + Q \cdot \begin{bmatrix} A \times cos(\theta) \\ B \times sin(\theta) \end{bmatrix}, \tag{4.18}$$

where Q is the rotation matrix about an angle, α, and A, B, $\vec{Z}$ are fitted parameters. For the normalized Lissajous curves, Eq. (4.18) is fitted with a non-linear least squares regression using the Bookstein constraint [70]. Eq. (4.18) may be rearranged to solve for the transformed MI signals $V_1{}'$ and $V_2{}'$,

$$\begin{bmatrix} V_1{}' \\ V_2{}' \end{bmatrix} = \begin{bmatrix} \frac{1}{A} & 0 \\ 0 & \frac{1}{B} \end{bmatrix} \cdot Q^{\top} \cdot \left(\begin{bmatrix} V_1 \\ V_2 \end{bmatrix} - \begin{bmatrix} Z_1 \\ Z_2 \end{bmatrix} \right), \tag{4.19}$$

where V_1 and V_2 are the normalized signals, and the phase angle may then be calculated as

$$\theta = tan^{-1}\left(\frac{V_2{}'}{V_1{}'}\right), \tag{4.20}$$

where tan^{-1} is the discontinuous arctangent function effectively unwrapping the phase.

Finally, detonation velocity is calculated with a numerical derivative of the phase angle,

$$v\left(t\right) = \frac{\lambda_k}{4\pi}\frac{d\theta}{dt}. \tag{4.21}$$

The scaled time variable defined in Eq. (4.13) may be used to eliminate the material wavelength, λ_k, from the velocity expression to obtain,

$$v\left(\hat{t}\right) = \frac{1}{2\pi}\frac{d\theta}{d\hat{t}}, \tag{4.22}$$

where Eq. (4.22) provides a continuous transition in velocity from the booster to the test explosive.

A numerical derivative for variable time-step is required to calculate the velocity appearing in Eq. (4.22). While multiple methods exist [65,71], a discrete formula was chosen based on the work of Savitzky and Golay [72],

$$f'\left(x^\star\right) \approx \sum_{k=1}^{3} 2kc_k\frac{f_k - f_{-k}}{x_k - x_{-k}}, \tag{4.23}$$

where the coefficients are $c_1 = 5/32$, $c_2 = 4/32$, and $c_3 = 1/32$, and k is the index about the point where the derivative is evaluated ($k = 0$). An additional low-pass filter is applied to compute a final velocity.

4.3.3 Time-Frequency Analysis

The objective of a time-frequency analysis is the direct measurement of the time-varying frequency content, $f\left(t\right)$, in Eq. (4.12). As a point of reference, time-frequency analysis is established in related fields of interferometry, including photonic Doppler velocimetry (PDV) [73,74] and velocity interferometer system for any reflector (VISAR) [75]. However, it was not until recent work [68] that these techniques were seriously considered for detonation velocity measurements. Time-frequency analysis holds several advantages for MI over phase unwrapping, including the direct measurement of velocity through frequency (and not by a numerical derivative), robust data analysis for low quality signals, and minimal filter settings with greater reproducibility in the results.

Two of the most widely used analysis methods are the short-time Fourier transform (STFT) and the continuous wavelet transform (CWT). Proper use of these transforms requires parameter tuning, which if done incorrectly can lead to a misrepresentation of the time-frequency content in a signal. Specifically, the CWT is defined using a tunable wavelet basis function (e.g. Morlet, Gabor, Daubechies) whereas STFT requires a windowing function (e.g. Hanning, Hamming, Gaussian) with variable window width. Neither method is able to provide resolution below the theoretical minimum [76], yet careful tuning of the filter parameters will adjust the relative weighting between time and frequency resolution. Consequently, the greater flexibility of CWT to be tuned may afford it some numerical advantages, such as reduced computational costs. A complete discussion of the short-time Fourier transform and continuous wavelet transform is beyond the scope of this work, therefore only basic theory and equations are presented; the interested reader is referred to other sources [77–79].

4.3.4 Short Time Fourier Transform

The windowed Fourier transform, or STFT, is defined for a time-varying signal $f(t)$ by,

$$STFT\left[f(\tau,\omega)\right] = \int_{-\infty}^{\infty} f(t)\, w(t-\tau)\, e^{-i\omega t} dt, \tag{4.24}$$

where $w(t)$ is a windowing function, τ is the integration variable, and ω is the angular frequency. For this work, a Hamming windowing function was chosen, and the window width was held constant as a percentage of the total signal length. The accuracy and precision limitations of a windowed Fourier transform are discussed in other work pertaining to photonic Doppler velocimetry (PDV) measurements [80, 81].

Time-frequency bin sizes for the STFT are determined from the sampling frequency and the period of the signal according to the relations,

$$\Delta t = 1/F_S, \tag{4.25a}$$

and

$$\Delta f = 1/T, \tag{4.25b}$$

where F_S is the sampling frequency and T is the period, or total length, of the signal. To ensure time-frequency bin sizes of 0.01 μs and 0.01 MHz, the MI signals were zero padded to extend the signal to a period of $T = 100$ μs before applying the STFT .

Detonation velocity is found by extracting the amplitude ridge line of the spectrogram. Here, the ridge line is determined by the maximum spectrogram amplitude at each value in time. Once a suitable window width is determined, the scaled time variable $\hat{t}$ from Eq. (4.13) is passed to the STFT so that the spectrogram frequency is directly proportional to velocity with a scale factor of unity.

4.3.5 Continuous Wavelet Transform

Formally, the CWT of a time-varying signal $f(t)$ is given by [82],

$$Wf(u,s) = \int_{-\infty}^{\infty} f(\xi) \frac{1}{\sqrt{s}} \psi^* \left(\frac{\xi - u}{s} \right) d\xi, \tag{4.26}$$

where Wf denotes the wavelet transform, u and s are the translation and scale variables, ξ is the integration variable, ψ is the mother wavelet, and ψ^* denotes its complex conjugate. Scale and translation are related to time and frequency through the choice of the mother wavelet. In Eq. (4.26), the function ψ should satisfy the admissibility condition [82] and have a zero mean value.

Following previous work [73–75, 77], a Gabor mother wavelet was chosen as the basis for the CWT and is given by the formula

$$\psi(t) = \frac{1}{(\sigma^2 \pi)^{1/4}} e^{-t^2/2\sigma^2} e^{i\eta t}, \tag{4.27}$$

where σ and η are the time spread and center frequency parameters. For the Gabor mother wavelet, time and frequency can be related to scale and translation via [76],

$$t = u, \tag{4.28a}$$

and

$$\omega = \eta / s. \tag{4.28b}$$

Kim and Kim [77] show that the Gabor wavelet shape is controlled by a single dimensionless parameter, and introduce the notation of a Gabor wavelet shaping factor $Gs = \sigma\eta$ where σ is set to unity. The shaping factor Gs governs the time-frequency resolution of the CWT according to the relations [83],

$$\sigma_{t_{u,s}} = \frac{Gs}{\sqrt{2}\omega}, \tag{4.29a}$$

and

$$\sigma_{\omega_{u,s}} = \frac{\omega}{\sqrt{2}Gs}, \tag{4.29b}$$

where $\sigma_{t_{u,s}}$ and $\sigma_{\omega_{u,s}}$ are the variances (or spread) in time and frequency of the CWT. The effect of Gs on the Gabor wavelet shape is depicted in Fig. 4.2.

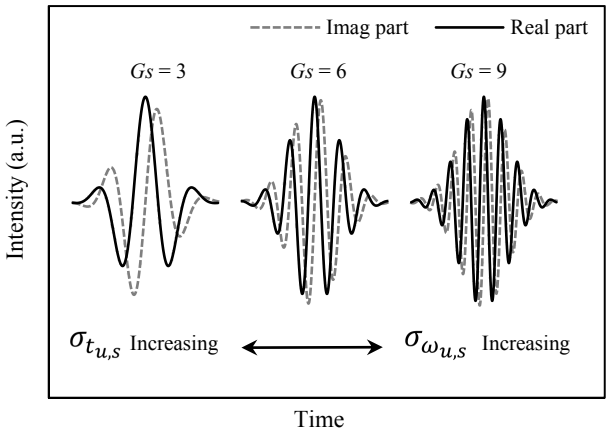

Figure 4.2. Gabor mother wavelet $\psi(t)$ for Gs of 3, 6, and 9. Reproduced from [68] with permission.

The relative weighting on time or frequency resolution is determined by the number of oscillations in the Gabor wavelet shape; in the limit $Gs \to \infty$ the GWT becomes similar to a time-independent Fourier transform. In the limit $Gs \to 0$, the number of oscillations decreases to improve time localization, however this also introduces error due to frequency spreading. When $Gs = 0$, the Gabor wavelet collapses to

a normal distribution and violates the admissibility condition (zero mean value). In general, the Gabor wavelet has a non-zero mean; however, it is suggested that $Gs \geq 3$ is sufficient to minimize the mean such that the conditions for a mother wavelet are satisfied [76, 84]. Consequently, a frequency bias is introduced near $Gs = 3$ and was corrected following other work [85].

To visualize the time-frequency intensity, a normalized scalogram is calculated in place of a spectrogram according to the formula [76],

$$N_W f\,(u,s) = \frac{|Wf\,(u,s)|^2}{s}. \tag{4.30}$$

Values of s may be calculated at will via Eq. (4.28b) so that any discretization of frequency may be transformed into an array of scale values and passed to the CWT. Hence, the desired frequency bin size may be achieved without zero padding.

Unlike the STFT window width, the Gs parameter is restricted to a small range of values between 3-5.5 [76]. It is bounded from below by the admissibility condition, and from above by acceptable temporal resolution. To motivate the upper limit, Eqs. (4.29a) and (4.29b) are combined,

$$\frac{\sigma_{t_{u,s}}}{T} = \frac{Gs}{2\sqrt{2}\pi}, \tag{4.31}$$

where T is the period at a particular frequency of the signal, and $\sigma_{t_{u,s}}$ is the acceptable time spread. Therefore, to resolve transient phenomena occurring over a time interval on the order of one period Eq. (4.31) implies that small Gs values $\lesssim 9$ are needed. A fixed Gs value between 3-5 was also used in similar work [84]. The same ridge extraction algorithm and scaled time variable from the STFT method are used to produce the final normalized scalogram and velocity result.

4.4 Comparison of the Analysis Techniques

An assessment of the different analysis techniques was made using MI data for two trials with triaminotrinitrobenzene (TATB) and ammonium nitrate and urea (ANUR) explosives. These trials are representative of a wide range of detonation phenomena, as well as the non-idealities present in MI signals. For each trial, the average signal-to-noise ratio, number of samples, and parameters for the final time-frequency calculations are shown in Table 4.1. In particular, the TATB data is of a higher quality (S/N = 140) and is presented to illustrate that all methods are capable of determining a time-resolved detonation velocity. The ANUR data is of a lower quality (S/N = 2.2) and is representative of the non-idealities in MI signals; the results clearly illustrate the benefits of using a time-frequency analysis over phase unwrapping techniques. Both signals were also de-sampled to 100 MHz for the calculations.

Table 4.1. Summary of the MI signals and final time-frequency calculations.

Test Article	**S/N**	t_i **(μs)**	t_f **(μs)**	**N**	**w**	Gs
TATB	140	-5.45	8.1	1,355	0.5%	4
ANUR	2.2	-6.0	60.0	6,600	4.0%	4

The experimental configuration was similar to the one described in Ch. 3 for small (6.52 mm) I.D. stainless steel tubes; only a brief description of the sample preparation is given here. The booster consisted of Primasheet 1000, and the test article consisted of either pressed TATB powder or a stoichiometric mixture of ANUR. Material properties of the explosives are summarized in Table 4.2, including the Chapman-Jouget detonation velocity and sample length. The average material wavelength values for Primasheet 1000 and TATB were determined from Eq. (4.3) and previous work [65]. The average wavelength for ANUR was estimated for the analysis because no previous data or mixture laws exist for this material at MI frequencies.

Table 4.2. Material properties of the explosives used for study.

Explosive	$\boldsymbol{\rho_{ave}}$ **(g/cm³)**	$\boldsymbol{\lambda}$ **(mm)**	$\mathbf{D_{CJ}}$ **(mm/μs)**	$\mathbf{L_{ex}}$ **(cm)**
Primasheet 1000	1.50	5.67	7.1	3.81
TATB	1.538	5.08	6.8	5.72
ANUR	1.08	5.0	5.5	5.72

4.4.1 High Quality MI Signal

MI output obtained for the high quality TATB signal is shown in Fig. 4.3. For this trial, a detonation wave in the booster transitioned into the test article, which also detonated throughout its entire length; however, the detonation velocity was unsteady. The TATB explosive was pressed to an average volume fraction of V_A=0.794 in five increments, and density gradients were formed. The density gradients appear as oscillations in the velocity results due to the dependency of the detonation wave speed on material density [1]. This conclusion was also verified by changing the number of pressing intervals and observing a corresponding change in the number and amplitude of the oscillations in velocity.

Lissajous curves for the MI output and unwrapped phase angle are shown in Figs. 4.4 and 4.5, respectively. Despite a high signal-to-noise ratio, the initial Lissajous curve appears skewed and filled as a result of the non-constant amplitude; most of the signal inside the curve is of the booster explosive for $t < 0$. After filtering, normalization, and transformation, the final Lissajous curve is well circularized, and the unwrapped phase angle is presented in Fig. 4.5. The final velocity result is shown in Fig. 4.6 directly compared to the discrete velocity result from peak-picking (open circles). For the final filtering step of the quadrature analysis, filter settings were chosen to best fit between the discrete velocity data.

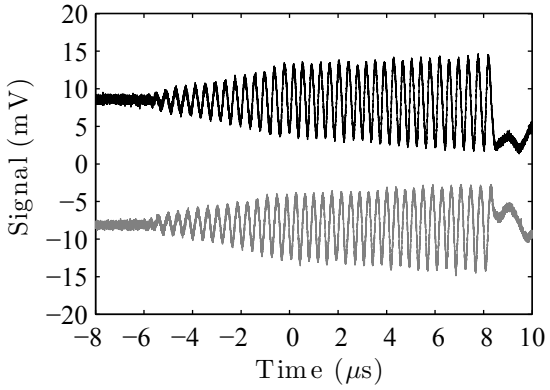

Figure 4.3. Two-channel microwave output signals for TATB (high quality). Transition between TATB and booster occurs at $t = 0$. Reproduced from [68] with permission.

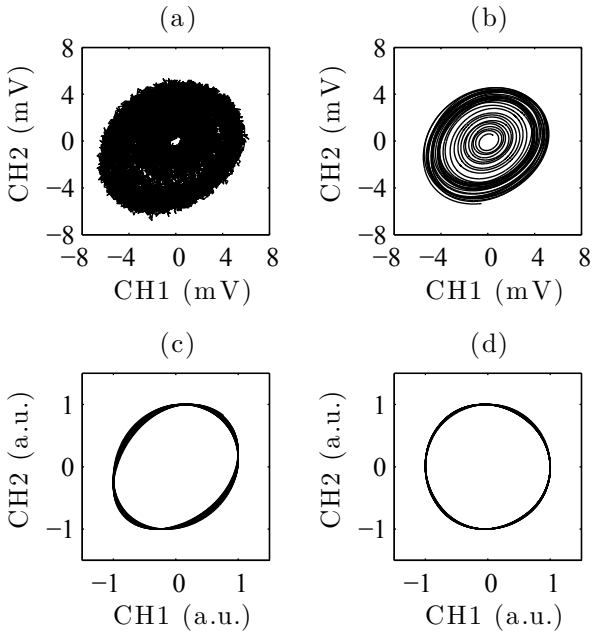

Figure 4.4. Lissajous curves for sequential operations on TATB data. Clockwise from top left: (a) original, (b) filtered, (c) normalized, and (d) transformed. Reproduced from [68] with permission.

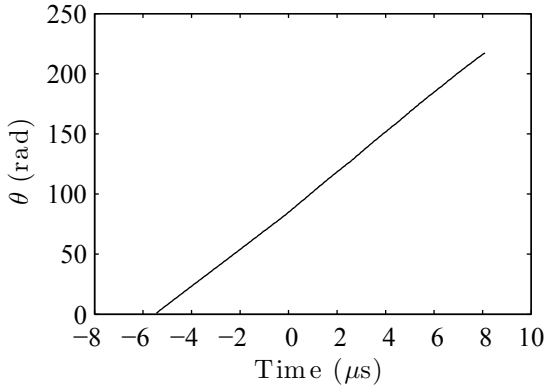

Figure 4.5. Unwrapped phase angle from the quadrature analysis for TATB. Reproduced from [68] with permission.

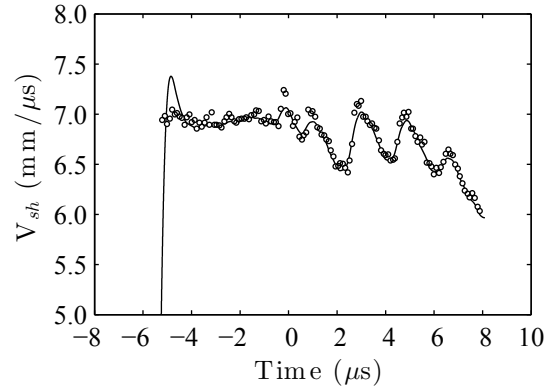

Figure 4.6. Direct comparison of quadrature (solid line) and peak-picking (open circles) analysis for TATB data. Reproduced from [68] with permission.

For an analysis of the TATB data using STFT, the MI signals were zero padded between -50 μs to 50 μs, increasing the signal length from 1,355 to 10,000 samples. Initially, the spectrogram was computed using four different window sizes as shown in Appendix A. Because the frequency content of the signal is concentrated between 2-3 MHz, a single window size was capable of resolving the frequency ridge line. A

final spectrogram in the time-modified $\hat{t}$-domain was computed using a window width w = 0.5% of the signal length, and the velocity result is shown in Fig. 4.7 in direct comparison with discrete peak-picking. The velocity result from STFT shows an excellent fit to the discrete calculations from peak-picking, as well as similarity with the quadrature analysis by extension.

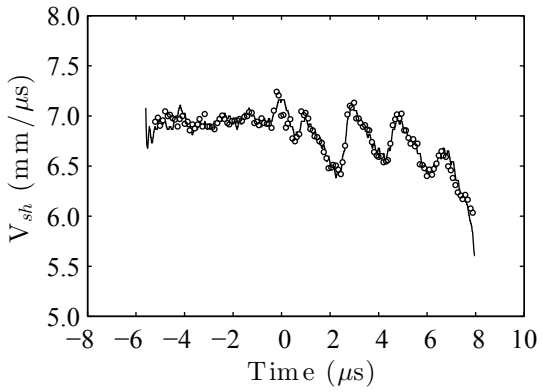

Figure 4.7. Direct comparison of STFT (solid line) and peak-picking (open circles) analysis for TATB data. Reproduced from [68] with permission.

Velocity calculations based on the CWT differ from the STFT approach due to the control of time-frequency resolution through the Gs parameter and not window width or signal length. The normalized scalogram was computed using Gs values within the range 3-5.5 [76] and is presented in Appendix B. From the initial scalogram calculations, a fixed value of $Gs = 4$ was selected. This value appears to be the minimum value (maximum temporal resolution) needed to resolve the MI signal and also satisfy the admissibility criteria. Although the frequency ridge lines in the normalized scalograms contain more noise than the spectrogram ridge lines from STFT, the CWT is a noise-robust operation and the ridges may be filtered if desired. The final velocity calculation using the CWT-based method is shown in Fig. 4.8 with no filtering and the overlaid peak-picking calculations. The direct comparison of CWT

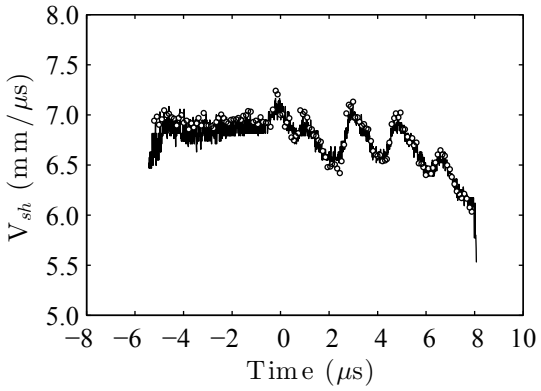

Figure 4.8. Direct comparison of CWT (solid line) and peak-picking (open circles) analysis for TATB data. Reproduced from [68] with permission.

and peak-picking velocity data confirms that both intersect, and that $Gs = 4$ is a suitable choice for the Gabor wavelet shaping factor.

Quadrature analysis, STFT, and CWT-based methods are equally successful at fitting the discrete peak-picking velocity data for this trial. However, it is emphasized that the discrete velocity calculations from peak-picking were critical in the determination of filter settings for both the quadrature and STFT methods. Moreover, the local maxima and minima of the two-channel output occur with sufficient frequency so that the average velocity calculations are representative of the instantaneous time-resolved detonation velocity. In contrast, tuning of the Gs parameter for the CWT was independent of the velocity result from peak-picking; a value of $Gs = 4$ may be used for a vast number of time-frequency analyses without any knowledge of the desired result.

4.4.2 Low Quality MI Signal

Achievable MI signals in explosives are often of a low quality, and velocity measurements in non-ideal systems remain challenging. Total reflection of the MI signal is

never realized due to partial transmission through the wave front of interest [6], as well as attenuation of the signal due to absorption and dispersion effects in the explosive media [1]. Furthermore, the shock or detonation wave may be a non-planar reflector due to sample diameter effects as well as material heterogeneities [86] resulting in poor signal quality. Other factors which may affect the signal quality include the possibility of a decoupled shock-reaction zone (e.g. shock initiation and detonation failure) giving rise to multiple harmonic frequencies [4], as well as the confinement of the test explosive acting as a waveguide for the MI signal [1]. When several of these non-idealities are present simultaneously, it may still be possible to extract useful velocity information with an advanced time-frequency analysis.

MI output for the low quality signal corresponding to ANUR is shown in Fig. 4.9. For this trial, several non-ideal phenomena are observed, including the failure of detonation immediately following the transition of the booster into the test article. The detonation failure was confirmed by the partial recovery of the confiner material, as well as the wave speed existing well-below the Chapman-Jouget detonation velocity for ANUR. In addition, the transmission of the MI signal is poor and the average signal-to-noise ratio of S/N = 2.2 is difficult for analysis. A final complication is the exponential decay in the wave velocity, which spreads the relevant frequency content of the signal over the range of 0.1-2.5 MHz.

Lissajous curves for the MI signal are shown in Fig. 4.10 and do not resemble the previous trial. An electromagnetic pulse was captured near -10 μs due to the firing an exploding bridge-wire detonator to initiate the booster explosive. However, the signal was cropped so that the pulse does not appear in the Lissajous curves (refer to Table 4.1). Despite the appearance of this data, quadrature analysis may still be used with considerable effort to unwrap the phase angle as shown in Fig. 4.11. The final velocity result presented in Fig. 4.12 fails to fully fit the discrete peak-picking result. Better agreement between quadrature analysis and peak-picking is achieved beyond 20 μs, however the transient event is not fully captured in the analysis.

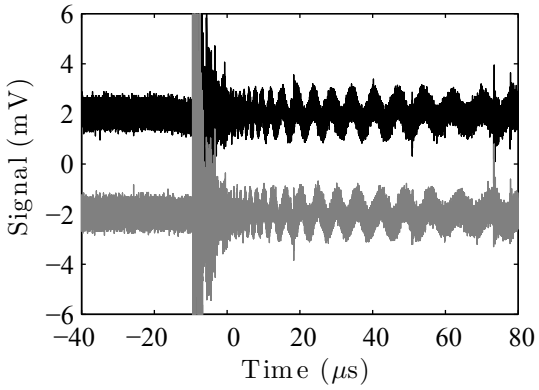

Figure 4.9. Two-channel microwave output signals for ANUR (low quality). Transition between ANUR and booster occurs at $t = 0$. Reproduced from [68] with permission.

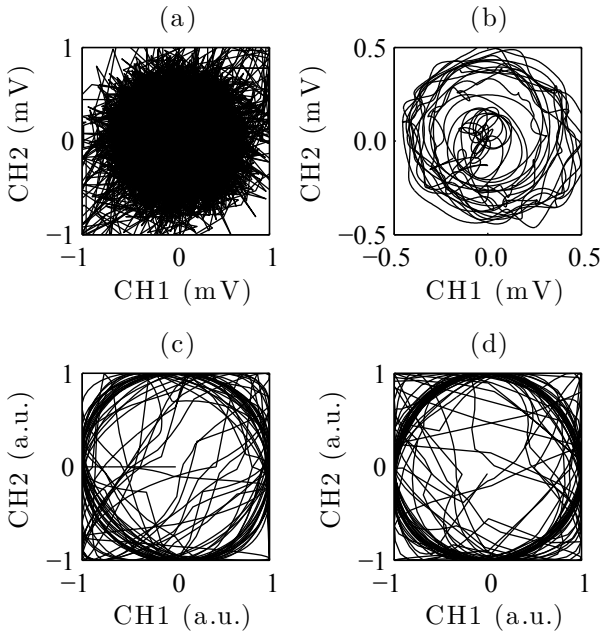

Figure 4.10. Lissajous curves for sequential operations on ANUR data. Clockwise from top left: (a) original, (b) filtered, (c) normalized, and (d) transformed. Reproduced from [68] with permission.

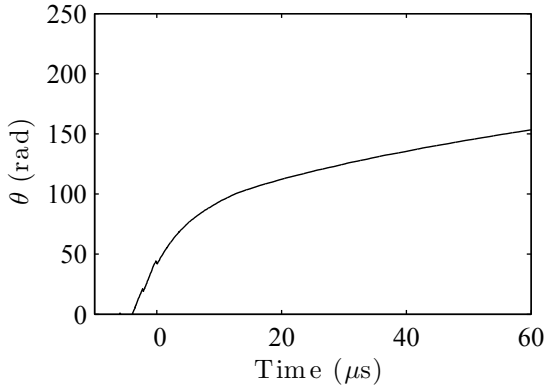

Figure 4.11. Unwrapped phase angle from the quadrature analysis for ANUR. Reproduced from [68] with permission.

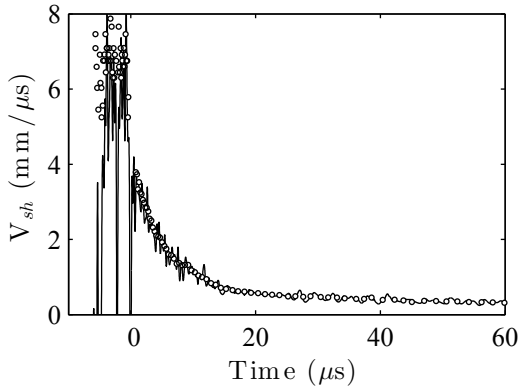

Figure 4.12. Direct comparison of quadrature (solid line) and peak-picking (open circles) analysis for ANUR data. Reproduced from [68] with permission.

Unlike quadrature analysis, the time-frequency methods appear to fit the discrete velocity calculations with less error, particularly near $t = 0$. Final STFT and CWT time-resolved detonation velocities are shown in Figs. 4.13 and 4.14, respectively, and are directly compared to the peak-picking analysis. (Refer to Appendices A and B for the spectrograms and normalized scalograms, respectively.) One challenge unique

to STFT is the determination of a suitable window width for the entire signal. For the chosen value of w = 4.0% signal length, there is excellent agreement between the discrete calculation for $t > 0$; however, the higher velocity corresponding to the booster appears smeared in Fig. 4.13. A different window width may have been applied to the time interval $t < 0$; instead, the window width was chosen to more closely fit the discrete calculations corresponding to the wave velocity in ANUR.

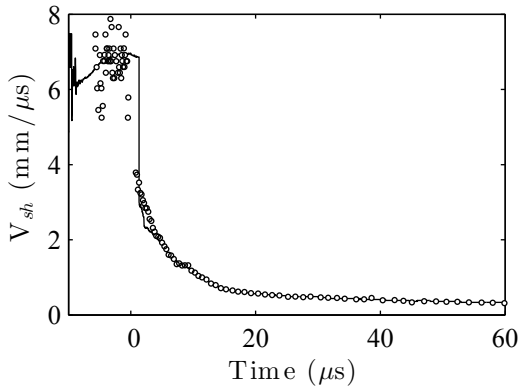

Figure 4.13. Direct comparison of STFT (solid line) and peak-picking (open circles) analysis for ANUR data. Reproduced from [68] with permission.

The potential advantage of a CWT-based analysis is illustrated by the time-resolved velocity calculations in Fig. 4.14. Not only does the CWT appear robust to noise for S/N = 2.2, but the value $Gs = 4$ achieves optimal time-frequency resolution required for a time-varying signal. This observation is significant because the same Gabor wavelet shaping factor was used in the previous trial; hence, no modification to the wavelet basis was required for the analysis of both signals presented in this work. Further, the ability to control the frequency bin size without the need for zero padding means that this method may be more computationally efficient than STFT-based calculations.

Overall, the effort required with phase unwrapping is highly dependent on the quality of the MI signal, and when several non-ideal effects are present the results of

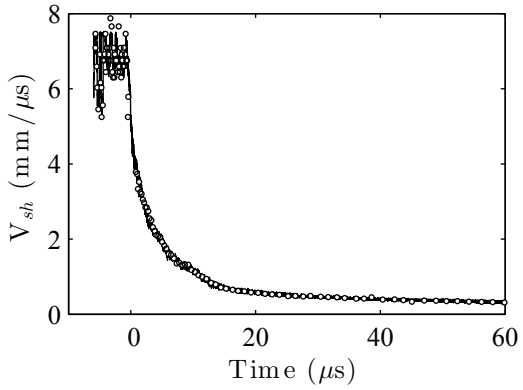

Figure 4.14. Direct comparison of CWT (solid line) and peak-picking (open circles) analysis for ANUR data. Reproduced from [68] with permission.

this trial show significant advantages for using a time-frequency analysis. The Lissajous curves in Fig. 4.10 might possibly be improved with additional filtering and more advanced normalization techniques; however, additional effort and filter parameters are required. Even if a semi- or fully-automated quadrature analysis is achieved, the STFT and CWT techniques may be implemented with a single filter parameter. The use of time-frequency analysis for MI yields a method with a single, bounded, filter parameter allowing for the standardization and reproducibility of detonation velocity measurements.

4.5 Uncertainty Quantification

Uncertainty quantification must account for both the measurement error and random sample variation in the final shock or detonation velocity calculations. Measurement and random error in any variable, X_i, may be combined in quadrature to

obtain a total error, ΔX_i. The total error within each variable is propagated into the measurement via the formula,

$$\frac{\Delta W}{W} = \sqrt{\sum_{i=1}^{N} \left(\frac{1}{W} \frac{\partial W}{\partial X_i} \Delta X_i \right)^2}, \tag{4.32}$$

where $W = W(X_i)$ is the resulting value from the X_i measured parameters, and all ΔX_i correspond to the same confidence interval level. For steady velocities, the time dependence of the frequency content in Eq. (4.12) is neglected, and the error in velocity is given by,

$$\frac{\Delta v}{v} = \sqrt{\left(\frac{\Delta \lambda_g}{\lambda_g} \right)^2 + \left(\frac{\Delta \bar{f}}{\bar{f}} \right)^2}, \tag{4.33}$$

where $\bar{f}$ is the average frequency. If a non-dimensional shock trajectory is constructed from Eqs. (4.16) and (4.17), a linear regression may be used to determine the slope (i.e. $\bar{f}$) and variance in slope (i.e. $\Delta \bar{f}$). The error in frequency due to the application of a time-frequency analysis is more difficult to quantify than a simple peak-picking technique.

Most of the error in velocity is due to error in the wavelength, rather than frequency. Cawsey *et al.* [1] were the first to quantify the error in wavelength, and show that a practical limit exists near 1-2% error in velocity; their analysis is further generalized here. When Eq. (4.32) is applied to Eq. (4.5), the error in wavelength is found to be a function of the sample permittivity and cut-off wavelength,

$$\frac{\Delta \lambda_g}{\lambda_g} = \sqrt{\left[\left(\frac{\lambda_g}{\lambda_0} \right)^2 \frac{\Delta \epsilon_r}{2} \right]^2 + \left[\left(\frac{\lambda_g}{\lambda_c} \right)^2 \frac{\Delta \lambda_c}{\lambda_c} \right]^2}. \tag{4.34}$$

Repeated use of Eq. (4.32) may be used to show that $\Delta \lambda_c / \lambda_c = \Delta d / d$, where d is the sample diameter; hence the error in wavelength has both geometric and material property error. Moreover, the relative permittivity is known to be a function of density; evidence suggests that density gradients are present in the explosive samples [67]. The Landau-Lifshitz/Looyenga (LLL) mixture law in Eq. (4.3) is used to effectively link $\Delta \epsilon_r$ with $\Delta \rho_0$ according to,

$$\Delta \epsilon_r = \sqrt{\alpha^2 + \beta^2}, \tag{4.35}$$

where the functions α and β are the error contributions of the bulk density variation and uncertainty in the material dielectric constant, respectively, given by the expressions,

$$\alpha = 3{\epsilon_r}^{2/3}\left({\epsilon_r}^{1/3} - 1\right)\frac{\Delta\rho_0}{\rho_0}, \tag{4.36}$$

and

$$\beta = {\epsilon_r}^{2/3}\left(\left({\epsilon_r}^{1/3} - 1\right)\frac{\rho_{TMD}}{\rho_0} + 1\right)^{-2}\frac{\rho_{TMD}}{\rho_0}\Delta\epsilon_{r,TMD}, \tag{4.37}$$

where ρ_0 is the bulk density, ρ_{TMD} is the theoretical maximum density, and $\Delta\epsilon_{r,TMD}$ is the error in the permittivity at 100% TMD (i.e. the error in material dielectric constant). It is useful to relate the error back to $\epsilon_{r,TMD}$ in addition to ρ_0 in order to determine which of the terms is the dominant effect when designing new experiments. Finally, the error in bulk density may be computed from the sample geometry and mass as,

$$\frac{\Delta\rho_0}{\rho_0} = \sqrt{\left(\frac{\Delta m}{m}\right)^2 + \left(\frac{2\Delta d}{d}\right)^2 + \left(\frac{\Delta L}{L}\right)^2}. \tag{4.38}$$

where m is the total mass, d is the diameter, and L is the length of the sample.

Uncertainty quantification for the time-resolved detonation velocity profiles should consider Eqs. (4.33) through (4.38), in addition several other sources of error. For example, the time-frequency analysis introduces an uncertainty in frequency as well as time; quadrature analysis requires the use of a numerical derivative which may introduce numerical artifacts, and all of the analysis techniques depend on the quality of the MI signal. One particular caution is that the time-frequency techniques suffer from an edge effect when part of the transform integration goes beyond the length of the signal, using zero-padding or otherwise. Some correction techniques have been proposed, such as reflecting the signal about the origin. See for example a discussion of the edge effect on CWT in Ref. [87].

4.6 Dynamic Wavelength Calibration

Velocity calculations are only possible when the material wavelength is known. The wavelength for simple porous explosives and binary systems may be calculated

using Eqs. (4.5), (4.3), and (4.4) from material dielectric constants. Unfortunately, both the booster explosive, PRIMASHEET® 1000, and the ANFO KP-1 samples are non-trivial compositions with some level of porosity. An alternative, dynamic wavelength calibration routine was developed for the current work.

Different calibration approaches are possible depending on the analysis technique; for example, counting the number of zero crossings with peak-picking or the number of windings with quadrature. Here, the CWT with a Gabor wavelet and shaping factor of $Gs = 4$ is used to determine the time-resolved frequency content in Eq. (4.15). When Eq. (4.15) is integrated over a known time interval and distance, a calibration formula may be obtained as,

$$\lambda_k = \frac{2L}{\int_{t_i}^{t_f} f\left(\hat{t}\right) d\hat{t}}, \tag{4.39}$$

where λ_k is the calibrated material wavelength, t_i and t_f are the limits of integration, and L is a measured length that the shock or detonation velocity traveled. The calibration in Eq. (4.39) is more advanced than a simple time-of-flight estimate because the actual time-frequency history is integrated (numerically robust).

The accuracy of Eq. (4.39) is low in comparison to microwave cavity measurements, and should not be used to determine the wavelength from a single experiment. However, when the same explosive materials are used in multiple experiments (possibly in different configurations) the relative permittivity may be extracted from Eq. (4.39) via an inversion of Eq. (4.5). Then, the mean sample permittivity may be used for velocity calculations; the sample variance may also be used in Eq. (4.34) to determine the error in velocity, in lieu of the material delectric constant at full density. Results of the dynamic wavelength calculations as well as the uncertainty calculations may be found in Appendix C.

5. MODEL DEVELOPMENT

5.1 Background

Reactive burn models are used to simulate the propagation or failure of detonation waves in arbitrary geometries. These models are necessary for simulating certain detonation phenomena, including: shock initiation, overdriven detonation failure, corner turning, and dead zones. All of these phenomena arise when considering the performance of real explosive devices, and as a result the details of these models are sometimes proprietary. No singular reference exists for explosive modeling, although Mader [88] published a basic methodology along with results for many explosives in his book. A concise report was also produced by Jones *et al.* [89], but each of these sources is incomplete; for example, they do not cover recent models including the SURF [90] and CREST [91] reactive burn models.

Reactive burn models are implemented in hydrocodes, which solve a form of the inviscid Euler equations [92]. Hydrocodes are primarily used in shock physics to model the interactions of shock waves in solid materials, as well as interfaces with liquids and gasses. Material strength is either neglected, or approximated by constitutive models because the shock pressures are several GPa − an order of magnitude above the yield strength for many materials. Above the yield strength, these materials behave plastically as a fluid, and the inviscid Euler equations are a good approximation of the physics. Additionally, heat transfer is neglected because the time scale of the shock wave is fast compared to the time scale of thermal diffusion. Hence, these models are not appropriate for simulating cook-off, low speed impact, or friction stimuli.

The basic components of a reactive burn model are shown schematically in Fig. 5.1. As the detonation wave passes into the unreacted explosive, an equation-of-state (EOS) is needed to determine the initial pressure rise in the explosive. Next, a thin

reaction zone exists between the leading shock wave and the Chapman-Jouguet (CJ) state, which also coincides with the sonic plane. All of the energy release in the reaction zone goes to support the shock, unless the explosive is non-ideal. In that case, the reaction front is curved and some region of the reaction zone is subsonic [93]. A reaction progress variable is used to define the extent of chemical reaction; together with a time-dependent rate law and mixture relations, the reaction zone is solved. For heterogeneous explosives, the global reaction rate is related to hot spot initiation and growth mechanisms [94, 95]. The treatment of the reaction zone is often the weakest aspect of reactive burn models, and research is ongoing to determine more physically based mixture and reaction laws. Finally, an EOS for the detonation products is required in order to solve the detonation wave, and determined the acceleration of the surrounding confiner material.

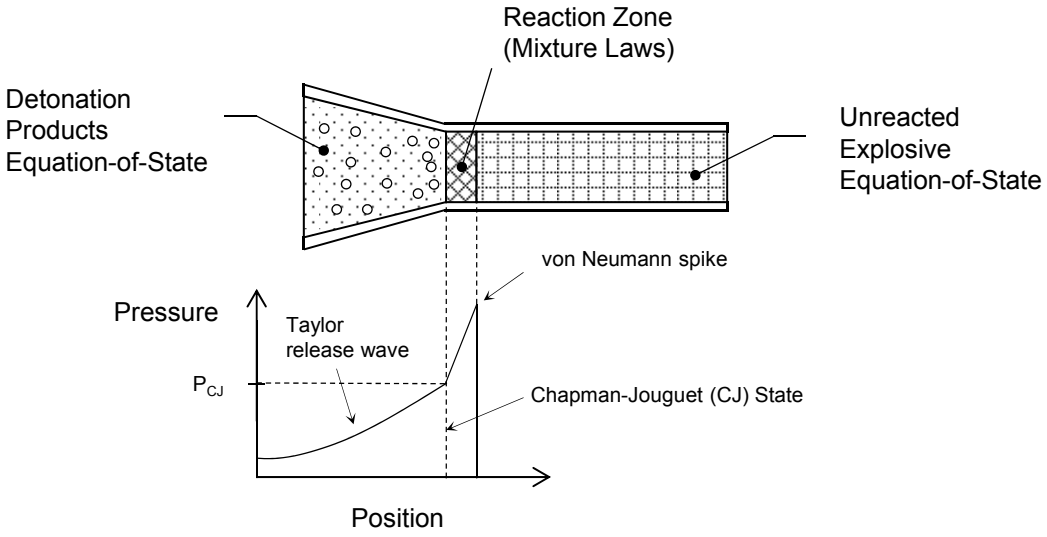

Figure 5.1. Structure of a detonation wave in a reactive burn model.

In the remainder of Ch. 5, all of the model developments for the ANFO KP-1 samples and relevant assumptions are discussed. This includes identification of the unknown model parameters which must be calibrated, as well as the fitting routines used, hydrocode implementation, and simulation geometry. The physical and ther-

mochemical properties of ANFO are also discussed in order to inform the model development.

5.2 Physical and Thermochemical Properties of ANFO

Ammonium nitrate plus fuel oil (ANFO) is a two-part binary explosive, with sensitivity and performance depending on a broad range of different physical and chemical parameters [86, 88, 96–104]. A typical composition for ANFO is approximately 5.5% fuel oil and 94.5% ammonium nitrate (AN) by weight [102]. The microstructure of ANFO is dominated by the particle morphology of AN; this particle morphology may include prills, crystals, and some intermediate (crushed) blends of the different particle types as show in Fig. 5.2. Commercial explosive-grade AN may even include glass micro-balloons for sensitization. Another important physical feature of AN is the individual particle porosity, which creates local sites for the liquid fuel to be absorbed [102]. This porosity is important to the intimacy of mixing, and ultimately explosive performance. ANFO is also very porous in the bulk material, with inter-particle void space. The average bulk density of ANFO is between 0.8 to 1.0 g/cm^3 [88], which is much less than the crystal density of AN at 1.725 g/cm^3. Hence, ANFO exhibits multiple heterogeneities that should be accounted for with the modeling effort.

The detonation velocity of ANFO mixtures varies between 3.5 to 5.5 km/s depending on the exact composition and the extent of chemical reaction [88]. Unlike more ideal explosives, the reaction zone thickness may be on the order of a few cm [104], the front of the detonation wave is curved [86,98], and the unconfined failure diameter is near 8 cm [88]. It is also possible that multiple chemical pathways exist [100], and that the reaction does not proceed to completion. For example, NOx formation has been experimentally observed with different ANFO compositions [97, 99, 103]; these results suggest that NOx formation should be considered for non-equilibrium detona-

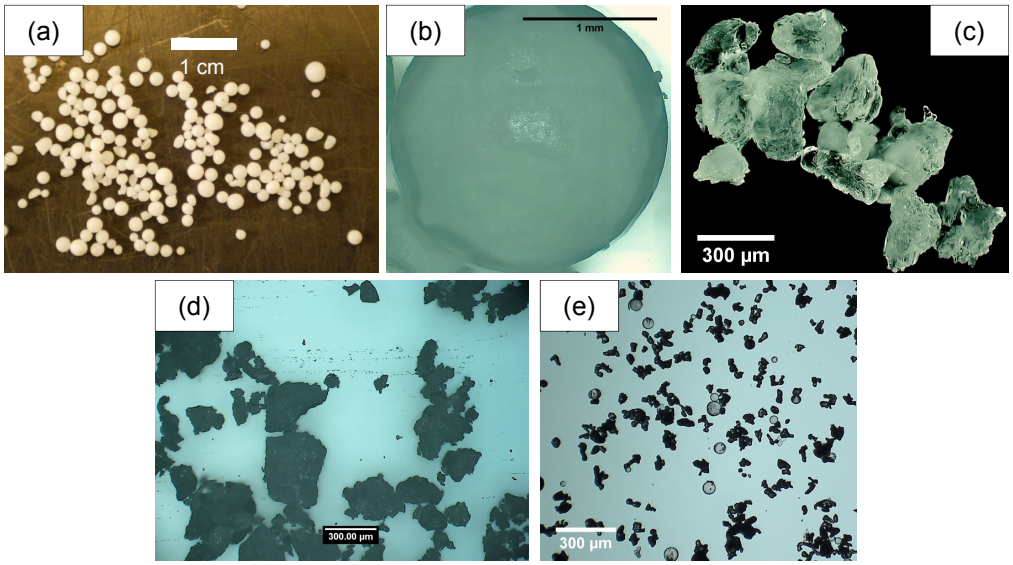

Figure 5.2. Particle morphology of ammonium nitrate: prills (a) and (b), crystalline (c), grounds (d), and grounds with micro-balloons (e). Hirox microscope images courtesy of Nick Cummock.

tion velocity calculations. Some of the variation in the measured detonation velocities for ANFO is also due to the thickness and sound speed of the confiner material [86].

5.2.1 Stoichiometry and Detonation Velocity Calculations

An optimal fuel weight percent for ANFO may be investigated via stoichiometetric relationships between the reactants and products. For the reactants, ammonium nitrate (chemical formula NH_4NO_3) is a mass detonable explosive with an oxygen balance of 20%. The extra oxygen affords the combustion of additional fuel; the reaction of AN with an arbitrary CHNO fuel going to complete combustion is given by the expression,

$$C_xH_yN_wO_z + a\,(NH_4NO_3) \rightarrow bCO_2 + cH_2O + dN_2. \tag{5.1}$$

Although complete combustion is never realized on the time scale of a shock wave, Eq. (5.1) may still be used to define the stoichiometry of ANFO. The CHNO atom balance for Eq. (5.1) has the matrix representation,

$$\begin{bmatrix} 0 & 1 & 0 & 0 \\ -4 & 0 & 2 & 0 \\ -2 & 0 & 0 & 2 \\ -3 & 2 & 1 & 0 \end{bmatrix} \times \begin{bmatrix} a \\ b \\ c \\ d \end{bmatrix} = \begin{bmatrix} x \\ y \\ w \\ z \end{bmatrix}, \tag{5.2}$$

with the solution $a = 2x + 0.5y - z$. To determine the stoichiometric weight percent of fuel in ANFO, a manipulation of the mass fraction,

$$wt.\%|_{st.} = \frac{m_{fuel,st.}}{m_{fuel,st.} + m_{an,st.}} = \frac{1}{1 + a\frac{MW_{an}}{MW_{fuel}}}, \tag{5.3}$$

yields an explicit relationship in terms of a and the molecular weights of AN and fuel. The detonation velocity of ANFO has been calculated at the weight percent given by Eq. (5.3) using two thermochemical equilibrium codes: TIGER [105] and CHEETAH [106]. These calculations are summarized in Table 5.1 for an initial bulk density of 0.8 g/cm^3, chosen as a reference value.

The TIGER and CHEETAH detonation velocities for ANFO vary between 4.58 and 4.73 km/s and are in agreement with some experimental measurements [88]. However, if the same detonation calculations are run at higher densities, velocities approaching 9 km/s are obtained. Increasing bulk density increases the energy density and subsequently the detonation velocity of ANFO. Real bulk densities are limited between 0.8 to 1.0 g/cm^3 because of the physical properties of AN prills and the dead pressing phenomenon [96]. ANFO is a heterogeneous explosive, and it is initiated via a hot spot mechanism [107]. Some degree of porosity is required for the initiation to be successful, at the cost of greater energy density.

Another observation about the thermodynamic calculations is that the assumption of chemical equilibrium at the CJ point is likely invalid. Finite-rate chemistry models should be considered (see for example [108]), and this will have an additional effect of further decreasing the predicted detonation velocity. Hence, TIGER and CHEETAH

calculations represent the best theoretical performance of ANFO at a given density; experimental testing is required to determine exactly how much chemical energy is liberated within the time scale of a shock wave. The slight difference in calculations from TIGER and CHEETAH may be attributed to the product species libraries; specifically, the calibrated EOS and heat capacity models.

Table 5.1. Stoichiometry and detonation velocity calculations for ANFO at an initial density of 0.8 g/cm^3.

Fuel	**Formula**	$\boldsymbol{MW}$	$\boldsymbol{a}$	$\boldsymbol{wt.\%|_{st.}}$	**TIGER**	**CHEETAH**
diesel	$C_{12}H_{23}$	167.312	35.5	5.56	4.70 km/s	4.61 km/s
fuel oil	$C_{10}H_{16.238}$	136.475	28.119	5.72	4.69 km/s	4.58 km/s
fuel oil-dn†	C_7H_{12}	96.171	20	5.67	4.73 km/s	4.63 km/s
dodecane	$C_{12}H_{26}$	170.336	37	5.44	4.67 km/s	4.59 km/s

†This formula corresponds to the fuel oil used by Dyno Nobel in ANFO circa 1994.

Unlike regular prilled ANFO, Kinepak$^{\text{TM}}$ and Kinepouch$^{\text{TM}}$ explosives have a nominal composition of 79% AN and 21% nitromethane (NM) by weight. These explosives are prepared by mixing the liquid NM fuel with the solid AN oxidizer prior to use; however, the NM fuel was replaced by diesel fuel for the small-scale MI experiments discussed in this work. A stoichiometric balance may be solved for the Kinepak$^{\text{TM}}$ ANFO by using the exact chemical composition of the solid; i.e. a blend of 95% AN and 5% glass micro-balloons by weight. The glass micro-balloons are represented by the chemical formula $O_{1.9}Si_{0.7}Na$, and Eq. (5.1) is expanded with silicon dioxide and sodium oxide in the products to obtain,

$$\begin{aligned} C_xH_yN_wO_z + a'\left[(0.95)\,NH_4NO_3 + (0.05)\,O_{1.9}Si_{0.7}Na\right] \rightarrow \\ b'CO_2 + c'H_2O + d'N_2 + e'SiO_2 + f'Na_2O. \end{aligned} \tag{5.4}$$

The CHNO atom balance for Eq. (5.4) is increased by two additional balances for Si and Na to obtain the matrix equation,

$$\begin{bmatrix} 0 & 1 & 0 & 0 & 0 & 0 \\ -3.8 & 0 & 2 & 0 & 0 & 0 \\ -1.9 & 0 & 0 & 2 & 0 & 0 \\ -2.945 & 2 & 1 & 0 & 2 & 1 \\ -0.035 & 0 & 0 & 0 & 1 & 0 \\ -0.05 & 0 & 0 & 0 & 0 & 2 \end{bmatrix} \times \begin{bmatrix} a' \\ b' \\ c' \\ d' \\ e' \\ f' \end{bmatrix} = \begin{bmatrix} x \\ y \\ w \\ z \\ 0 \\ 0 \end{bmatrix}, \tag{5.5}$$

with the solution $a' = 2.10526x + 0.526316y - 1.05263z$ (which is similar to the solution for ANFO of $a = 2x + 0.5y - z$). In order to calculate a stoichiometric fuel weight percent, the molecular weights of AN and $O_{1.9}Si_{0.7}Na$ are combined to determine an effective molecular weight for the Kinepak$^{\text{TM}}$. In this way, Eq. (5.3) remains mostly unchanged with a slight modification to the molar quantities,

$$wt.\%|_{st.} = \frac{1}{1 + a' \frac{MW_{kp}}{MW_{fuel}}}, \tag{5.6}$$

where $MW_{kp} = 79.6376$ g/mol is the molecular weight of Kinepak$^{\text{TM}}$. The balanced stoichiometry and detonation velocities for Kinepak$^{\text{TM}}$ ANFO are shown in Table 5.2 and compared with the baseline ANFO values. Of note, only the CHEETAH detonation velocity values are listed. TIGER suffered from numerical convergence errors when the glass micro-balloons were included in the composition; specifically, convergence failed on the condensed phase product species, including silicon dioxide and sodium oxide.

The primary difference between regular prilled ANFO and the Kinepak$^{\text{TM}}$ ANFO is the particle morphology (refer to Fig. 5.2). The Kinepak$^{\text{TM}}$ ANFO uses a fine AN crystalline powder which can be easily pressed to higher bulk densities, nominally 1.05 to 1.35 g/cm^3 depending on the tamping. The inclusion of the glass micro-balloons sensitizes the mixture to initiation, so that the higher density mixture may be detonated. However, the thermochemical equilibrium calculations show that for

Table 5.2. Summary of stoichiometry and detonation velocity calculations for ANFO and Kinepak^{TM} ANFO at an initial density of 0.8 g/cm^3. Note: $\boldsymbol{D_{CJ}}$ was calculated using CHEETAH and has units of km/s.

	ANFO			**Kinepak^{TM} ANFO**		
Fuel	$\boldsymbol{a}$	$\boldsymbol{wt.\%\vert_{st.}}$	$\boldsymbol{D_{CJ}}$	$\boldsymbol{a'}$	$\boldsymbol{wt.\%\vert_{st.}}$	$\boldsymbol{D_{CJ}}$
diesel	35.5	5.56	4.61	37.3684	5.32	4.41
fuel oil	28.119	5.72	4.58	29.5989	5.47	4.38
fuel oil-dn†	20	5.67	4.63	21.0526	5.42	4.43
dodecane	37	5.44	4.59	38.9473	5.21	4.39

†This formula corresponds to the fuel oil used by Dyno Nobel in ANFO circa 1994.

the same bulk density, the regular prilled ANFO will have the higher detonation velocities up to 5% (i.e. the glass micro-balloons are an ineffective fuel).

5.3 Unreacted Equation-of-State

Many different forms of the unreacted EOS have been proposed for solid explosives [109]. While the validity of each has been debated, a practical consideration is how well the experimental data may be extrapolated to the shock pressures of interest (up to tens of GPa [110]). Historically, unreacted EOS are fitted to shock-particle velocity relationships obtained from plate impact experiments; the shock state is discussed in greater detail in Sec. 5.3.1. More recently, isentropic compression data has been made available up to the same pressure ranges as those observed in plate impacts [111]; it is likely that future EOS will incorporate these results as well.

Some of the more common EOS include that of Hayes [109], Birch [112], Murnaghan [113], Hildebrand [114], Grüneisen [115], Lee [116], and others [117, 118]. Several of these EOS were developed from the Earth sciences, for example to model earthquakes and estimate the pressure at the center of the Earth's core. Perhaps

the most widely used EOS for modeling an unreacted explosive is the Mie-Grüneisen EOS; this form was adopted for the ANFO KP-1 model and will be discussed in greater detail.

The incomplete form of Mie-Grüneisen defines pressure as a function of energy and volume. This form is familiar to shock physics applications, and follows from Grüneisen's postulate that the lattice frequencies are a function of volume alone [115],

$$\left(\frac{\partial p}{\partial e}\right)_v = \frac{\Gamma(v)}{v}. \tag{5.7}$$

The approximation in Eq. (5.7) is reasonable for a cubic solid when temperatures are low enough to keep specific heat below the Dulong-Petit asymptotic limit [114]. An incomplete form of the Mie-Grüneisen EOS is found by integrating Eq. (5.7),

$$p(v,e) = \frac{\Gamma(v)}{v}e + \phi(v), \tag{5.8}$$

where $\phi(v)$ is the arbitrary reference function motivated by Segletes [119],

$$\phi(v) = p_{ref}(v) - \frac{\Gamma(v)}{v}e_{ref}(v). \tag{5.9}$$

The Mie-Grüneisen EOS defined in Eqs. (5.8) and (5.9) is incomplete, as it does not provide a way to calculate the temperature. Work is on-going to derive thermodynamically complete EOS based on Grüneisen's postulate for homogeneous materials (e.g. [120–122]). This work is also continued in Chapter 6.

In summary of Eqs. (5.7)−(5.9), the user input consists of the Grüneisen parameter, $\Gamma(v)$, and the reference function, $\phi(v)$. For the ANFO KP-1 model, the product of the Grüneisen parameter and density is assumed to be constant; this is a common approximation used in other work [119], and the functional form of Eq. (5.7) is given as,

$$\frac{\Gamma(v)}{v} = \Gamma_0\rho_0. \tag{5.10}$$

The Grüneisen parameter at ambient density, Γ_0, may then be estimated using the thermodynamic identity,

$$\Gamma = \frac{v\alpha K_T}{c_v}, \tag{5.11}$$

where α is the coefficient of thermal expansion, K_T is the isothermal bulk modulus, and c_v is the specific heat. Some of the thermodynamic quantities in Eq. (5.11) for pure AN at ambient density and 298 K are provided in Table 5.3.

Table 5.3. Select thermodynamic quantities for pure AN at 298 K.

Parameter	**Value**
ρ_0	1.725 g/cm^3
Γ_0	1.0
c_v	0.4 cal/g K

In addition to determining the initial pressure rise in the unreacted explosive, the Mie-Grüneisen EOS also affects the numerical stability of the reactive burn model. Most hydrocodes will calculate the first and second derivatives of the principle isentrope as a part of the numerical solution. The first derivative of the isentrope is related to the unreacted material sound speed, c, as [109]

$$(\rho c)^2 = -\left(\frac{\partial p}{\partial v}\right)_s, \tag{5.12}$$

which must be a positive quantity for the EOS to make physical sense (i.e. no imaginary sound speed values). The second derivative of the isentrope is related to the fundamental derivative, $\mathcal{G}$, via [123]

$$\mathcal{G} = \frac{v^3}{2c^2}\left(\frac{\partial^2 p}{\partial v^2}\right)_s, \tag{5.13}$$

which is a measure of the convexity of an isentrope [109]. The sign of $\mathcal{G}$ determines whether the characteristics will build to form a shock wave ($\mathcal{G} > 0$) or rarefaction shock ($\mathcal{G} < 0$). Both $(\rho c)^2$ and $\mathcal{G}$ may become negative for high enough levels of compression when using the form of the Grüneisen parameter in Eq. (5.10) [119].

It is possible to obtain analytical expressions for both the material sound speed and fundamental derivative when using the Mie-Grüneisen EOS. The derivation is

discussed briefly, beginning with an expansion of the derivative of pressure along an isentrope,

$$\left(\frac{\partial p}{\partial v}\right)_s = \left(\frac{\partial p}{\partial v}\right)_e - p\left(\frac{\partial p}{\partial e}\right)_v. \tag{5.14}$$

Eq. (5.14) is combined with Eqs. (5.7)−(5.13) to determine an analytical expression for the derivative of pressure along an isentrope as,

$$\left(\frac{\partial p}{\partial v}\right)_s = \phi' - p\Gamma_0\rho_0. \tag{5.15}$$

The second partial derivative in Eq. (5.13) may be evaluated with the identity,

$$\left(\frac{\partial \mathcal{X}}{\partial v}\right)_s = \left(\frac{\partial \mathcal{X}}{\partial v}\right)_e - p\left(\frac{\partial \mathcal{X}}{\partial e}\right)_v, \tag{5.16}$$

where $\mathcal{X}$ is any function $\mathcal{X}(v, e)$ of energy and volume. If Eq. (5.15) is substituted for $\mathcal{X}$ in Eq. (5.16), the second derivative is given explicitly as,

$$\left(\frac{\partial^2 p}{\partial v^2}\right)_s = \phi'' - \phi'\Gamma_0\rho_0 + p\left(\Gamma_0\rho_0\right)^2. \tag{5.17}$$

When assembling new Mie-Grüneisen EOS, it is important to check the sign of both Eqs. (5.15) and (5.17) for instabilities over the entire pressure-volume range of interest. Additional information on the instability modes associated with the Mie-Grüneisen EOS may be found in work by Segletes [119, 124]. In Secs. 5.3.1 and 5.3.2, the unreacted EOS is further developed using a Hugoniot reference function and p-α porosity model to match the initial density.

5.3.1 Hugoniot Reference Curve

The Hugoniot reference curve is the set of all possible states across a shock wave, and is used as a reference function for the Mie-Grüneisen EOS in Eq. (5.9). The Hugoniot state is depicted in Fig. 5.3, with a steady 1d shock wave in a coordinate system attached to the wave. The inviscid Euler equations are used to step through the jump in pressure. Conservation of mass, momentum, and energy are given by

$$\dot{m}'' = \rho\left(U_s - u_p\right) = \rho_0 U_s, \tag{5.18}$$

$$p + \rho \left(U_s - u_p\right)^2 = p_0 + \rho_0 {U_s}^2, \tag{5.19}$$

and

$$\rho \left(U_s - u_p\right) \left(e + \frac{1}{2}\left(U_s - u_p\right)^2 + \frac{p}{\rho}\right) = \rho_0 U_s \left(e_0 + \frac{1}{2}{U_s}^2 + \frac{p_0}{\rho_0}\right), \tag{5.20}$$

respectively, where $\dot{m}''$ is the mass flux assumed constant for steady state, U_s is the shock velocity, and u_p is the particle velocity with respect to a fixed reference frame. To solve the system of equations, an EOS is required for closure; the Hugoniot pressure, p_H, and energy, e_H, do not appear in Eqs. (5.18)−(5.20) because the Hugoniot state is the simultaneous solution to the Euler equations in addition to the EOS.

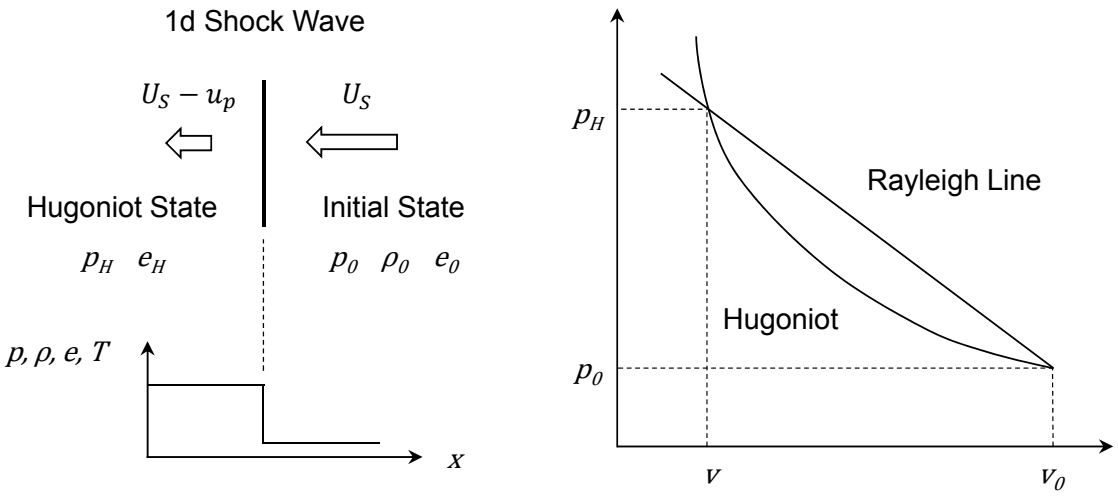

Figure 5.3. Schematic for a 1d shock wave and the Hugoniot reference curve.

When the conservation of mass (Eq. (5.18)) and conservation of momentum (Eq. (5.19)) are combined, the parameterized Rayleigh line is obtained,

$$\frac{p - p_0}{1/\rho - 1/\rho_0} = -\dot{m}''^2, \tag{5.21}$$

which describes the physical path taken from the initial state to the final state, having a linear slope in pressure-volume space (see Fig. 5.3). In contrast, the Hugoniot curve is not a path but the locus of possible jump states, and the area between the Rayleigh

line and Hugoniot is approximately the amount of energy dissipated by the shock wave [110].

Without a calibrated equation of state, the measured shock-particle velocity relationship is used to defined the Hugoniot. From experimental results, a quadratic formula describes the shock-particle relationship in most materials [110],

$$U_s = c_0 + s u_p + q {u_p}^2, \tag{5.22}$$

where values of c_0, s, and q may be found in the literature [54,110]. From Eq. (5.22), the Hugoniot pressure and energy are calculated through the sequence,

$$\mu = 1 - \rho_0 v = \frac{u_p}{U_s}, \tag{5.23}$$

$$p_H = p_0 + \rho_0 \mu {U_s}^2, \tag{5.24}$$

and

$$e_H = \frac{p_H + p_0}{2\rho_0}\mu + e_0, \tag{5.25}$$

where μ is the material or engineering strain.

The Hugoniot reference curve may also be made explicit in volume in a variety of ways. For example, the Hugoniot pressure and energy may be alternatively expressed as functions of the volume and particle velocity,

$$p_H(v) = p_0 + \frac{{u_p}^2}{v_0 - v}, \tag{5.26}$$

and

$$e_H(v) = e_0 + (v_0 - v)\, p_0 + \frac{1}{2}{u_p}^2, \tag{5.27}$$

to obtain the Hugoniot-based reference function (refer to Eq. (5.9)),

$$\phi_H(v) = \left[1 - \frac{\Gamma(v)}{v}(v_0 - v)\right] p_0 - \frac{\Gamma(v)}{v} e_0 + \left[\frac{1}{v_0 - v} - \frac{1}{2}\frac{\Gamma(v)}{v}\right] {u_p}^2, \tag{5.28}$$

where p_0, e_0, and v_0 are the initial pressure, energy, and volume, respectively. The particle velocity may be further expressed in terms of strain as the solution of Eqs. (5.22) and (5.23) to obtain,

$$u_p = \frac{-(s - 1/\mu) + \sqrt{(s - 1/\mu)^2 - 4qc_0}}{2q}. \tag{5.29}$$

Currently, no experimental U_s-u_p Hugoniot data exists for the ANFO KP-1 samples; however, some data is available for pure AN. In assembling the unreacted EOS for this work, the contributions of the diesel fuel and glass micro-balloons to the unreacted EOS were neglected. When the bulk mechanical response is dominated by the AN particles, this assumption is somewhat reasonable. Still, limited data is available even for porous AN. Dremin *et al.* (1970) [125] report the shock Hugoniot for AN at 0.86 g/cm^3 to be $U_s = 2.20 + 1.96u_p$ km/s; however this density is fixed, and it is not trivial to extrapolate to other initial densities.

The shock Hugoniot of AN near the crystal density is known with greater accuracy than any porous density. Thus, the ANFO KP-1 samples are modeled using the crystalline EOS for pure AN extended via the p-α porosity model discussed in Sec. 5.3.2. The U_s-u_p Hugoniot data for pure AN is summarized in Table 5.4, as determined by Dremin *et al.* [125].

Table 5.4. U_s-u_p Hugoniot for pure AN.

Parameter	**Value**
ρ_0	1.725 g/cm^3
c_0	2.2 km/s
s	1.96
q	0

5.3.2 P-α Porosity Model

The p-α porosity model is a phenomenological model that separates the volume change due to shock compression from the volume change due to void collapse. Over the years, many different porosity models have been applied to extrapolate from higher density shock Hugoniots (e.g. snowplow [126]). The p-α model originally proposed by Herrmann (1969) [127], and later improved by Carroll and Holt (1972) [128], is

one attempt at a simplified description, which achieves some of the correct crushing behavior at both low and high stresses. However, the porosity model does not consider material strength; i.e. the model is only a modification to the hydrodynamic response. Additionally, no allotment is made to adjust temperatures − which are naturally random variables (e.g. hot spot temperature distributions) for porous explosives [104].

The p-α porosity model introduces a distension parameter defined by the density ratio,

$$\alpha = \frac{\rho_M}{\rho}, \tag{5.30}$$

where ρ_M corresponds to the matrix material, ρ corresponds to the porous material, and both the matrix and porous densities correspond to the same pressure and temperature. When evaluating the unreacted EOS, the distension parameter is used to modify the look-up of pressure and energy in the fully dense matrix EOS according to the relations,

$$p\left(\rho, T, \alpha\right) = p_M\left(\alpha\rho, T\right)/\alpha, \tag{5.31}$$

and

$$e\left(\rho, T, \alpha\right) = e_M\left(\alpha\rho, T\right). \tag{5.32}$$

A phenomenological model is then used to define the crushing history, $\alpha\left(t\right)$, depending on the shock pressure determined from the hydrocode.

In general, the crushing history is subdivided into an elastic and compaction region, representing reversible and irreversible crushing behavior, respectively. When pressure is constantly increasing (e.g. $\dot{p} > 0$ for a supported shock wave), the crushing history may be traced in p-α space as shown in Fig. 5.4. For pressures above the crush pressure limit, p_s, the distension parameter is unity, and the unreacted EOS is the same as the matrix material. For pressures in the compaction region (below the crush pressure limit and above the elastic pressure limit), a polynomial relation for $\alpha\left(p\right)$ is used. One form often used in the literature is the second order polynomial [127],

$$\alpha\left(p\right) = 1 + \left(\alpha_0 - 1\right)\left(\frac{p_s - p}{p_s - p_e}\right)^2, \tag{5.33}$$

where p_e is the elastic pressure limit and $\alpha_0 = \rho_{M0}/\rho_0$ is the initial value for the distension parameter. In this way, only three model constants are required to define the irreversible compaction behavior.

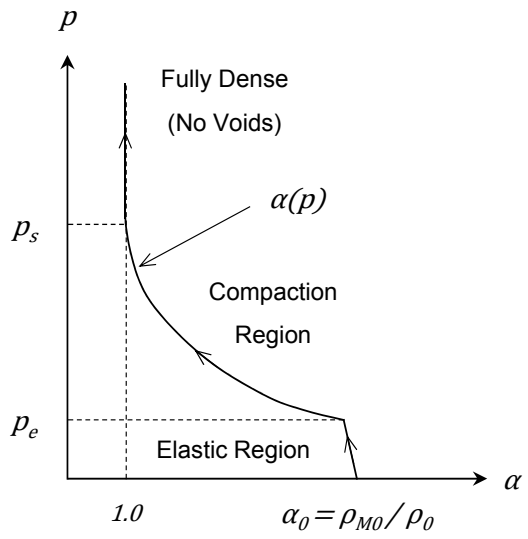

Figure 5.4. Schematic for the crushing history in a shock wave with the p-α porosity model.

Finally, the elastic region is defined implicitly by the variation of sound speed,

$$c = h(\alpha)\, c_0, \tag{5.34}$$

where c_0 is the bulk sound speed of the matrix material, $h(\alpha)$ is a smoothly varying function with the properties $h(1) = 1$, $h(\alpha_0) = c_e/c_0$ where c_e is the sound speed in the virgin porous material, and c is the bulk sound speed defined by thermodynamic relations [127]. Using the functional forms of $\alpha(p)$ implied by Eqs. (5.33) and (5.34), the crushing history is solved via a time integration internal to the hydrocode. In practice, the chain rule is used to determine the time rate of change in the distension parameter,

$$\dot{\alpha} = \frac{d\alpha}{dp} \cdot \frac{dp}{dt}, \tag{5.35}$$

which links together the phenomenological model with the pressure rise. A description of the p-α porosity model becomes more complicated when the pressure decreases, and some volume is recovered through elastic relaxation.

During preparation of the ANFO KP-1 explosive charges, minimal force was required to press the samples to the target density of 50% TMD. Higher densities were also pressed with no elastic relaxation; hence, a reasonable approximation is to assume that all of the volume compression in the MI experiments is due to irreversible compaction. In this case, the elastic pressure limit, p_e, is set to zero to eliminate the elastic region (as well as the need to include an elastic sound speed parameter). Only the crush pressure limit, p_s, remains to be fit since the initial matrix and porous densities are known. Prior numerical investigations have found that a default value of 100 MPa is reasonable for a wide range of calculations [129]. This value was also assumed for the current model; all p-α model parameters for the ANFO KP-1 samples are shown in Table 5.5.

Table 5.5. P-α model parameters for the ANFO KP-1 samples.

Parameter	**Value**
ρ_{M0}	1.725 g/cm^3
ρ_0	0.826 g/cm^3
p_s	100 MPa
p_e	0

5.4 Detonation Product Equation-of-State

The reaction products of explosives exhibit non-ideal gas behavior. Many different fitting forms for a product EOS are given in the literature; two of the most commonly used EOS are the BKW [88] and Jones-Wilkins-Lee (JWL) [116] forms. Because the JWL equation is more accessible with experimental and calculated parameter values,

it was selected for the ANFO KP-1 model. In summary of the JWL EOS, Lee *et al.* (1968) [116] proposed an improvement to Jones' and Wilkins' forms, so that the pressure-volume-energy relationship of the detonation products should follow,

$$p = A\left(1 - \frac{\omega}{R_1\mathbf{V}}\right)e^{-R_1\mathbf{V}} + B\left(1 - \frac{\omega}{R_2\mathbf{V}}\right)e^{-R_2\mathbf{V}} + \frac{\omega e}{v}, \tag{5.36}$$

where $\mathbf{V}$ stands for the relative volume v/v_0, and e and v are the specific internal energy and specific volume, respectively. From this form, the equation for an adiabat is given by [116],

$$p\left(\triangle\right) = Ae^{-R_1\mathbf{V}} + Be^{-R_2\mathbf{V}} + C\mathbf{V}^{-\omega-\mathbf{1}}, \tag{5.37}$$

where $\triangle$ denotes the adiabat.

The parameters A, B, R_1, R_2, and ω are needed to calibrate the JWL EOS, and may be determined in one of two ways. First, a cylinder test may be used in which the radial expansion of the wall of a confined explosive is measured [116]. The products are assumed to lie on the CJ adiabat, which is calculated through an iterative approach combining the experimental results with hydrocode simulations. This method has been criticized by Mader and Davis [88] that the fitted JWL EOS is only useful in describing a single experiment. In the second approach, a thermochemical code such as CHEETAH [106] is used to predict the equilibrium composition of the detonation products, and expand them adiabatically to the reference state. The predicted adiabat may be fitted with Eq. (5.37) to determine the JWL EOS parameters without performing any experiments. For this work, CHEETAH was used to calculate the JWL parameters for a stoichiometric mixture of Kinepak$^{\text{TM}}$ AN and diesel fuel at an initial density of 0.826 g/cm^3. The parameter values, as well as the CJ state, are summarized in Table 5.6.

The release of chemical energy in a reactive burn model is obtained via an energy shift in either the reactant or product EOS. For example, the JWL EOS may be shifted down in energy by a value equal to the enthalpy of detonation. Alternatively, the unreacted EOS may be increased in energy by the same amount; it is not uncommon

Table 5.6. JWL parameters and CJ calculation for the ANFO KP-1 model at an initial density of 0.826 g/cm^3.

Parameter	**Value**
A	178.42 GPa
B	2.85 GPa
R_1	6
R_2	2
ω	0.399
P_{CJ}	4.37 GPa
D_{CJ}	4.52 km/s
T_{CJ}	3049 K

to observe different bookkeeping of the energy shift depending on which hydrocode is used.

5.5 Ignition and Growth Reactive Burn Model

The ANFO KP-1 reactive burn model is based on an ignition and growth-type reaction rate [94], together with mixture laws for the partially reacted EOS. A general class of pressure-dependent rate laws are given by the formula [130],

$$\dot{\lambda} = \sum_j s_j(\lambda)\, r_j(p, \rho, ...), \tag{5.38}$$

where λ is the mass fraction of the reaction products, $s_j(\lambda)$ is a function representing the burn surface topology, and $r_j(p, \rho, ...)$ is a pressure-dependent burn rate that may also be a function of density and other state variables. The rate law defined by Eq. (5.38) is phenomenological, and it is commonly used to describe sub-grid phenomena in continuum simulations.

The mass fraction of the reaction products, λ, is defined via a volume mixture equation,

$$(1-\lambda)\,V_{UR} + \lambda V_{DP} = V, \tag{5.39}$$

where V_{UR}, V_{DP}, and V are the volume of the unreacted explosive, detonation products, and total volume, respectively, within a single computational cell. Using conservation of volume for a single cell, Eq. (5.39) is rearranged to solve for the detonation product mass fraction,

$$\lambda = \frac{V_{DP}}{V}. \tag{5.40}$$

which is used to illustrate different burn surface topologies. Two important cases are hole burning for spherical hot spots [94], and inward spherical grain burning [130], as depicted in Fig. 5.5.

Hole burning assumes that the volume fraction of detonation products is determined by an inclusion. For a spherical hot spot of radius R, the detonation products will occupy a volume $V_{DP} = \frac{4}{3}\pi R^3$. Assuming that the cell volume, V, is fixed, the mass fraction will go with the radius of the hot spot as $\lambda \sim R^3$. The surface area of the hot spot goes with the square of the radius, so that the burn surface topology function goes with the mass fraction as $s\,(\lambda) \sim \lambda^{2/3}$. A similar derivation is possible for inward spherical grain burning, where the mass fraction and radius of unreacted explosive are related by $1 - \lambda \sim R^3$. Additional descriptions of the burn surface topology functions are given in Table 5.7 from Refs. [90, 130].

The full ignition and growth reactive burn model (IGRB) contains three terms thought to be related to the ignition, growth, and completion of reaction [131]. These terms have combined hole and grain burning topologies in order to slow down the reaction rate near completion ($\lambda = 1$), while still maintaining the initial spherical burning hot spot behavior. The IGRB model requires the calibration of fifteen different constants, and as remarked by Starkenberg [130], "is probably more detailed than is required for the representation of detonation propagation and failure." A

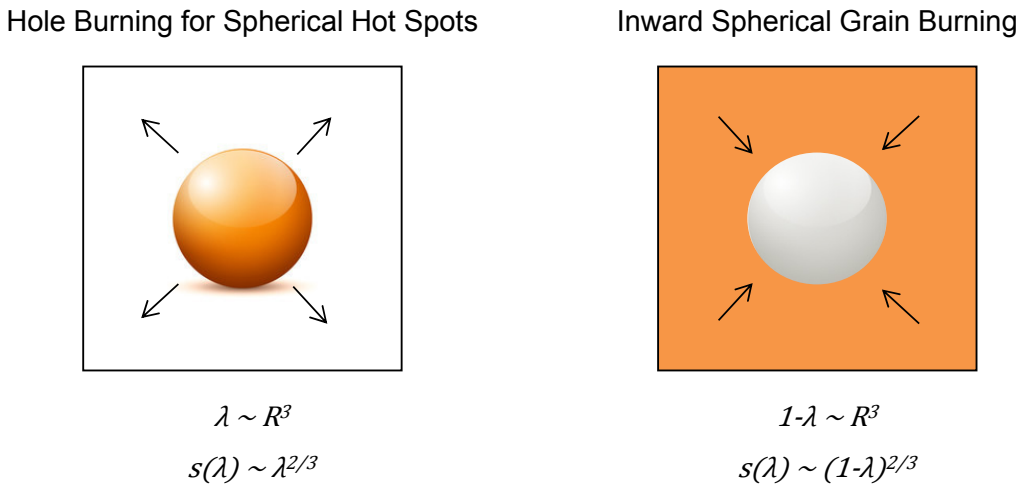

Figure 5.5. Burn surface topologies for spherical hot spots and grain burning inside a computational cell.

Table 5.7. Different burn surface topology functions from Refs. [90, 130].

$s\,(\lambda)$	**Type**
$(1-\lambda)$	bulk reaction
$\lambda^{2/3}$	hole burning for spherical hot spots
λ^{n}	generalized hole burning
$(1-\lambda)^{2/3}$	inward spherical grain burning
$(1-\lambda)^{n}$	generalized grain burning
$(1-\lambda)^{2/9}\,\lambda^{2/3}$	hole burning with grain burning maximized at $\lambda = \frac{3}{4}$

simplified form of ignition and growth based on the original form proposed by Lee and Tarver [94] is defined by the equations,

$$\dot{\lambda} = I\,(1-\lambda)^{2/9}\,\eta^{r} + G\,(1-\lambda)^{2/9}\,\lambda^{2/3} p^{z}, \tag{5.41}$$

and

$$\eta = \rho/\rho_0 - 1 - a, \tag{5.42}$$

where I is the coefficient of ignition, G is the coefficient of growth, η is the relative compression, a is a compression threshold, r is the density exponent, and z is the pressure exponent. The ignition term is set to zero until a minimum compression value is reached (i.e. $\rho/\rho_0 > 1 + a$), and it is turned off when the reaction progress exceeds a certain threshold (i.e. $\lambda > \lambda_{ig}$). In contrast, the growth term is always 'on' and reduces to zero when $\lambda = 0$ or $\lambda = 1$.

Some physical significance is associated with the burn surface topology functions, pressure, and density exponents in Eq. (5.41). For example, the $\lambda^{2/3}$ factor in the growth term represents hole burning for spherical hot spots. The hole burning topology function is multiplied by a generalized grain burning function in order to maximize the reaction rate at $\lambda = 3/4$, as shown in Fig. 5.6. The value of $\lambda = 3/4$ corresponds to the maximum volume fraction that randomly packed spheres can occupy (the actual volume fraction of cubic and hexagonal close packed spheres is calculated to be $\approx 74.05\%$). The ignition term contains the same grain burning function as the growth term in order to achieve consistency in the depletion behavior of the unreacted explosive. One difference between the topology functions for ignition and growth is that the ignition term does not contain a hole burning function, since it must form the hot spots.

Lee and Tarver [94] discuss how the exponent of the relative compression term, η, is associated with different mechanisms of hot spot formation. It may be shown that pressure goes with the relative compression as $p \sim \eta^2$, and particle velocity with relative compression as ${u_p}^2 \sim \eta^3$, over the range of values of interest for shock initiation. Energy requirements for two possible mechanisms of hot spot formation are the kinetic energy $\frac{1}{2}{u_p}^2 \sim \eta^3$ associated with the stagnation of microjets, and the plastic work $\int p^2 dt \sim \eta^4$ needed to collapse small voids [131]. Early studies found that an exponent of four (rather than three) resulted in the best model fits to embedded manganin gage data for PBX-9404, TATB, PETN and TNT [94]. However, later studies considered non-physical values of the compression exponent as high as

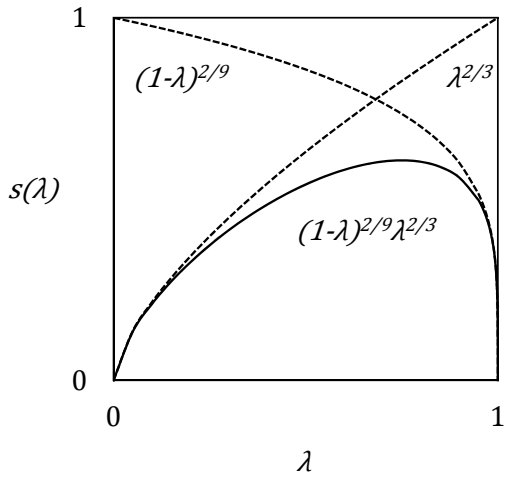

Figure 5.6. Burn surface topology functions used for the IGRB model.

twenty [131]. For the current work, the exponent is fixed at four in order to represent a hot spot formation mechanism based on plastic work.

The dependence of the reaction growth term on pressure also contains some physical significance. Low pressure deflagration rates are known to exhibit p^z behavior, with values of the exponent between 0.8 and 1.0 [100]. Fitted forms of the IGRB model tend to use an exponent between 1.0 and 2.0 for explosives [130], which may suggest a crack burning mechanism with increased surface area at the higher shock pressures. A few examples are available where an IGRB-type model has been calibrated for non-ideal explosives. In these case, the fitted pressure exponent is usually lower; Price and Ghee [132] used a value of 1.0 for ANFO, urea nitrate, and potassium chlorate and paraffin; James *et al.* [133] used a value of 1.1 for ANFO and 0.6 for an AN/aluminum mixture; and Kim and Yoh [134] as well as Souers *et al.* [135] used a value of 1.3 for ANFO. Haskins and Cook [136] show that the lower exponents give increasing non-ideal detonation behavior, and obtained a velocity decrement of 50% using 1.0 for a representational model based on ANFO. From the previous modeling experience [132–136] and experimental burning rate measurements for ANFO [100], a

pressure exponent of 0.9 was fixed in the current model to represent a weak pressure dependence for the ANFO KP-1 samples.

The form of ignition and growth in Eqs. (5.41) and (5.42) contains a total of six tunable model constants: I, a, r, λ_{ig}, G, and z. Typical values for these parameters are shown in Table 5.8, which inform the region of the parameter space to be considered. The fitting routine used for IGRB is discussed in greater detail in Sec. 5.7; in particular, values for the exponents r and z are imposed as 4 and 0.9, respectively.

Table 5.8. Typical values for the IGRB model constants in cgs units.

Parameter	**Low**	**High**
I	1e6	1e17
a	0	0.2
r	4	20
λ_{ig}	0.01	0.5
G	1e-15	1e-2
z	1	2

The ignition and growth rate (Eq. (5.41)) is coupled to a set of mixture laws, which govern the EOS within the reaction zone. Although much attention has been given to the unreacted explosive and its detonation products, far less is understood about the EOS of an intermediate mixture; there is considerable debate surrounding which equilibrium conditions may be assumed in the reaction zone (see for example Ref. [137]). One of the simplest forms for a mixture EOS imposes mechanical and thermal equilibrium (see for example Kipp *et al.* [138, 139]) and it is expressed as,

$$p\left(\rho, T, \lambda\right) = \lambda p_{DP}\left(\rho, T\right) + \left(1 - \lambda\right) p_{UR}\left(\rho, T\right), \tag{5.43}$$

and

$$e\left(\rho, T, \lambda\right) = \lambda e_{DP}\left(\rho, T\right) + \left(1 - \lambda\right) e_{UR}\left(\rho, T\right), \tag{5.44}$$

where the subscripts UR and DP indicate the unreacted explosive and detonation products, respectively. A common, uniform cell temperature T is not physical for a hot spot mechanism; however IGRB is not a thermally-based model. In addition, Eqs. (5.43) and (5.44) are computationally efficient, which can significantly decrease the cost of massively parallel simulations. Hence, Eqs. (5.43) and (5.44) have been implemented for the current ANFO KP-1 model; other models which assume mechanical but not thermal equilibrium may be found elsewhere (e.g. Ref. [137]).

5.6 Hydrocode Implementation

The reactive burn model developed for the ANFO KP-1 test samples was implemented in CTH [140–142], a three-dimensional shock physics hydrocode. CTH is described as an ongoing project of Sandia National Laboratories, with some details of the code appearing in work published by McGlaun *et al.* (1990) [140] and Hertel *et al.* (1995) [141]. CTH is used to model multidimensional, multi-material, large deformation shock wave physics, and employs a fixed Eulerian mesh with a two-step solution scheme. The first step of the solution scheme solves the Lagrangian forms of the governing equations (i.e. mass, momentum, and energy) as explicit finite-volume equations in time. At the end of the Lagrangian step, the mesh is distorted so that a second, remap step is needed which utilizes material interface tracking algorithms. Additional details about the CTH hydrocode may be found elsewhere [142]; an excellent reference for hydrocodes is the text by Zukas [143].

Because of the influence of sample diameter on detonation failure [132] and shock front curvature [98], a minimum of 2d (and potentially 3d) simulation geometries were required for this work. In order to more effectively investigate both the 2d and 3d geometries, as well as minimizing the transcription error of model parameters between the different input files, a master code was written using the APREPRO language (An Algebraic Preprocessor for Parameterizing Finite Element Analyses) [144]. The master code was used to automatically generate input decks for CTH based on smaller

files containing user input instructions. For example, the user input files allow a single command to switch between the 2d cylindrical and 3d rectangular (i.e. Cartesian) explosive charge geometries, where the y-x plane in 2d is mirrored on the z-x plane in 3d. The master code is given in Appendix D.

It has been observed in previous work [66] that even relatively small geometries on the order of a few cm's may require large amounts of RAM and CPU time. Hence, the geometry was kept to the minimum dimensions possible, which included the cylindrical ANFO sample and some space allotment for the confiner thickness. A common computational domain was chosen to be 1.25 x 10 cm^2 and 1.25 x 1.25 x 10 cm^3 for the 2d and 3d geometries, respectively. The 2d geometry allows for a half model of the explosive charge (the solution is symmetric about the longitudinal axis), whereas the 3d geometry allows for a one-quarter model with symmetry boundary conditions on the z-x and z-y planes.

All of the boundary conditions used were either symmetric or material outflow with zero ambient pressure. The symmetric condition was used for all boundaries on the interior of the charge, as well as the explosive booster end (bottom) of the domain, so as to simplify calculations. Specifically, the bottom symmetry condition behaves as an infinite impedance wall on which the explosive charge is rested. This boundary condition has the additional benefit of discouraging recirculation zones which may attempt to draw material back into the mesh from the outside. Mass is allowed to leave the domain through all other boundaries, including the top and sides surrounding the explosive charge. The 2d and 3d geometries used for this work are shown in Figs. 5.7 and 5.8, respectively, with the domain mirrored across the symmetry boundaries for improved visualization.

A fixed, Eulerian mesh is automatically generated over the computational domain. However, CTH does offer a basic capability for adaptive mesh refinement (AMR) based on the subdivision of the domain into different blocks with varying levels of refinement. For the present work, the computational domain was sized to have an 8:1 aspect ratio (y:x in 2d; z:x and z:y in 3d) so that eight equally-sized blocks constitute

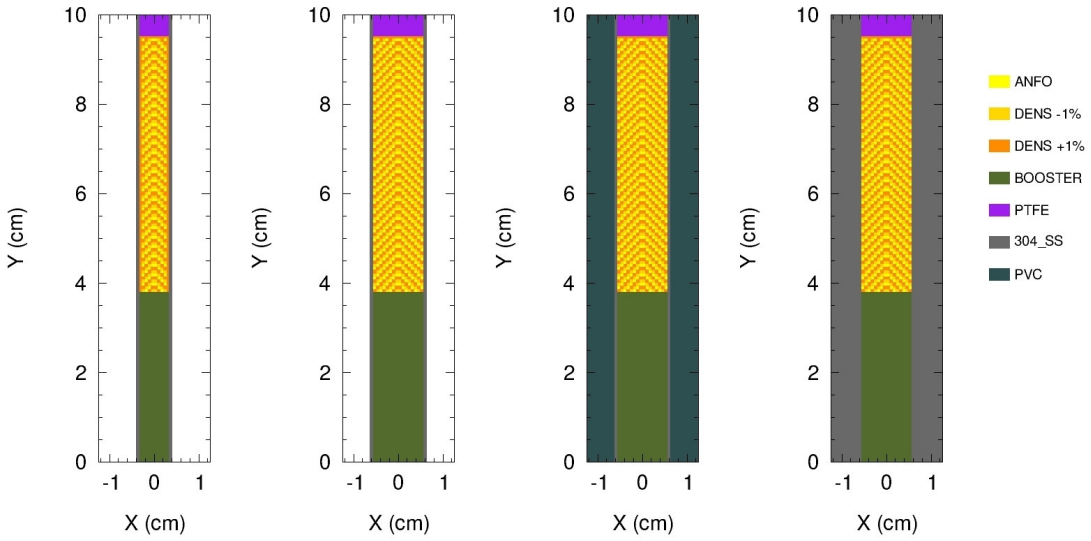

Figure 5.7. Different sample geometries used for 2d cylindrical "half model" calculations. From left to right: SM, THN, PVC, and THK charge configurations.

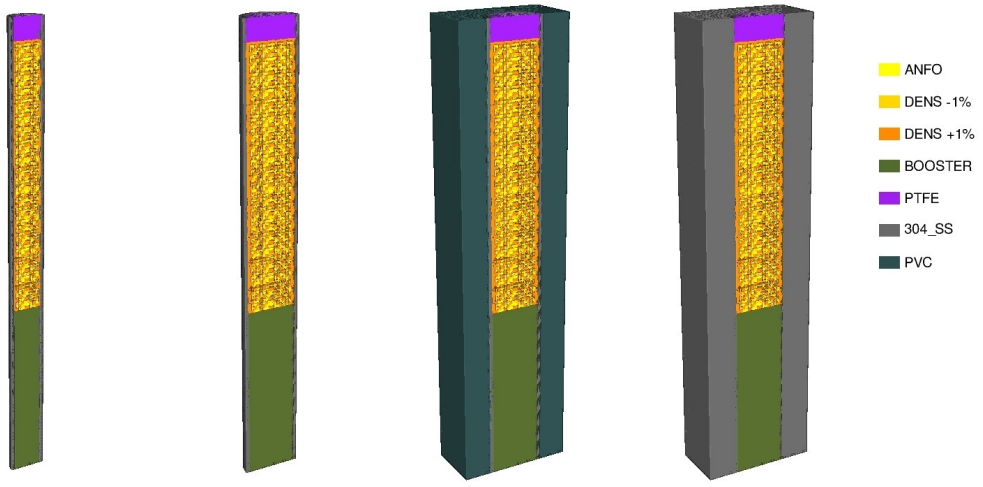

Figure 5.8. Different sample geometries used for 3d Cartesian "quarter model" calculations. From left to right: SM, THN, PVC, and THK charge configurations.

the level zero refinement. Each block is refined to the next level by a subdivision of the edges into 12 to produce either 12^2 or 12^3 cells; with four levels of refinement this allows a maximum mesh resolution of 65.1 μm or 15.36 zones per mm. The mesh resolution may be increased by allowing higher levels of refinement (effectively halving the cell size and doubling the number of zones per mm); however, it was too computationally expensive to run a refinement level-based mesh resolution study for the fully 3d cases.

Previous work [130, 145] suggests a target resolution of 10 to 20 zones per mm for these calculations when using an ignition and growth-type reactive burn model. A good rule-of-thumb is to achieve a minimum of eight cells across the reaction zone [88]; the reaction zone thickness may be a few mm for non-ideal explosives such as TATB [145], and up to a few cm for binary explosives such as ANFO [104]. Hence, some modeling results for ANFO have been reported with convergence using as few as 2 zones per mm [133–135]. A handful of mesh resolution studies were performed on the simpler 2d geometries, where it was determined that 4-20 zones per mm were sufficient; see for example Kittell *et al.* (2014) [66]. The decision to fix the resolution at 15.36 zones per mm was due to the zoning requirements of AMR (i.e. the 8:1 computational domain, which is more easily divided by powers of two) and the feasibility of the parametric studies.

All of the CTH simulations were run with permission on the Cray supercomputers at Sandia National Laboratories. Most of the 2d cases were calculated using 128 cores, with CPU wall times between 4 and 5 minutes. In this manner, detailed parametric studies were feasible to conduct in only a few hours. In contrast to the 2d simulations, the 3d simulations required a minimum of 512 cores with CPU wall times near 48 hours. These performance benchmarks represent an increase of at least three orders of magnitude in the CPU cost moving from 2d cylindrical to 3d rectangular geometries.

Two additional challenges for implementing the models in CTH were the treatment of the explosive booster, and the inclusion of numerical heterogeneities in the ANFO material. Each of these topics is discussed in greater detail in Sec. 5.6.1 and 5.6.2,

respectively. All remaining details concerning the CTH implementation, beyond what has been covered in this chapter, may be found in the master code given in Appendix D together with the CTH User's Manual and Input Instructions [142].

5.6.1 Explosive Booster Model

The explosive booster used in all of the experiments was PRIMASHEET® 1000, a flexible sheet explosive manufactured by the Ensign-Bickford Aerospace and Defense Company. The booster was modeled using a programmed burn at the CJ detonation velocity; this reduces the simulation complexity while still maintaining the relevant physics. Programmed burns are simple to implement based on Huygens construction for the wave propagation; however, they do require an accurate EOS for the detonation products and knowledge of the complete CJ state. Some details of the detonation velocity and material composition are given by the manufacturer for PRIMASHEET® 1000. Unfortunately, there is known to be some discrepancy between the manufacturer's material data and performance predictions using thermochemical equilibrium code such as CHEETAH and TIGER.

Specifically, the manufacturer listed detonation velocity of 7.1 km/s and initial density of 1.44 g/cm^3 do not seem to correspond to the nominal composition of 63% PETN and 37% binder (acetyl tributyl citrate and nitrocellulose). Multiple iterations of the binder composition in TIGER and CHEETAH were only able to predict detonation velocities between 6.7 and 6.9 km/s at 1.44 g/cm^3. In order to achieve an explosive model with a more accurate bulk density and detonation velocity, ethylene glycol dinitrate (EGDN) was added to the binder composition as an energetic additive. A final composition of 63% PETN, 28% EGDN, and 9% acetyl tributyl citrate seemed to match all of the material properties well; JWL EOS parameters as well as the CJ state are summarized in Table 5.9 as determined from TIGER.

Table 5.9. JWL parameters and CJ calculation for PRIMASHEET® 1000. These values were determined using TIGER for a composition of 63% PETN, 28% EGDN, and 9% ATBC at 1.44 g/cm^3.

Parameter	Value
A	711.31 GPa
B	27.83 GPa
R_1	5.782
R_2	1.941
ω	0.359
P_{CJ}	18.52 GPa
D_{CJ}	7.10 km/s
T_{CJ}	3878 K

5.6.2 Creating Numerical Heterogeneities in Density

It is well known that ANFO is a heterogeneous explosive (refer to Sec. 5.2). The ignition and growth model attempts to capture the effects of some of these heterogeneities with a sub-grid model for the burning surface area. However, the IGRB model may not be robust in the simulation if it is inserted as a single continuous material, especially during the calibration of model parameters. Numerical heterogeneities were considered to complement the sub-grid models, and achieve more robust simulations; in particular, these types of heterogeneities introduce asymmetries which help to separate the stable models from those which are less stable. An obvious choice for a numerical heterogeneity is a fluctuation in the initial density, since there are known density gradients in many of the test samples; see for example Ref. [67].

For this work, 2d boxes and 3d cubes were inserted having a nominal, lower (-1%), and higher (+1%) initial density with an edge length of 0.7 mm. This edge length was chosen to obtain nine to ten variations in density across the I.D. of the smallest

diameter tubes (6.52 mm). A periodic tiling pattern was chosen as shown in Fig. 5.9, which is also visible in the simulation geometries shown in Figs. 5.7 and 5.8. The tiling pattern is a simple one, and is arranged so that no two adjacent tiles share the same initial density.

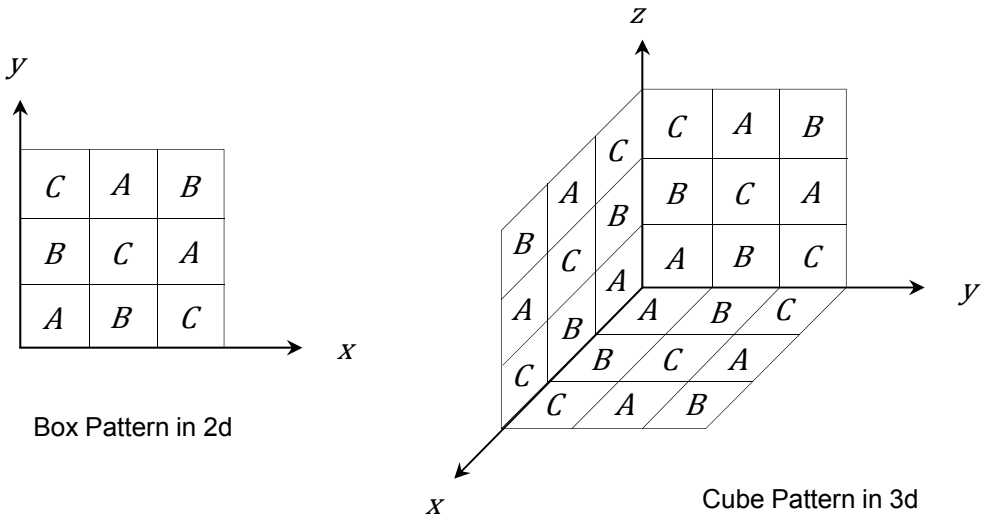

Figure 5.9. Periodic tiling pattern for the numerical heterogeneities in density. Letters correspond to (A) the mean, (B) -1% lower, and (C) +1% higher initial densities.

No precedent exists for a numerically heterogeneous reactive burn model; ultimately the choice of a tiling pattern was based on discussions with staff members at Sandia National Laboratories. Some suggestions included a two-material ±1% checkerboard pattern, as well as a random tile distribution. The decision to use a three-material pattern was made to achieve grater complexity than a two-material checkerboard, yet control the mean density more precisely than a random seeding. It is currently unknown how important the pattern is for numerical heterogeneities; future work should consider other shapes, randomization, and more incremental changes to the initial density.

5.7 Model Calibration and Validation

Often, the question is asked whether or not simulation results are "correct." An entire field of verification and validation dedicated to computer simulation models is well-established, and provides many useful guidelines for testing the underlying models influencing the simulation results. Informally, *verification* seeks to determine whether or not the appropriate equations have been implemented and solved correctly. Once a model has been verified, *validation* seeks to determine whether or not the physics are represented correctly. Model *calibration* involves adjusting the unknown model parameters in order to match a certain reference datum with the greatest accuracy. For this work, calibration and validation of the ANFO KP-1 model is accomplished using the experimental MI data; more rigorous validation procedures should be considered in future work with a wider data set, especially one including large-scale experiments (up to tens of cm).

Model verification is mostly achieved by using the CTH hydrocode, and is not discussed in great detail. Specifically, the IGRB model components including the Mie-Grüneisen, JWL, and mixture EOS together with the p-α porosity model have been previously verified by the CTH development team. Some additional effort was made in this work to ensure that the CTH input decks were error-free with reasonable numerical schemes via inspection of the output, as well as on-the-fly visualization. A reliable input deck was generalized into the APREPRO master code given in Appendix D. The master code prevents transcription errors when adjusting model constants and other high-level simulation parameters; for example, the geometry type (2d cylindrical or 3d rectangular) and confiner material may be set with a single command read by the master code.

Calibration and validation procedures for the ANFO KP-1 model were finalized with some trial and error. Four of the six unknown IGRB model constants (I, a, λ_{ig}, and G) were calibrated via multiple 2d CTH simulation runs, while the compression ratio and pressure exponents in Eq. (5.41) were fixed at 4 and 0.9, respectively, as

discussed in Sec. 5.5. The calibration was conducted using one of the four test configurations shown in Fig. 5.7, where the other cases are reserved for model validation. The calibration was performed with assistance from the DAKOTA code [146], and an efficient Latin hypercube sampling (LHS) algorithm developed at Sandia National Laboratories [147].

The decision to use a sampling algorithm, rather than a parameter optimization routine, was made because of the highly nonlinear effects of the IGRB model constants on the simulations. Multivariable optimization techniques, especially gradient-based methods, may converge to local minima rather than the best solution over the whole parameter space; this scenario was encountered many times in preliminary studies. Two of the more common and well-respected sampling algorithms are LHS and Monte Carlo, and each was considered for sampling the IGRB parameter space.

The only major difference between LHS and Monte Carlo sampling is how the parameter space is partitioned. An abbreviated explanation is that for a fixed sample size, N, the LHS algorithm divides each parameter into N bins; the random samples are arranged so that only one point exists within each bin in the hyperdimensional space. The advantage of LHS over Monte Carlo is that statistical significance might possibly be achieved with fewer samples [146]. If each sample corresponds to a computationally expensive computer simulation, then LHS is usually preferred over Monte Carlo, especially for uncertainty quantification. The 2d CTH simulations used to calibrate the IGRB model are not exceedingly expensive to run, so LHS was used to populate the parameter space with many samples (as high as $N = 1000$). It was reasoned that the combination of an efficient sampling algorithm and large sample size should locate the best calibration point, even if the behavior of the model parameters is highly nonlinear.

The DAKOTA code was used to manage the different LHS runs, where the level of automation introduced by DAKOTA required a single "goodness-of-fit" metric for

each combination of the input parameters. An objective function was chosen for this work based on a sum of squared percent errors (SSPE),

$$Obj = \sqrt{\frac{1}{N}\sum_{i=1}^{N}\left(1 - \frac{V_{i,CTH}}{V_i, Experiment}\right)^2} \tag{5.45}$$

where i corresponds to a discrete point, x_i, on the longitudinal axis of the explosive charge, and V is the spatially-resolved shock or detonation velocity. Eq. (5.45) was chosen to be a stringent criteria, equally weighting all sections of the experimental MI data. Velocity is a more physical quantity than the time resolved shock trajectory; preliminary studies that considered an objective function based on matching the shock trajectory did not always guarantee a smooth and well-behaved velocity result. These preliminary studies revealed that the experimental shock trajectories may be fit with "chugging" or "pulsing" instabilities.

Model validation is less quantitative than the calibration procedures; it is also complicated by the fact that all reactive burn models, including IGRB, are fundamentally flawed. These models do not capture the inherent probabilistic nature of ANFO [104] and do not scale well [88]; often, these types of models will be calibrated for each explosive diameter tested. Model validation procedures for this work consist of using the calibrated IGRB model constants to simulate the remaining MI test cases. Several predictions are also made for additional experiments that could be performed in future work. These experiments include the same MI test configurations at different initial densities, larger diameter charges, and large scale wedge tests to determine the shock sensitivity. Such predictions are critical to the model validation, and may improve understanding for using both large and small scale explosive tests.

5.7.1 Front Tracking Code

Continuous measurement of the reactive wave front was accomplished using the FORTRAN 90 post processing code shown in Appendix E. Instantaneous velocity calculations were complicated by the shock detection algorithm, which is not necessar-

ily trivial; see for example a recent discussion by Menikoff and Shaw to detect shock waves based on a function of the Hugoniot [90]. In this work, at least four different quantities were considered to detect the time of arrival of shock waves, including a minimum pressure, distension, reaction, and motion threshold. Ultimately, the time resolution of the simulation output and the location of the measurements were found to be equally important as the threshold condition.

The final version of the front tracking code relies on 400 gage measurements output from the CTH simulations. These gauges are spaced on the longitudinal axis by increments of one-quarter wavelength to coincide directly with MI peak picking data. More dense spacing did not allow sufficient Δt to calculate the velocity with a finite difference algorithm, and less dense spacing did not resolve the velocity profile as well. In addition, five columns (80 gages along the axis) span the radius of each explosive charge. In this way, all time of arrival measurements are averaged across the radius; the average compensates for slight shock front curvature as well as centerline anomalies due to the symmetry boundary condition.

6. MODEL REFINEMENTS TO THE MIE-GRÜNEISEN EOS

The ignition and growth model used to simulate the MI experiments is independent of temperature, despite that real chemical reactions are thermally-driven processes. This is because less detailed information is known about the temperature of shock and reactive waves, especially for those in heterogeneous materials. Some work was conducted while at Sandia to develop a physically-based Mie-Grüneisen equation of state (EOS) that is capable of temperature predictions. The work presented here is currently under review for publication in *Combustion Theory and Modelling*, and is approved for unclassified unlimited release from Sandia (SAND2015-7099 J). The theory is demonstrated for the secondary explosive, hexanitrostilbene (HNS), although it could be easily implemented for ammonium nitrate (AN) using the specific heat data from Ref. [104].

6.1 Scope

A physically-based form of the Mie-Grüneisen Equation of State (EOS) is derived for calculating 1d planar shock temperatures, as well as hot spot temperature distributions from heterogeneous impact simulations. This form utilizes a multi-term Einstein oscillator model for specific heat, and is completely algebraic in terms of temperature, volume, an integrating factor, and the cold curve energy. Moreover, any empirical relation for the reference pressure and energy may be substituted into the equations via the use of a generalized reference function. The complete EOS is then applied to calculations of the Hugoniot temperature and simulation of hydrodynamic pore collapse using data for the secondary explosive, hexanitrostilbene (HNS). From these results, it is shown that the choice of EOS is even more significant for determining hot spot temperature distributions than planar shock states. The

complete EOS is also compared to an alternative derivation assuming that specific heat is a function of temperature alone, i.e. $c_v(T)$. Temperature discrepancies on the order of 100-600 K were observed corresponding to the shock pressures required to initiate HNS (near 10 GPa). Overall, the results of this work will improve confidence in temperature predictions. By adopting this EOS, future work may be able to assign physical meaning to other thermally sensitive constitutive model parameters necessary to predict the shock initiation and detonation of heterogeneous explosives.

6.2 Background

It is well known that material heterogeneities will sensitize explosives to initiation leading to a detonation [107]. These heterogeneities form local sites for energy deposition and elevated temperatures known as hot spots [95]. Experimental [148] and computational [149] results show that under certain conditions (i.e. strong shocks up to tens of GPa) the collapse of small pores causes jetting, and a hot spot is formed at the site of the jet impact. Moreover, it is possible to simulate the passage of shock waves through heterogeneous materials and then identify local hot spots at the mesoscale [150]; this includes simulations of pore collapse with Arrhenius kinetics to capture the initiation of reaction [151]. The transition to a fully supported detonation may be observed as well [152]; however, these simulations are sensitive to the available material models including the equation of state (EOS). Specifically, a wide range of hot spot temperatures may be calculated depending on the EOS of the unreacted explosive.

One approach to developing an EOS is to assume that Grüneisen's postulate [115] holds over the state space of interest, and then employ the incomplete form of Mie-Grüneisen. This form is convenient because it may be made to fit measured shock-particle velocity relationships or isentropic compression data while also being computationally efficient and simple to parameterize. However, the incomplete form is defined in energy and volume space, and lacks a functional relationship mapping it

to the complete thermal state. A physically-based specific heat model is required to complete the EOS, and it must be a function of both volume and temperature to satisfy the condition of thermodynamic compatibility [120]. Moreover, the derivation of a complete form of the Mie-Grüneisen EOS depends on the choice of a reference curve and functional form of Grüneisen gamma so that different presentations of the EOS may be found in the literature (see for example Refs. [120]− [118]).

In this work, a complete Mie-Grüneisen EOS is derived using a physically-based Einstein oscillator model for specific heat. The derivation is unique in that it is highly generalized, yet completely algebraic in terms of temperature, volume, an integrating factor, and the cold curve energy. The complete EOS is then applied to determine hot spot temperature distributions for the secondary explosive hexanitrostilbene (HNS). Specifically, calculations of the Hugoniot (1d planar) shock temperature and the collapse of a 10 μm pore are discussed. Additional emphasis is placed on the effects of volume scaling, and the consequences of an EOS derivation assuming that specific heat is a function of temperature alone. Overall, the objectives of this work are to improve the confidence in temperature predictions for shock and impact loading of both homogeneous and heterogeneous systems. Then, physical meaning may be associated with thermally sensitive kinetic and strength parameters necessary to predict the shock initiation and detonation of explosives.

6.3 Derivation of the Equation of State

6.3.1 Incomplete Form of Mie-Grüneisen

The incomplete form of Mie-Grüneisen defines pressure as a function of specific volume and energy, and is the governing equation for current EOS development. This form is familiar to shock physics applications, so emphasis is placed on the notation required to generalize relationships between different reference curves. The incomplete

form follows from Grüneisen's postulate that the lattice frequencies are a function of volume alone [115],

$$\left(\frac{\partial p}{\partial e}\right)_v = \frac{\Gamma(v)}{v}. \tag{6.1}$$

This approximation is reasonable for a cubic solid when temperatures are low enough to keep specific heat below the Dulong-Petit asymptotic limit [114]. The incomplete form of the Mie-Grüneisen EOS is found by integrating Eq. (6.1),

$$p(v,e) = \frac{\Gamma(v)}{v}e + \phi(v), \tag{6.2}$$

where $\phi(v)$ is the arbitrary reference function motivated by Segletes [119],

$$\phi(v) = p_{ref}(v) - \frac{\Gamma(v)}{v}e_{ref}(v). \tag{6.3}$$

The reference function, $\phi(v)$, is preferred to using the reference pressure, $p_{ref}(v)$, and energy, $e_{ref}(v)$, separately, as it allows for concise mathematical relationships. Additionally, it permits explicit equations to solve the cold curve and isentrope.

Now, the most common empirical relationship used to construct the Mie-Grüneisen EOS is the shock-particle (U_s-u_p) velocity relationship defining the Hugoniot state. In this case, a Hugoniot-based reference function, $\phi_H(v)$, may be expanded using the shock jump relations. Hugoniot pressure and energy are expressed as functions of volume and particle velocity,

$$p_H(v) = p_0 + \frac{{u_p}^2}{v_0 - v}, \tag{6.4}$$

and

$$e_H(v) = e_0 + (v_0 - v)\,p_0 + \frac{1}{2}{u_p}^2, \tag{6.5}$$

to obtain a generalized yet compact form of the Hugoniot-based reference function,

$$\phi_H(v) = \left[1 - \frac{\Gamma(v)}{v}(v_0 - v)\right]p_0 - \frac{\Gamma(v)}{v}e_0 + \left[\frac{1}{v_0 - v} - \frac{1}{2}\frac{\Gamma(v)}{v}\right]{u_p}^2, \tag{6.6}$$

where p_0, e_0, and v_0 are the initial pressure, energy, and volume, respectively. As will be shown later, e_0 is chosen to agree with the reference temperature, T_0, and specific heat model. Eq. (6.6) can be made explicit for a known U_s-u_p relationship, and substituted wherever the reference function, $\phi(v)$, appears.

6.3.2 Solution of the Cold Curve and Isentropes

Relationships between three primary types of reference curves (the Hugoniot, cold curve, and isentropes) are shown schematically in Fig 6.1. These relationships are governed by the incomplete form of Mie-Grüneisen in energy-volume space; in this discussion they represent a consistent EOS surface calibrated to the Hugoniot state. However, the interested reader could reverse the following procedures to derive any two curves (including the Hugoniot) from the remaining third curve, or from another reference altogether (e.g. isotherm). Overall, the results of this section generalize and unify the procedures necessary to move from one reference curve to another and will help to derive the path-independent EOS.

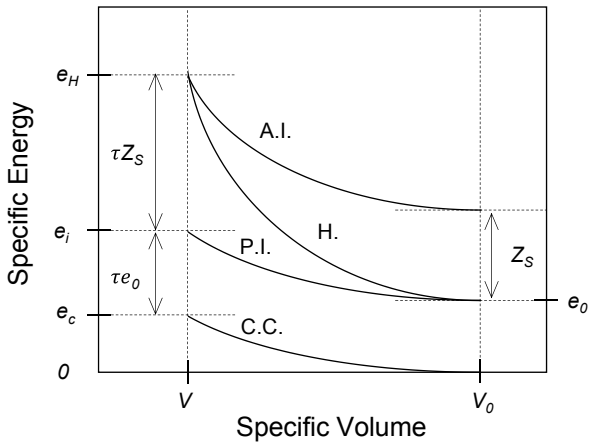

Figure 6.1. Depiction of the reference curves related by the incomplete Mie-Grüneisen EOS; abbreviations are C.C. (cold curve), P.I. (principal isentrope), H. (Hugoniot), and A.I. (arbitrary isentrope).

Concerning the cold curve, the total pressure of an arbitrary solid may be decomposed as the sum of two components in temperature and volume space [114],

$$p\left(v,T\right)=p_{th}\left(v,T\right)+p_{c}\left(v\right), \tag{6.7}$$

where the thermal component, p_{th}, is a function of the vibrational and thermal energies of the solid, and is in general non-linear with respect to temperature. The other component is the cold pressure, p_c, which is due to intermolecular forces present at zero Kelvin. Likewise, energy may be decomposed into a thermal and cold component,

$$e\left(v,T\right)=e_{th}\left(v,T\right)+e_c\left(v\right). \tag{6.8}$$

Both e_c and p_c vary with volume alone and lie on the so-called cold curve, or zero Kelvin isotherm (which is also an isentrope). In lieu of measurements of the cold curve, e_c and p_c are calculated from an integration of the Hugoniot reference function. An equation for the cold curve is found by evaluating the thermodynamic consistency relationship at zero Kelvin to obtain [119],

$$p_c=-\frac{de_c}{dv}, \tag{6.9}$$

and is substituted into Eq. (6.2) to obtain the ODE,

$$-\frac{de_c}{dv}-\frac{\Gamma\left(v\right)}{v}e_c=\phi_H\left(v\right). \tag{6.10}$$

Prior experience has found it is easier to solve Eq. (6.10) numerically; however, an analytic solution does exist. The following integrating factor [117],

$$\tau\left(v\right)=exp\left[-\int_{v_0}^{v}\frac{\Gamma\left(\hat{v}\right)}{\hat{v}}d\hat{v}\right], \tag{6.11}$$

may be used to rearrange the ODE in Eq. (6.10) into an exact differential and solved,

$$e_c\left(v\right)=-\tau\left(v\right)\int_{v_0}^{v}\frac{\phi_H\left(\hat{v}\right)}{\tau\left(\hat{v}\right)}d\hat{v}, \tag{6.12}$$

where the initial cold curve energy was made to vanish ($e_c\left(v_0\right)=0$) and integrating factor reduced to unity ($\tau\left(v_0\right)=1$) at the ambient density condition. The cold curve pressure may then be calculated either via Eq. (6.2) or Eq. (6.9) to obtain the same relation. A final remark about the cold curve is that when U_s-u_p Hugoniot data is used to construct ϕ_H in Eq. (6.6), the substitution of the cold curve back into the EOS will yield the same surface. That is, a reference function based on either the Hugoniot

or cold curve is the same function. This may be easily verified by substitution of Eqs. (6.9) and (6.12) into Eq. (6.3).

Calculations of the isentropes are fundamentally similar to the cold curve; from thermodynamic relationships, it may be shown that the principal isentrope shares the same differential form as the cold curve [117],

$$p_i = -\frac{de_i}{dv}, \tag{6.13}$$

where p_i and e_i are the pressure and energy along the principal isentrope, respectively. The principal isentrope is distinguished from other isentropes during integration with the initial energy condition of e_0 at ambient density. Substituting Eq. (6.13) into Eq. (6.2) and combining with Eq. (6.12), a compact relationship between the principal isentrope and the cold curve is determined to be,

$$e_i = e_c + \tau e_0, \tag{6.14}$$

where the isentrope pressure may be recovered from Eq. (6.13). In this analysis, Eq. (6.14) shows that the cold curve and principal isentrope are coincident when e_0 is set to zero (which is common practice in may hydrocode implementations). The thermal energy between the cold curve and principal isentrope may also be viewed graphically in Fig. 6.1.

Finally, any arbitrary energy state (including the Hugoniot) may be decomposed as the sum of the principal isentrope plus a volume scaled function of entropy. This decomposition is illustrated graphically in Fig. 6.1, and follows from a similar integration of Eq. (6.13) through the ambient density state along an arbitrary isentrope [109],

$$e = e_i + \tau Z_S, \tag{6.15}$$

where Z_S is the function of entropy of the shocked state [117]. Additional details for the derivation of Eq. (6.15) may be found in other work [118]; a key feature is that the parameter Z_S is constant along the arbitrary isentrope in Fig. 6.1. Overall, Eqs. (6.12), (6.14), and (6.15) follow as consequences of the incomplete form of Mie-Grüneisen, and allow one to move freely from one reference curve to another via the integrating factor, τ, and function of entropy, Z_S.

6.3.3 Thermodynamic Closure and Compatibility

The incomplete form of Mie-Grüneisen is closed through the solution of temperature-based expressions for energy and entropy. However, a known reference temperature is needed to define any other thermal state. Two options are the cold curve zero temperature, and the initial temperature, T_0. From these reference temperatures, a seemingly limitless number of integrations could be taken to reach the final thermal state. In this work, only two integration pathways in temperature-volume space are discussed as shown in Fig. 6.2. Note that the complete EOS is path independent, and could be obtained via either integration route.

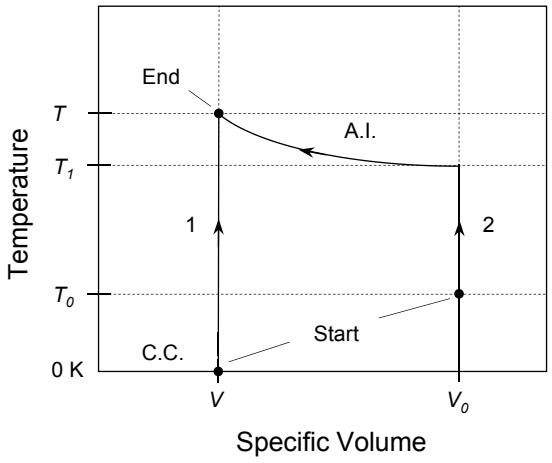

Figure 6.2. Select integration pathways in temperature-volume space from a known reference temperature to the final state; abbreviations are C.C. (cold curve) and A.I. (arbitrary isentrope).

Using the first integration pathway shown in Fig. 6.2, energy is found by integrating specific heat from the cold curve zero temperature at constant volume,

$$e\left(v,T\right)=e_c\left(v\right)+\int_0^T c_v\left(v,\hat{T}\right)d\hat{T}. \tag{6.16}$$

Likewise, entropy is found by integrating Maxwell's relation with respect to the cold curve zero temperature,

$$s\left(v,T\right)=\int_{0}^{T}\frac{c_{v}\left(v,\hat{T}\right)}{\hat{T}}d\hat{T}, \tag{6.17}$$

where the entropy along the cold curve is set to zero ($s_c = 0$) since the cold curve is also an isentrope. Although Eqs. (6.16) and (6.17) are straightforward, it is not obvious what constraints should be placed on the specific heat model. Since the lower limit of integration is zero, it is intuitive that c_v and c_v/T should vanish at zero Kelvin. Beyond this, the specific heat model must be physically-based, and a function of both temperature and volume in the final parameterization of the EOS.

Several relationships are known between the Grüneisen parameter and specific heat, so that they are not independent of each other. Mixed partial derivatives of Helmholtz free energy may be evaluated to yield the thermodynamic compatibility relationship [120],

$$\frac{\Gamma\left(v\right)}{v}\frac{\partial c_{v}}{\partial T}=\frac{1}{T}\frac{\partial c_{v}}{\partial v}, \tag{6.18}$$

which is a first order linear homogeneous PDE for the specific heat. Eq. (6.18) is also the simplification of a more generalized relationship under Grüneisen's postulate [114]. This relationship is necessary to derive a path-independent EOS and cannot be satisfied by specific heat having temperature dependence alone. Multiple approaches exist to solve the PDE in Eq. (6.18) including the separation of variables technique. Menikoff [109, 120] has shown a solution to the PDE through temperature scaling of the ambient density specific heat model,

$$c_{v}\left(v,T\right)=c_{v}\left(v_{0},T/\tau\left(v\right)\right), \tag{6.19}$$

where $\tau\left(v\right)$ is the integrating factor from Sec. 6.3.2. The approach of Menikoff is adopted for this work as it allows for algebraic simplifications of the final EOS.

6.3.4 Einstein Oscillator Model for Specific Heat

Modern theories for specific heat are based on lattice vibrations known as phonons [155]. The essential features for any specific heat model include a vanishing value near zero Kelvin, T^3 behavior at low temperature, and an asymptotic limit (Dulong-Petit) above a characteristic temperature. Some of these features are incorporated by the Debye and Einstein models for phonon mode density, and further details may be found in a reference for solid state physics [155]. In this work, the Einstein model is used as the elevated temperatures resulting from shock waves correspond with internal vibrational modes [154]; these are better captured by Einstein's model [155]. Moreover, this form is explicit, and certain temperature integrals are analytically defined. An arbitrary number of oscillators may be summed to define the total specific heat at ambient density,

$$c_v\left(v_0, T\right) = \sum_{i=1}^{N} c_{v_i} E_i\left(\frac{\theta_i}{T}\right), \tag{6.20}$$

where $E_i\left(\xi_i\right)$ are the Einstein oscillator functions defined as,

$$E_i\left(\xi_i\right) = \frac{{\xi_i}^2 exp\left(\xi_i\right)}{\left[exp\left(\xi_i\right) - 1\right]^2}. \tag{6.21}$$

For the multi-term Einstein oscillator model, the user input is the set of characteristic temperatures (θ_i) and high temperature limiting coefficients (c_{v_i}) for specific heat, which are fit to experimental data. With this form, the temperature integrals of specific heat at ambient density are analytically defined to be,

$$\int_0^T c_v\left(v_0, \hat{T}\right) d\hat{T} = \sum_{i=1}^{N} \frac{c_{v_i}\theta_i}{exp\left(\theta_i/T\right) - 1}, \tag{6.22}$$

and

$$\int_0^T \frac{c_v\left(v_0, \hat{T}\right)}{\hat{T}} d\hat{T} = \sum_{i=1}^{N} c_{v_i}\left(\frac{\theta_i/T}{exp\left(\theta_i/T\right) - 1} + \frac{\theta_i}{T} - ln\left(exp\left(\theta_i/T\right) - 1\right)\right). \tag{6.23}$$

Now, the integrals of specific heat appearing in the temperature-based EOS (e.g. Eqs. (6.16) and 6.17) are more general and occur at an arbitrary volume state. From

the solution proposed by Menikoff in Eq. (6.19), integration at arbitrary volume is related to integration at ambient density through the change of variables technique,

$$\int_0^T c_v\left(v,\hat{T}\right)d\hat{T} = \tau\left(v\right)\int_0^{T/\tau(v)} c_v\left(v_0,\hat{\xi}\right)d\hat{\xi}, \tag{6.24}$$

and

$$\int_0^T \frac{c_v\left(v,\hat{T}\right)}{\hat{T}}d\hat{T} = \int_0^{T/\tau(v)} \frac{c_v\left(v_0,\hat{\xi}\right)}{\hat{\xi}}d\hat{\xi}. \tag{6.25}$$

In this way, all temperature integrals may be solved analytically in the final parameterized form of the EOS.

6.3.5 Summary of the Complete Form

The volume scaled form of specific heat in Eq. (6.19) guarantees that thermodynamic compatibility will hold; hence, the energy and entropy functions in Eqs. (6.16) and (6.17) may now be expanded with the Einstein oscillator model. The complete EOS is summarized explicitly as,

$$e\left(v,T\right) = e_c\left(v\right) + \tau\left(v\right)\sum_{i=1}^{N}\frac{c_{v_i}\theta_i}{exp\left(\tau\left(v\right)\theta_i/T\right)-1}, \tag{6.26}$$

$$p\left(v,T\right) = \frac{\Gamma\left(v\right)}{v}e\left(v,T\right) + \phi\left(v\right), \tag{6.27}$$

and

$$s\left(v,T\right) = \sum_{i=1}^{N} c_{v_i}\left(\frac{\tau\theta_i/T}{exp\left(\tau\theta_i/T\right)-1} + \frac{\tau\theta_i}{T} - ln\left(exp\left(\tau\theta_i/T\right)-1\right)\right), \tag{6.28}$$

where Eqs. (6.26)−(6.28) are purely algebraic in terms of temperature, volume, integrating factor τ, and cold curve energy e_c. The reference function, $\phi\left(v\right)$, is a linear combination of the reference pressure and energy so it does not contribute any integral-differential terms to Eq. (6.27). Note that the EOS is written in a fully generalized form; U_s-u_p Hugoniot data may be incorporated via the substitution of $\phi_H\left(v\right)$ in Eq. (6.27). Finally, the energy corresponding to an initial temperature state, T_0, is found by evaluating Eq. (6.26) at (v_0, T_0) to obtain,

$$e_0 = \sum_{i=1}^{N}\frac{c_{v_i}\theta_i}{exp\left(\theta_i/T_0\right)-1}. \tag{6.29}$$

Eqs. (6.26)−(6.29) are the result of the derivation beginning with Grüneisen's postulate, Menikoff's volume scaling relationship, and a physically-based Einstein oscillator model for specific heat. It was derived via integration from the cold curve, although it is possible to obtain from any other integration in temperature-volume space (refer to Fig. 6.2). The cold curve itself, $e_c(v)$, may be derived from any empirical reference including the Hugoniot (refer to Eqs. (6.6) and (6.12)).

6.4 Temperature Calculations

6.4.1 Numerical Solution and Volume Scaling Relationships

The complete EOS is both algebraic and non-linear in temperature. A numerical solution is required to solve for temperature, and volume scaling relations are discussed to assist with calculations. These relationships also provide insight into the EOS surface and its behavior. The energy function in Eq. (6.26) is evaluated at the temperature $T = \tau T^\star$ to obtain,

$$e(v, \tau T^\star) = e_c + \tau e(v_0, T^\star), \tag{6.30}$$

which rearranged,

$$\frac{e - e_c}{\tau} = \sum_{i=1}^{N} \frac{c_{v_i}\theta_i}{exp(\theta_i/T^\star) - 1}. \tag{6.31}$$

may be numerically solved for $T^\star$, and the actual temperature determined to be $T = \tau T^\star$. A similar volume scaling relationship is found with the entropy function; when Eq. (6.28) is evaluated at the same temperature $T = \tau T^\star$, the result,

$$s(v, \tau T^\star) = s(v_0, T^\star), \tag{6.32}$$

confirms that $T = \tau T^\star$ is also an equation for the isentrope passing through $T^\star$ at ambient density. This result could have been obtained through manipulation of Maxwell's relations and Grüneisen gamma, and it is independent of the specific heat model. Temperatures along the principal isentrope passing through the point $s(v_0, T_0)$ are given by $T_i{=}\tau T_0$ in agreement with previous work [118, 120].

6.4.2 Specific Heat Approximations

Alternative forms for a complete EOS abound in the literature and in hydrocode implementation (see for example Refs. [120]− [118]). One approximation is to introduce specific heat as a function of temperature alone; in this case, the derivation of the complete EOS is path-dependent and will lead to slight discrepancies between different integrations. This is illustrative for two reasons; first it allows one to estimate the temperature variation due to the volume scaled specific heat, and consequently bound temperature estimates with 'maximal' and 'minimal' integrations. Second, it allows for a more critical assessment of previous and future EOS derivations.

The two integration pathways shown in Fig. 6.2 are now revisited assuming the approximation $c_v(T)$. Formulas are obtained for the Hugoniot temperature rather than the complete EOS surface; these formulas imply global trends and will bound the temperature deviation due to volume scaling. Using the approximation $c_v(T)$ along the first integration pathway, an approximate Hugoniot temperature is defined through integration from the cold curve at constant volume,

$$e_H - e_c = \int_0^{T_H} c_v\left(\hat{T}\right) d\hat{T}, \tag{6.33}$$

where e_H and T_H are the Hugoniot energy and temperature, respectively. This integration represents a limiting case, where specific heat is integrated as far from the conditions of its calibrated model parameters as possible; i.e. at the highest compression states, and temperatures which extend to zero Kelvin.

In contrast to the first integration path, the second integration occurs mostly at the ambient density state (refer to Fig. 6.2). In this case, the Hugoniot temperature is defined through a manipulation of Eq. (6.15) and is the solution to the equation,

$$\frac{e_H - e_i}{\tau} = \int_{T_0}^{T_1} c_v\left(\hat{T}\right) d\hat{T}, \tag{6.34}$$

where $T_1 = T_H/\tau$ is the isentrope foot temperature passing through the final state as shown in Fig. 6.2. The second integration path is more accurate for several reasons, including temperature integration beginning at T_0 and following the ambient density

state. Possible sources of variation were initially thought to be due to the interpretation of T_1; however, under Grüneisen's postulate the equation for an isentrope is independent of specific heat. The relation $T_1 = T_H/\tau$ is a general result and follows from the discussion in Sec. 6.4.1. It may further be shown that Hugoniot temperature calculations from Eq. (6.34) are equivalent to the complete EOS through the judicious choice of e_0 in Eq. (6.29) (compare the forms of Eqs. (6.34) and (6.31)). Hence, integrations along the second path without volume scaling may yield the same Hugoniot temperatures predicted by the complete EOS. Viewed another way, the second path utilizes volume-scaling techniques automatically through the definition of the isentrope foot temperature, T_1.

All path-dependent temperature calculations will fall somewhere between Eqs. (6.33) and (6.34); this conclusion is explained in further detail in Sec. 6.4.3 with the discussion of numerical results. To give definition to the lower and upper bounds on temperature, Eq. (6.33) is hereafter referred to as the $c_v\,(T)$ approximation since it represents the largest departure from the complete EOS. The $c_v\,(T)$ approximation is compared with the complete EOS using calculations of the Hugoniot temperature as well as hot spot temperature distributions for a secondary explosive.

6.4.3 Hugoniot Temperature Calculations for Hexanitrostilbene

Hugoniot temperatures were calculated using data for the secondary explosive, hexanitrostilbene (HNS). This data includes a quadratic U_s-u_p relationship, constant Grüneisen parameter, and two-term Einstein oscillator model for specific heat (see Table 6.1). Corresponding Hugoniot calculations are shown in Fig. 6.3 as a function of specific volume. These results indicate that the $c_v\,(T)$ approximation under-predicts the shock temperature; this difference is monotonically increasing with higher compression states. For example, the temperature difference corresponding to a shock pressure of 1 GPa (u_p=0.19 km/sec, v =0.54 cm^3/g) is only 12 °C, whereas the temperature difference corresponding to a shock pressure of 10 GPa (u_p=1.19 km/sec,

v =0.43 cm^3/g) is 102 °C. For engineering applications utilizing fine-grained HNS, the minimum pressure to initiate a detonation may be on the order of 10 GPa [139] and even higher. Thus, large differences in temperature may be observed owing to the use of the $c_v(T)$ approximation.

Table 6.1. Crystalline EOS data for the explosive hexanitrostilbene.

Parameter[a]	Units	Value
ρ_0	g/cm^3	1.74
c_0	km/sec	2.762
s		1.853
q	sec/km	-0.1125
Γ_0		1.625
c_{v_1}	J/g·K	0.828
c_{v_2}	J/g·K	1.282
θ_1	K	257
θ_1	K	1868

[a]For a shock-particle relationship given by $U_s = c_0 + su_p + q{u_p}^2$ and Grüneisen parameter defined by $\rho\Gamma = \rho_0\Gamma_0$.

Temperature discrepancies may be explained without appealing to the numerical examples; however, the calculations for HNS illustrate the underlying concepts. First, it is emphasized that all specific heat models monotonically increase with temperature, rising from a zero value along the cold curve to the asymptotic limit above a certain temperature. Now, it is also shown in this work as well as that of others [109, 120] that specific heat monotonically decreases with volume through the volume scaling relationships. The combination of these two effects on the integrals of specific heat (e.g. Eqs. (6.33) and (6.34)) will change the temperature limits of integration in a predictable way.

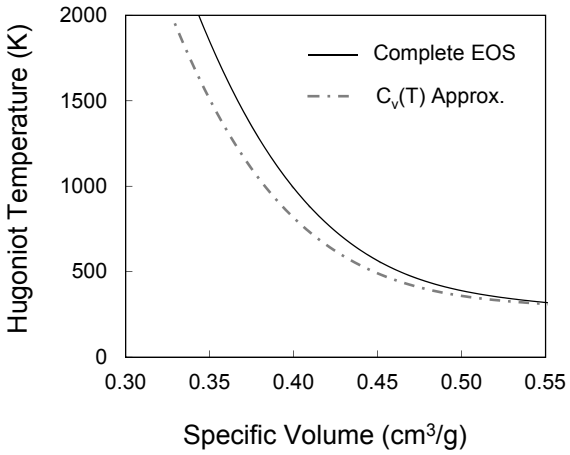

Figure 6.3. Hugoniot temperature calculations using the complete EOS and $c_v\,(T)$ approximation.

When specific heat $c_v\,(T)$ is integrated in volume along the first integration pathway of Fig. 6.2, energy is artificially high as specific heat is not scaled down for the lower volume. If the temperature is calculated corresponding to a fixed energy state, the upper limit of integration must decrease to calculate the same energy. Hence, the $c_v\,(T)$ approximation integrated from the cold curve at the compressed state will always yield the lowest predicted temperatures. This includes all other integrations and the complete EOS. Moreover, this result could be used as a low temperature bound to check current and future EOS results.

In contrast to the $c_v\,(T)$ approximation, the complete EOS (or any integration along the second path of Fig. 6.2) should calculate the highest possible temperature of all the methods discussed. This explanation is similar to the one given for the low temperature limit; namely, the specific heat has been decreased at the higher compression states through volume scaling relations. Lower energies are obtained corresponding to the same fixed temperature, so the temperature limits of integration are increased to calculate the same energy state. Overall, it is important to frame these results in light of Grüneisen's postulate. All volume scaling relations and

the temperature discrepancies are a consequence of the assumption that Grüneisen gamma is a function of volume alone. This assumption may or may not be accurate for higher temperatures corresponding with hot spots. Nevertheless, confidence in temperature predictions is still improved by following Grüneisen's postulate through to its logical conclusion.

6.5 Hydrodynamic Pore Collapse

A physically-based EOS is critical for planar shock calculations as well as simulations of shock interactions with heterogeneities. Heterogeneous impacts will give rise to temperature distributions around the Hugoniot state, and the distributions are a function of the EOS. The distributions also represent a significant extrapolation of limited empirical data. As an example of a heterogeneous impact with hot spot formation, the collapse of a single pore is discussed. Chemical reaction and phase changes are not considered to focus attention on temperature calculations for inert materials. HNS EOS data used for the Hugoniot calculations is again considered in the pore collapse setting. This explosive is a suitable candidate to study hot spot formation via the pore collapse and jetting mechanism; HNS has a relative low yield stress near 140 MPa [156] and is initiated in most engineering applications with strong shocks (near 10 GPa). Thus, strength models may be reasonably ignored, and the effects of the EOS on pore collapse and hot spot temperature distributions carefully investigated.

6.5.1 Model Details

The collapse of a 10 μm pore was simulated using the shock physics hydrocode CTH in 2d cylindrical (quasi-3d) coordinates. This pore size was chosen based on recent work investigating pore collapse in fine-grained HNS [152]. The collapse was simulated using a reverse ballistics calculation; a symmetry interface condition was imposed to represent contact with an infinite impedance flyer plate. Eqs. (6.26)−(6.28)

were evaluated to construct tabular SESAME-type input for CTH. The impact velocity was 2.25 km/sec and the corresponding planar shock state is U_s=6.36 km/sec, P_H=24.9 GPa, and T_H=1410. The same shock state is found using the $c_v\,(T)$ approximation, except that the shock temperature is determined to be T_H=1150 K (260 K lower than the complete EOS).

The computational domain is 16 μm by 32 μm; the initial position of the pore was chosen so that collapse occurs near the center of the domain. A fixed grid of gages 5 μm by 9 μm encloses the location of jet impact and records temperature values. From this data, an approximation of the volume distribution, mean, and standard deviation may be calculated. Mesh resolution was determined based on the convergence of the mean gage temperature and standard deviation at 4.1 ns (corresponding to the jet impact event). An acceptable mesh resolution was determined to be 20 zones/μm; however, a fine resolution of 80 zones/μm was used to allow smaller bin sizes for the subsequent histogram calculations. Refer to Fig. 6.4 for the mesh convergence results, and Fig. 6.5 for the pore collapse sequence as well as the location of an array of gages used to determine mesh convergence.

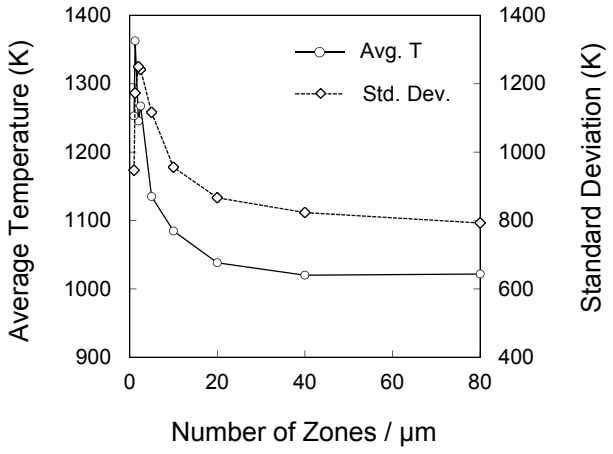

Figure 6.4. Mean temperature and standard deviation of gauges during jet impact at 41 ps.

6.5.2 Hot Spot Temperatures

An image sequence of the temperature distributions during pore collapse with the complete EOS is shown in Fig. 6.5. The left side of each individual frame is mirrored to show the position of temperature gages used to conduct the mesh resolution study in Fig. 6.4. Additionally, a solid gray contour in the mirrored images shows the location where temperature is in excess of 1500 K. This threshold was used to positively identify temperatures above the principal Hugoniot state (T_H=1410) and locate where the hot spot first appears in relation to the bulk heating. Although the size of the pore and impact conditions differ from original work performed by Mader [149], many similarities are observed. Chief among these is that the jetting event is capable of producing temperatures in excess of the bulk heating, and these temperatures occur locally at the site of the jet impact.

The temperature distributions shown in Fig. 6.6 were constructed with a dense gage array (40 gages/μm) and provide a clearer picture of the high temperature tail where hot spot distributions may be found. In rendering the histograms, the low temperature tail was omitted (i.e. those states below the bulk state as indicated by the vertical asymptotes on Fig. 6.6). Histograms for the complete EOS and $c_v\,(T)$ approximation are presented on the same axes and show that the $c_v\,(T)$ approximation predicts lower hot spot temperatures, as indicated by the location of the peaks. At 4.0 ns, a single pronounced high temperature peak is found near T=4420 K for the complete EOS and T=3840 K for the $c_v\,(T)$ approximation; the difference in location of the peaks is nearly 600 K and is greater than the 260 K difference between the Hugoniot temperatures. This difference in temperature is not surprising in light of the volume scaling techniques and discussion in Sec. 6.4.3. What is more interesting is the similarity in the shape of the histograms. It may appear that the $c_v\,(T)$ approximation has merely shifted the distribution to a lower temperature; however, no constant value can be found to align the two separate data sets. This may be a further indication

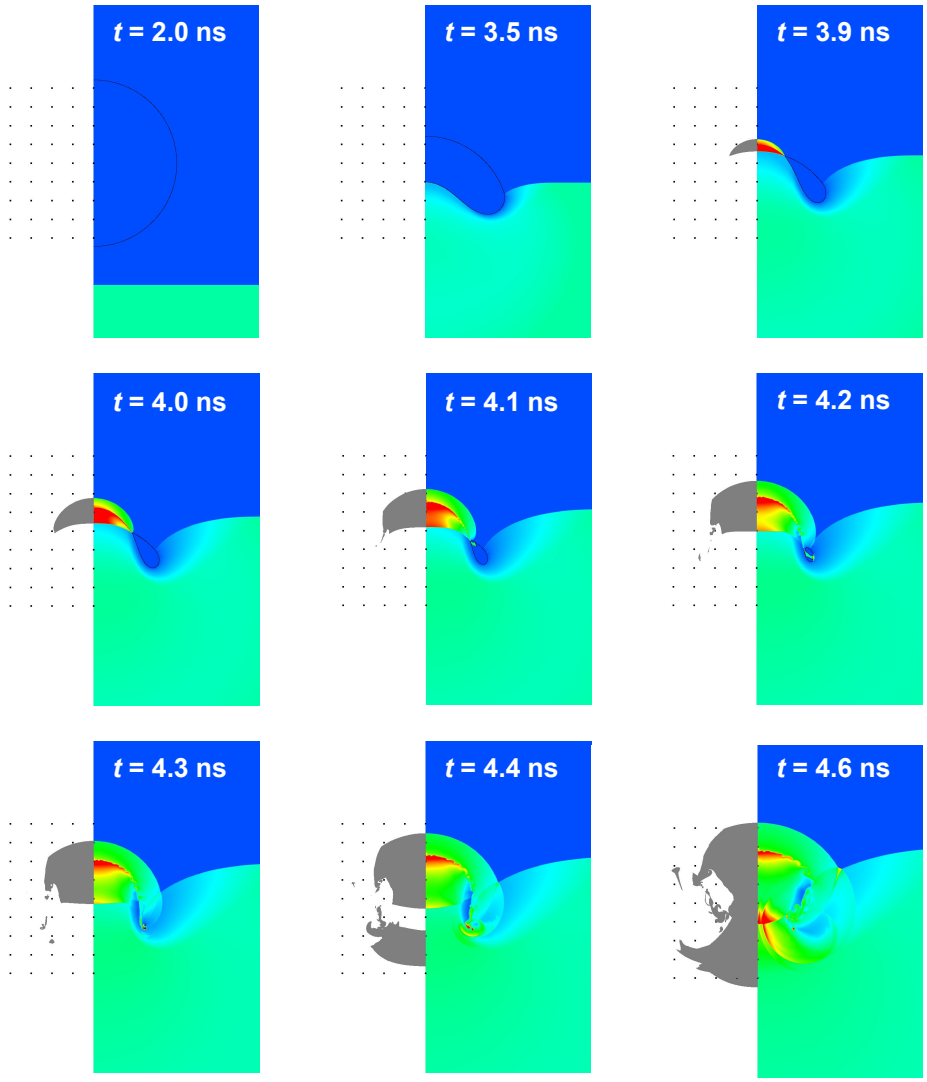

Figure 6.5. Temperature during the collapse of a 10 μm pore in HNS using the complete EOS. Shaded areas indicate temperatures in excess of 1500 K. Dots indicate the locations of temperature gages.

that temperature discrepancies owing to the EOS are increased at elevated levels of compression.

The hot spot temperature distributions in Fig. 6.6 also show that two distinct temperature peaks develop after the collapse. The jetting event causes both a forward

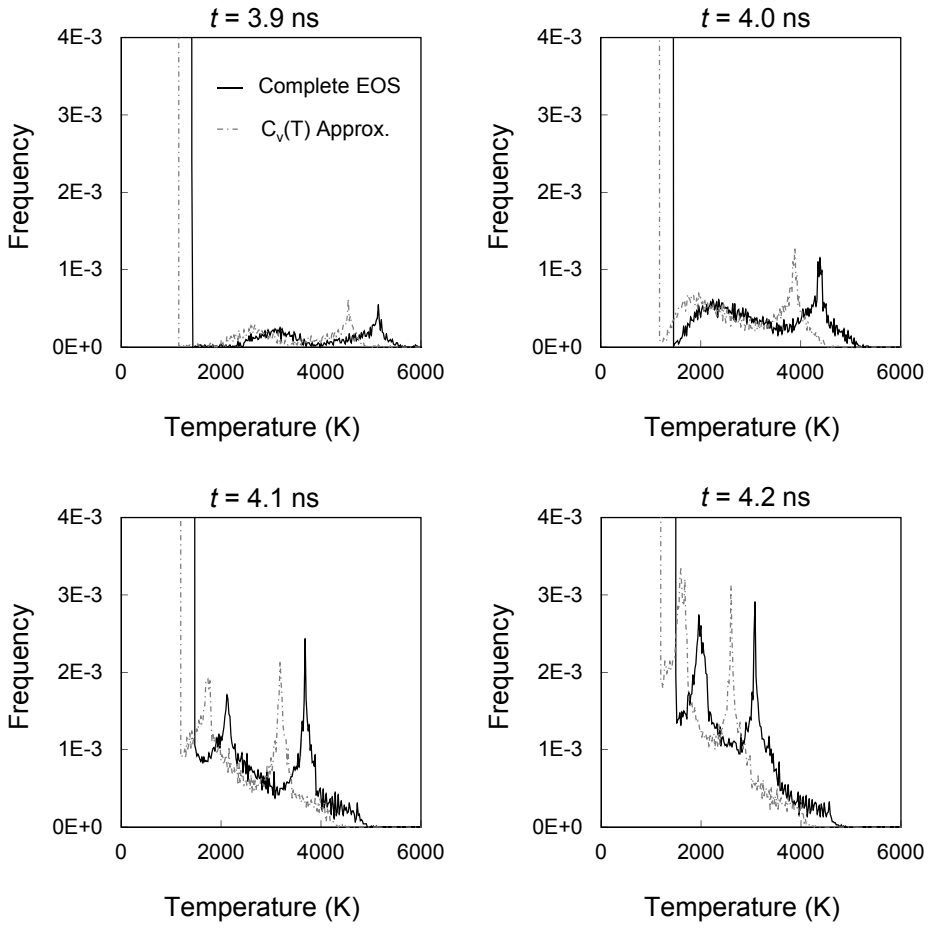

Figure 6.6. Temperature distributions corresponding to the image sequence of Fig. 6.5.

(into the pristine material) as well as rearward running shock as shown in Fig. 6.5. The rearward shock strength and temperature are less than the front, but interactions with density discontinuities manifest themselves in a more complicated downstream shock pattern. Thus, the higher temperature peak corresponds to the forward running shock, and the lower peak with the rearward running shock, respectively. Both peaks contribute to hot spot formation [149], but the hotter peak is likely to be most influential. In this regard, it is important to note that the high temperature peak cools off rapidly from T=5150 K at t=3.9 ns to T=3080 K at t=4.2 ns. The relevance

of these results is simply that the hot spot distribution is highly dynamic, and that the choice of EOS is even more significant than for simple planar shock calculations. Future work should consider the effects of phase change and chemical reaction on the shape of these temperature distributions.

6.6 Summary of Model Refinements

A physically-based Mie-Grüneisen EOS was derived using a multi-term Einstein oscillator model for specific heat. This derivation is unique from other Mie-Grüneisen EOS found in the literature in that it is highly generalized yet completely algebraic in terms of temperature, volume, an integrating factor, and the cold curve energy. Additionally, any empirical relation for the reference pressure and energy may be substituted directly into the equations defining the complete thermal state. This form offers much flexibility when shaping the EOS surface, and it is self-consistent with respect to fundamental thermodynamic relationships (e.g. Maxwell's relations and compatibility equation). Lastly, the derivation was extended to explain why the approximation $c_v(T)$ may yield different EOS surfaces owing to the choice of integration pathway in temperature-volume space.

To apply the new EOS and demonstrate its path-independence, calculations are presented using data for the secondary explosive, hexanitrostilbene (HNS). Specifically, Hugoniot temperatures were calculated using both the complete EOS and $c_v(T)$ approximation. The lowest temperatures were found using the $c_v(T)$ approximation, and the highest temperatures using the complete EOS, as explained by volume scaling relationships. Moreover, the temperature discrepancy was shown to be monotonically increasing at higher levels of compression; for a shock input pressure of 10 GPa this difference is greater than 100 °C. These results were shown to raise awareness of the delicate relationship between temperature calculations and other derivations for a complete EOS under the assumption of Grüneisen's postulate.

Finally, the complete EOS was used in a hydrodynamic pore collapse simulation to determine hot spot temperature distributions. HNS was again selected as its strength may be reasonably ignored, and the effects of the EOS on hot spot temperature distributions carefully investigated. Temperature distributions above the bulk thermal state were located at the site of jet impact in agreement with previous work. Further, these results show that the resulting hot spot temperature distributions from pore collapse are highly dynamic. Thus, the choice of EOS for hot spot calculations is even more significant than for simple planar calculations. Future work will seek to apply the EOS to heterogeneous impact simulations and study the formation of hot spots at the mesoscale. With the improved confidence in temperature predictions, new physical meaning may be associated with thermally sensitive kinetic and strength parameters necessary to predict the shock initiation and detonation of explosives.

7. RESULTS

7.1 Overview

The results of the work include experimental and computational studies performed on the baseline ANFO KP-1 non-ideal explosive. The results section has been organized beginning with the experimental measurements, and working towards the measurements that should be made in order to validate the model predictions and confirm interpretations of the underlying physics. In summary of the results, the MI experiments were used to inform some of the reactive wave behavior relevant to small scale explosive testing. Four different experimental geometries were used to provide a good data set for model calibration as well as validation. These experiments are then simulated in 2d and 3d geometries using the shock physics hydrocode CTH, which provides much more detailed information than what may be obtained from the experimental technique alone. Finally, model validation is concluded with some predictions of additional experiments and changes to the initial density of the ANFO samples. Overall, the high level of integration between experimental and computational results is necessary in order to better understand the baseline non-ideal explosive, and eventually a wider range of HMEs.

7.2 Small Scale Experiments

A peak picking technique was used to analyze all sixteen shots comprising the small scale experiments. This technique was selected in favor of time-frequency methods and quadrature analysis because of the high quality of the MI output signals (see Appendix C). Shock position and velocity results are shown in Fig. 7.1, and are grouped by color according to the charge geometries; refer to Table 3.1 for a description of the THK, PVC, THN, and SM experimental configurations. The MI data is highly

repeatable, as it is nearly impossible to distinguish between the four different tests within each group. This high level of repeatability is most likely due to the tight control of sample density. The standard deviation of the ANFO packing density was found to be 0.003 g/cm^3, or 0.4% of the average initial density. Slight variations in density have been known to affect the MI results in previous work [1, 67], and much care was taken here to obtain identical density ANFO samples.

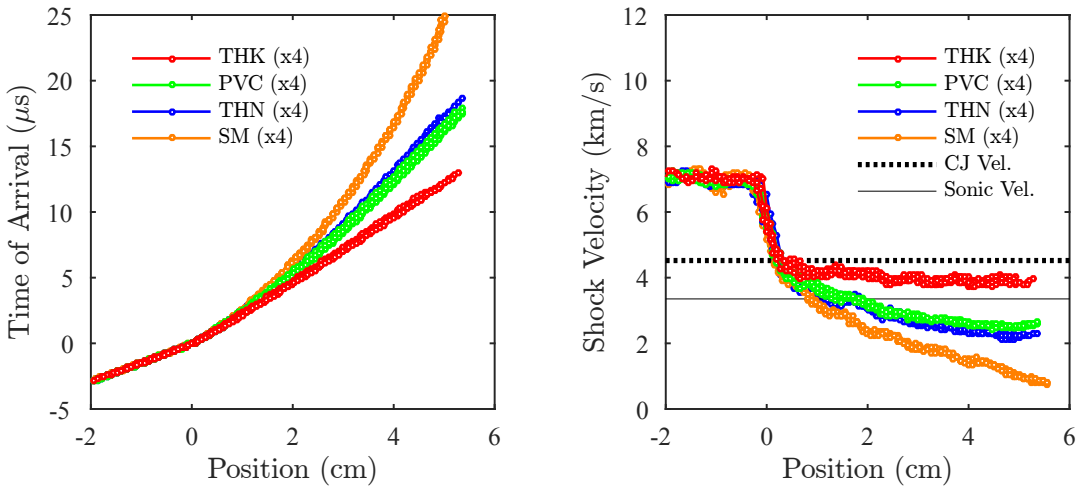

Figure 7.1. Analyzed MI data for all sixteen ANFO KP-1 tests, showing the shock trajectory (left) and shock velocity (right).

All of the velocity results in Fig. 7.1 indicate overdriven detonation failure; however the failure rate is controlled by the level of confinement and sample diameter. The highest velocities correspond to the thick walled stainless steel confiners (THK), and are near 4 km/s. The gradual decrease in shock velocity for the THK case may be observed more clearly via comparison to the CJ detonation velocity, indicated by the dashed horizontal line in Fig. 7.1. As none of the velocities are steady, all cases represent transient reactive wave phenomena. Decreasing the level of confinement increases the failure rate, so that all velocity measurements in a particular group either lie above or below the other experimental data.

Perhaps the most significant observation from the MI data is that all the ANFO velocity curves appear to start at the same initial velocity. Moreover, this velocity is close to the predicted CJ velocity of 4.52 km/s, and might possibly coincide with the infinite diameter velocity as well. Dr. Kirk Yeager was the first to recognize that the initial velocity is similar to measurements from large diameter cylinder tests using ANFO, although this discussion was a private communication. In recognition of his observation, this point is hereafter referred to as the Kirk Yeager (KY) inflexion point. At this time, it is unknown what factors affect the position of the KY inflexion point, for example, if it is the input pressure or initial density. It is theorized here that for high enough input pressures, the overdriven detonation failure curves will begin at the CJ detonation velocity. In this way, the small scale experiments might possibly be used to augment or replace large scale tests, which are more costly and present larger testing hazards.

Another observation of the MI data is the similarity yet subtle difference between the PVC and THN cases. Both of these geometries share the same thin steel confiner; the geometries differ by the presence of an outer PVC sleeve. The corresponding velocity histories are identical over the first 2 cm into the ANFO samples, and then the failure rate is greater for the THN case near the sonic velocity line. If the PVC was a significant effect, it might be expected to deviate from the THN case at the very beginning (e.g. THK and SM show different initial failure rates). Instead, the greatest difference between the PVC and THN velocity histories occurs at the end of the sample length. One explanation is that the reactive wave is transitioning from supersonic to subsonic deflagration. The influence of the PVC confinement may be more important for subsonic deflagration towards the end of these experiments, where it might be expected that the PVC would support the higher pressures and faster reaction rates. This expected behavior is proposed as follows: upstream pressures should increase due to the greater yield strength of the combined PVC-steel tube than the steel tube alone, assuming that the maximum pressure during a deflagration event occurs right before the rupture of the confiner.

7.2.1 Measurement and Random Errors

The results of a detailed error analysis on the MI data are summarized in Table 7.1, while the complete error analysis may be found in Appendix C. For these experiments, the measurement error was determined to be 1-3% for both the booster and ANFO explosives, as shown in Table 7.1. The measurement error was lower for the 11.28 mm diameter charges (∼1.5%) than for the smaller 6.52 mm diameter charges (∼3%), owing to greater uncertainty from the tolerance in the sample tube diameters. For the larger diameter charges, measurement error is limited by the accuracy of the sample permittivity, and not density. Random sample errors were also quantified using the results from a dynamic wavelength calibration, as summarized in Table 7.1. For ANFO, the random sample error is close to 2.6% and 3.2% for the large and small diameters, respectively. One observation is that the measurement and random errors are similar for the smaller diameter ANFO charges, whereas the random sample error is greater than the measurement error for the larger diameter charges.

Table 7.1. Summary of the measurement and random sample errors in density, permittivity, and velocity assuming a 95% confidence interval.

Ex.	**Dia.**	**Measurement Error**			**Random Error**		
	(mm)	$\Delta\rho_0/\rho_0$	$\Delta\epsilon_r/\epsilon_r$	$\Delta v/v$	$\Delta\rho_0/\rho_0$	$\Delta\epsilon_r/\epsilon_r$	$\Delta v/v$
PS 1000	11.28	2.02%	2.52%	1.36%	2.23%	7.93%	4.27%
	6.52	4.80%	4.53%	2.96%	2.23%	7.93%	5.09%
ANFO	11.28	2.02%	2.83%	1.53%	0.84%	4.86%	2.63%
	6.52	4.81%	4.64%	3.05%	0.84%	4.86%	3.19%

Concerning the booster explosive, random sample errors were much higher than measurement errors, with values closer to 4-5%. The increased error in the booster explosive velocity may be attributed to the greater uncertainty in density, as well as variable material properties. The booster is a flexible sheet explosive with elastic

behavior; after pressing, the sheet explosive usually relaxes to a slightly lower density. Moreover, the nominal composition of 63% PETN may not be homogeneously mixed as the explosive is folded and divided into pressing increments. Hence, the pressed booster explosives are less uniform in density and composition than the ANFO samples, and this is reflected in the random sample variation.

Overall, the total error in velocity could be improved with a more exact knowledge of the permittivity of the explosive samples. Original work [1] determined a theoretical limit for the lowest achievable error to be between 1-2%, which is just $\sim$1% below the level of error determined in this work. Hence, only minor improvements to the accuracy of the measurement may be obtained here. A final remark about the error analysis is that additional uncertainties in the time and displacement of the shock wave are implied. Confidence intervals are not shown in Fig. 7.1 for clarity, as they would require error bars in both the x and y axes attached to each discrete velocity point; this would define an envelope around each velocity curve. Since position is the integral of velocity, integration of the error in velocity will produce larger uncertainty in the shock wave position towards the ends of the explosive charge. Some error may also exist in the time resolution of the MI signal peaks; however, in practice this error is negligible [1].

7.3 Model Calibration

Of the four different experimental configurations used in this work, model calibration was performed on the PVC data only. The PVC experiments represent an intermediate level of confinement that can be modeled well in CTH; the remaining MI data is then used for comparison to the model predictions under lighter and heaver confinement. In addition, preliminary studies revealed much difficulty fitting the weaker confinement cases (e.g. THN and SM). This observation suggests that some of the underlying physics in the light confinement experiments are not well captured by the IGRB model, as discussed in greater detail in Sec. 7.4. In contrast, the THK

confinement may be modeled well in CTH, although it is thought to be less sensitive to the IGRB model parameters than the PVC cases. Specifically, the greater change in velocity is assumed to provide for more robust criteria when fitting the model parameters.

Partial correlation coefficients between the four unknown IGRB parameters and the velocity error function (Eq. (5.45)) are shown in Fig. 7.2. These statistics were determined from DAKOTA using a Latin hypercube sampling ($n = 700$) of the parameter space, where the sampling limits are given in Table 7.2. Some of these limits did not significantly interfere with the correlation coefficients (i.e. for a and λ_{ig}). For the other parameters, trial and error was required to determine reasonable sampling limits. The final range of I and G values were determined via an order of magnitude analysis. Ignition occurred for values of I on the order 10^6, although a wide range of values yield reasonable results. Unfortunately, the growth prefactor was observed to have a highly non-linear effect on the velocity profile. Values of G above 10^{-3} caused prompted reaction and steady detonation, whereas values of G below 10^{-4} were not large enough to grow the reaction. The final range of G values represents the narrow band where the best fit to the MI data may be obtained.

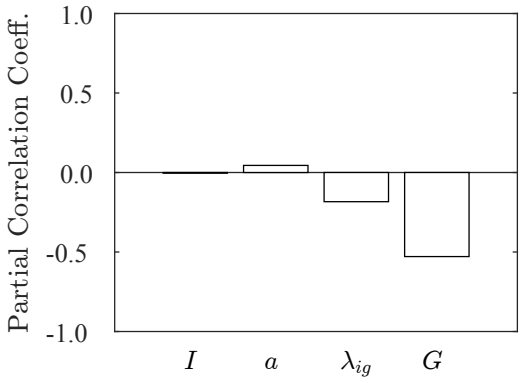

Figure 7.2. Partial correlation coefficients for the unknown IGRB model parameters.

Table 7.2. Parameter bounds for the Latin hypercube sampling and calibrated model fit. All values are in cgs units.

Parameter	**Low**	**High**	**Fit**
I	1e5	1e8	1e6
a	0	0.4	0.2
λ_{ig}	0.01	1	0.5
G	0	3e-4	1.5e-4

Correlation coefficients were also determined between the different inputs and error function as shown in Table 7.3. From these coefficients, no significant cross-correlation was found between the IGRB model parameters. In addition, scatter plots between the velocity error function and parameter values are shown in Fig. 7.3, and confirm the trends observed in the correlation coefficients. Namely, that G is the most sensitive parameter and a is most likely the least sensitive parameter. The accepted calibration point is shown in Fig. 7.3 as a green marker, having the minimum sum of squared percent error near 11%. The fitted parameter values are also given in Table 7.2.

Table 7.3. Simple correlation matrix among all inputs and outputs for the IGRB model.

	$\boldsymbol{I}$	$\boldsymbol{a}$	$\boldsymbol{\lambda_{ig}}$	$\boldsymbol{G}$	**% Error**
$\boldsymbol{I}$	1.00000e-0				
$\boldsymbol{a}$	-1.19361e-2	1.00000e-0			
$\boldsymbol{\lambda_{ig}}$	-2.44263e-2	-3.57644e-3	1.00000e-0		
$\boldsymbol{G}$	-2.29256e-3	4.36011e-4	2.07354e-2	1.00000e-0	
% Error	1.66553e-3	3.76839e-2	-1.67153e-1	-5.24267e-1	1.00000e-0

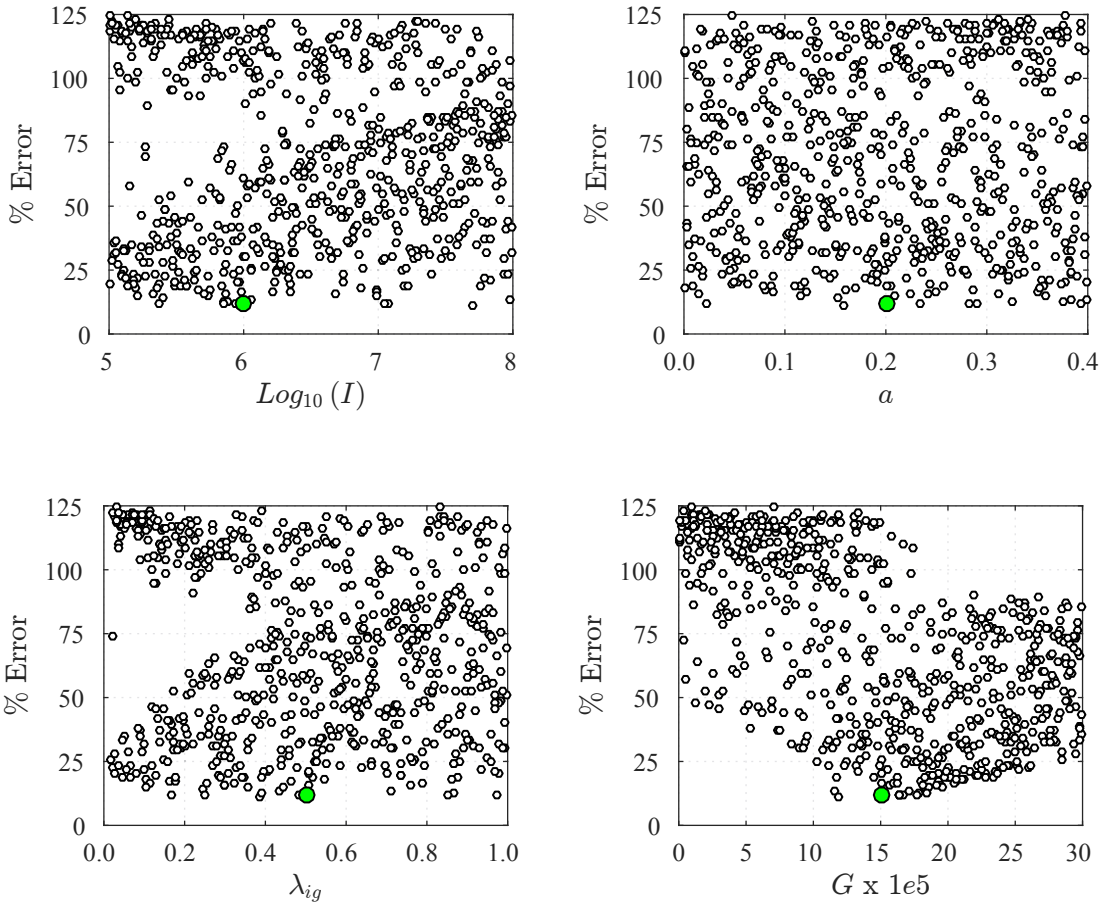

Figure 7.3. Scatter plots between the simulation error function and the unknown IGRB model constants. The accepted calibration point is indicated with a green marker.

The decision to fit the MI data using a single objective function is a compromise between automation and intuition. Eq. (5.45) was intended to equally weight the velocity fit over the entire sample length. In reality, some solutions minimize the objective function in physically unrealistic ways, for example, pulsating waves and exact velocities that go unstable late in time. These unphysical results have been largely removed with the current choice of parameter limits; however, the LHS study did uncover two solutions which compensate a smaller growth term with a higher ignition limit. The two less-physical solutions are visible in Fig. 7.3, bottom right,

between the G x 1e5 values of 10 and 15. These two cases were not considered for the calibration point because of the intuition gained in developing the IGRB model.

7.4 2D and 3D Simulations

Using the fitted IGRB model constants from Sec. 7.3, all four experimental configurations were simulated in CTH with 2d as well as 3d geometries. A comparison between the 2d simulation results and the averaged MI data is shown in Fig. 7.4, which also highlights the calibrated fit to the PVC velocity data. Specifically for the calibration fit, the agreement between simulation and MI velocity data is very good, with only minor fluctuations in the velocity, possibly due to the numerical derivative. Moreover, the prediction of the THK velocity is in agreement with the MI data, thus providing some initial validation of the model.

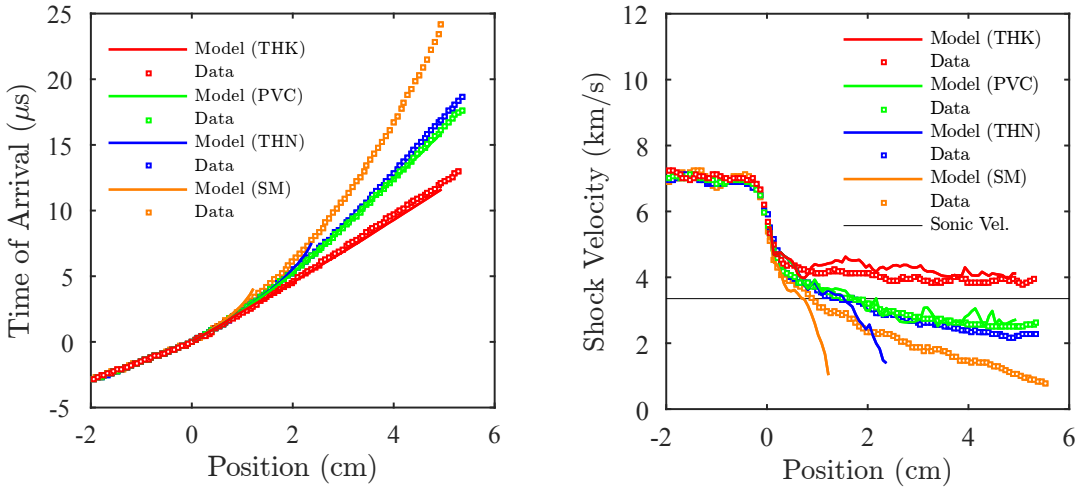

Figure 7.4. Comparison between the averaged MI data and 2d CTH simulations using the calibrated IGRB model.

Unlike the PVC and THK cases, simulations of the THN and SM experiments fail abruptly at different downstream locations near the sonic velocity line in Fig. 7.4. Before the failure, each velocity profile tracks reasonable well to the MI data through

the first 1.5 cm or 1 cm of the THN and SM cases, respectively. This may indicate that the initial physics are captured by the IGRB model; however, if the reactive waves are transitioning from supersonic to subsonic deflagration, thermal effects and some compaction behavior would not be resolved. Interestingly, the simulations also seem to fail whenever thin confinement is used, which might suggest instability coupled to the simulation geometry.

Whatever the exact cause, the failure of the THN and SM cases is more significant than a poor choice of IGRB parameters. Preliminary studies were unsuccessful in fitting these cases over an even larger parameter space. The partial fit to the THN and SM data in Fig. 7.4 is probably more accurate than many of the total fits obtained in the preliminary calibration studies using the weaker confinement data. The best total fits obtained for the THN and SM cases were un-physical, as most employed pulsating or 'chugging' waves to match the MI data. No IGRB model constants were found to achieve a smooth decrease in velocity that resembles the light confinement MI data.

In order to determine the influence of simulation geometry, 3d calculations were run for each of the 2d cases. The direct comparison of 2d and 3d velocity profiles for ANFO is shown in Fig. 7.5 and reveals no measureable difference in the output from the shock tracking algorithm. The array of pressure gages was located across the x-axis in 2d, and along the line $y = x$ in 3d, yet the average time of arrival was found to be identical between the 2d and 3d simulations. This result should not be interpreted to mean that the different simulation geometries are of equal value, as many numerical results may be compared beyond the shock trajectory.

Contour maps of the pressure and extent of reaction at $t = 15$ μs are shown in Figs. 7.6 and 7.7 for the 2d and 3d geometries, respectively. At $t = 15$ μs, both the THN and SM simulations have failed, and no longer follow the MI data. Two major observations from these contour maps are the relative similarity between the 2d and 3d results, and the pressure waves inside the confiner walls, which propagated farther downstream than the reaction front. These pressure waves are interesting in light

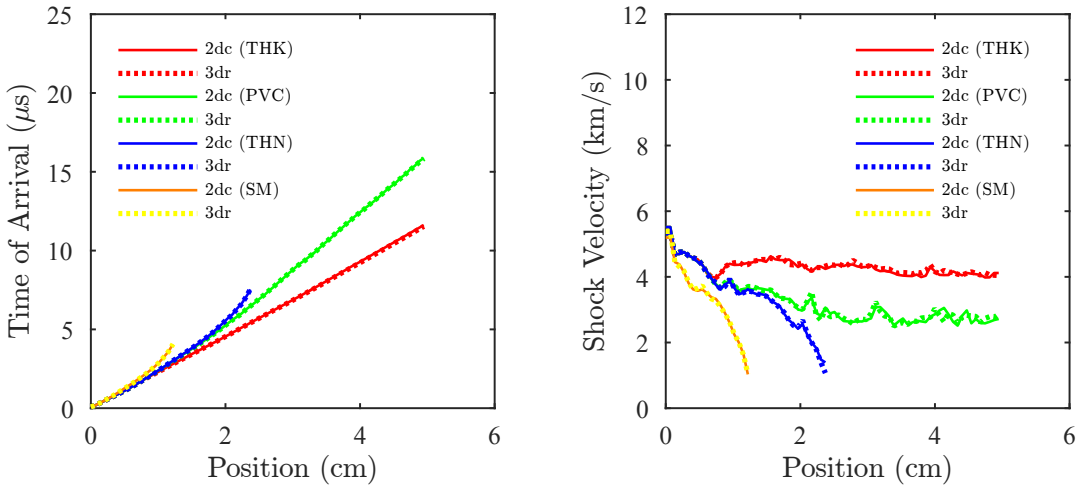

Figure 7.5. Comparison between the 2d cylindrical and 3d rectangular shock trajectories and velocities for the ANFO samples (no booster).

of recent work, which suggests that high sound speed confinement may pre-compress the ANFO near the wall and transport energy ahead of the detonation wave [86]. The simulation results shown here do not seem to indicate a pressure rise in the unreacted ANFO; however, the contact angle of the leading wave front varies slightly with the different levels of confinement. Jackson *et al.* [86] also find that the shock front curvature is reduced for stiffer, thicker confinements as observed qualitatively in Figs. 7.6 and 7.7.

Additional simulations are needed in order to confirm the effects that the confinement has on the propagation of the wave front. It is likely that both the sound speed and thickness of the confiner are important variables for supersonic and subsonic wave propagation. For the THK and PVC cases, regions of high pressure near the shock front in the walls contribute to lower radial losses i.e. more energy is directed downstream and into the wave front. The shape of the pressure regions in the walls is clearly influenced by the sound speed of the confining material, which is ∼5 km/s for steel and ∼2 km/s for PVC. Because the shock velocities are between 2-5 km/s, the

effect of the outer confiner material is either to attenuate the pressure waves (PVC) or propagate them farther downstream (THK), giving rise to the triangular and rounded pressure lobes in Figs. 7.6 and 7.7.

The pressure variations inside the confiner walls might also be coupled to pressure variations inside the ANFO samples. The pressure variations that occur inside the ANFO samples are unsteady, and usually appear close to the center axis (see for example the dark regions of low pressure in the THN case, just behind the wave front). Pressure variations inside the ANFO samples are mitigated with increasing levels of confinement, and disappear altogether for the more planar waves.

The CTH simulations provide a greater wealth of information than what is obtained from the MI experiments alone. For example, pressure measurements may be extracted from the simulations, and used to inform some of the experimentally observed behaviors. Material (i.e. Lagrangian) pressure gage histories are shown in Fig. 7.8 for all configurations and simulation geometries. Four gage locations, spaced 1 cm apart and at a radial distance 80% of the sample diameter, are presented to show the gradual decay in the leading shock wave pressure. Not only does the leading shock pressure decrease with distance into the ANFO samples, it also decreases with weaker confinement. The PVC and THN cases which share the same initial velocity are now observed to correspond more closely to different types of pressure waves (e.g. step versus triangular). Hence, it is clear that the PVC simulations have greater pressure support than for the THN case.

Pressure gage histories also show that the time of arrival is identical between the 2d and 3d simulations; however, the late time behavior is slightly different. Some of the late time response near $t = 20$ μs in the THK and PVC cases occurs when the reactive wave reaches the end of the computational domain, and this data is not meaningful. Additionally, the THN and SM cases indicate that the maximum pressure does not always coincide with the leading shock wave. When these simulations are allowed to continue past failure, the reaction rate is able to increase and achieve reaction once

again within the ANFO sample; the arrival of a second reactive wave corresponds to the maximum pressure in the bottom row of Fig. 7.8.

7.5 Model Predictions

Additional calculations were performed in order to provide further model validation and to direct future work. These calculations explore aspects of the IGRB model, such as shock sensitivity, changes to initial density via the p-α porosity model, and infinite diameter detonation velocity. Because no experimental data is available under these different conditions, the calculations are blind predictions which could either be used to support or rejected the model in future work. Of note, whenever the initial density is changed, the detonation product EOS must be recalculated using the CHEETAH thermochemical equilibrium code. It is assumed here that the calibrated reaction rate constants do not also change with the initial density, however this may be a poor assumption limiting the predictive capabilities of the variable density model.

7.5.1 Shock Sensitivity

Shock sensitivity is usually determined by the run distance or time to detonation for a given input pressure. This information may be obtained from a large scale wedge test, and the results are summarized in a Pop-plot [94]. For this work, the BCAT code [157] was used to generate and post process multiple 1d CTH simulations using the CAL RB and POP RB commands. Because of the 1d implementation, numerical heterogeneities were not considered as was done for the 2d and 3d geometries. Instead, the model parameters correspond to a single initial density. Some iteration was required to use the BCAT code, because the equation of the Pop-plot is required in order to determine an appropriate mesh size and resolution. Beginning with an initial fit corresponding to the explosive TATB, manual convergence was achieved to the numerical values given in Table 7.4. The shock initiation results are shown in

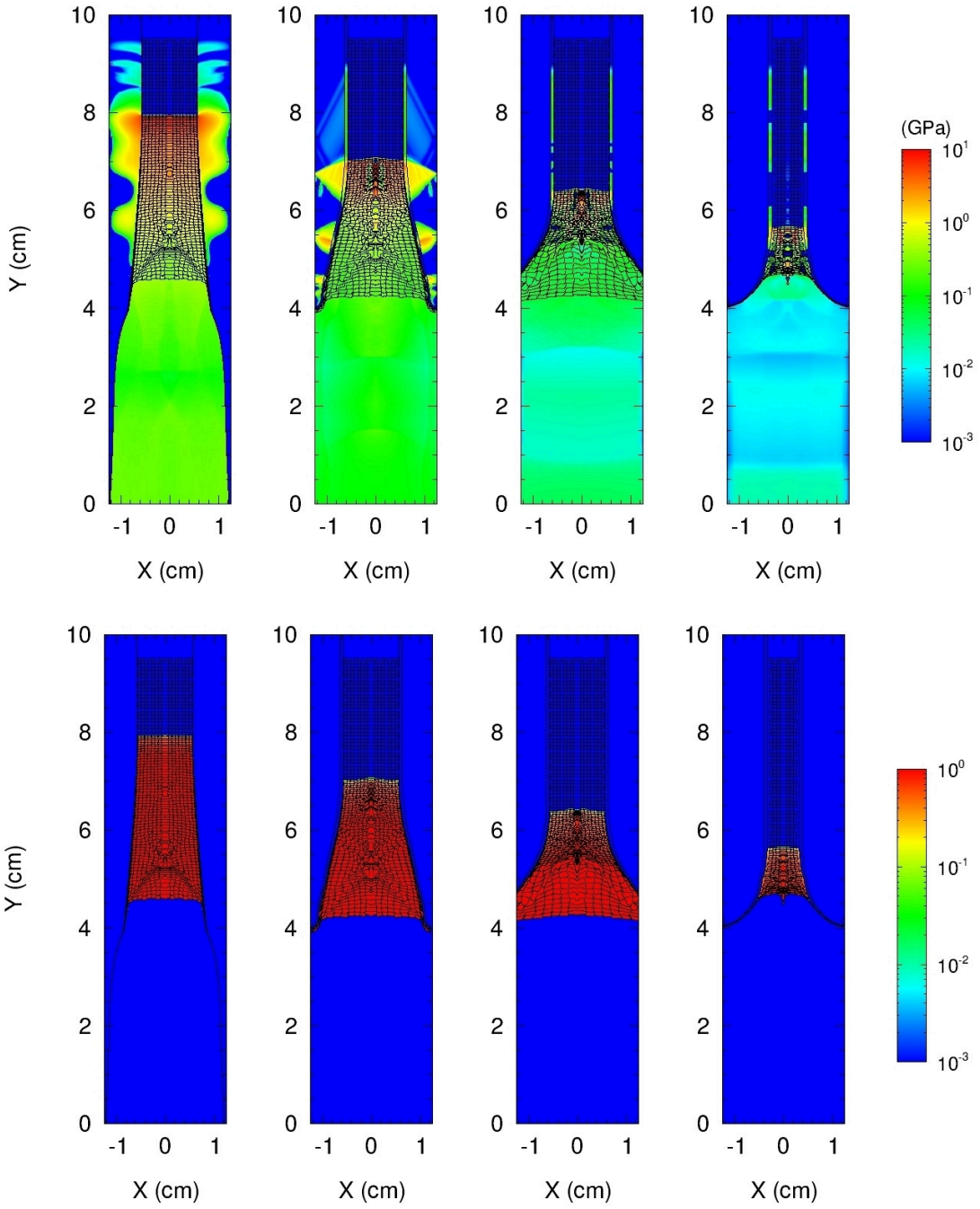

Figure 7.6. Contour maps for the pressure (top) and extent of reaction (bottom) at $t = 15$ μs in the different 2d simulations. Geometries from left to right are: THK, PVC. THN, and SM.

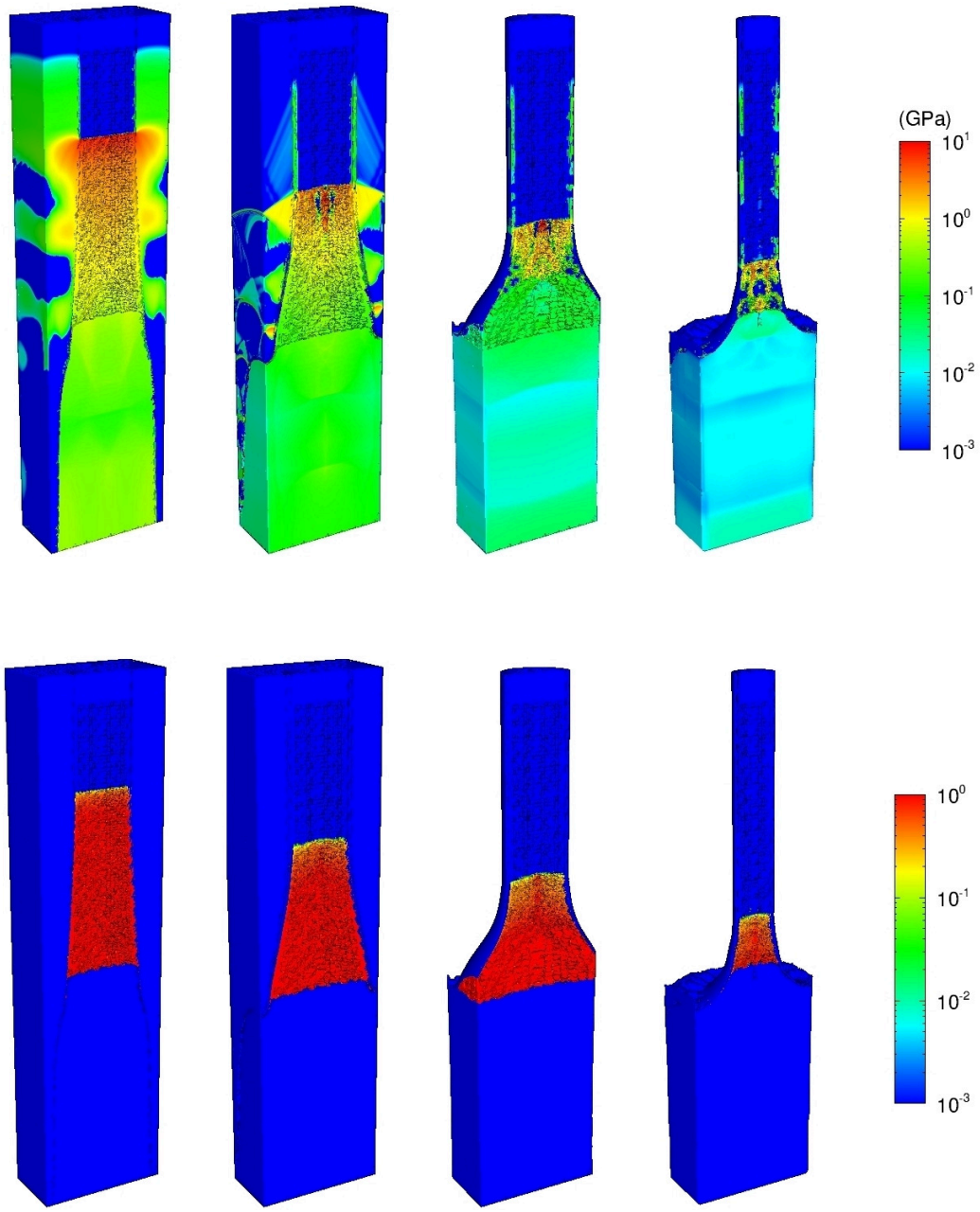

Figure 7.7. Contour maps for the pressure (top) and extent of reaction (bottom) at $t = 15$ μs in the different 3d simulations. Geometries from left to right are: THK, PVC. THN, and SM.

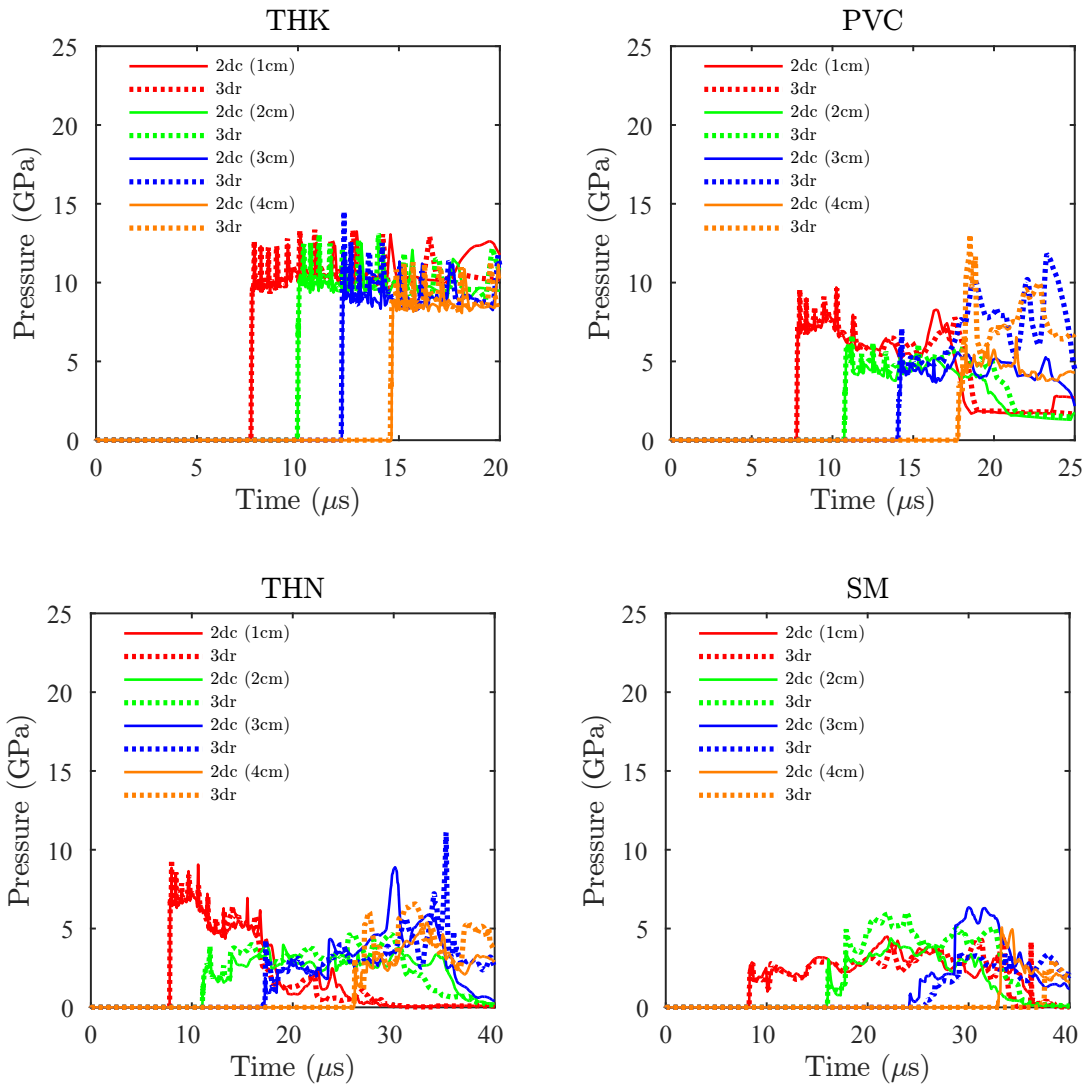

Figure 7.8. Material pressure gage histories for the different MI experiment configurations. Data corresponds to measurements taken at a radial distance 80% of the sample I.D.

the Pop-plots of Fig. 7.9 for the initial ANFO densities of 50, 60, 70, and 80% TMD. The range of input pressures considered was adjusted for each new density in order to obtain a similar range of run times and distances to detonation. Outside of this pressure range, the Pop-plots were not linear in a logarithmic space and the BCAT code experienced resolution and zoning difficulties.

Table 7.4. Final input parameters† for the BCAT code corresponding to the CAL RB command.

%TMD	a_x	b_x	a_t	b_t	p_{min}	p_{max}
50	0.9	0.6	0.6	0.5	3	9
60	1.34	0.6	0.94	0.5	6	17
70	1.6	0.6	1.17	0.5	9	25
80	1.8	0.6	1.33	0.5	13	36

†Where $log_{10}(p) = a_x - b_x log_{10}(x_d) = a_t - b_t log_{10}(t_d)$ having the units of pressure in GPa, run distance in mm, and time to detonation in μs.

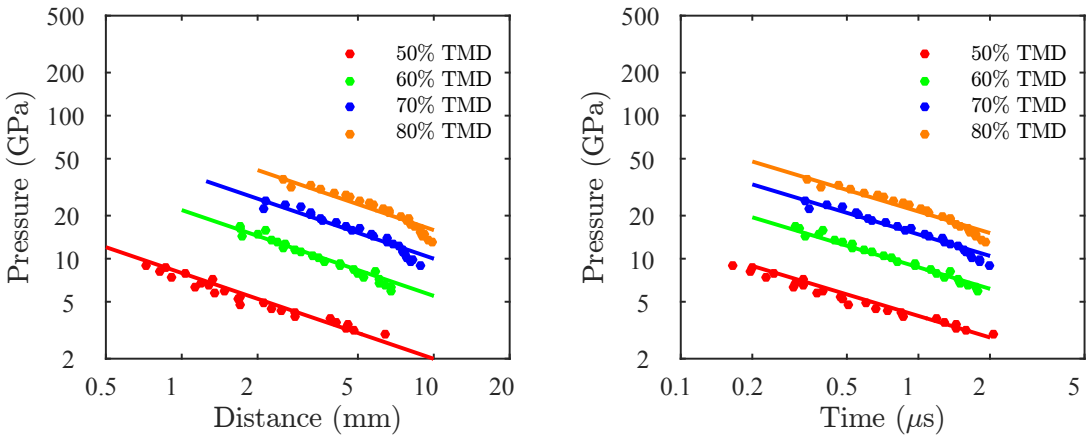

Figure 7.9. Pop-plots from BCAT for the calibrated IGRB model. Equations for the lines may be found in Table 7.4.

One trend in the Pop-plots of Fig. 7.9 is that increasing pressure will decrease the run distance and time to detonation. Less sensitive explosives are characterized by longer run distances and times at the same initial pressure, and are affected greatly by changes to the initial density. Interestingly, the higher density calculations in Fig. 7.9 are less sensitive than the 50% TMD calculation, which is at least qualitatively correct. ANFO explosives require high levels of porosity in order to promote hot

spot formation, and achieve detonation. Previous studies also found that higher density ANFO samples were less likely to initiate, as related to the dead-pressing phenomenon [96]. The ranking of sensitivity between the 60, 70, and 80% TMD calculations is as expected, and could indicate that some of the underlying physics of varying the initial density have been captured by the IGRB and p-α porosity models. Ultimately, large scale wedge test data is needed to validate these Pop-plots predictions.

7.5.2 Density Modifications

In order to investigate the effects of initial density on the KY inflexion point and failure rate in the MI experiments, the PVC and THK cases were rerun using the same initial densities of 50, 60, 70, and 80% TMD considered in Sec. 7.5.1. Numerical heterogeneities in the initial density were implemented as was done previously in the 2d simulations. These density fluctuations require additional CHEETAH calculations of the JWL EOS for each density $\pm 1\%$. The THN and SM cases were not considered, as the calibrated IGRB model does not fit a majority of that experimental data. The 2d simulation results are shown in Fig. 7.10 along with the averaged MI data for 50% TMD as a reference.

In describing the overall behavior of the simulation results, changes to the initial density had an opposite effect between the PVC and THK cases. For the weaker confinement PVC case, increasing the density resulted in a higher rate of failure with lower shock velocities. In addition, abrupt failure occurred so that none of the higher density simulations were able to propagate a reactive wave to the end of the sample (much like the calibrated THN case). In contrast, increasing density resulted in higher velocities in the THK simulations by the end of the explosive charge. Generally speaking, changes in density affect both the shock sensitivity and detonation velocity, and these are competing effects. Lower densities increase the shock sensitivity, and it is likely that the PVC case is on the verge of ignition; in this scenario higher

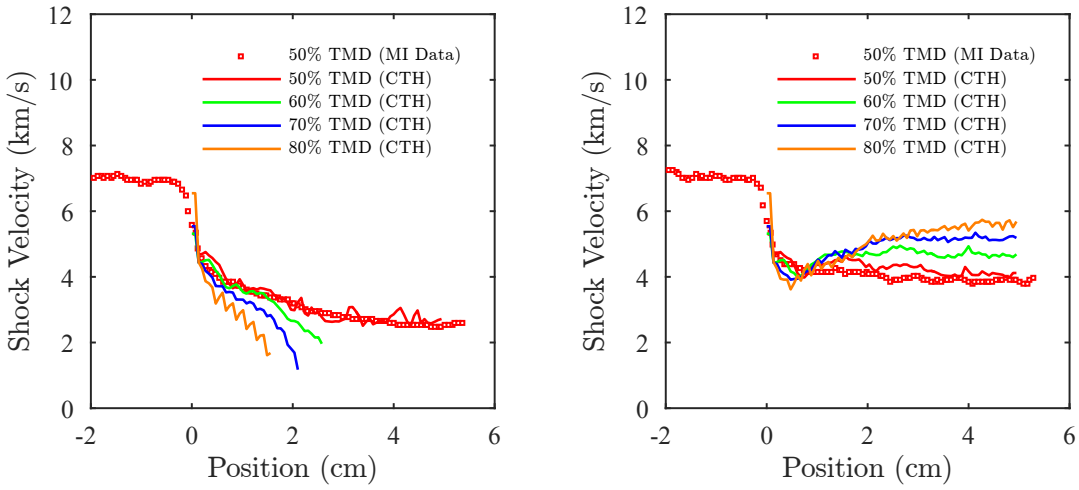

Figure 7.10. CTH predictions for varying the initial density in the PVC experiments (left) and THK experiments (right) without modification to the IGRB model constants.

densities would extinguish the ignition term faster. Higher densities also increase the theoretical detonation velocity via greater energy density, provided that a steady detonation wave may be achieved. The THK simulations are well supported and probably more similar to a steady detonation wave; therefore, it is not surprising to observe the higher velocities with increasing density.

In contrast to the overall velocity profiles, changing the initial density had no influence on the location of the KY inflexion point. This result was not expected, as it is theorized in this work that the KY point coincides with the infinite diameter velocity. As the IGRB model predicts some of the anticipated behavior, it is all the more significant that the simulation results show the KY point as being stationary. Three different possibilities exist to explain this result, as follows: (1) the IGRB model constants should be recalibrated for each density, and the KY point depends on reaction kinetics, (2) some physics are not well captured by the model, or (3) the KY point is, in fact, stationary across a wide range of initial densities. Future

work should be able to determine which of the three possibilities is correct with few additional experiments.

Table 7.5. Modifications to G in the calibrated IGRB model to achieve steady shock velocities.

%TMD	**50**	**60**	**70**	**80**
Gx1e4	1.5	4	8	15

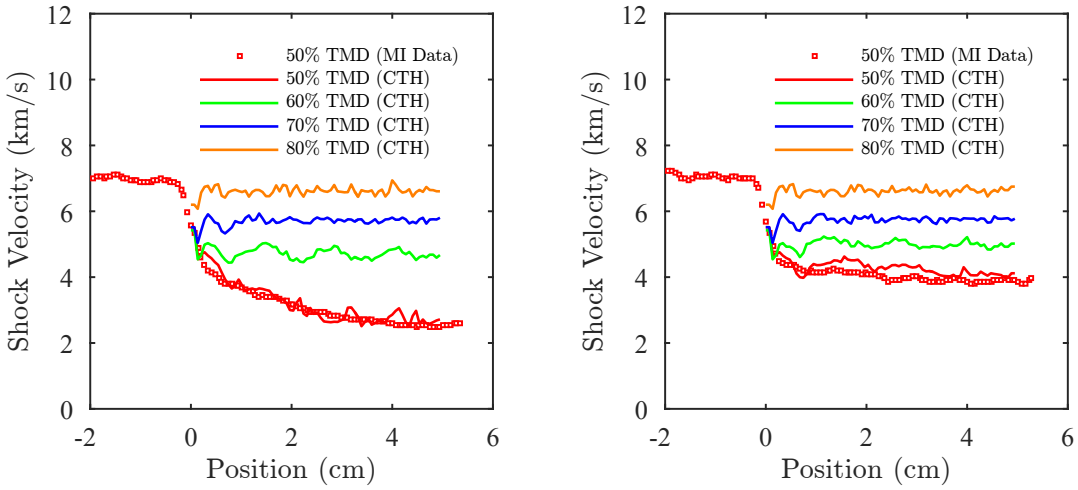

Figure 7.11. CTH predictions for varying the initial density in the PVC experiments (left) and THK experiments (right) with modification to the IGRB model constants as summarized in Table 7.5.

A brief numerical investigation was conducted to determine if the KY inflexion point may be changed with the CTH simulations. The G parameter from the calibrated IGRB model was increased until all the THK simulation results displayed steady shock velocities, as summarized in Table 7.5. The results of the modified IGRB model are shown in Fig. 7.11 for the same PVC and THK cases. As expected, the KY point increased; however, two unanticipated outcomes were the similarity

between the PVC and THK cases, and the overall higher shock velocities at the end of the charge compared to the original predictions in Fig. 7.10.

The similarity of the PVC and THK cases in Fig. 7.11 suggests that the IGRB model should be re-calibrated for each new density. Increasing values of G were able to achieve some of the anticipated behavior in the THK case; however the anticipated behavior in the PVC configuration is captured better with the calibrated model in Fig. 7.10. Physical intuition suggests that the PVC cases should exhibit lower shock velocities with a higher failure rate than the THK case. This is further evidence that all of the IGRB model constants (i.e. I, a, λ_{ig}, and G) should be re-calibrated for each new density.

7.5.3 Large Diameter Charge

The final prediction discussed in this work is a simulation of a large, unconfined 50 cm diameter ANFO charge using the calibrated IGRB model. A 2d simulation was implemented with a computational domain of 30 x 60 cm^2. The same numerical heterogeneities were included in the simulation, as well as the same booster explosive modeled with a preprogrammed burn. Material, pressure, and reaction progress contour maps are shown in Fig. 7.12 for the simulation at time $t = 80$ μs. These images show only a slight shock front curvature near outer radius of the charge, and a thin reaction zone slightly less than 1 cm in length. From an initial inspection of Fig. 7.12, one might conclude that the shock front is too planar, and the reaction zone too thin to match actual ANFO data. Unfortunately, a true comparison is lacking from the missing experimental measurements, and future work might instead investigate the results using detonation shock dynamics (DSD) [158]. A well-calibrated κ-n curve from the literature might also be used to inform whether or not the simulated shock front curvature is reasonable.

Regardless of appearance, the large diameter simulation was primarily run to estimate an infinite diameter detonation velocity. A shock trajectory analysis determined

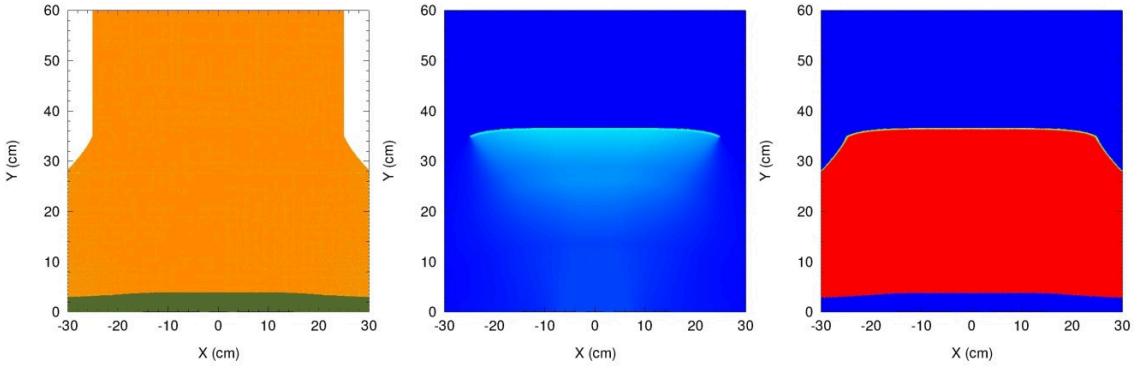

Figure 7.12. Select CTH images at $t = 80$ μs for the large diameter simulation. Contour maps from left to right: material, pressure, and extent of reaction.

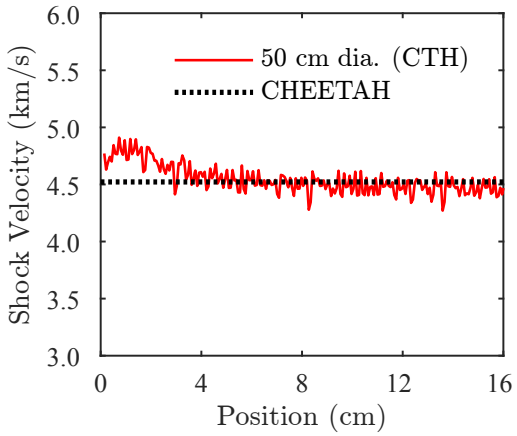

Figure 7.13. Predicted detonation velocity for the large diameter ANFO KP-1 charge and comparison to CHEETAH calculations.

that the wave velocity is steady, possibly as early as 4 cm into the explosive charge, and the full computational domain of 60 cm was not necessary. The spatially-resolved velocity curve is shown in Fig. 7.13 up to 16 cm, in order to illustrate the slight detonation transient near the beginning of initiation. As expected, the wave velocity asymptotes to the CJ value as predicted by CHEETAH; for the velocity scale used

in Fig. 7.13, fluctuations visible in the velocity correspond to the numerical heterogeneities and the numerical derivative. Because the CJ detonation velocity is used to compute the JWL EOS, the asymptotic limit of the CJ value is not surprising. The velocity result in Fig. 7.13 is also slightly faster than the THK simulations, and all of the experimental MI data.

In order to provide some perspective on the velocity results, a reminder is made that the large diameter simulation is based on a reactive burn model calibrated from small scale experimental data. The diameter of the charge is over 40 times larger, and the mass of ANFO over 20,000 times greater, than what was used in the calibration experiments. If any useful prediction may be found from the large diameter simulation results, than the applicability of the small scale to inform large scale detonation phenomena will surely have been demonstrated.

8. SUMMARY AND CONCLUSIONS

A small scale experiment for non-ideal and homemade explosives (HMEs) was investigated, analyzed, and subsequently modeled in an attempt to provide more predictive capabilities and threat assessment of improvised explosive devices (IEDs). The experiment utilizes a 35 GHz microwave interferometer (MI), and was demonstrated in previous work as capable of gathering detailed experimental data on different HME formulations; however, it had not been determined if the small scale data was relevant to large scale explosive performance or model calibration and validation. In this work, a baseline non-ideal explosive was evaluated using four different experimental configurations using a minimum (1-5 g) of material. The effects of the confiner material as either low sound speed PVC ($\sim$2 km/s) or high sound speed 304 stainless steel ($\sim$5 km/s), as well as thickness and sample diameter, were used to modify the behavior of overdriven failing detonation waves. It was found that this type of data is useful for informing large scale explosive performance as well as model calibration and validation.

These experiments were conducted on a baseline ammonium nitrate plus fuel oil (ANFO) explosive with glass micro-balloons, and were shown to be highly repeatable with a tight control of the sample bulk density (less than 1% variation). The error in the velocity measurements was found to depend more on random sample variation than the measurement error, which could be reduced with greater accuracy in the material dielectric constants. Moreover, the time-resolved shock velocity histories indicate the presence of a common inflexion point for all levels of confinement; this point likely corresponds to the infinite diameter velocity, and was named in honor of the observation by Dr. Kirk Yeager as the KY inflexion point. It is unknown at this time how the KY inflexion point is affected by the input pressure or sample

density; several experiments have been proposed for future work to determine the exact behavior.

Of the four different confinement geometries used (THK, PVC, THN, and SM), only the PVC and THK cases seem amenable to modeling with an ignition and growth reactive burn (IGRB) model. It is likely that the experiments are transitioning from supersonic to subsonic deflagration waves, which depend on thermal effects and powder compaction in addition to shock wave propagation. Some evidence for this observation may be found in the PVC and THN cases, which exhibit identical behavior until the velocity decreases close to the sonic value; at which point the greater yield strength of the PVC confiner may result in a greater upstream pressure that would transport energy downstream into the subsonic reactive wave. Another indication of the physics is that the IGRB model does not resolve thermal effects and powder compaction, and it could not be successfully fitted to the entire THN and SM data. A calibrated IGRB model fitted to the PVC data was shown to be capable of matching initial segments of the THN and SM data.

The IGRB explosive model was implemented in the shock physics hydrocode CTH using 2d as well as 3d geometries, and calibrated using the PVC data. The PVC case was chosen in order to subsequently validate the model under both weaker and stronger confinement scenarios. Numerical heterogeneities were included to improve the model robustness, and to help the IGRB parameters converge towards a more stable solution. In summary of the calibration process, no significant cross-correlation was observed, and the ignition prefactor, G, was determined to be the most statistically relevant parameter in the fitting process; the ignition threshold limit, λ_{ig}, was the second most significant parameter. No measureable differences were observed in the shock velocity results between 2d and 3d simulations; however, some of the late time downstream behavior was different including the pressure histories. Consequently, 2d simulations were used for a majority of the work due to the significant reduction in the computational requirements.

Once calibrated, the IGRB model was validated against the THK case as well as portions of the THN and SM data. Without additional experimental measurements, it is impossible to continue the model validation. Instead, several predictions were made for the shock sensitivity, changes to the initial density, and large diameter detonation velocity. The results of some of these predictions appear to be correct qualitatively; for example, shock sensitivity is reduced for increasing the sample initial density. This is related to the dead pressing phenomenon in ANFO and also hot spot theories of initiation, which state that the collapse of small voids is necessary for the initiation of the explosive to occur. The results of the variable density model also indicate that the IGRB parameters should be re-calibrated for each new density under consideration. Although most of the results are qualitatively correct, some of the predictions - which include the KY inflexion point being stationary with increasing density - are not intuitively correct, and may be reversed with different IGRB parameter values.

Overall, the results of the work emphasize the importance of the small scale MI experiments for collecting high-fidelity data on a wide range of new HME formulations. Using sufficient levels of confinement, only a few grams of explosive are needed to determine large scale initiation and detonation parameters, as well as calibrate a simple IGRB model. These results are significant, given that most of the established explosives tests including rate sticks and wedge tests require several kg of material, and are not feasible to perform on every new HME formulation due to time and cost. Future applications of the work may include higher fidelity simulations of IEDs; for example, the calibrated IGRB model might possibly be used to simulate the effect of an initiator on a HME. Full predictive capabilities will depend on the maturation of the explosive models, which currently do not account for the probabilistic nature relevant to initiation. When the more advanced models are available, this type of small scale transient reactive wave data should provide an excellent data set for additional model validations.

LIST OF REFERENCES

LIST OF REFERENCES

[1] G. F. Cawsey, J. L. Farrands, and S. Thomas. Observations of detonation in solid explosives by microwave interferometry. *P. Roy. Soc. A-Math Phys.*, 248(1255):499–521, 1958.

[2] J. S. Hey, J. T. Pinson, and P. G. Smith. A radio method of determining the velocity of a shock wave. *Nature*, 179:1184–1185, 1957.

[3] R. Buser and W. Buser. Determination of plasma properties by free-space microwave techniques. *J. Appl. Phys.*, 33(7):2275–2282, 1962.

[4] A. D. Krall, B. C. Glancy, and H. W. Sandusky. Microwave interferometry of shock waves. I. Unreacting porous media. *J. Appl. Phys.*, 74(10):6322–6327, 1993.

[5] K. D. Froome. Determination of the velocity of short electromagnetic waves by interferometry. *P. Roy. Soc. A-Math Phys.*, 213(1112):123–141, 1952.

[6] B. C. Glancy, H. W. Sandusky, and A. D. Krall. Microwave interferometry of shock waves. II. Reacting porous media. *J. Appl. Phys.*, 74(10):6328–6334, 1993.

[7] J. L. Farrands and G. F. Cawsey. Microwave observation of detonation. *Nature*, 177:34–35, 1955.

[8] G. G. Luther and B. J. Warthen. Microwave interferometry to elucidate shock properties. In *American Physical Society Topical Conference on Shock Compression of Condensed Matter*, pages 1755–1757. AIP Publishing, Colorado Springs, CO, June 28–July 2 1994.

[9] P. J. Rae, B. B. Glover, J. A. Gunderson, and W. L. Perry. Free-field microwave interferometry for detonation front tracking and run-to-detonation measurements. In *17th American Physical Society Topical Conference on Shock Compression of Condensed Matter*, pages 434–437. AIP Publishing, Chicago, IL, June 26–July 1 2011.

[10] E. G. Johnson. A microwave technique for studying detonation phenomena. In *Proc. 4th Intern. Symp. on Detonation*, pages 584–594, White Oak, MD, October 1965.

[11] P. L. Stanton, E. L. Venturini, and R. W. Dietzel. Microwave interferometer techniques for detonation study. In *Proc. 8th Intern. Symp. on Detonation*, pages 485–498, Albuquerque, NM, July 1985.

[12] B. A. Aničin, B. Jojić, D. Blagojević, M. Adžić, and V. Milosavljević. Flame plasma and the microwave determination of solid propellant regression rates. *Combust. Flame*, 64(3):309–319, 1986.

[13] V. E. Zarko, D. V. Vdovin, and V. V. Perov. Methodical problems of solid-propellant burning-rate measurements using microwaves. *Combust. Explos. Shock*, 36(1):62–71, 2000.

[14] V. M. Bel'skii, A. L. Mikhailov, A. V. Rodinov, and A. A. Sedov. Microwave diagnostics of shock-wave and detonation processes. *Combust. Explos. Shock*, 47(6):639–650, 2011.

[15] R. V. Jones. *Most secret war*. Penguin, UK, 2009.

[16] B. C. Glancy and A. D. Krall. Microwave interferometric measurements of particle and wave velocities in porous media. Technical Report NSWC-TR-88-362, Naval Surface Warfare Center, Silver Springs, MD, 1990.

[17] B. Koch. Reflexion de micro-ondes par des phenomenes de detonation. *Compt. Rend. Acad. Sci., Paris*, 236:661–663, 1953.

[18] M. A. Cook, R. L. Doran, and G. J. Morris. Measurement of detonation velocity by Doppler effect at three-centimeter wavelength. *J. Appl. Phys.*, 26(4):426–428, 1955.

[19] H. Eyring, R. E. Powell, G. H. Duffy, and R. B. Parlin. The stability of detonation. *Chem. Rev.*, 45(1):69–181, 1949.

[20] T. J. Boyd and P. Fagan. A microwave technique for measuring detonation velocities. In *Proc. 2nd Intern. Symp. on Detonation*, pages 151–156, Washington, DC, February 1955.

[21] E. G. Johnson. A microwave technique of determining growth to detonation. *AIAA J.*, 3(11):2109–2111, 1965.

[22] E. G. Johnson. A microwave technique for studying detonation phenomena. Technical Report No. S-87, Rohm and Haas Co. Huntsville AL Redstone Arsenal Research Div., 1965.

[23] D. H. Edwards, E. M. Job, and T. R. Lawrence. Observations on gaseous detonation waves using a microwave interferometer. *Nature*, 195:372–373, 1962.

[24] D. L. Johnson. Microwave measurement of the solid propellant burning rates. Technical report, Giannini Controls Corp., Duarte, 1962.

[25] J. C. Jenks and J. B. Devault. Microwave measurements of solid propellant burning rates and burning profiles. In *Bulletin of the First Meeting, ICRPG Working group on Static Testing, CPIA Publication No. 24*, September 1963.

[26] R. B. Cole. High pressure solid propellant combustion studies using a closed bomb. Technical Report No. S-68, Rohm and Haas Co. Huntsville AL Redstone Arsenal Research Div., 1965.

[27] D. S. Dean and D. T. Green. The use of microwaves for the detection of flaws and measurement of erosion rates in materials. *J. Sci. Instrum.*, 44(9):699–701, 1967.

[28] D. T. Green. Application of microwaves to the measurement of solid propellant burning rates and to non-destructive testing. Technical report, Technical Memorandum 514, Rocket Propulsion Establishment, Westcott, United Kingdom, 1968.

[29] H. L. Wood and W. F. O'Brien. Progress report. Technical report, NASA Research Grant NGR 47-004-024, Virginia Polytechnic Institute, Blacksburg, Va., 1968.

[30] H. L. Wood. Final report. Technical report, NASA Research Grant NGR 47-004-024, Virginia Polytechnic Institute, Blacksburg, Va., 1970.

[31] S. V. Shelton. A technique for measurement of solid propellant burning rates during rapid pressure transients. In *Bulletin of the 4th ICRPG Combustion Conference, CPIA Publication No. 162, Vol. I*, pages 361–372, Silver Springs 1967.

[32] L. D. Strand, A. L. Schultz, and G. K. Reedy. Determination of solid-propellant transient regression rates using a microwave Doppler shift technique. Technical Report TR-32-1569, Jet Propulsion Laboratory, California Institute of Technology, 1972.

[33] L. D. Strand, A. L. Schultz, and G. K. Reedy. Microwave Doppler shift technique for determining solid propellant transient regression rates. *J. Spacecraft Rockets*, 11(2):75–83, 1974.

[34] L. D. Strand and R. P. McNamara. Feasibility demonstration of a variable frequency driver-microwave transient regression rate measurement system. In *AIAA 14th Aerospace Sciences Meeting*, pages No. 76–105, Washington, D.C., January 1976.

[35] L. D. Strand and R. P. McNamara. A variable-frequency driver-microwave transient regression rate measurement system. *Progress in Astronautics and Aeronautics*, 63:155–172, 1978.

[36] L. D. Strand, K. R. Magiawala, and R. P. McNamara. Microwave measurement of the solid propellant pressure-coupled response function. In *AIAA/SAE/ASME 15th Joint Propulsion Conference*, pages 485–498, Las Vegas, NV, June 1979.

[37] L. D. Strand, K. R. Magiawala, and R. P. McNamara. Microwave measurement of the solid-propellant pressure-coupled response function. *J. Spacecraft Rockets*, 17(6):483–488, 1980.

[38] W. C. Schuemann, L. S. Zajdel, and J. H. Rice. Development of a rocket motor burn rate measurement system. Technical Report ABL-TR-71-8, Hercules Incorporated, Allegany Ballistics Laboratory, Cumberland, 1971.

[39] J. Gittins, R. D. Gould, P. D. Penny, and P. C. Wellings. Solid propellant combustion instability. *J. British Interplanet. Soc.*, 25(6):597, 1972.

[40] R. D. Gould and P. D. Penny. An experimental investigation of the burning rate of propellant ANB 3066 under oscillatory pressure and oscillatory velocity conditions. Technical Report AFRPL TR-73-95, Rocket Propulsion Establishment, Westcott, Aylesbury, Bucks., U.K., 1973.

[41] A. C. Alkidas, A. T. Clary, G. Giles, and S. V. Shelton. Measurement of steady state and transient solid propellant burning rates with microwaves. Technical Report AFOSR-TR-74-0458, Georgia Institute of Technology, School of Mechanical Engineering, Atlanta, GA, 1974.

[42] L. H. Russell. Burning velocities of a solid propellant, via a microwave technique, at elevated pressures and pressurization rates. Technical Report No. NSWC/TR-79-387, Naval Surface Weapons Center, Dahlgren Lab, VA, 1979.

[43] D. H. Edwards, G. Hooper, and R. J. Meddins. Microwave velocity measurements of marginal detonation waves. *J. Phys. D: Appl. Phys.*, 3(7):1130–1133, 1970.

[44] D. H. Edwards, G. Hooper, and J. M. Morgan. A study of unstable detonations using a microwave interferometer. *J. Phys. D: Appl. Phys.*, 7(2):242–248, 1974.

[45] D. H. Edwards, G. Hooper, and J. M. Morgan. An experimental investigation of the direct initiation of spherical detonations. *Acta Astronaut.*, 3(1):117–130, 1976.

[46] D. H. Edwards and J. M. Morgan. Instabilities in detonation waves near the limits of propagation. *J. Phys. D: Appl. Phys.*, 10(17):2377, 1977.

[47] G. H. McCall, W. L. Bongianni, and G. A. Miranda. Microwave interferometer for shock wave, detonation, and material motion measurements. *Rev. Sci. Instrum.*, 56(8):1612–1618, 1985.

[48] N. J. Burnside, S. F. Son, B. W. Asay, and P. M. Dickson. Deflagration to detonation experiments in granular HMX. In *JANNAF Propulsion Systems Hazards Subcommittee Meeting*, Palm Beach, FL 1997.

[49] H. L. Wood, W. F. O'Brien, and C. B. Dale. Measurement of solid propellant burning rates employing microwave techniques. In *Proc. of the 6th Int. Symp. on Air Breathing Engines*, Paris, France 1983.

[50] W. F. O'Brien, H. L. Wood, J. J. Kliger, and C. B. Dale. Multiple reflection theory for microwave measurement of solid propellant burning rates. Technical report, Virginia Polytechnic Institute and State University Blacksburg, Oct. 1984.

[51] R. H. W. Waesche and W. F. O'Brien. Evaluation of techniques for direct measurement of burning rates in nozzleless motors. Technical report, NASA Ames Research Center Rept., Atlantic Research Corp., Gainesville, VA, Sept. 1987.

[52] G. Luther, L. Vesser, and B. Warthen. A microwave interferometer to measure particle and shock velocities simultaneously. In *American Physical Society Topical Conference on Shock Compression of Condensed Matter*, pages 775–778. Elsevier Science Publishers, Williamsburg, VA, June 17–20 1991.

[53] B. J. Warthen and G. G. Luther. A microwave interferometer to measure transient properties. Technical Report No. EGG–11265–5015, Los Alamos National Laboratory (LANL), 1994.

[54] S. P. Marsh. *LASL shock Hugoniot data*. Vol. 5. University of California Press, Berkeley, 1980.

[55] D. T. Foss, R. J. Roby, and W. F. O'Brien. Development of a dual-frequency microwave burn-rate measurement system for solid rocket propellant. *J. Propul. Power*, 9(4):497–498, 1993.

[56] V. S. Bozic, D. D. Blagojevic, and B. A. Anicin. Measurement system for determining solid rocket propellant burning rate using reflection microwave interferometry. *J. Propul. Power*, 13(4):457–462, 1997.

[57] V. S. Bozic, D. D. Blagojevic, and B. A. Anicin. Measurement system for determining solid propellant burning rate using transmission microwave interferometry. *J. Propul. Power*, 14(4):421–428, 1998.

[58] J. Lee. *Development of a broadband microwave interferometer for diagnostic measurements of detonations*. Master's thesis, McGill University, Montreal, Québec, Canada, 1992.

[59] A. V. Rodionov, V. A. Kanakov, and S. Yu. Lupov. Methods of processing the results of radio interferometeric measurements of gas-dynamic parameters. In *Extreme States of Matter. Detonation. Shock Waves*, pages 680–685. Int. Conf. VII Kharitonov Topical Scientific Readings RFNC-VNIIEF, Sarov 2005.

[60] V. A. Kanakov, S. Yu. Lupov, V. V. Parkhachev, and A. V. Rodionov. Multimode radio interferometry as a means of increasing the number of measured parameters of explosives. In *Extreme States of Matter. Detonation. Shock Waves*, pages 665–670. Int. Conf. VII Kharitonov Topical Scientific Readings RFNC-VNIIEF, Sarov 2007.

[61] E. N. Bogdanov, V. M. Bel'skii, and A. V. Rodionov. The effect of shock-compressed air in front of an accelerated plate on radio interferometry measurements of velocity. In *Extreme States of Matter. Detonation. Shock Waves*, pages 680–686. Int. Conf. VII Kharitonov Topical Scientific Readings RFNC-VNIIEF, Sarov 2007.

[62] V. A. Kanakov, S. Y. Lupov, Y. I. Orekhov, and A. V. Rodionov. Techniques for retrieval of the boundary displacement data in gas-dynamic experiments using millimeter-waveband radio interferometers. *Radiophys. Quantum El.*, 51(3):210–221, 2008.

[63] A. V. Rodionov, V. M. Bel'skii, and E. N. Bogdanov et al. Determination of the depth of initiation of detonation radio wave method of plastic-bonded HMX and TATB. In *Extreme States of Matter. Detonation. Shock Waves*, pages 69–73. Int. Conf. VII Kharitonov Topical Scientific Readings RFNC-VNIIEF, Sarov 2009.

[64] J. W. Tringe, R. J. Kane, K. S. Vandersall, M. C. Converse, F. Garcia, and C. M. Tarver. Microwave interferometry for understanding deflagration-to-detonation and shock-to-detonation transitions in porous explosives. In *Proc. 15th Intern. Symp. on Detonation*, pages 284–291, San Francisco, CA, July 2014.

[65] R. S. Janesheski, L. J. Groven, and S. F. Son. Detonation failure characterization of homemade explosives. *Propell. Explos. Pyrot.*, 39(4):609–616, 2014.

[66] D. E. Kittell, P. J. Renslow, L. J. Groven, and S. F. Son. Modelling small scale detonation expreiments with pressed TATB. In *Proc. 15th Intern. Symp. on Detonation*, pages 1584–1593, San Francisco, CA, July 2014.

[67] D. E. Kittell, J. O. Mares, and S. F. Son. A comparison of wavelet, quadrature, and peak-to-peak methods for determining shock velocity from microwave interferometer data. In *Proc. 15th Intern. Symp. on Detonation*, pages 192–201, San Francisco, CA, July 2014.

[68] D. E. Kittell, J. O. Mares, and S. F. Son. Using time-frequency analysis to determine time-resolved detonation velocity with microwave interferometry. *Rev. Sci. Instrum.*, 86(4):044705, 2015.

[69] P. L. M. Heydemann. Determination and correction of quadrature fringe measurement errors in interferometers. *Appl. Optics*, 20(19):3382–3384, 1981.

[70] W. Gander, G. H. Golub, and R. Strebel. Least-squares fitting of circles and ellipses. *BIT Numerical Mathematics*, 34(4):558–578, 1994.

[71] R. De Levie, S. Sarangapani, and P. Czekaj. Numerical differentiation by Fourier transform as applied to electrochemical interfacial tension data. *Anal. Chem.*, 50(1):110–115, 1978.

[72] A. Savitzky and M. J. Golay. Smoothing and differentiation of data by simplified least squares procedures. *Anal. Chem.*, 36(8):1627–1639, 1964.

[73] S. Liu, D. Wang, T. Li, G. Chen, Z. Li, and Q. Peng. Analysis of photonic Doppler velocimetry data based on the continuous wavelet transform. *Rev. Sci. Instrum.*, 82(2):023103, 2011.

[74] H. Song, X. Wu, C. Huang, Y. Wei, and X. Wang. Measurement of fast-changing low velocities by photonic Doppler velocimetry. *Rev. Sci. Instrum.*, 83(7):073301, 2012.

[75] A. Sur, A. S. Rav, G. Pandey, K. D. Joshi, and S. C. Gupta. Analysis of velocimetry data based on continuous wavelet transform: application to shock wave physics experiments. In *Advanced Electronic Systems (ICAES), IEEE International Conference on*, pages 147–151, September 2013.

[76] J.-C. Hong and Y. Y. Kim. Determination of the optimal gabor wavelet shape for the best time-frequency localization using the entropy concept. *Exp. Mech.*, 44(4):387–395, 2004.

[77] Y. Y. Kim and E.-H. Kim. Effectiveness of the continuous wavelet transform in the analysis of some dispersive elastic waves. *J. Acoust. Soc. Am.*, 110(1):86–94, 2001.

[78] C. Torrence and G. P. Compo. A practical guide to wavelet analysis. *B. Am. Meteorol. Soc.*, 79(1):61–78, 1998.

[79] I. Daubechies. The wavelet transform, time-frequency localization and signal analysis. *IEEE T. Inform. Theory*, 36(5):961–1005, 1990.

[80] D. H. Dolan. Accuracy and precision in photonic Doppler velocimetry. *Rev. Sci. Instrum.*, 81(5):053905, 2010.

[81] T. A. Ota. Numerical study of the effect of normalized window size, sampling frequency, and noise level on short time Fourier transform analysis. *Rev. Sci. Instrum.*, 84(10):103906, 2013.

[82] S. Mallat. *A Wavelet Tour of Signal Processing, 2nd edition*. Academic Press, New York, 1999.

[83] I. Simonovski and M. Boltežar. The norms and variances of the Gabor, Morlet, and general harmonic wavelet functions. *J. Sound Vib.*, 264(3):545–557, 2003.

[84] Y. Q. Deng, C. Wang, L. Chai, and Z. Zhang. Determination of the optimal gabor wavelet shaping factor for accurate phase retrieval with wavelet-transform. *Appl. Phys. B-Lasers O.*, 81(8):1107–1111, 2005.

[85] J. Slavič, I. Simonovski, and M. Boltežar. Damping identification using a continuous wavelet transform: application to real data. *J. Sound Vib.*, 262(2):291–307, 2003.

[86] S. I. Jackson, C. B. Kiyanda, and M. Short. Experimental observations of detonation in ammonium-nitrate-fuel-oil (ANFO) surrounded by a high-sound-speed, shockless, aluminum confiner. *P. Combust. Inst.*, 33(2):2219–2226, 2011.

[87] M. Boltežar and J. Slavič. Enhancements to the continuous wavelet transform for damping identifications on short signals. *Mech. Syst. Signal Pr.*, 18(5):1065–1076, 2004.

[88] C. L. Mader. *Numerical modeling of explosives and propellants*. CRC Press, New York, 1998.

[89] D. A. Jones, G. Kemister, and R. A. Borg. Numerical simulation of detonation in condensed phase explosives. Technical Report DSTO-TR-0705, Aeronautical and Maritime Research Lab, Melbourne, Australia, 1998.

[90] R. Menikoff and M. S. Shaw. Reactive burn models and ignition & growth concept. In *EPJ Web of Conferences, Vol. 10, p. 00003*. EDP Sciences, 2010.

[91] C. A. Handley. The CREST reactive burn model. In *Proc. 13th Intern. Symp. on Detonation*, pages 864–870, Norfolk, VA, July 2006.

[92] C. A. Handley. *Numerical modelling of two HMX-based plastic-bonded explosives at the mesoscale*. PhD thesis, University of St Andrews, Fife, Scotland, United Kingdom, 2011.

[93] W. W. Wood and J. G. Kirkwood. Diameter effect in condensed explosives: the relation between velocity and radius of curvature of the detonation wave. *J. Chem. Phys.*, 22(11):1920–1924, 1954.

[94] E. L. Lee and C. M. Tarver. Phenomenological model of shock initiation in heterogeneous explosives. *Phys. Fluids*, 23(12):2362–2372, 1980.

[95] J. E. Field, N. K. Bourne, S. J. P. Palmer, S. M. Walley, J. Sharma, and B. C. Beard. Hot-spot ignition mechanisms for explosives and propellants [and discussion]. *Philos. T. Roy. Soc. A*, 339(1654):269–283, 1992.

[96] S. Nie, J. Deng, and A. Persson. The dead-pressing phenomenon in an ANFO explosive. *Propell. Explos. Pyrot.*, 18(2):73–76, 1993.

[97] J. H. Rowland, R. Mainiero, and D. A. Hurd. Factors affecting fumes production of an emulsion and ANFO/emulsion blends. In *P. Annual Conf. Explos. Blast Tech.*, pages 133–142. ISEE, 1999.

[98] R. A. Catanach and L. G. Hill. Diameter effect curve and detonation front curvature measurements for ANFO. In *12th American Physical Society Topical Conference on Shock Compression of Condensed Matter*, pages 906–909. AIP Publishing, Atlanta, GA, June 24–29 2001.

[99] M. Sapko, J. Rowland, R. Mainiero, and I. Zlochower. Chemical and physical factors that influence NO_x production during blasting - exploratory study. In *P. Annual Conf. Explos. Blast Tech.*, pages 317–330. ISEE, 2002.

[100] V. P. Sinditskii, V. Y. Egorshev, A. I. Levshenkov, and V. V. Serushkin. Ammonium nitrate: combustion mechanism and the role of additives. *Propell. Explos. Pyrot.*, 30(4):269–280, 2005.

[101] A. Miyake, H. Kobayashi, H. Echigoya, S. Kubota, Y. Wada, Y. Ogata, H. Arai, and T. Ogawa. Detonation characteristics of ammonium nitrate and activated carbon mixtures. *J. Loss Prevent. Proc.*, 20(4):584–588, 2007.

[102] B. Zygmunt and D. Buczkowski. Influence of ammonium nitrate prills' properties on detonation velocity of ANFO. *Propell. Explos. Pyrot.*, 32(5):411–414, 2007.

[103] A. Maranda, J. Paszula, I. Zawadzka-Malota, B. Kuczynska, , W. Witkowski, K. Nikolczuk, and Z. Wilk. Aluminum powder influence on ANFO detonation parameters. *Cent. Eur. J. Ener. Mat.*, 8(4):279–292, 2011.

[104] M. R. Baer, D. K. Gartling, and P. E. DesJardin. Probabilistic models for reactive behavior in heterogeneous condensed phase media. *Combust. Theor. Model*, 16(1):75–106, 2012.

[105] M. L. Hobbs and M. R. Baer. Nonideal thermoequilibrium calculations using a large product species data base. *Shock Waves*, 2(3):177–187, 1992.

[106] L. Fried and P. Souers. CHEETAH: a next generation thermochemical code. Technical Report UCRL-ID-117240, Lawrence Livermore National Laboratory, 1994.

[107] F. P. Bowden and A. D. Yoffe. *Initiation and growth of explosives in liquids and solids*. Cambridge University Press, Cambridge, 1952. Reprinted 1989.

[108] W. Fickett. Detonation in miniature. *Am. J. Phys.*, 47(12):1050–1059, 1979.

[109] R. Menikoff. Empirical equations of state for solids. In *ShockWave Science and Technology Reference Library*. Springer Berlin Heidelberg, 2007.

[110] P. W. Cooper. *Explosives engineering*. Wiley-VCH, New York, 1996.

[111] C. A. Hall, J. R. Asay, M. D. Knudson, W. A. Stygar, R. B. Spielman, T. D. Pointon, , D. B. Reisman, A. Toor, and R. C. Cauble. Experimental configuration for isentropic compression of solids using pulsed magnetic loading. *Rev. Sci. Instrum.*, 72(9):3587–3595, 2001.

[112] F. Birch. Equation of state and thermodynamic parameters of NaCl to 300 kbar in the high-temperature domain. *J. Geophys. Res.*, 91(B5):4949–4954, 1986.

[113] R. Jeanloz. Shock wave equation of state and finite strain theory. *J. Geophys. Res.*, 94(B5):5873–5886, 1989.

[114] F. G. Fumi and M. P. Tosi. On the Mie-Grüneisen and Hildebrand approximations to the equation of state of cubic solids. *J. Phys. Chem. Solids*, 23(4):395–404, 1962.

[115] E. Grüneisen. *Handbuch der Physik*, volume 10. Verlag Julius Springer, Berlin, 1926.

[116] E. L. Lee, H. C. Horning, and J. W. Kury. Adiabatic expansion of high explosive detonation products. Technical Report UCRL-50422, Lawrence Livermore Radiation Lab, University of California, 1968.

[117] B. D. Lambourn. An improved EOS for non-reacted explosives. In *14th American Physical Society Topical Conference on Shock Compression of Condensed Matter*, pages 165–168. AIP Publishing, Baltimore, MD, July 31–August 5 2005.

[118] B. D. Lambourn, N. J. Whitworth, C. A. Handley, and H. R. James. A finite-strain, non-reacted EOS for PBX9502. In *15th American Physical Society Topical Conference on Shock Compression of Condensed Matter*, pages 137–140. AIP Publishing, Kohala Coast, HI, June 24–29 2007.

[119] S. B. Segletes. Thermodynamic stability of the Mie-Grüneisen equation of state, and its relevance to hydrocode computations. *J. Appl. Phys.*, 70(5):2489–2499, 1991.

[120] R. Menikoff. Complete Mie-Grüneisen equation of state. Technical Report LA-UR-12-22592, Los Alamos National Laboratory (LANL), 2012.

[121] J. M. Winey, G. E. Duvall, M. D. Knudson, and Y. M. Gupta. Equation of state and temperature measurements for shocked nitromethane. *J. Chem. Phys.*, 113(17):7492–7501, 2000.

[122] W. C. Davis. Complete equation of state for unreacted solid explosive. *Combust. Flame*, 120(3):399–403, 2000.

[123] P. A. Thompson. A fundamental derivative in gasdynamics. *Phys. Fluids*, 14(9):1843–1849, 1971.

[124] S. B. Segletes. Further examinations on the thermodynamic stability of the Mie-Grüneisen equation of state. *J. Appl. Phys.*, 76(8):4560–4566, 1994.

[125] A. N. Dremin, K. K. Shvedov, and O. S. Avdonin. Shock compressibility and temperature of certain explosives in the porous state. *Combust. Explos. Shock*, 6(4):449–455, 1970.

[126] M. G. Salvadori, R. Skalak, and P. Weidlinger. Waves and shocks in locking and dissipative media. *J. Eng. Mech. Div. ASCE*, 86(2):77–106, 1960.

[127] W. Herrmann. Constitutive equation for the dynamic compression of ductile porous materials. *J. Appl. Phys.*, 40(6):2490–2499, 1969.

[128] M. M. Carroll and A. C. Holt. Static and dynamic pore-collapse relations for ductile porous materials. *J. Appl. Phys.*, 43(4):1626–1636, 1972.

[129] D. A. Crawford, A. L. Brundage, E. N. Harstad, Jr. E. S. Hertel, R. G. Schmitt, S. C. Schumacher, and J. S. Simmons. CTH User's Manual and Input Instructions. Technical report, Sandia National Laboratories, 2011. Albuquerque, NM, USA.

[130] J. Starkenberg and T. M. Dorsey. An assessment pf the performance of the history variable reactive burn explosive initiation model in the CTH code. Technical Report ARL-TR-1667, Army research Laboratory, Aberdeen Proving Ground, MD, 1998.

[131] C. M. Tarver, J. O. Hallquist, and L. M. Erickson. Modeling short pulse duration shock initiation of solid explosives. In *Proc. 8th Intern. Symp. on Detonation*, pages 951–961, Albuquerque, NM, July 1985.

[132] M. A. Price and A. H. Ghee. Modeling for detonation and energy release from peroxides and non-ideal improvised explosives. *Cent. Eur. J. Ener. Mat.*, 6(3–4):239–254, 2009.

[133] H. R. James, B. D. Lambourn, C. A. Handley, N. J. Whitworth, H. N. Angseesing, P. J. Haskins, M. D. Cook, A. D. Wood, R. I. Briggs, and P. R. Ottley. An investigation of the detonation characteristics of some non-ideal explosive compositions based upon ammonium nitrate. In *Proc. 13th Intern. Symp. on Detonation*, pages 110–120, Norfolk, VA, July 2006.

[134] K. H. Kim and J. J. Yoh. A particle level-set based eulerian method for multi-material detonation simulation of high explosive and metal confinements. *P. Combust. Inst.*, 34(2):2025–2033, 2013.

[135] P. C. Souers, S. Anderson, J. Mercer, E. McGuire, and P. Vitello. JWL++: a simple reactive flow code package for detonation. *Propell. Explos. Pyrot.*, 25(2):54–58, 2000.

[136] P. J. Haskins and M. D. Cook. Detonation failure in ideal and non-ideal explosives. In *15th American Physical Society Topical Conference on Shock Compression of Condensed Matter*, pages 881–884. AIP Publishing, Kohala Coast, HI, June 24–29 2007.

[137] M. Cowperthwaite. A constitutive model for calculating chemical energy release rates from the flow fields in shocked explosives. In *Proc. 7th Intern. Symp. on Detonation*, pages 498–505, Annapolis, MD, June 1981.

[138] M. E. Kipp and J. W. Nunziato. Numerical simulation of detonation failure in nitromethane. In *Proc. 7th Intern. Symp. on Detonation*, pages 608–619, Annapolis, MD, June 1981.

[139] M. E. Kipp and R. E. Setchell. A shock initiation model for fine-grained hexanitrostilbene. In *Proc. 9th Intern. Symp. on Detonation*, pages 209–218, Portland, OR, June 1990.

[140] J. M. McGlaun and S. L. Thompson. CTH: a three-dimensional shock wave physics code. *Int. J. Impact Eng.*, 10(1):351–360, 1990.

[141] E. S. Hertel, R. L. Bell, M. G. Elrick, A. V. Farnsworth, G. I. Kerley, J. M. McGlaun, S. V. Petney, S. A. Silling, P. A. Taylor, and L. Yarrington. CTH: a software family for multi-dimensional shock physics analysis. In *Proc. 19th Intern. Symp. on Shock Waves*, pages 377–382. Springer Berlin Heidelberg, July 1995.

[142] D. A. Crawford, A. L. Brundage, E. N. Harstad, K. Ruggirello, R. G. Schmitt, S. C. Schumacher, and J. S. Simmons. CTH User's Manual and Input Instructions. Technical report, Sandia National Laboratories, 2013. Albuquerque, NM, USA.

[143] J. A. Zukas. *Introduction to hydrocodes*. Elsevier, Amsterdam, 2004.

[144] G. Sjaardema. An algebraic preprocessor for parameterizing finite element analyses. Technical Report SAND98–92-2291, Sandia National Laboratories, 1992.

[145] C. M. Tarver and E. M. McGuire. Reactive flow modeling of the interactions of TATB detonation waves with inert materials. In *Proc. 12th Intern. Symp. on Detonation*, pages 641–649, San Diego, CA, August 2002.

[146] B. M. Adams, W. J. Bohnhoff, K. R. Dalbey, J. P. Eddy, M. S. Eldred, D. M. Gay, K. Haskell, P. D. Hough, and L. P. Swiler. DAKOTA, a multilevel parallel object-oriented framework for design optimization, parameter estimation, uncertainty quantification, and sensitivity analysis: version 5.0 user's manual. Technical Report SAND2010-2183, Sandia National Laboratories, 2009.

[147] L. P. Swiler and G. D. Wyss. A user's guide to Sandia's latin hypercube sampling software: LHS UNIX library and standalone version. Technical Report SAND04-2439, Sandia National Laboratories, 2004.

[148] N. K. Bourne and J. E. Field. Explosive ignition by the collapse of cavities. *P. Roy. Soc. A-Math Phys.*, 455(1987):2411–2426, 1999.

[149] C. L. Mader. Initiation of detonation by the interaction of shocks with density discontinuities. *Phys. Fluids*, 8(10):1811–1816, 1965.

[150] M. R. Baer. Modeling heterogeneous energetic materials at the mesoscale. *Thermochim. Acta*, 384(1):351–367, 2002.

[151] T. L. Jackson, J. D. Buckmaster, J. Zhang, and M. J. Anderson. Pore collapse in an energetic material from the micro-scale to the macro-scale. *Combust. Theory Model.*, 19(3):347–381, 2015.

[152] C. D. Yarrington, R. R. Wixom, and D. L. Damm. Mesoscale simulations using realistic microstructures and first principles equation of state. In *Proc. 45th CS/33rd APS/33rd EPSS/27th PSH JANNAF Joint Subcommittee Meeting*, Monterey, CA, December 3–6 2012.

[153] B. L. Wescott, D. S. Stewart, and W. C. Davis. Equation of state and reaction rate for condensed-phase explosives. *J. Appl. Phys.*, 98(5):053514, 2005.

[154] J. M. Winey, Y. A. Gruzdkov, Z. A. Dreger, B. J. Jensen, and Y. M. Gupta. Thermomechanical model and temperature measurements for shocked ammonium perchlorate single crystals. *J. Appl. Phys.*, 91(9):5650–5656, 2002.

[155] C. Kittel and P. McEuen. *Introduction to solid state physics*, volume 8. Wiley, New York, 1976.

[156] V. K. Mohan and J. E. Field. Impact initiation of hexanitrostilbene. *Combust. Flame*, 56(3):269–277, 1984.

[157] G. I. Kerley. BCAT User's Manual and Input Instructions v1.20. Technical report, Sandia National Laboratories, 2000. CTH Distribution Tape.

[158] J. B. Bdzil and D. S. Stewart. Modeling two-dimensional detonations with detonation shock dynamics. *Phys. Fluids A-Fluid*, 1(7):1261–1267, 1989.

APPENDICES

A. SPECTROGRAMS FROM STFT

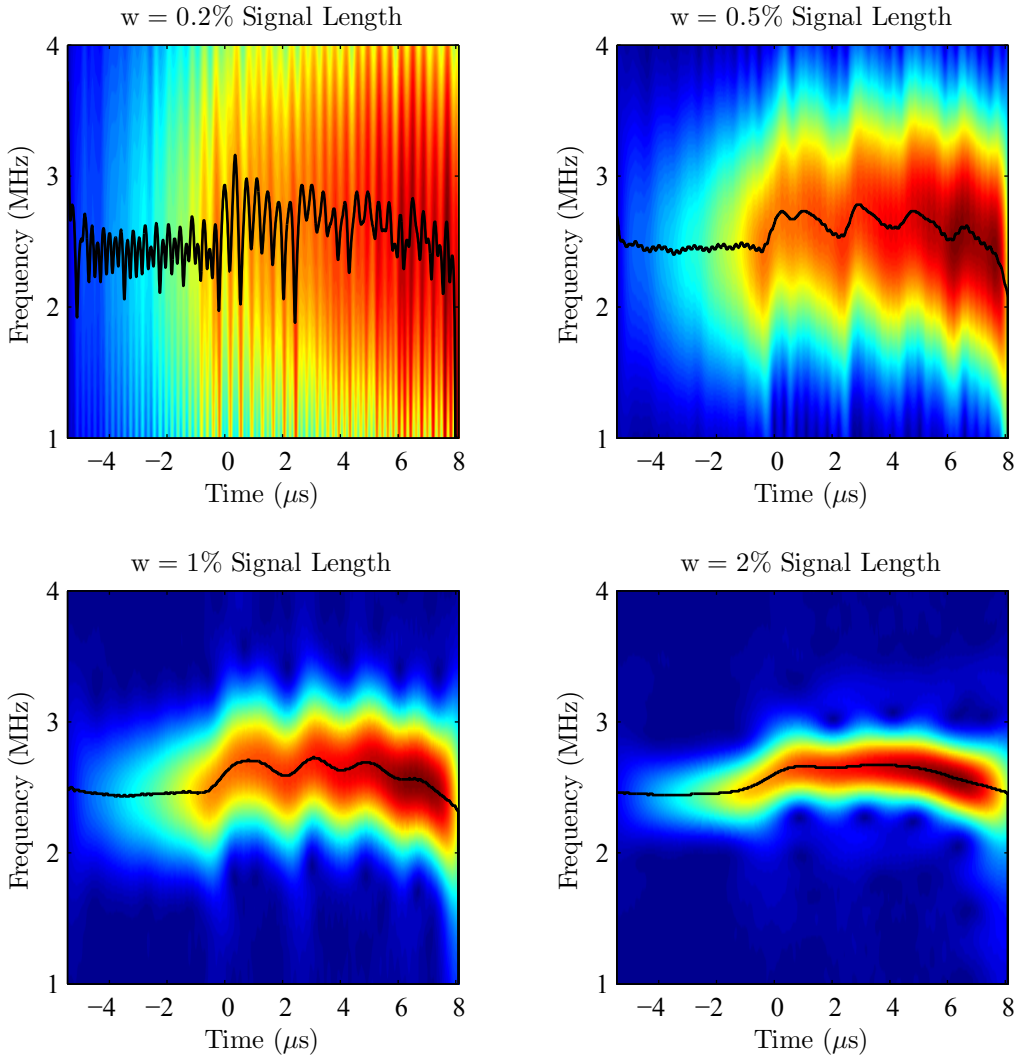

Figure A.1. Spectrogram of the high quality TATB signal in Fig. 4.3 for various window sizes, w, as a percentage of total signal length. Reproduced from [68] with permission.

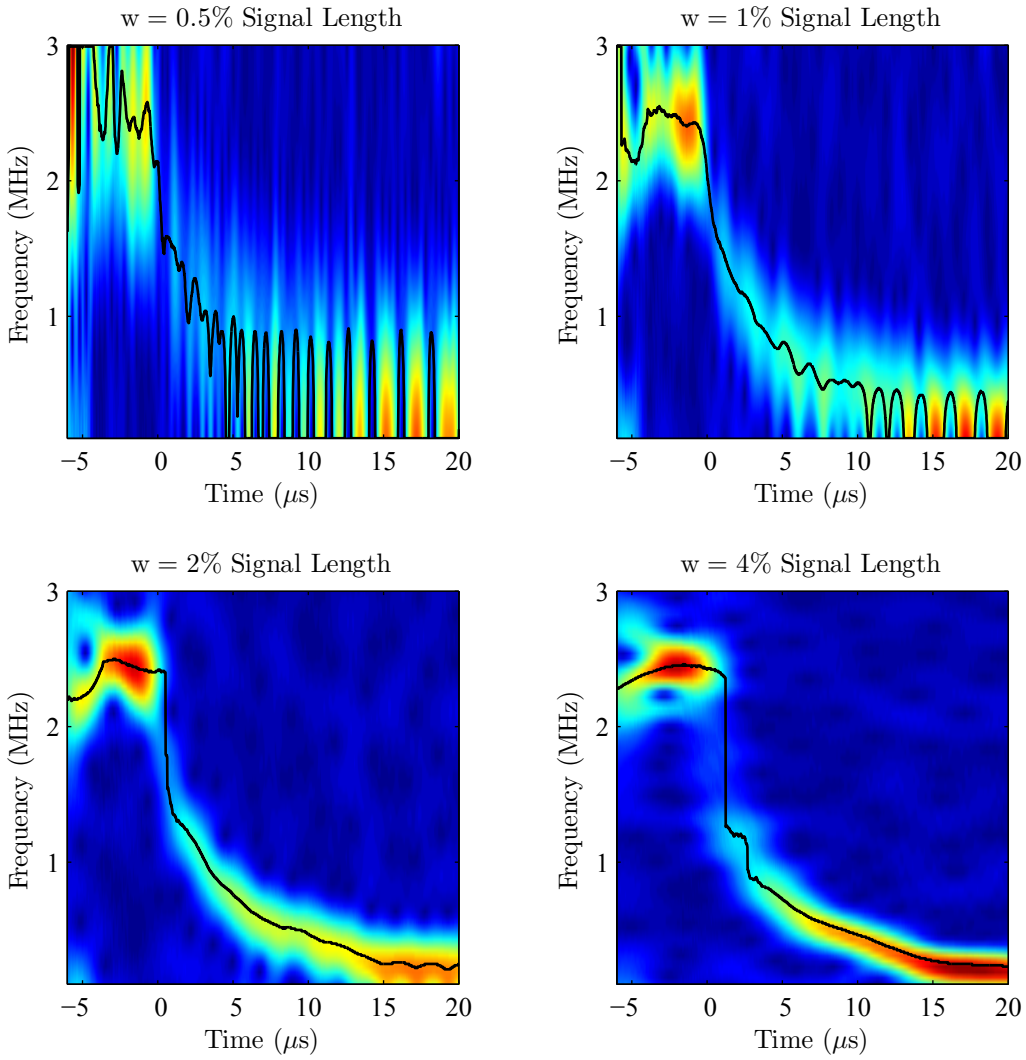

Figure A.2. Spectrogram of the lower quality ANUR signal in Fig. 4.9 for various window sizes, w, as a percentage of total signal length. Black solid lines indicate the maximum amplitude ridge.

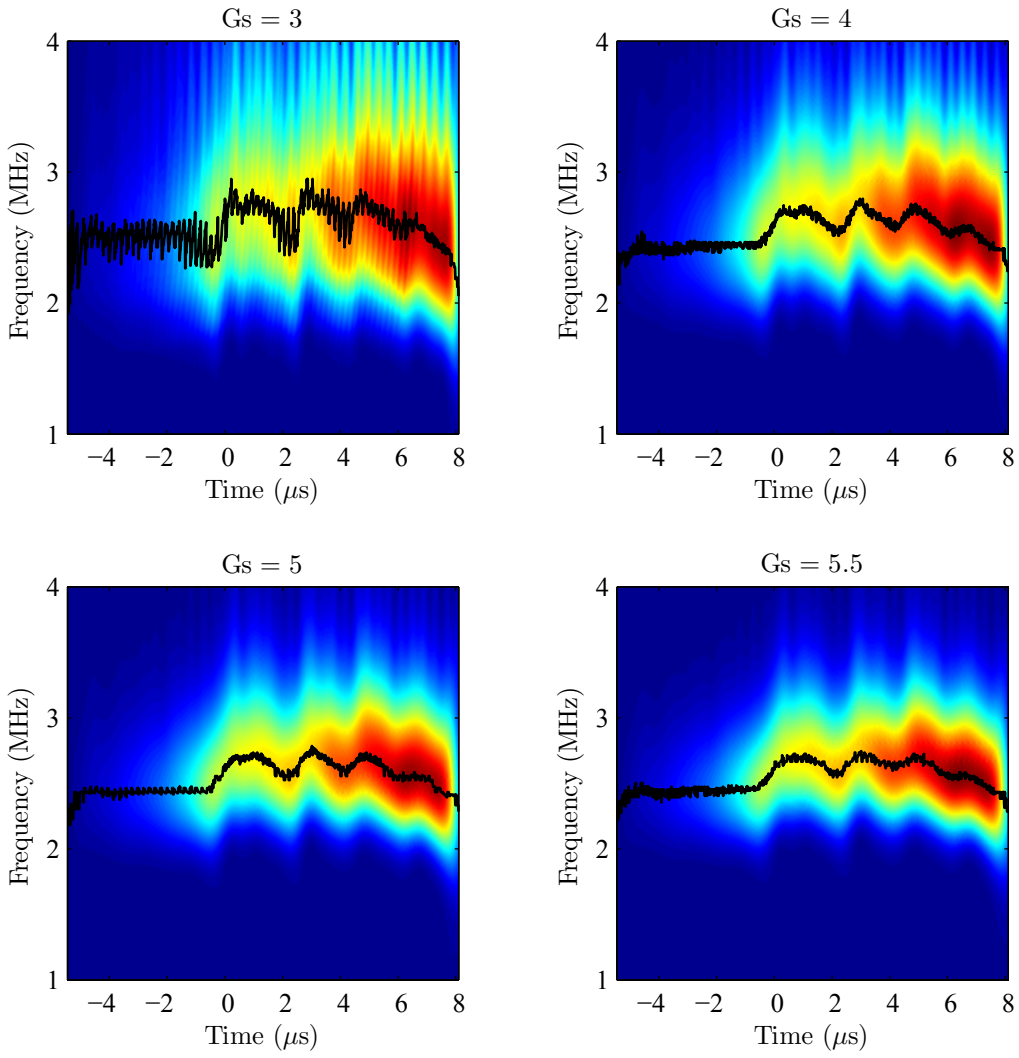

Figure B.1. Normalized scalogram of the high quality TATB signal in Fig. 4.3 for different values of the Gabor wavelet shaping factor, Gs. Reproduced from [68] with permission.

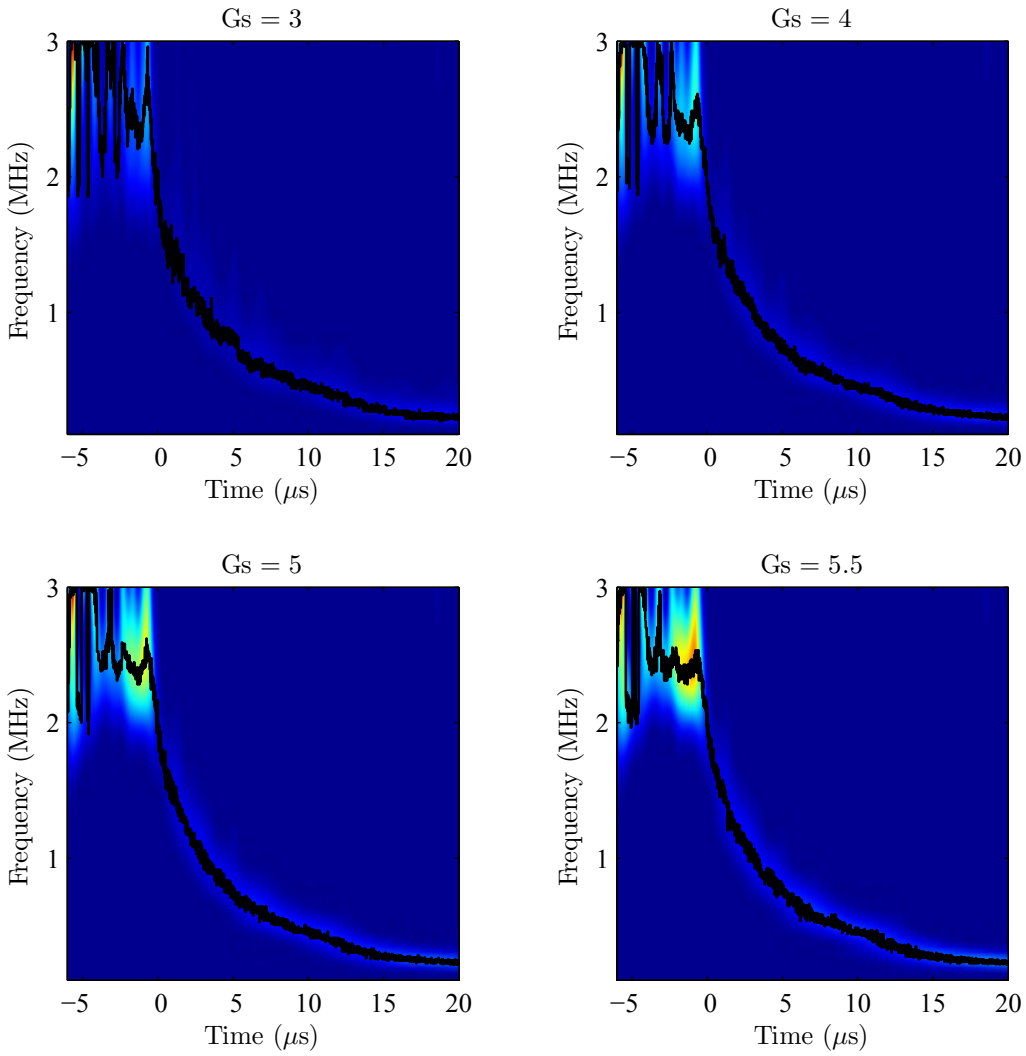

Figure B.2. Normalized scalogram of the lower quality ANUR signal in Fig. 4.9 for different values of the Gabor wavelet shaping factor, Gs. Black solid lines indicate the maximum amplitude ridge.

C. DATA PROCESSING AND ERROR ANALYSIS

Velocity calculations require values of permittivity for each explosive used. For multicomponent explosives such as PRIMASHEET® 1000 and ANFO, it is prohibitive to calculate the permittivity using mixture laws alone. Instead, permittivity values are extracted using a dynamic wavelength calibration, as discussed in Sec. 4.6. The Gabor wavelet transform and Eq. (4.39) are fully automated, provided that the time limits of integration are known. Permittivity results from all sixteen experiments are shown in Fig. C.1 for PRIMASHEET® 1000 and ANFO KP-1, plotted against the initial density as percent TMD. The relative permittivity values may be compared between all experiments, whereas other measured values (e.g. wavelength) depend on the sample diameter. A full list of the measured values is shown in Table C.1.

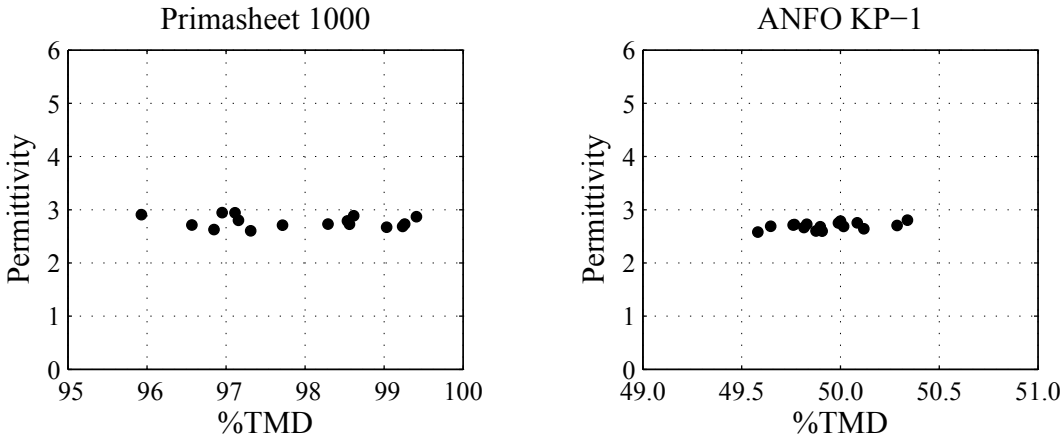

Figure C.1. Relative permittivity calculations for the booster and ANFO KP-1 explosives from sixteen different MI tests using dynamic wavelength calibration.

An error analysis for the velocity was also performed considering both measurement uncertainty and random sample errors, following the equations derived in Sec. 4.5. A list of the measurement errors is given in Table C.2, corresponding to 95% confidence intervals. In summary of the measurement errors, the uncertainty in mass,

Table C.1. Average material density, permittivity, and wavelength for the booster and ANFO KP-1 explosives.

Explosive	**Diameter** (mm)	$\boldsymbol{\rho_0}$ ($\mathbf{g/cm^3}$)	$\boldsymbol{\rho_{TMD}}$ ($\mathbf{g/cm^3}$)	$\boldsymbol{\epsilon_r}$	$\boldsymbol{\lambda_0}$ (mm)	$\boldsymbol{\lambda_c}$ (mm)	$\boldsymbol{\lambda_g}$ (mm)
PS 1000	11.28	1.441	1.472	2.77	8.56	19.25	5.34
	6.52	1.441	1.472	2.77	8.56	11.12	5.80
ANFO KP-1	11.28	0.826	1.655	2.69	8.56	19.25	5.42
	6.52	0.826	1.655	2.69	8.56	11.12	5.91

Δm, is twice the mass balance accuracy of 3.1 mg, as two measurements were made. The uncertainty in diameter, Δd, was taken from the manufacturer data assuming a 2σ rule for the part tolerance; uncertainty in diameter was also verified by hand measurements. The uncertainty in sample length, ΔL, is double the precision of the calipers (0.002"), and the uncertainty in the TMD (or density corrected) permittivity has the assumed value of 0.05, based on a typical level of scatter observed from cavity measurements.

In order to account for the random sample errors, the standard deviation of the bulk density and permittivity measurements were calculated for PRIMASHEET® 1000 and the ANFO KP-1 samples as shown in Table C.3. The standard deviations were doubled to estimate 95% confidence intervals for $\Delta\rho_0$ and $\Delta\epsilon_r$, assuming a 2σ rule. The total error in velocity due to the random error was determined by substitution of $\Delta\epsilon_r$ directly into Eq. (4.34). Measurement and random errors are presented in the results Ch. 7, Table 7.1.

The MI data was analyzed using a peak picking method described in Ch. 4. Peak picking was found to be an effective technique because of the high quality of the raw MI output signals; more complex analysis techniques, such as quadrature and time-frequency analysis, were not required. The raw data and peak picking results for all sixteen shots are shown in Figs. C.2−C.14, using the same image sequence of six

Table C.2. Measurement errors reported with a 95% confidence interval.

Quantity	**95% CI**	
	Sm. Dia.	**Lg. Dia.**
Δm (mg)	6.2	6.2
Δd (mm)	0.16	0.11
ΔL (mm)	0.05	0.05
$\Delta\epsilon_{r,TMD}$	0.05	0.05

Table C.3. Standard deviation of the bulk density and permittivity measurements.

$\boldsymbol{\sigma}$	**PS 1000**	**ANFO KP-1**
ρ_0 (g/cm^3)	0.016	0.003
ϵ_r	0.110	0.065

figures. Some of these figures include additional calculations to inform the analysis, and a complete description of the image sequence is discussed next.

Raw MI output signals are shown in the top row of Figs. C.2−C.14, where $t = 0$ corresponds to the fiber optic trigger, and all of the peaks are indicated with red markers. Two channel output was obtained from a quadrature mixer, where the first channel has a phase *lead* of 90° **(top left)**, and the second channel has a phase *lag* of 90° **(top right)**. From visual inspection of the signal amplitude, it is not always possible to locate the start and end times of each explosive. The time, Δt, between successive minima and maxima **(middle left)** may be plotted to identify a time interval corresponding to the booster explosive, for example $t = 0$ to $t = 5$ μs in Fig. C.2.

A non-dimensional shock trajectory plot **(middle right)** is constructed next by replacing the $\lambda_k/2$ in Eq. (4.17) with a value of unity. The portion of the curve

corresponding to the explosive booster (as determined from the Δt plot) may be fit with a linear equation, shown in red. The slope of the line corresponds to a steady frequency in MHz, which may be converted directly into velocity via Eq. (4.15). The frequency slope is subtracted from the non-dimensional trajectory plot in order to produce a graph of the wavelength deviation **(bottom left)**. The wavelength deviation curve makes identification of the transition time between explosives easier.

Finally, with a knowledge of all the transition times, the dynamic wavelength calibration was used to extract a sample permittivity from each test. The average permittivity values from all sixteen tests were used to define an average material wavelength for all of the velocity calculations (see Table C.1). The final results of the peak picking analysis have been transformed from the velocity-time domain into the velocity-position domain **(bottom right)**, as this information is more physical to understanding the behavior of the reactive wave as it moves farther downstream into the explosive charge.

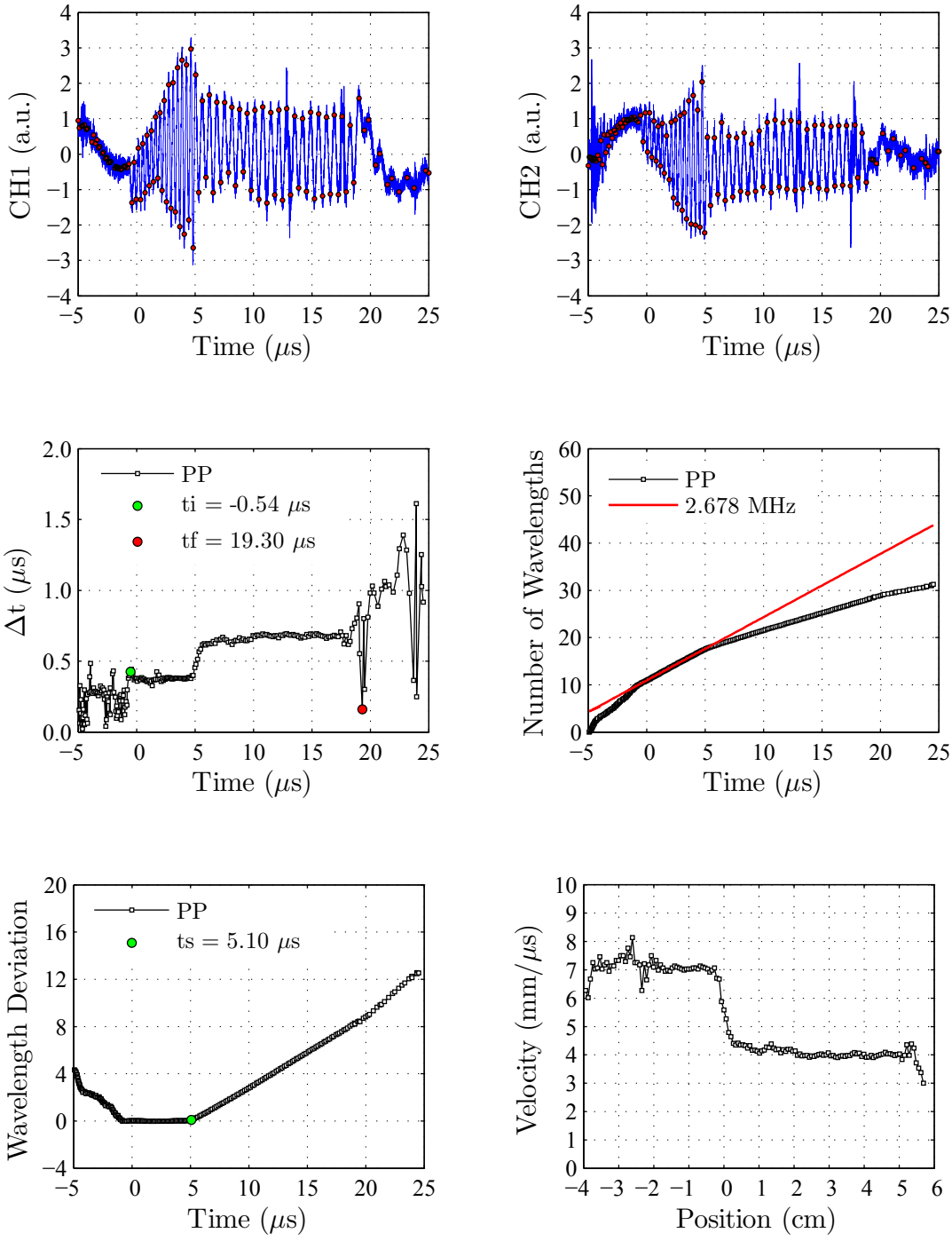

Figure C.2. MI data analysis for shot THK-1.

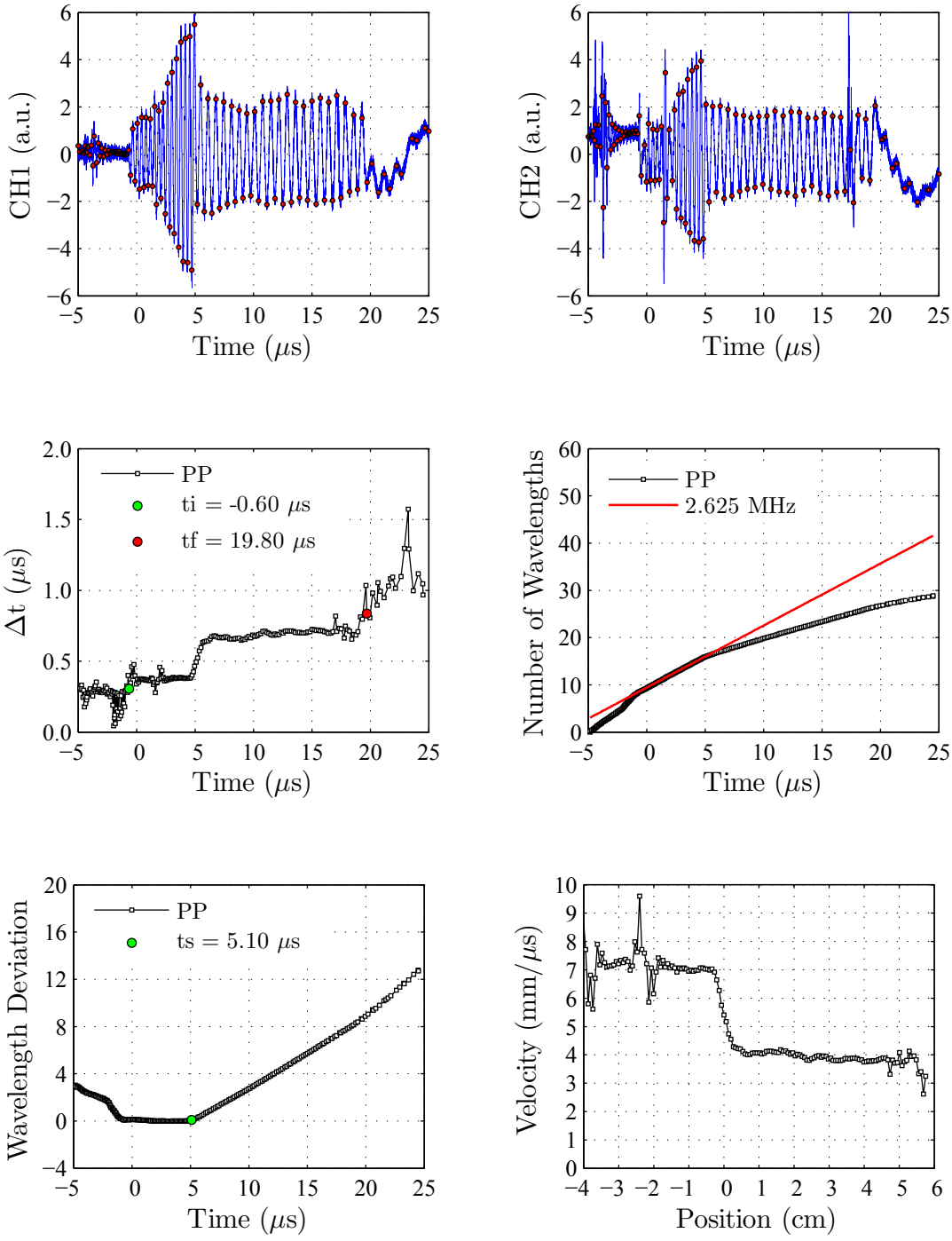

Figure C.3. MI data analysis for shot THK-2.

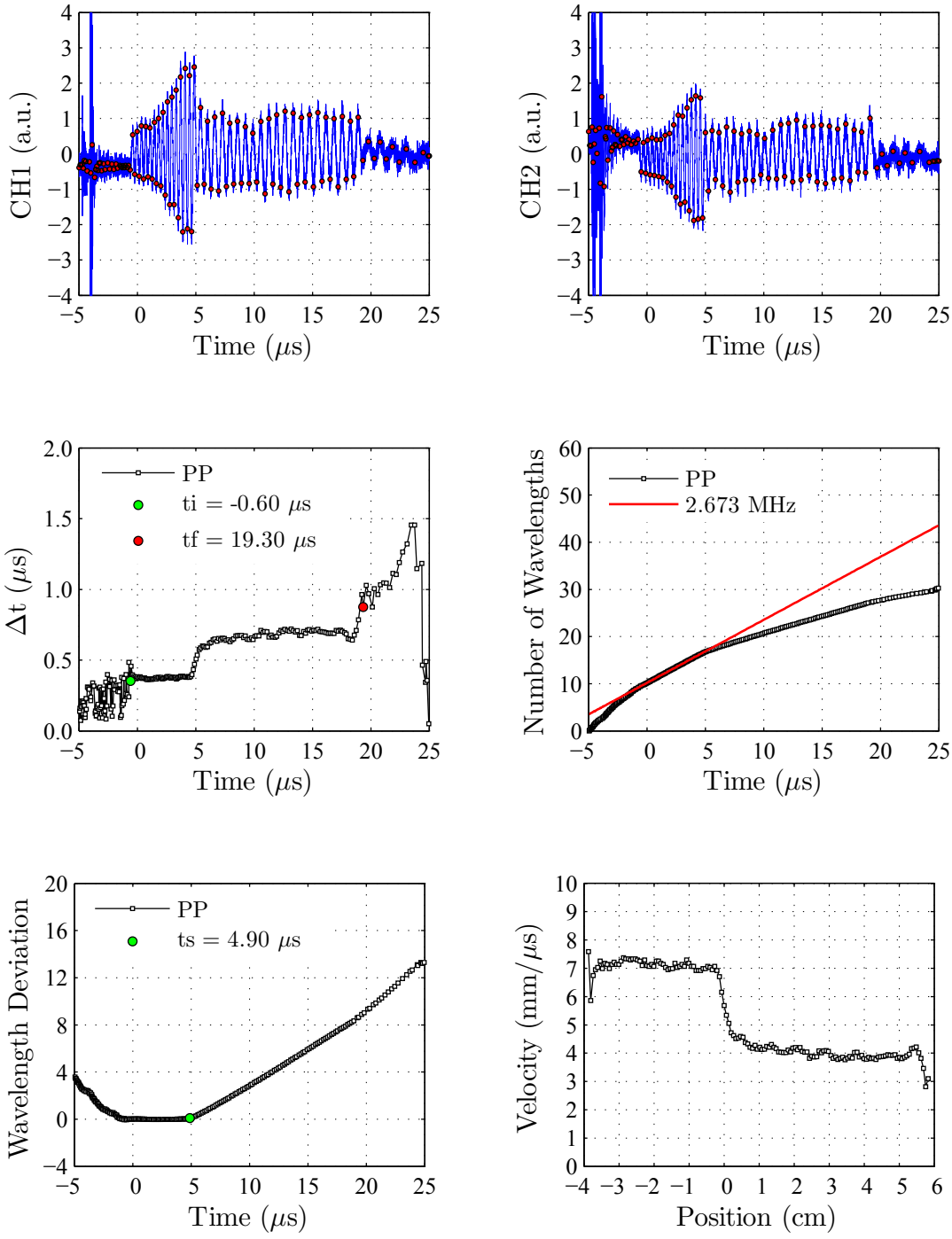

Figure C.4. MI data analysis for shot THK-3.

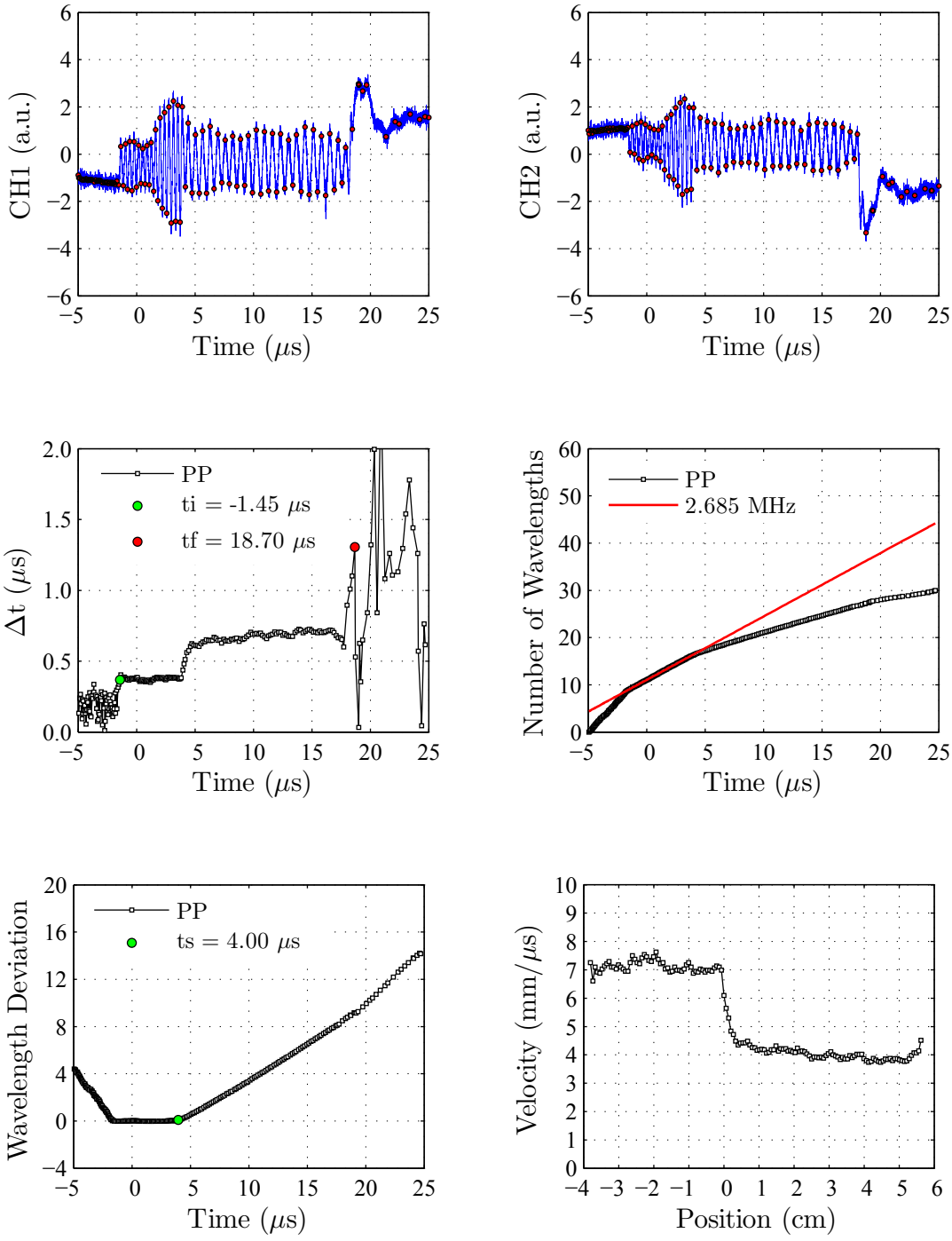

Figure C.5. MI data analysis for shot THK-4.

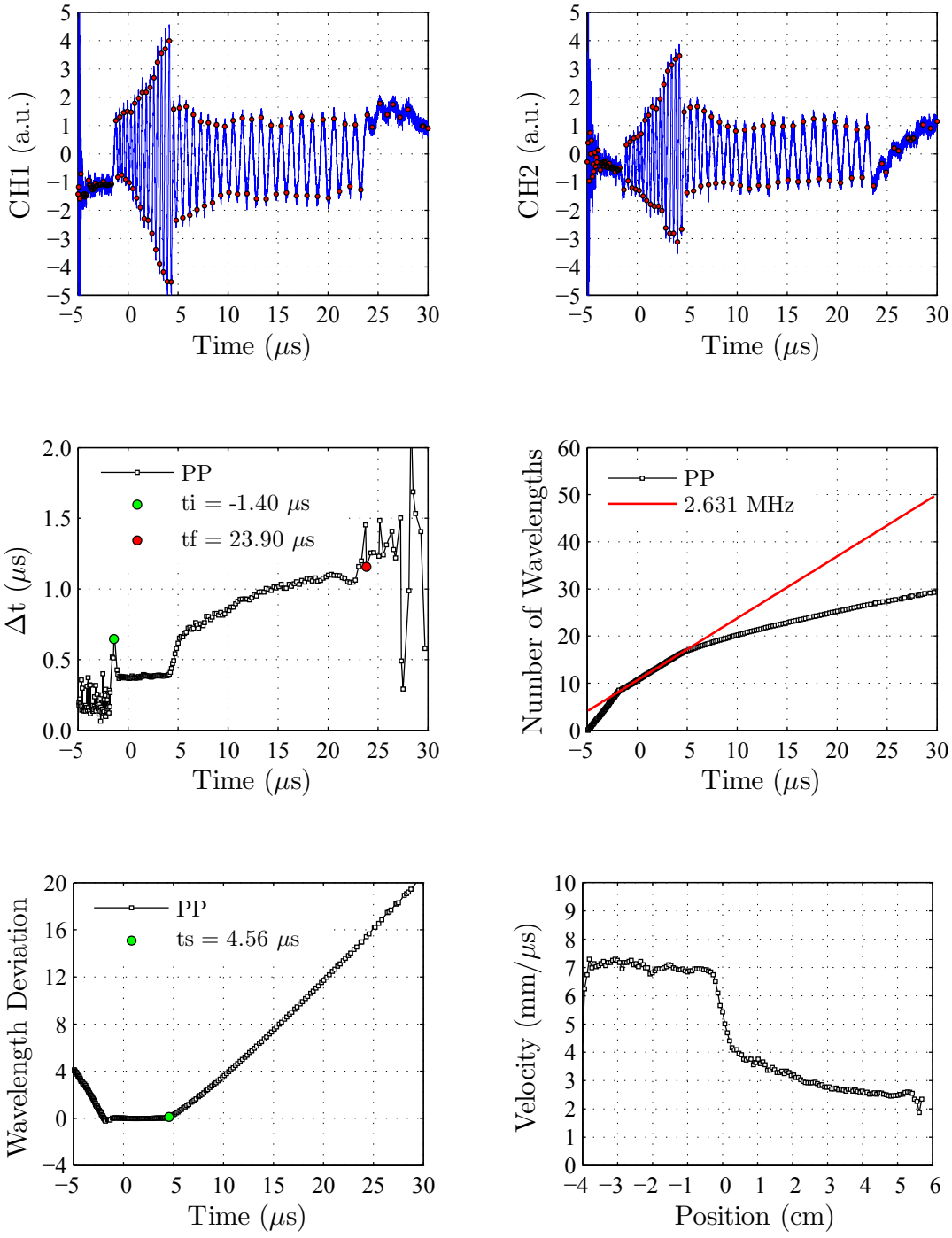

Figure C.6. MI data analysis for shot PVC-1.

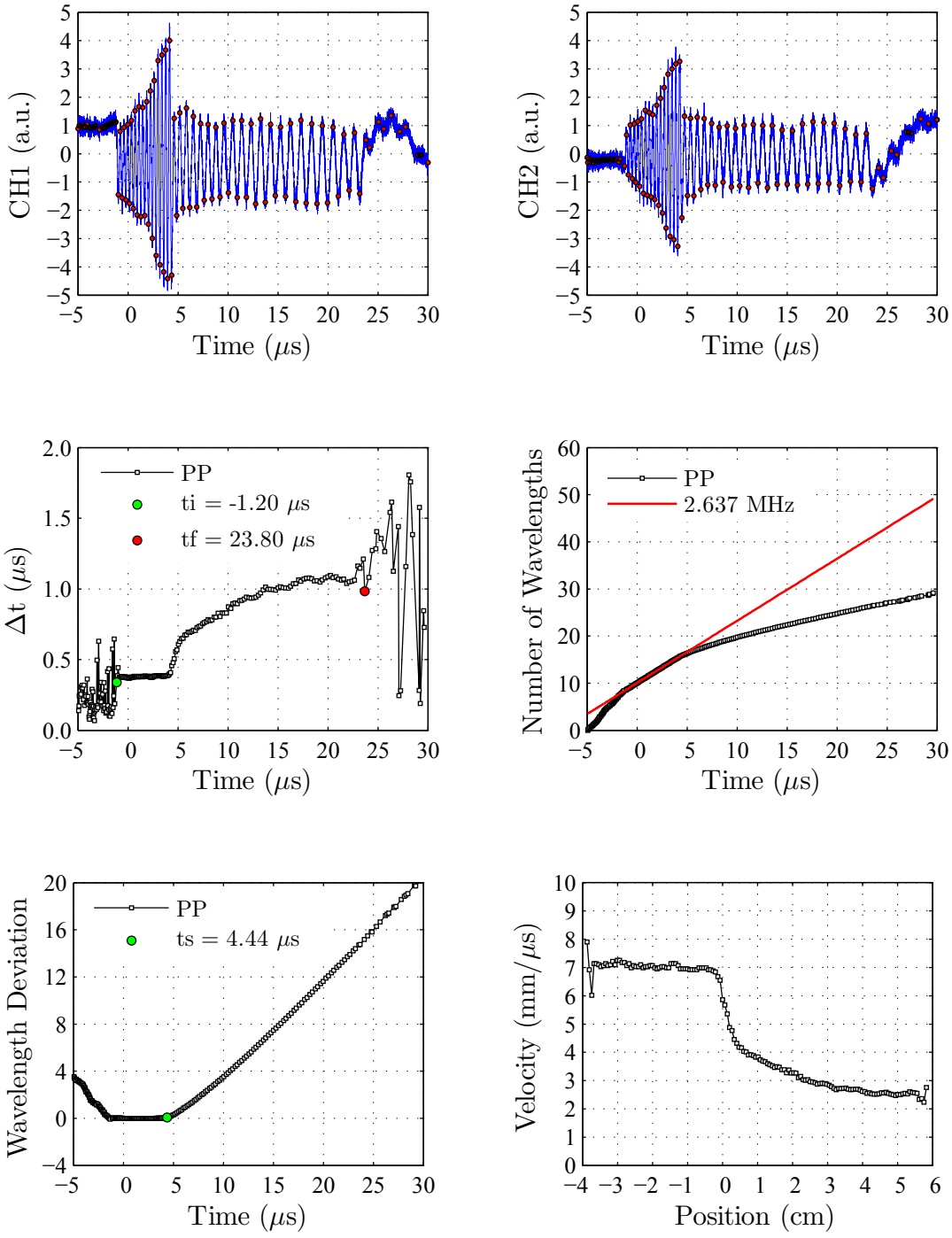

Figure C.7. MI data analysis for shot PVC-2.

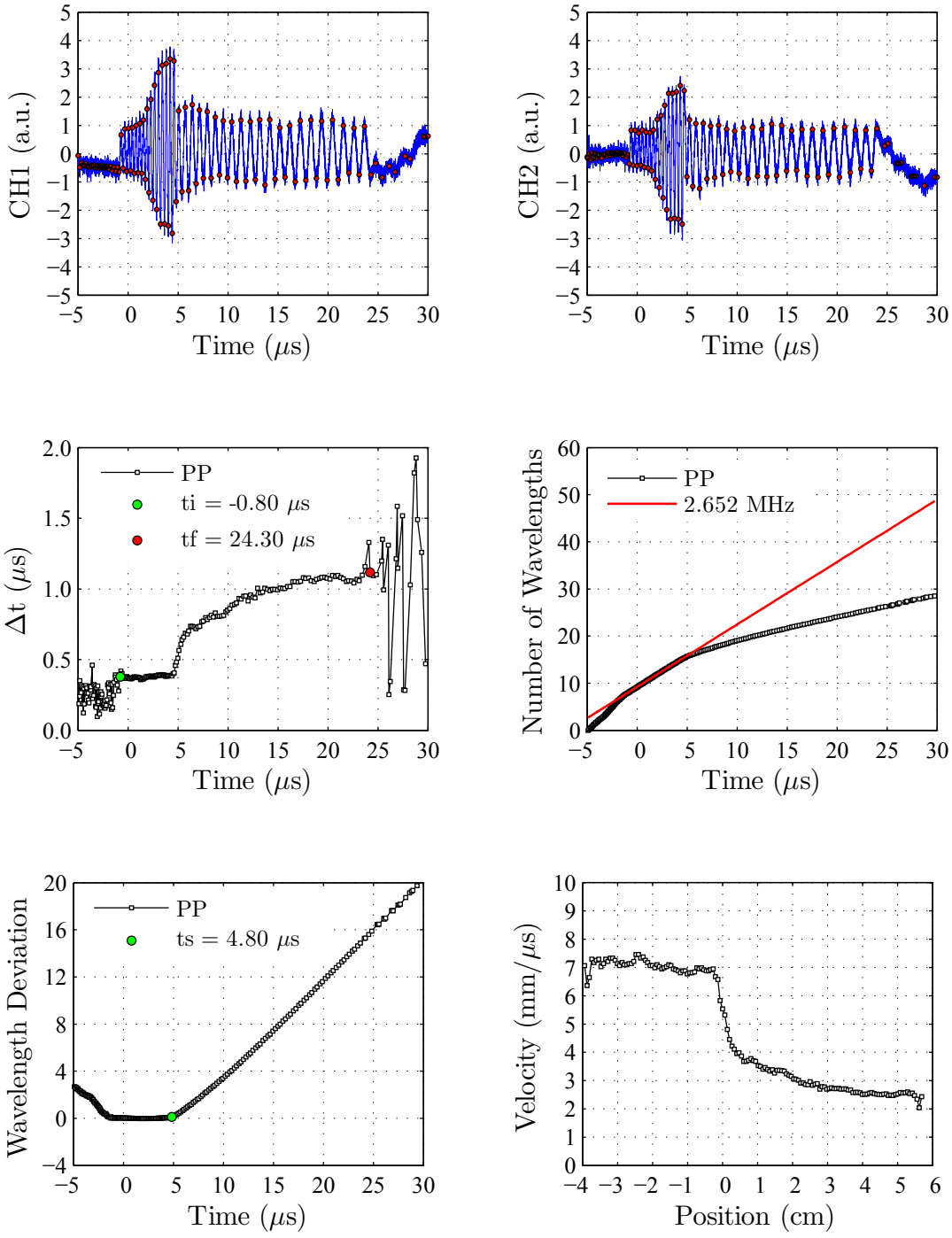

Figure C.8. MI data analysis for shot PVC-3.

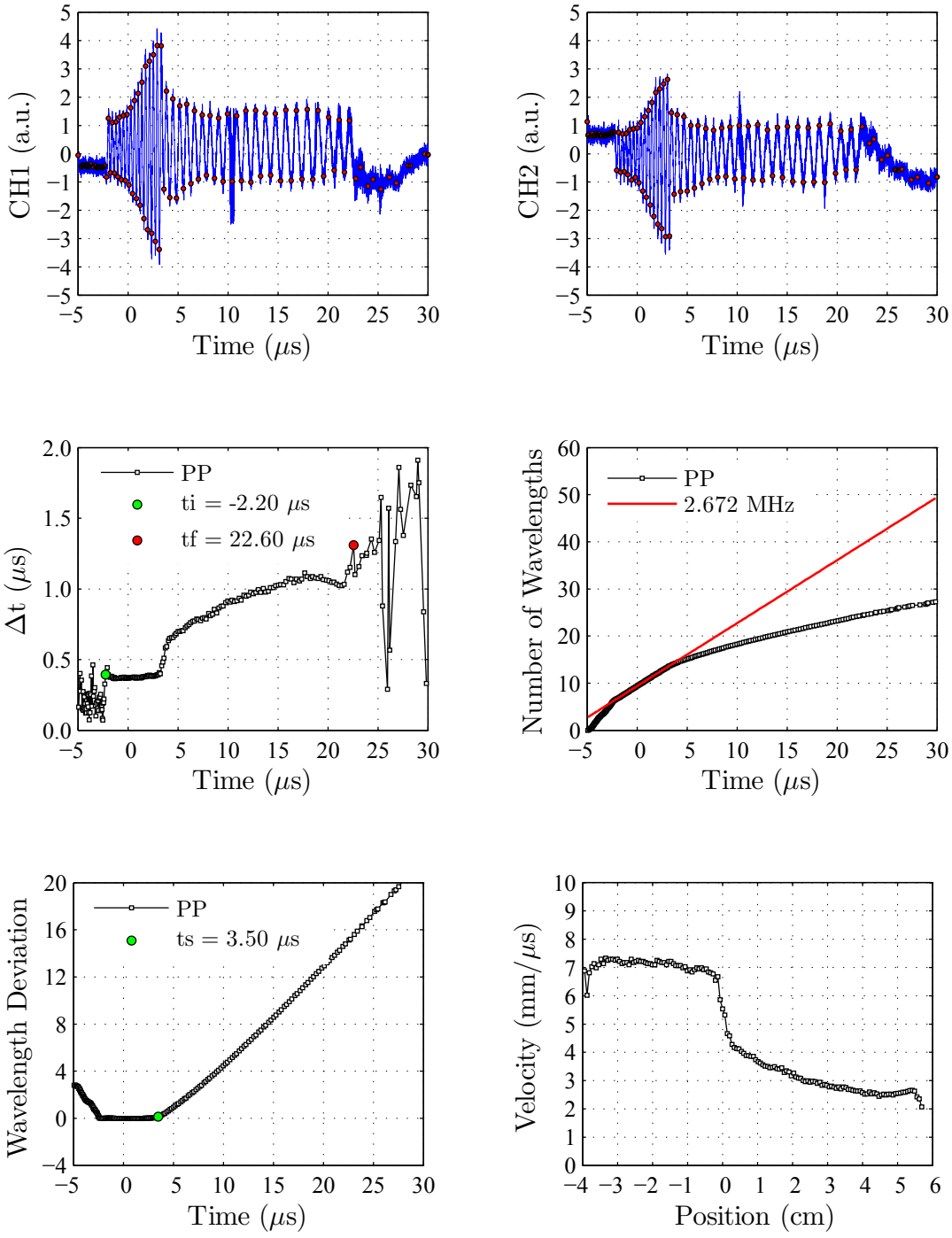

Figure C.9. MI data analysis for shot PVC-4.

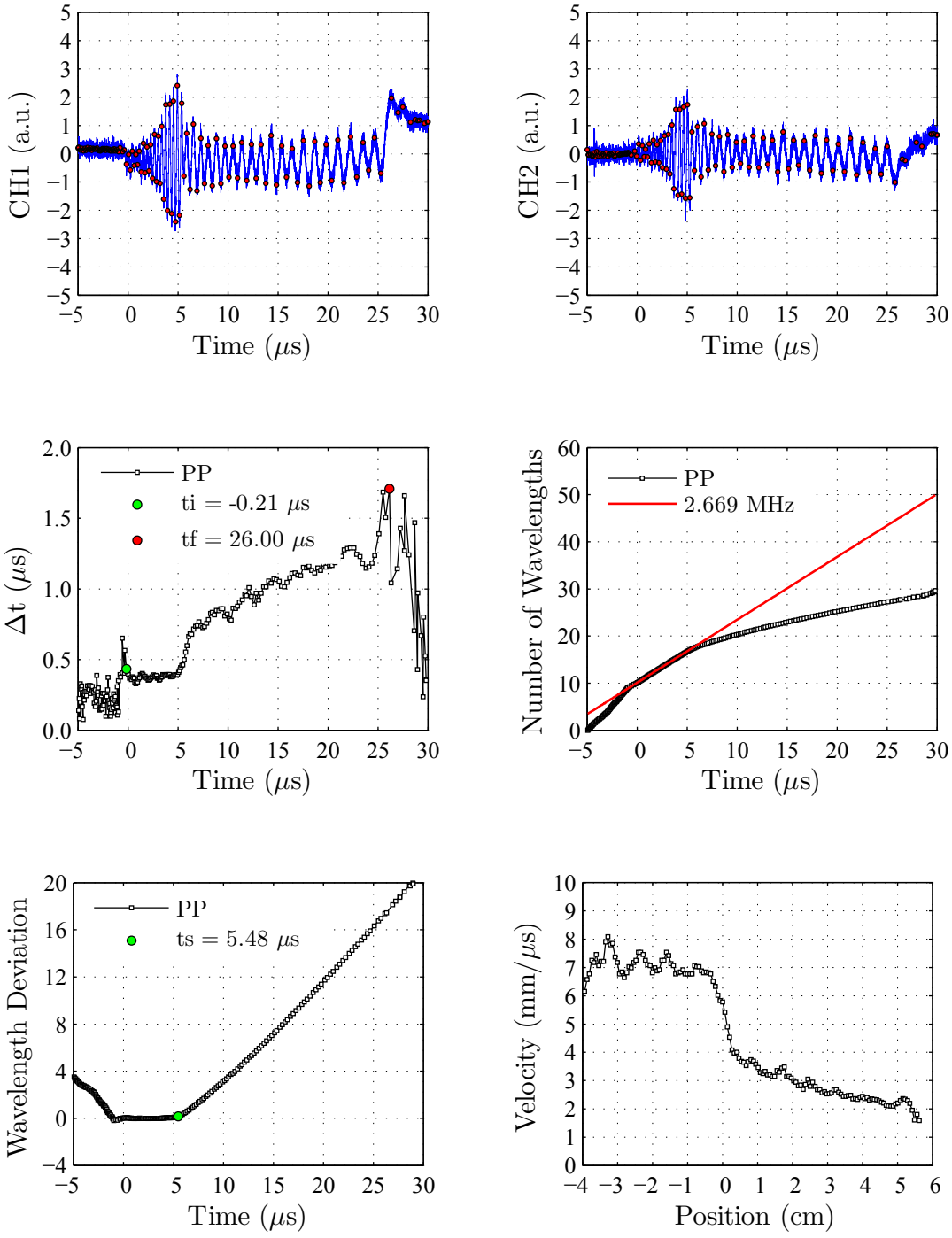

Figure C.10. MI data analysis for shot THN-1.

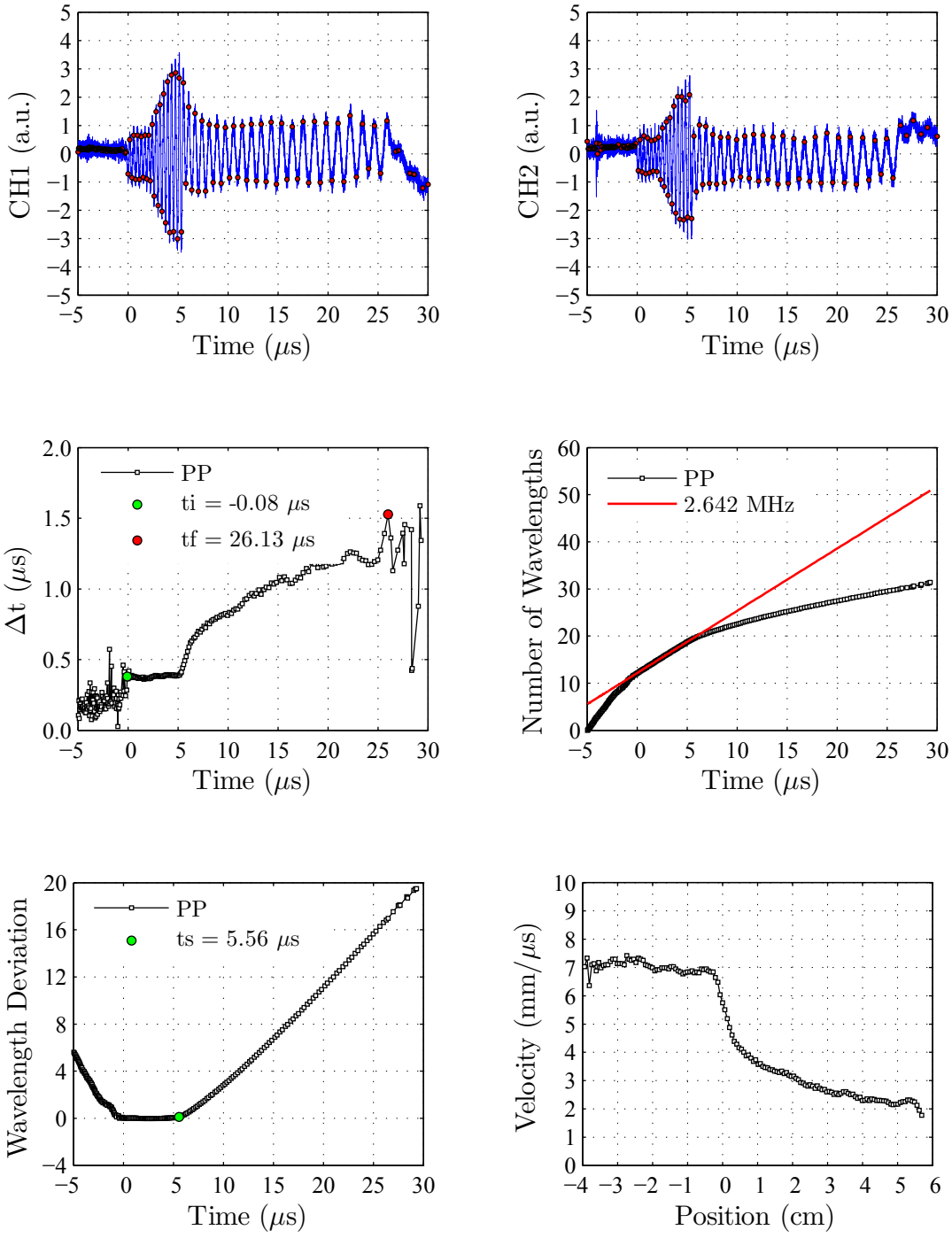

Figure C.11. MI data analysis for shot THN-2.

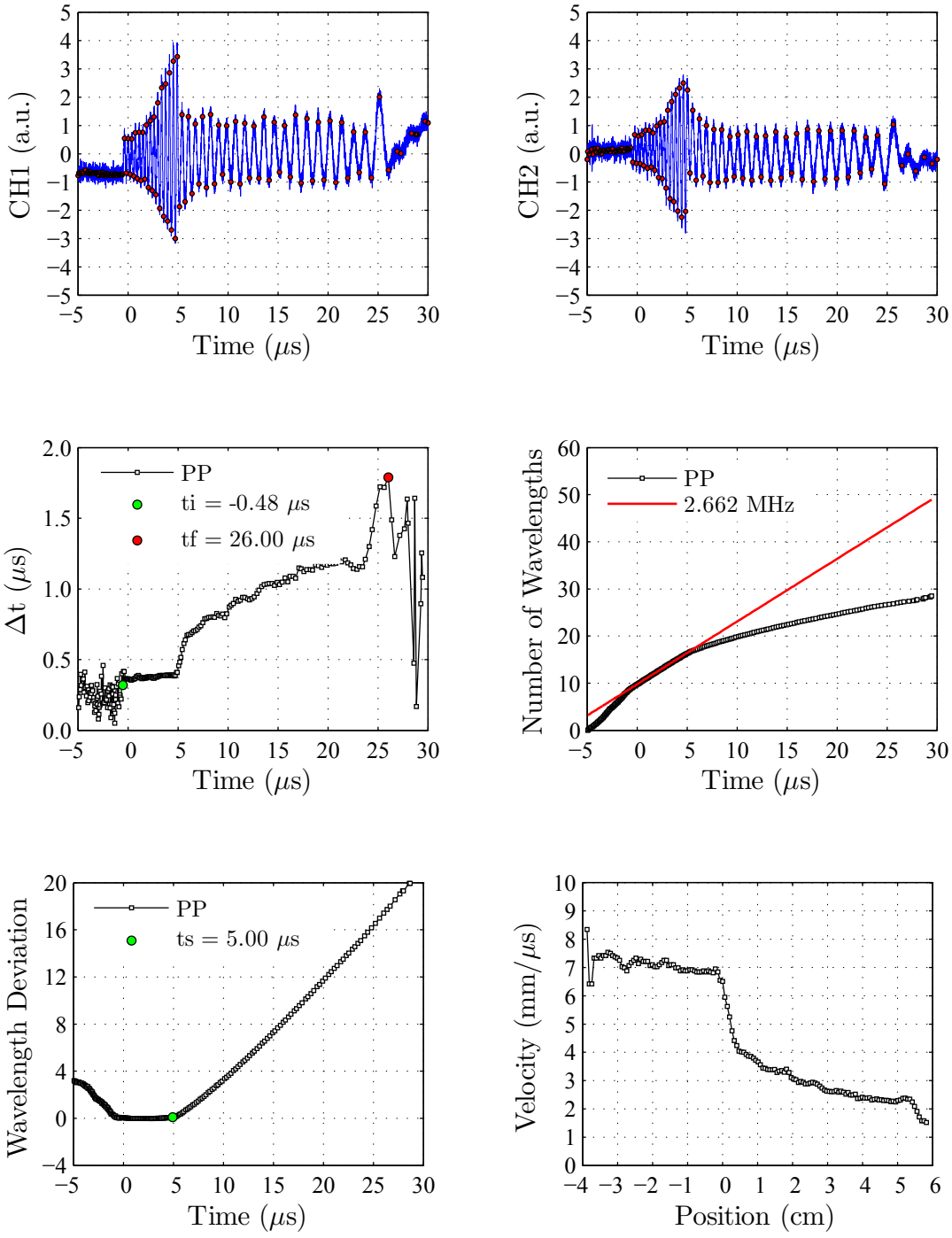

Figure C.12. MI data analysis for shot THN-3.

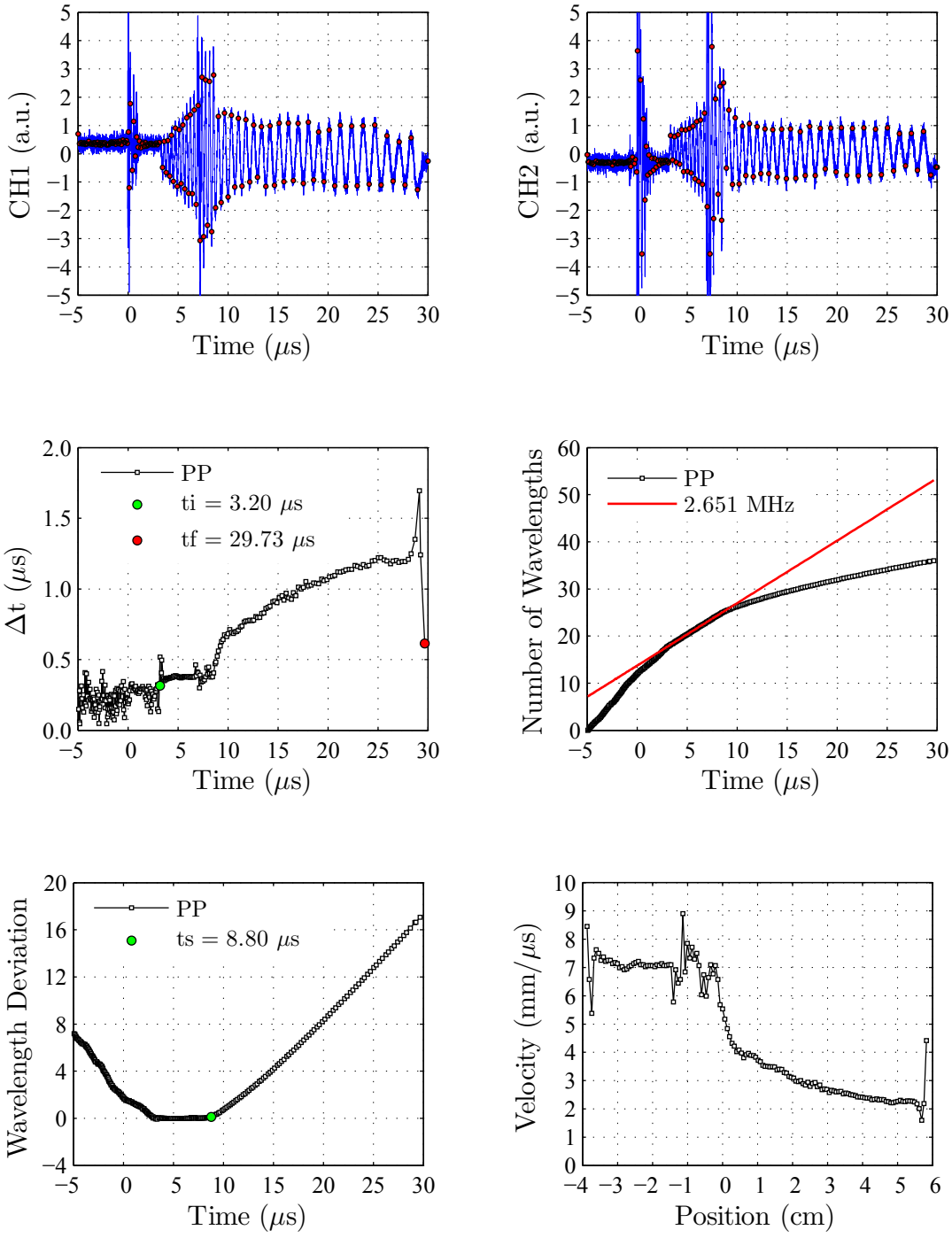

Figure C.13. MI data analysis for shot THN-4.

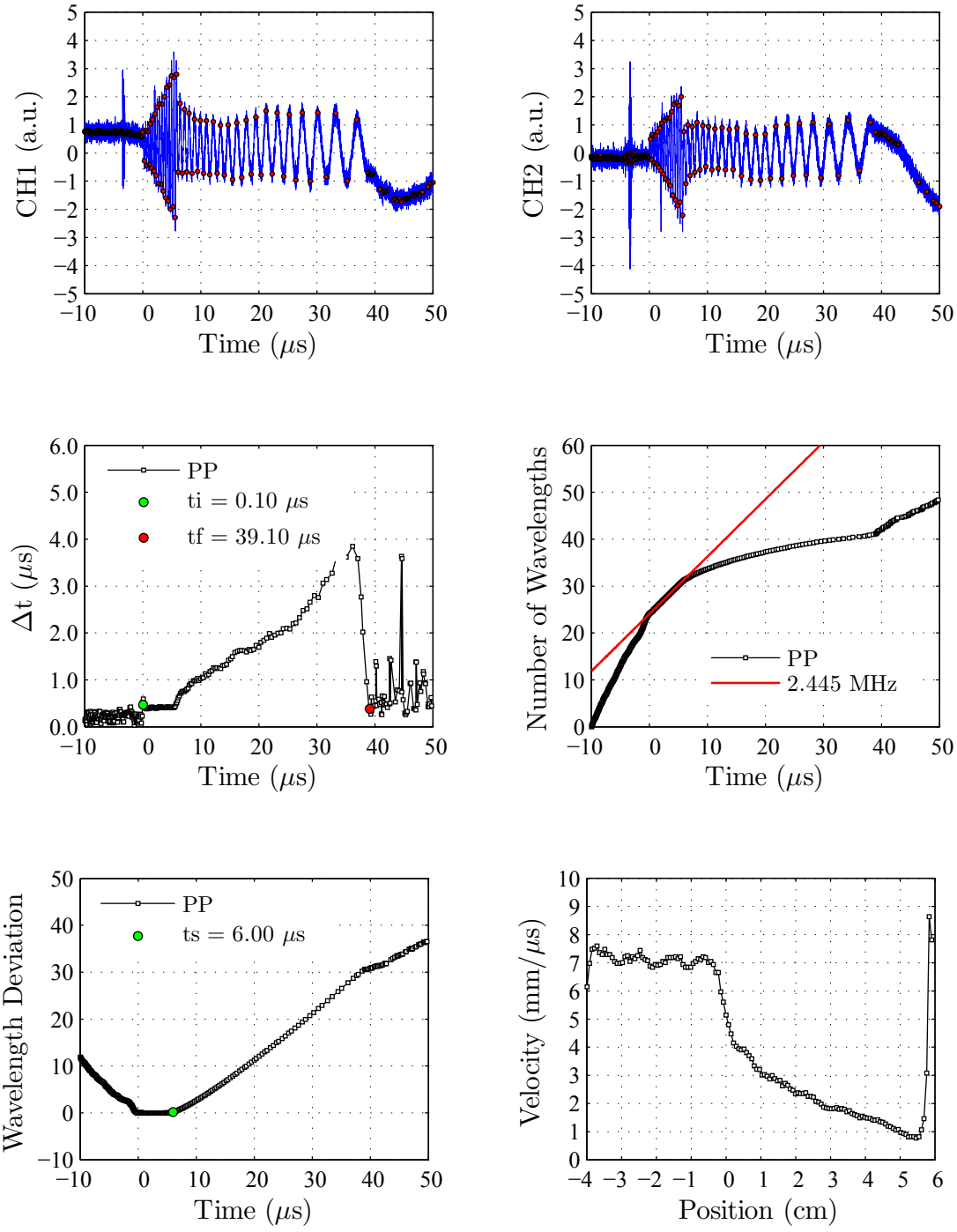

Figure C.14. MI data analysis for shot SM-1.

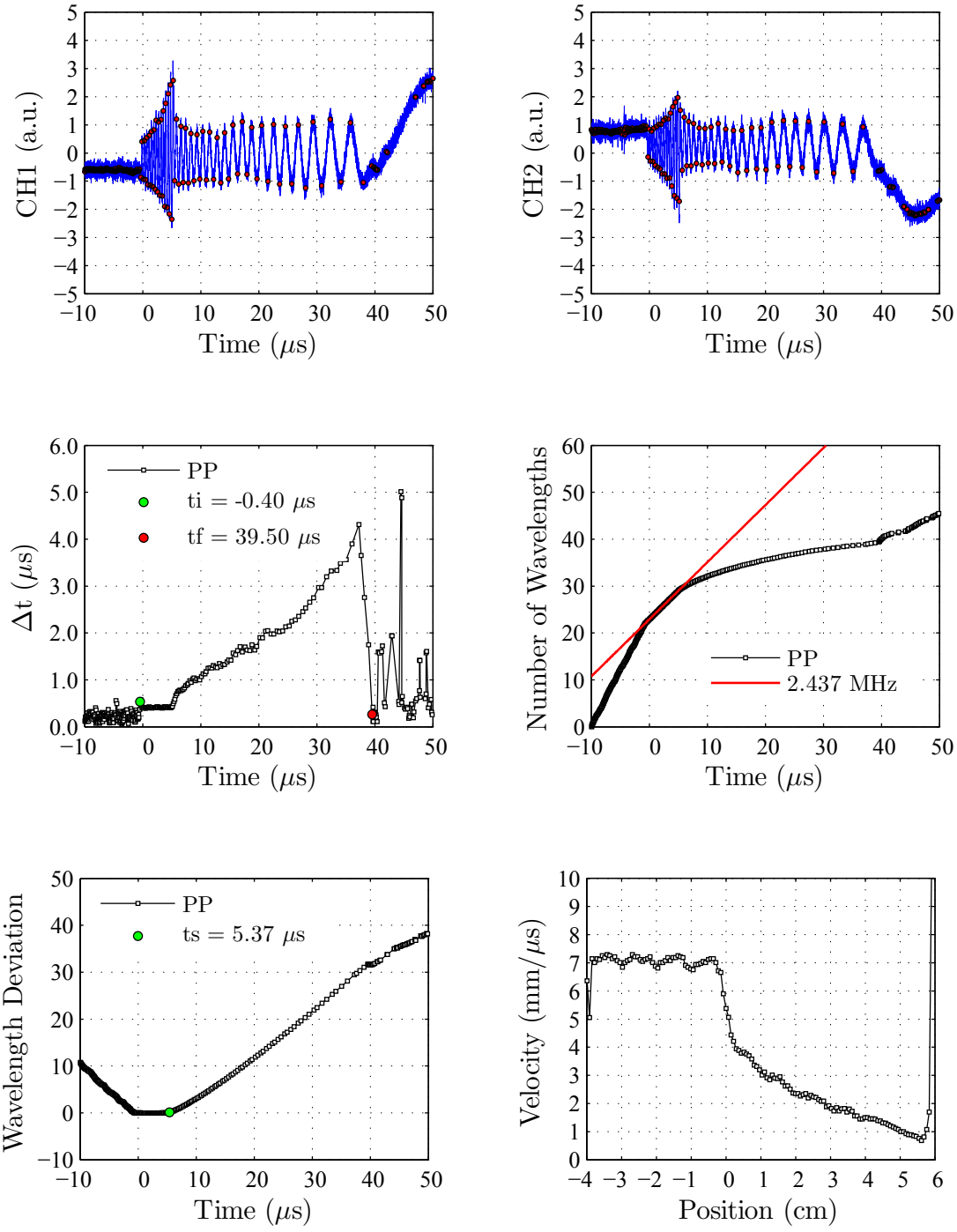

Figure C.15. MI data analysis for shot SM-2.

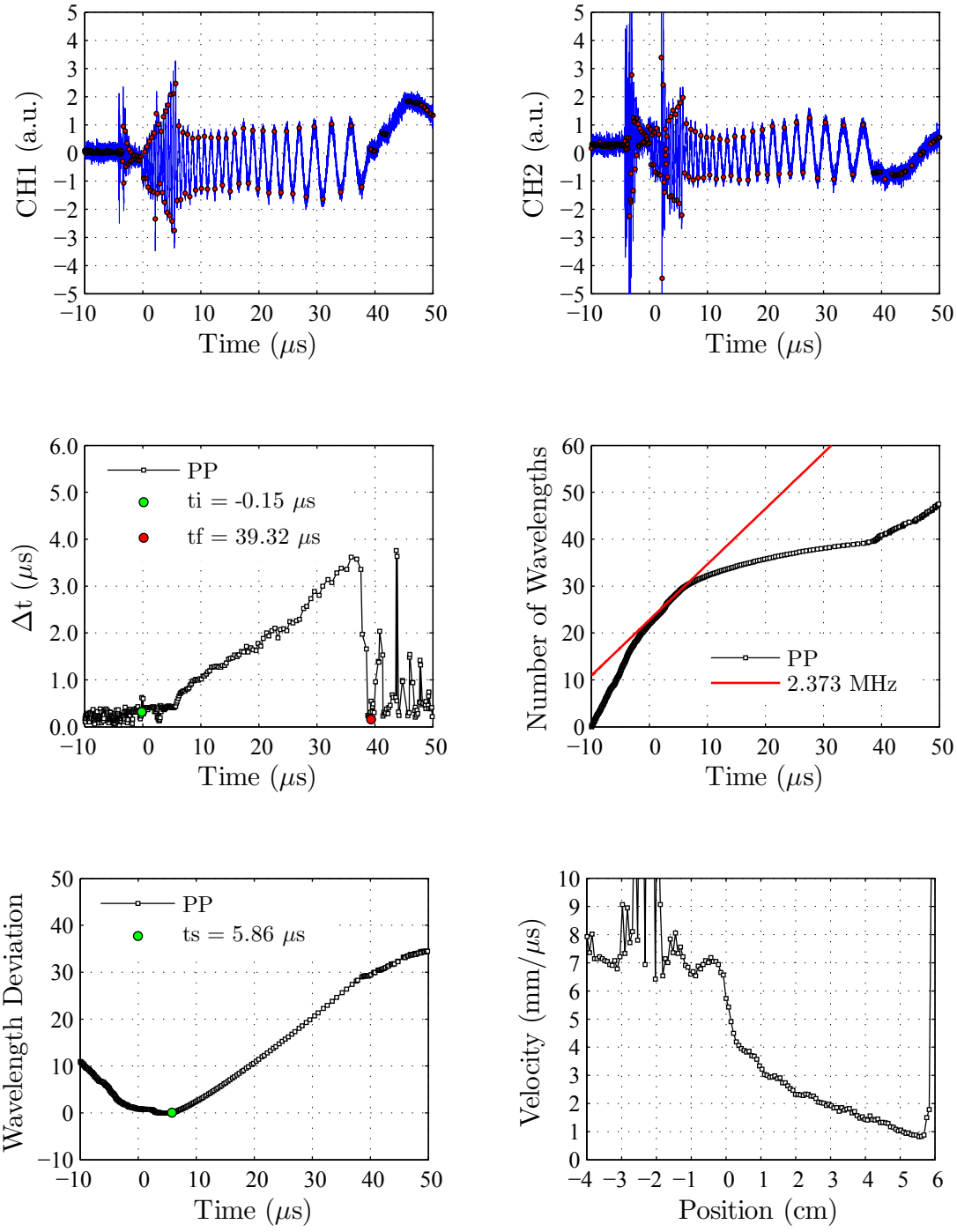

Figure C.16. MI data analysis for shot SM-3.

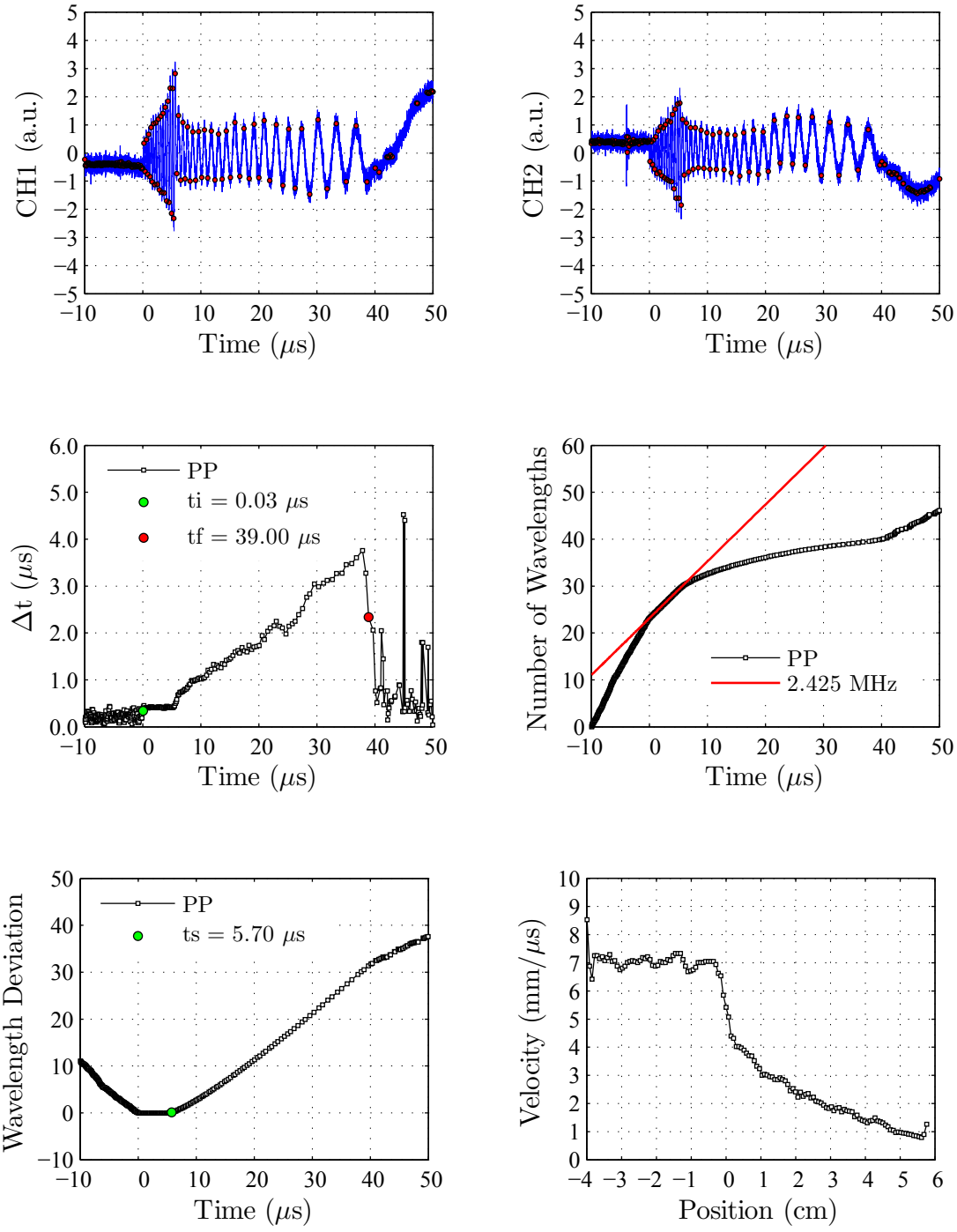

Figure C.17. MI data analysis for shot SM-4.

D. APREPRO MASTER CODE

```
*=====================================================*
*        MICROWAVE INTERFEROMETER EXPERIMENT          *
*                                                     *
*                       v1.1                          *
*                                                     *
*                                                     *
*                                                     *
*   Fully generalized aprepro template to create a CTH *
* input deck for the Purdue M.I. small-scale explosive *
* characterization experiment. Parameter values are    *
* stored in the file params.in so this file should not *
* be modified. The material insertion includes a       *
* numerically heterogeneous density model for ANFO and *
* the user option to generate either 2dc or 3dr        *
* geometries. Send comments to dekitte@sandia.gov.     *
*                                                     *
* Author: D.E. Kittell                                *
*         Fluid and Reactive Processes                *
*         Sandia National Laboratories                *
*         Albuquerque, NM 87185                       *
*                                                     *
* Notes: 08/20/15 created and tested 2dc and 3dr geom. *
*        09/17/15 adapted jwl eos for tiger input     *
*        10/19/15 volume average for reaction progress *
*        11/19/15 added an option to turn on PVC      *
*                                                     *
*     Sandia National Laboratories is a multi-program  *
*     laboratory managed and operated by Sandia        *
*     Corporation, a wholly owned subsidiary of        *
*     Lockheed Martin Corporation, for the U.S.        *
*     Department of Energy's National Nuclear Security *
*     Administration under contract DE-AC04-94AL85000. *
*                                                     *
* =====================================================*
* Aprepro variable definitions
* =====================================================
*
* --------------ADAPTIVE MESH REFINEMENT---------------
*
*     GEOMETRY: {GEOM = "2dc"}
*         MAXL: {AMR_MAXL = 4}
```

```
*         MAXB: {AMR_MAXB = 600}
*   RESOLUTION: {RES=1.25/(12*(2**AMR_MAXL)*100)*1.0e6} um
*
* ----------------------CONTROL-----------------------
*
*   FINAL TIME: {T_STOP = 30} us
*
* ---------------------CONFINER-----------------------
*
*           RI: {RI = 0.5639} cm
*           RO: {RO = 0.6349} cm
*     MATERIAL: {CONFINER = "mgrun 304_SS"}
*     STRENGTH: {STRENGTH = "st 304_SS"}
*
* --------------------PVC OPTIONS---------------------
* Mie-Gruneisen EOS from Otsuka, Tanaka, and Itoh (06)
*
*         PVC: {PVC = "ON"} ("OFF" or "ON")
*          RO: {PVC_R0 = 1.380} g/cc
*          T0: {PVC_T0 = 298} K
*          CS: {PVC_CS = 2.3e5} cm/s
*          S1: {PVC_S1 = 1.47}
*          S2: {PVC_S2 = 0}
*          G0: {PVC_G0 = 0.40}
*          CV: {PVC_CV = 1.0e11} erg/g-eV
*
* -----------------ANFO CUBE DETAILS------------------
*
*         XMIN: {XMIN = 0} cm
*         XMAX: {XMAX = 0.62} cm
*         YMIN: {YMIN = 0} cm
*         YMAX: {YMAX = 0.62} cm
*         ZMIN: {ZMIN = 3.81} cm
*         ZMAX: {ZMAX = 9.53} cm
*         EDGE: {EDGE = 0.07} cm
*           NX: {NX = floor((XMAX-XMIN)/EDGE)}
*           NY: {NY = floor((YMAX-YMIN)/EDGE)}
*           NZ: {NZ = floor((ZMAX-ZMIN)/EDGE)}
*    CUBES/DIA: {floor(2*RI/EDGE)}
*
* ------------------TRACER PLACEMENT-----------------
*
* NUMBER OF TRACERS ALONG THE AXIS: {NTRA_AXIS = 80}
* SPACING BETWEEN AXIAL TRACERS: {TRA_DX = 0.067775} cm
* NUMBER OF TRACERS ACROSS THE RADIUS: {NTRA_RADI = 5}
*
* --------MIE-GRUNEISEN EOS FOR CRYSTALLINE AN----------
*
*           RO: {MGR_R0 = 1.725} g/cc
*           RP: {MGR_RP_LOW  = 0.818} g/cc   (low)
*               {MGR_RP_NOM  = 0.826} g/cc   (nominal)
```

```
*               {MGR_RP_HIGH = 0.834} g/cc   (high)
*           T0: {MGR_T0 = 298} K
*           CS: {MGR_CS = 2.2e5} cm/s
*           S1: {MGR_S1 = 1.96}
*           S2: {MGR_S2 = 0}
*           G0: {MGR_G0 = 1.0}
*           CV: {MGR_CV = 2.5e11} erg/g-eV
*            B: {MGR_B = 0}
*           XB: {MGR_XB = 1}
*           NB: {MGR_NB = 0}
*           PS: {MGR_PS = 1e9}
*         NSUB: {MGR_NSUB = 10}
*
* -----------IGNITION AND GROWTH PARAMETERS-------------
*
*           G0: {IGRB_G0 = 1e6}
*           S0: {IGRB_S0 = 0.222}
*           A0: {IGRB_A0 = 0.2}
*           Y0: {IGRB_Y0 = 4}
*           W0: {IGRB_W0 = 0.5}
*           G1: {IGRB_G1 = 1.5e-4}
*           S1: {IGRB_S1 = 0.222}
*           Q1: {IGRB_Q1 = 0.667}
*           Y1: {IGRB_Y1 = 0.9}
*           W1: {IGRB_W1 = 1}
*           G2: {IGRB_G2 = 0} *disabled
*           S2: {IGRB_S2 = 0} *disabled
*           Q2: {IGRB_Q2 = 0} *disabled
*           Y2: {IGRB_Y2 = 0} *disabled
*           W2: {IGRB_W2 = 1} *disabled
*         NSUB: {IGRB_NSUB = 2}
*
* ------JONES-WILKINS-LEE EOS FOR ANFO PRODUCTS---------
*
* PARAMETERS FOR ANFO
* CHEETAH:
*  com, an, 89.94, micro-glass, 4.73, diesel, 5.33, weight
*  standard run, rho, 0.826
*
*           R0: {JWL_LOW_R0   = 0.818} g/cm^3   (low)
*               {JWL_NOM_R0   = 0.826} g/cm^3   (nominal)
*               {JWL_HIGH_R0  = 0.834} g/cm^3   (high)
*           AG: {JWL_LOW_AG   = 171.8248E+10} dynes/cm^2
*               {JWL_NOM_AG   = 178.4200E+10}
*               {JWL_HIGH_AG  = 185.1488E+10}
*           BG: {JWL_LOW_BG   = 2.7129E+10} dynes/cm^2
*               {JWL_NOM_BG   = 2.8522E+10}
*               {JWL_HIGH_BG  = 2.9934E+10}
*           R1: {JWL_LOW_R1   = 5.9911}
*               {JWL_NOM_R1   = 6.0002}
*               {JWL_HIGH_R1  = 6.0085}
```

```
*           R2: {JWL_LOW_R2   = 2.0000}
*               {JWL_NOM_R2   = 2.0000}
*               {JWL_HIGH_R2  = 2.0000}
*           WG: {JWL_LOW_WG   = 0.3990}
*               {JWL_NOM_WG   = 0.3993}
*               {JWL_HIGH_WG  = 0.3996}
*          PCJ: {JWL_LOW_PCJ  = 4.273E+10} dynes/cm^2
*               {JWL_NOM_PCJ  = 4.367E+10}
*               {JWL_HIGH_PCJ = 4.462E+10}
*          DCJ: {JWL_LOW_DCJ  = 4.488E+05} cm/s
*               {JWL_NOM_DCJ  = 4.522E+05}
*               {JWL_HIGH_DCJ = 4.556E+05}
*          TCJ: {JWL_LOW_TCJ  = 3050.7/11604.5} Electron volts
*               {JWL_NOM_TCJ  = 3049.3/11604.5}
*               {JWL_HIGH_TCJ = 3047.9/11604.5}
*          BRN: {JWL_LOW_BRN  = 0}
*               {JWL_NOM_BRN  = 0}
*               {JWL_HIGH_BRN = 0}
*
* ---------JWL EOS FOR BOOSTER EXPLOSIVE----------------
*
* TIGER CALCULATION FOR THE JWL EOS
*   INPUT > com, petn, 63, egdn, 28, atbc, 9
*   INPUT > jwl, p, 1, rho, 1.44
*
*           R0: {JWL_PS_R0 = 1.44} g/cc
*           AG: {JWL_PS_AG = 7.11306E+12} dynes/cm^2
*           BG: {JWL_PS_BG = 2.78344E+11} dynes/cm^2
*           R1: {JWL_PS_R1 = 5.78156E+0}
*           R2: {JWL_PS_R2 = 1.94145E+0}
*           WG: {JWL_PS_WG = 3.59220E-1}
*          PCJ: {JWL_PS_PCJ = 1.85154E+11} dynes/cm^2
*          DCJ: {JWL_PS_DCJ = 7.09691E+05} cm/s
*          TCJ: {JWL_PS_TCJ = 3.34166E-01} Electron volts
*          BRN: {JWL_PS_BRN = 1}
*
* -----------------SPYMASTER LABELS---------------------
*
*         MAT1: {MAT1_NAME = "ANFO"}
*         MAT2: {MAT2_NAME = "DENS -1%"}
*         MAT3: {MAT3_NAME = "DENS +1%"}
*         MAT4: {MAT4_NAME = "BOOSTER"}
*         MAT5: {MAT5_NAME = "PTFE"}
*         MAT6: {MAT6_NAME = "304_SS"}
*         MAT7: {MAT7_NAME = "PVC"}
*
*********************************************************
*eor* cthin
*********************************************************
{ECHO(OFF)}
```

```
                        % 2dc switch %
                        %------------%
{if(GEOM=="2dc")}
{ECHO(ON)}
2DC SMALL-SCALE DETONATION FAILUE EXPERIMENT FOR ANFO
{ECHO(OFF)}
                        %------------%
                        % 3dr switch %
                        %------------%
{elseif(GEOM=="3dr")}
{ECHO(ON)}
3DR SMALL-SCALE DETONATION FAILUE EXPERIMENT FOR ANFO
{ECHO(OFF)}
{endif}
{ECHO(ON)}
*********************************************************
* control / time step / edit                            *
*********************************************************
control
  mmp0
  tstop={T_STOP*1e-6}
  tbad=1e99
  autorestart
  numbu=3
  matcs=1
  xdtc
  dtstart=1e-10
endc
*
maxdt
  time=0.  dtmax=1.0e-8
endm
*
mindt
  time=0.  dtmin=1.0e-14
endm
*
edit
  shortt
    time=0.  dt=1.0e-7
  ends
  longt
    time=0.  dt=1.0e-6
  endl
  restt
    time=0.  dt=1.0e-2 *not intending to be restarted
  endrest
ende
*********************************************************
* discard input                                         *
*********************************************************
```

```
discard
* Discard material sound speed above 100 km/s
  mat -1 dens=1e99 csl=1.0e7
* Discard negative densities
  mat -1 pressure 1.0e20 dens 0.1e-3
* Discard material above 1.5 eV (17,407 K)
  mat -1 teml 1.5 density 1e99 pressure 1e99
* Discard negative temperatures
  mat -1 temp 1e-3 density 1e99 pressure 1e99
* Discard materials moving faster than 10 km/s
  mat -1 vmage 1.0e6 density 1e99 pressure 1e99
* Discard small flecks
  mat -1 volfract 1e-5 denl 0 dens 1e99 *small flecks
endd
*********************************************************
* adaptive mesh refinement                              *
*********************************************************
{ECHO(OFF)}
                         %------------%
                         % 2dc switch %
                         %------------%
{if(GEOM=="2dc")}
{ECHO(ON)}
amr
  2dc
    debug
    gmin = 0.0, 0.0
    gmax = 1.25, 10.0
    bx = 1
    by = 8
    nx = 12
    ny = 12
    maxl = {AMR_MAXL}
    maxb = {AMR_MAXB}
{ECHO(OFF)}
                         %------------%
                         % 3dr switch %
                         %------------%
{elseif(GEOM=="3dr")}
{ECHO(ON)}
amr
  3dr
    debug
    gmin = 0.0, 0.0, 0.0
    gmax = 1.25, 1.25, 10.0
    bx = 1
    by = 1
    bz = 8
    nx = 12
    ny = 12
    nz = 12
```

```
    maxl = {AMR_MAXL}
    maxb = {AMR_MAXB}
{ECHO(OFF)}
{endif}
{ECHO(ON)}
*
* Indicator that automatically unrefines any cell
* with some void space present. Good when charge
* is surrounded by void instead of air
*
  indicator
    value void
    unrabove -1
  endi
*
* Indicator that refines all materials with
* a density greater than 0.1 g/cc (all materials)
*
  indicator
    value dens
    refabove 0.1
  endi
*
* Allow unrefinement of blocks with the lowest 50%
* of pressure difference and refine blocks with the
* greatest 5% of pressure difference. This indicator
* is good for refining shock and detonation waves.
*
  indicator
    difference P
    loghistogram
    vmin 1e8
    unrbelow 0.5
    refabove 0.95
  endi
enda
*********************************************************
* boundary conditions                                   *
*********************************************************
boundary
  bhy
{ECHO(OFF)}
                        %------------%
                        % 2dc switch %
                        %------------%
{if(GEOM=="2dc")}
{ECHO(ON)}
    bxb=0, bxt=2
    byb=0, byt=2
{ECHO(OFF)}
                        %------------%
```

```
                        % 3dr switch %
                        %------------%
{elseif(GEOM=="3dr")}
{ECHO(ON)}
    bxb=0, bxt=2
    byb=0, byt=2
    bzb=0, bzt=2
{ECHO(OFF)}
{endif}
{ECHO(ON)}
  endh
endb
*********************************************************
* material insertion                                    *
*********************************************************
{ECHO(OFF)}
                        %------------%
                        % 2dc switch %
                        %------------%
{if(GEOM=="2dc")}
{ECHO(ON)}
diatoms
*
  package 'anfo_nom'
    material 1
{ECHO(OFF)}
%=======================================
% 2-D CUBE INSERTION OF NOMINAL DENSITY
%=======================================
{i=0} {j=0}

% step in z-direction ("y-axis")
{Loop(NZ)}
  {j+=1} {i=0}

  % step in x-direction
  {Loop(NX)}
    {i+=1}
    {FLAG=nint(fmod(j,3))} {FLAG=nint(fmod(FLAG,3))}

    % decide which pattern (A, B, or C) to use
    {if((FLAG==0)&&(fmod(i,3)==1))} % Pat.A
      {X1 = (i-1)*EDGE+XMIN}
      {X2 = i*EDGE+XMIN}
    {elseif((FLAG==1)&&(fmod(i,3)==0))} % Pat.B
      {X1 = (i-1)*EDGE+XMIN}
      {X2 = i*EDGE+XMIN}
    {elseif((FLAG==2)&&(fmod(i,3)==2))} % Pat.C
      {X1 = (i-1)*EDGE+XMIN}
      {X2 = i*EDGE+XMIN}
    {else}
```

```
      {X1 = 0}
      {X2 = 0}
    {endif}

    % other coordinates are pattern independent
    {Z1 = (j-1)*EDGE+ZMIN}
    {Z2 = j*EDGE+ZMIN}

    % write only the non-trivial blocks to file
    {if((X1!=X2)&&(X2<=RI))}
      {ECHO(ON)}
    insert box
      p1={X1} , {Z1}
      p2={X2} , {Z2}
  endi
      {ECHO(OFF)}
    {endif}
  {EndLoop}
{EndLoop}
{ECHO(ON)}
  endpackage
*
  package 'anfo_low'
    material 2
{ECHO(OFF)}
%=======================================
% 2-D CUBE INSERTION OF LOW DENSITY
%=======================================
{i=0} {j=0}

% step in z-direction ("y-axis")
{Loop(NZ)}
  {j+=1} {i=0}

  % step in x-direction
  {Loop(NX)}
    {i+=1}
    {FLAG=nint(fmod(j,3))} {FLAG=nint(fmod(FLAG,3))}

    % decide which pattern (A, B, or C) to use
    {if((FLAG==1)&&(fmod(i,3)==1))} % Pat.A
      {X1 = (i-1)*EDGE+XMIN}
      {X2 = i*EDGE+XMIN}
    {elseif((FLAG==2)&&(fmod(i,3)==0))} % Pat.B
      {X1 = (i-1)*EDGE+XMIN}
      {X2 = i*EDGE+XMIN}
    {elseif((FLAG==0)&&(fmod(i,3)==2))} % Pat.C
      {X1 = (i-1)*EDGE+XMIN}
      {X2 = i*EDGE+XMIN}
    {else}
      {X1 = 0}
```

```
      {X2 = 0}
    {endif}

    % other coordinates are pattern independent
    {Z1 = (j-1)*EDGE+ZMIN}
    {Z2 = j*EDGE+ZMIN}

    % write only the non-trivial blocks to file
    {if((X1!=X2)&&(X2<=RI))}
      {ECHO(ON)}
    insert box
      p1={X1} , {Z1}
      p2={X2} , {Z2}
    endi
      {ECHO(OFF)}
    {endif}
  {EndLoop}
{EndLoop}
{ECHO(ON)}
  endpackage
*
  package 'anfo_high'
    material 3
    insert box
      p1=0., {ZMIN}
      p2={RI}, {ZMAX}
    endinsert
  endpackage
*
  package 'booster'
    material 4
    insert box
      p1=0., 0.
      p2={RI}, {ZMIN}
    endinsert
  endpackage
*
  package 'waveguide'
    material 5
    insert box
      p1=0., {ZMAX}
      p2={RI}, 10.
    endinsert
  endpackage
*
  package 'confiner'
    material 6
    insert box
      p1={RI}, 0.
      p2={RO}, 10.
    endinsert
```

```
  endpackage
*
{ECHO(OFF)}
                          %------------%
                          % Insert PVC %
                          %------------%
{if(PVC=="ON")}
{ECHO(ON)}
  package 'pvc'
    material 7
    insert box
      p1={RO}, 0.
      p2=10., 10.
    endinsert
  endpackage
{ECHO(OFF)}
{endif}
{ECHO(ON)}
*
enddiatoms
{ECHO(OFF)}
                          %------------%
                          % 3dr switch %
                          %------------%
{elseif(GEOM=="3dr")}
{ECHO(ON)}
diatoms
*
  package 'anfo_nom'
    material 1
{ECHO(OFF)}
%=======================================
% 3-D CUBE INSERTION OF NOMINAL DENSITY
%=======================================
{i=0} {j=0} {k=0}

% step in z-direction
{Loop(NZ)}
  {k+=1} {j=0}

  % step in y-direction
  {Loop(NY)}
    {j+=1} {i=0}

    % step in x-direction
    {Loop(NX)}
      {i+=1}
      {FLAG=nint(fmod(fmod(j,3)+fmod(k,3),3))}

      % decide which pattern (A, B, or C) to use
      {if((FLAG==0)&&(fmod(i,3)==1))} % Pat.A
```

```
        {X1 = (i-1)*EDGE+XMIN}
        {X2 = i*EDGE+XMIN}
      {elseif((FLAG==1)&&(fmod(i,3)==0))} % Pat.B
        {X1 = (i-1)*EDGE+XMIN}
        {X2 = i*EDGE+XMIN}
      {elseif((FLAG==2)&&(fmod(i,3)==2))} % Pat.C
        {X1 = (i-1)*EDGE+XMIN}
        {X2 = i*EDGE+XMIN}
      {else}
        {X1 = 0}
        {X2 = 0}
      {endif}

      % other coordinates are pattern independent
      {Y1 = (j-1)*EDGE+YMIN}
      {Y2 = j*EDGE+YMIN}
      {Z1 = (k-1)*EDGE+ZMIN}
      {Z2 = k*EDGE+ZMIN}

      % write only the non-trivial blocks to file
 {if((X1!=X2)&&((X2**2)+(Y2**2)<=(RI**2)))}
        {ECHO(ON)}
    insert box
      p1={X1} , {Y1} , {Z1}
      p2={X2} , {Y2} , {Z2}
    endi
        {ECHO(OFF)}
      {endif}
    {EndLoop}
  {EndLoop}
{EndLoop}
{ECHO(ON)}
  endpackage
*
  package 'anfo_low'
    material 2
{ECHO(OFF)}
%=======================================
% 3-D CUBE INSERTION OF LOW DENSITY
%=======================================
{i=0} {j=0} {k=0}

% step in z-direction
{Loop(NZ)}
  {k+=1} {j=0}

  % step in y-direction
  {Loop(NY)}
    {j+=1} {i=0}

    % step in x-direction
```

```
    {Loop(NX)}
      {i+=1}
      {FLAG=nint(fmod(fmod(j,3)+fmod(k,3),3))}

      % decide which pattern (A, B, or C) to use
      {if((FLAG==1)&&(fmod(i,3)==1))} % Pat.A
        {X1 = (i-1)*EDGE+XMIN}
        {X2 = i*EDGE+XMIN}
      {elseif((FLAG==2)&&(fmod(i,3)==0))} % Pat.B
        {X1 = (i-1)*EDGE+XMIN}
        {X2 = i*EDGE+XMIN}
      {elseif((FLAG==0)&&(fmod(i,3)==2))} % Pat.C
        {X1 = (i-1)*EDGE+XMIN}
        {X2 = i*EDGE+XMIN}
      {else}
        {X1 = 0}
        {X2 = 0}
      {endif}

      % other coordinates are pattern independent
      {Y1 = (j-1)*EDGE+YMIN}
      {Y2 = j*EDGE+YMIN}
      {Z1 = (k-1)*EDGE+ZMIN}
      {Z2 = k*EDGE+ZMIN}

      % write only the non-trivial blocks to file
      {if((X1!=X2)&&((X2**2)+(Y2**2)<=(RI**2)))}
        {ECHO(ON)}
    insert box
      p1={X1} , {Y1} , {Z1}
      p2={X2} , {Y2} , {Z2}
    endi
        {ECHO(OFF)}
      {endif}
    {EndLoop}
  {EndLoop}
{EndLoop}
{ECHO(ON)}
  endpackage
*
  package 'anfo_high'
    material 3
    insert cylinder
      ce1=0., 0., {ZMIN}
      ce2=0., 0., {ZMAX}
      r={RI}
    endinsert
  endpackage
*
  package 'booster'
    material 4
```

```
    insert cylinder
      ce1=0., 0., 0.
      ce2=0., 0., {ZMIN}
      r={RI}
    endinsert
  endpackage
*
  package 'waveguide'
    material 5
    insert cylinder
      ce1=0., 0., {ZMAX}
      ce2=0., 0., 10.
      r={RI}
    endinsert
  endpackage
*
  package 'confiner'
    material 6
    insert cylinder
      ce1=0., 0., 0.
      ce2=0., 0., 10.
      r={RO}
      ri={RI}
    endinsert
  endpackage
*
{ECHO(OFF)}
                        %------------%
                        % Insert PVC %
                        %------------%
{if(PVC=="ON")}
{ECHO(ON)}
  package 'pvc'
    material 7
    insert cylinder
      ce1=0., 0., 0.
      ce2=0., 0., 10.
      r=10.
      ri={RO}
    endinsert
  endpackage
{ECHO(OFF)}
{endif}
{ECHO(ON)}
*
enddiatoms
{ECHO(OFF)}
{endif}
{ECHO(ON)}
*********************************************************
* equation-of-state / strength models                   *
```

```
*********************************************************
eos ses=250000
*
  mat1 igrb=user
    g0={IGRB_G0} s0={IGRB_S0} a0={IGRB_A0} y0={IGRB_Y0}
     w0={IGRB_W0}
    g1={IGRB_G1} s1={IGRB_S1} q1={IGRB_Q1} y1={IGRB_Y1}
     w1={IGRB_W1}
    g2={IGRB_G2} s2={IGRB_S2} q2={IGRB_Q2} y2={IGRB_Y2}
     w2={IGRB_W2} nsub={IGRB_NSUB}
    eosur=mgrun=user
      r0={MGR_R0} cs={MGR_CS} s1={MGR_S1} s2={MGR_S2}
      g0={MGR_G0} t0={MGR_T0/11604.5} cv={MGR_CV}
      b={MGR_B} xb={MGR_XB} nb={MGR_NB} rp={MGR_RP_NOM}
      ps={MGR_PS}
    eosrp=jwl=user
      r0={JWL_NOM_R0}
      ag={JWL_NOM_AG} bg={JWL_NOM_BG}
      r1={JWL_NOM_R1} r2={JWL_NOM_R2}
      wg={JWL_NOM_WG}
      pcj={JWL_NOM_PCJ} dcj={JWL_NOM_DCJ}
      tcj={JWL_NOM_TCJ} brn={JWL_NOM_BRN}
*
  mat2 igrb=user
    g0={IGRB_G0} s0={IGRB_S0} a0={IGRB_A0} y0={IGRB_Y0}
     w0={IGRB_W0}

    g1={IGRB_G1} s1={IGRB_S1} q1={IGRB_Q1} y1={IGRB_Y1}
     w1={IGRB_W1}
    g2={IGRB_G2} s2={IGRB_S2} q2={IGRB_Q2} y2={IGRB_Y2}
     w2={IGRB_W2} nsub={IGRB_NSUB}
    eosur=mgrun=user
      r0={MGR_R0} cs={MGR_CS} s1={MGR_S1} s2={MGR_S2}
      g0={MGR_G0} t0={MGR_T0/11604.5} cv={MGR_CV}
      b={MGR_B} xb={MGR_XB} nb={MGR_NB} rp={MGR_RP_LOW}
      ps={MGR_PS}
    eosrp=jwl=user
      r0={JWL_LOW_R0}
      ag={JWL_LOW_AG} bg={JWL_LOW_BG}
      r1={JWL_LOW_R1} r2={JWL_LOW_R2}
      wg={JWL_LOW_WG}
      pcj={JWL_LOW_PCJ} dcj={JWL_LOW_DCJ}
      tcj={JWL_LOW_TCJ} brn={JWL_LOW_BRN}
*
  mat3 igrb=user
    g0={IGRB_G0} s0={IGRB_S0} a0={IGRB_A0} y0={IGRB_Y0}
     w0={IGRB_W0}
    g1={IGRB_G1} s1={IGRB_S1} q1={IGRB_Q1} y1={IGRB_Y1}
     w1={IGRB_W1}
    g2={IGRB_G2} s2={IGRB_S2} q2={IGRB_Q2} y2={IGRB_Y2}
     w2={IGRB_W2} nsub={IGRB_NSUB}
```

```
    eosur=mgrun=user
      r0={MGR_R0} cs={MGR_CS} s1={MGR_S1} s2={MGR_S2}
      g0={MGR_G0} t0={MGR_T0/11604.5} cv={MGR_CV}
      b={MGR_B} xb={MGR_XB} nb={MGR_NB} rp={MGR_RP_HIGH}
      ps={MGR_PS}
    eosrp=jwl=user
      r0={JWL_HIGH_R0}
      ag={JWL_HIGH_AG} bg={JWL_HIGH_BG}
      r1={JWL_HIGH_R1} r2={JWL_HIGH_R2}
      wg={JWL_HIGH_WG}
      pcj={JWL_HIGH_PCJ} dcj={JWL_HIGH_DCJ}
      tcj={JWL_HIGH_TCJ} brn={JWL_HIGH_BRN}
*
  mat4 jwl=user
    r0={JWL_PS_R0}
    ag={JWL_PS_AG} bg={JWL_PS_BG}
    r1={JWL_PS_R1} r2={JWL_PS_R2}
    wg={JWL_PS_WG}
    pcj={JWL_PS_PCJ} dcj={JWL_PS_DCJ}
    tcj={JWL_PS_TCJ} brn={JWL_PS_BRN}
*
  mat5 mgrun PTFE
*
  mat6 {CONFINER}
*
{ECHO(OFF)}
                        %------------%
                        % Insert PVC %
                        %------------%
{if(PVC=="ON")}
{ECHO(ON)}
  mat7 mgrun=user
    r0={PVC_R0} cs={PVC_CS} s1={PVC_S1} s2={PVC_S2}
    g0={PVC_G0} t0={PVC_T0/11604.5} cv={PVC_CV}
{ECHO(OFF)}
{endif}
{ECHO(ON)}
*
ende
*
epdata
*
  matep6 {STRENGTH}
*
endep
*********************************************************
* pre-programmed burn input                             *
*********************************************************
heburn
{ECHO(OFF)}
                        %------------%
```

```
                          % 2dc switch %
                          %------------%
{if(GEOM=="2dc")}
{ECHO(ON)}
  mat = 4
  d = {JWL_PS_DCJ}
  dline = 0,0 to {RI},0
  radius = {2*RES*(1e-4)}
  time = 0.
{ECHO(OFF)}
                          %------------%
                          % 3dr switch %
                          %------------%
{elseif(GEOM=="3dr")}
{ECHO(ON)}
  mat = 4
  d = {JWL_PS_DCJ}
  ddisk = 0,0,0 to {RI},0,0 and 0,{RI},0
  radius = {2*RES*(1e-4)}
  time = 0.
{ECHO(OFF)}
{endif}
{ECHO(ON)}
endh
*********************************************************
* convection options                                    *
*********************************************************
convct
  convection=0
  interface=SMYRA
endconvct
*********************************************************
* record extremum values                                *
*********************************************************
extremum
  maximum
    velocity
    pressure
  endm
  dynamic
ende
*********************************************************
* tracer placement                                      *
*********************************************************
tracer
{ECHO(OFF)}
{SPACING = RI/NTRA_RADI}
                          %------------%
                          % 2dc switch %
                          %------------%
{if(GEOM=="2dc")}
```

```
 {i=0}
  {L1 = ZMIN}
  {L2 = ZMIN + (NTRA_AXIS-1)*TRA_DX}
  {Loop(NTRA_RADI)}
    {i+=1}
    {X1 = (i-1)*SPACING}
    {ECHO(ON)}
  add {X1},{L1} to {X1},{L2} n={NTRA_AXIS}
    {ECHO(OFF)}
  {EndLoop}
                        %------------%
                        % 3dr switch %
                        %------------%
{elseif(GEOM=="3dr")}
  {i=0}
  {L1 = ZMIN}
  {L2 = ZMIN + (NTRA_AXIS-1)*TRA_DX}
  {Loop(NTRA_RADI)}
    {i+=1}
    {X1 = (i-1)*SPACING}
    {ECHO(ON)}
  add {X1*.7071},{X1*.7071},{L1} to {X1*.7071},{X1*.7071},{L2}
n={NTRA_AXIS}
    {ECHO(OFF)}
  {EndLoop}
{endif}
{ECHO(ON)}
endt
*********************************************************
* Using Spymaster User's Guide v5.3 for SPY Syntax     *
*********************************************************
spy

 UserVariable("PGPA","Pressure (GPa)");
 UserVariable("PMAX","Pressure (GPa)");
 UserVariable("LAMBDA","Extent of Rxn");
 UserVariable("ALPHA","Distension");
 UserVariable("VMAX","Velocity (km/s)");

 define PGPA()\{
   variable value;
   value = Get("P");
   return value/(1.0e10);\}

 define PMAX()\{
   variable value;
   value = Get("MAXP");
   return value/(1.0e10);\}

 define LAMBDA()\{
   variable x1, x2, x3, v1, v2, v3;
```

```
 x1 = Get("XRN1");
   x2 = Get("XRN2");
   x3 = Get("XRN3");
   v1 = Get("VOLM+1");
   v2 = Get("VOLM+2");
   v3 = Get("VOLM+3");
   return x1*v1+x2*v2+x3*v3;\}

 define ALPHA()\{
   variable a1, a2, a3, v1, v2, v3;
   a1 = Get("ALPI1");
   a2 = Get("ALPI2");
   a3 = Get("ALPI3");
   v1 = Get("VOLM+1");
   v2 = Get("VOLM+2");
   v3 = Get("VOLM+3");
   return a1*v1+a2*v2+a3*v3;\}

 define VMAX()\{
   variable value;
   value = Get("MXVEL");
   return value/(1.0e5);\}

 PlotTime(0,0.1e-6);

 Save("PGPA,LAMBDA");
 SaveTime(0,0.1e-6);
 SpyTitle("SMALL SCALE DETONATION FAILUE EXPERIMENT");

 SaveHis("POSITION,VMAX,PMAX,LAMBDA,ALPHA");
 SaveTracer(ALL);
 HisTime(0,0.005e-6);

 ImageFormat(1024,1024);

{ECHO(OFF)}
                        %------------%
                        % 2dc switch %
                        %------------%
{if(GEOM=="2dc")}
{ECHO(ON)}

 define main ()
 \{
   pprintf(" PLOT: Cycle=%d, Time=%e, Dt=%e\n",
     CYCLE,TIME,DT);

%================================================
%         Plot2D Mats
%================================================
```

```
 Image("mats");
     XLimits(-1.25,1.25);
     YLimits(0.0,10.0);
     Window(0,0,0.75,1);
     ToggleMats(ON, ON, ON, ON, ON);
     MatColors(YELLOW,GOLD,DARK_ORANGE,DARK_OLIVE_GREEN,
                 PURPLE,DIM_GRAY,DARK_SLATE_GRAY);
     MatNames("{MAT1_NAME}","{MAT2_NAME}","{MAT3_NAME}",
              "{MAT4_NAME}","{MAT5_NAME}","{MAT6_NAME}",
              "{MAT7_NAME}");
     DrawMatLegend("",0.05,0.35,0.2,0.8);
     Label(sprintf("Mats at %6.2f |c03BC|cs",TIME*1e6));
     XBMirror(ON);
     Axes(ON);
     Plot2DMats(0.1);
   EndImage;

%================================================
%         Plot2D PGPA
%================================================

   Image("pres");
     XLimits(-1.25,1.25);
     YLimits(0.0,10.0);
     Window(0,0,0.75,1);
     ColorMapRange(0.001,10,LOG_MAP);
     Label(sprintf("Pressure at %6.2f |c03BC|cs",TIME*1e6));
     XBMirror(ON);
     Axes(ON);
     Plot2D("PGPA");
     DrawColorMap("(GPa)",0.85,0.35,1,0.8);
     ToggleMats(OFF, OFF, OFF, ON, ON);
     Draw2DMatContour();
  EndImage;

%================================================
%         Plot2D Tracer Array
%================================================
%
%   Image("tracer");
%     XLimits(-1.25,1.25);
%     YLimits(0.0,10.0);
%     Window(0,0,0.75,1);
%     ColorMapRange(0.001,10,LOG_MAP);
%     Label(sprintf("Pressure at %6.2f |c03BC|cs",TIME*1e6));
%     XBMirror(ON);
%     Axes(ON);
%     Plot2D("PGPA");
%     DrawColorMap("(GPa)",0.85,0.35,1,0.8);
%     ToggleMats(OFF, OFF, OFF, OFF, OFF, ON);
%     Draw2DMatContour();
```

```
%     Color(BLACK);
%     DrawTracers;
%  EndImage;
%
%=============================================
%         Plot2D LAMBDA
%=============================================

   Image("xrn");
     XLimits(-1.25,1.25);
     YLimits(0.0,10.0);
     Window(0,0,0.75,1);
     ColorMapRange(0.001,1,LOG_MAP);
     Label(sprintf(
        "Extent of Rxn at %6.2f |c03BC|cs",TIME*1E6));
     XBMirror(ON);
     Axes(ON);
     Plot2D("LAMBDA");
     DrawColorMap("   ",0.85,0.35,1,0.8);
     ToggleMats(OFF, OFF, OFF, ON, ON);
     Draw2DMatContour();
   EndImage;

 \}
{ECHO(OFF)}
                        %------------%
                        % 3dr switch %
                        %------------%
{elseif(GEOM=="3dr")}
{ECHO(ON)}

 define main ()
 \{
   pprintf(" PLOT: Cycle=%d, Time=%e, Dt=%e\n",
     CYCLE,TIME,DT);

%=============================================
%         Plot3D Mats
%=============================================
   Image("mats");
     XLimits(-1.25,1.25);
     YLimits(-1.25,1.25);
     ZLimits(0.0,10.0);
     ToggleMats(ON, ON, ON, ON, ON);
     MatColors(YELLOW,GOLD,DARK_ORANGE,DARK_OLIVE_GREEN,
                 PURPLE,DIM_GRAY,DARK_SLATE_GRAY);
     MatNames("{MAT1_NAME}","{MAT2_NAME}","{MAT3_NAME}",
              "{MAT4_NAME}","{MAT5_NAME}","{MAT6_NAME}",
              "{MAT7_NAME}");
     DrawMatLegend("",0.05,0.35,0.2,0.8);
     RotateX(-70);
```

```
 RotateZ(30);
     Label(sprintf("Mats at %6.2f |c03BC|cs",TIME*1e6));
     XBMirror(ON);
     YBMirror(OFF);
     Axes(OFF);
     Plot3DMats;
   EndImage;

%================================================
%         Plot3D confiner to see petals
%================================================

   Image("conf");
     XLimits(-1.25,1.25);
     YLimits(-1.25,1.25);
     ZLimits(0.0,10.0);
     ToggleMats(OFF, OFF, OFF, OFF, OFF, ON,OFF);
     MatColor(6,DIM_GRAY);
     RotateX(-70);
     RotateZ(-120);
     Label(sprintf("Confiner at %6.2f |c03BC|cs",TIME*1e6));
     XBMirror(ON);
     YBMirror(ON);
     Axes(OFF);
     Plot3DMats;
   EndImage;

%================================================
%         Plot3D PGPA
%================================================

   Image("pres");
     XLimits(-1.25,1.25);
     YLimits(-1.25,1.25);
     ZLimits(0.0,10.0);
     RotateX(-70);
     RotateZ(30);
     ColorMapRange(0.001,10,LOG_MAP);
     Label(sprintf("Pressure at %6.2f |c03BC|cs",TIME*1e6));
     XBMirror(ON);
     YBMirror(OFF);
     Axes(OFF);
     Paint3DMat(1,"PGPA");
     Paint3DMat(2,"PGPA");
     Paint3DMat(3,"PGPA");
     Paint3DMat(4,"PGPA");
     Paint3DMat(5,"PGPA");
     Paint3DMat(6,"PGPA");
{ECHO(OFF)}
                        %------------%
                        % Insert PVC %
```

```
                          %------------%
{if(PVC=="ON")}
{ECHO(ON)}
     Paint3DMat(7,"PGPA");
{ECHO(OFF)}
{endif}
{ECHO(ON)}
     DrawColorMap("(GPa)",0.85,0.35,1,0.8);
   EndImage;
%================================================
%         Plot3D Extent of Reaction
%================================================
   Image("xrn");
     XLimits(-1.25,1.25);
     YLimits(-1.25,1.25);
     ZLimits(0.0,10.0);
     RotateX(-70);
     RotateZ(30);
     ColorMapRange(0.001,1,LOG_MAP);
     Label(sprintf(
       "Extent of Rxn at %6.2f |c03BC|cs",TIME*1E6));
     XBMirror(ON);
     YBMirror(OFF);
     Axes(OFF);
     Paint3DMat(1,"XRN1");
     Paint3DMat(2,"XRN2");
     Paint3DMat(3,"XRN3");
     Paint3DMat(4,"XRN1");
     Paint3DMat(5,"XRN1");
     Paint3DMat(6,"XRN1");
{ECHO(OFF)}
                          %------------%
                          % Insert PVC %
                          %------------%
{if(PVC=="ON")}
{ECHO(ON)}
     Paint3DMat(7,"XRN1");
{ECHO(OFF)}
{endif}
{ECHO(ON)}
     DrawColorMap("  ",0.85,0.35,1,0.8);
   EndImage;

 \}
{ECHO(OFF)}
{endif}
{ECHO(ON)}
endspy
*makempeg -fs 0 -fe 1055 -fr 2 -base mats
* Note: sizing is [Umin,Vmin,Umax,Vmax]
*******************************************************
```

E. FORTRAN POST PROCESSING CODE

```
PROGRAM POSTPROC
!**********************************************************************
! PROGRAM POSTPROC (for miexpr_v1 template only)
!
! A refined code to calculate the t-x shock trajectory from CTH hscth
! tracer data. Shock detection based on the motion of the Lagrangian
! gauges. Calculates the instantaneous shock velocity for direct
! comparison to MI data. Only works for the save command:
!
!     SaveHis("POSITION,VMAX,PMAX,LAMBDA,ALPHA");
!
! By D.E.Kittell - October 19, 2015
!**********************************************************************
  IMPLICIT NONE
  INTEGER, PARAMETER :: DP = SELECTED_REAL_KIND(14)
  INTEGER :: i,j,k,EOF,NLINES,NTRACERS,NX,NY,&
    NVARS,CID(7),GVARS,CMAX,C_XPOS,C_YPOS,C_ZPOS,&
    C_ALPH,C_LAMB,C_PMAX,C_VMAX
  CHARACTER (len=30) :: FID,NAME,TEXT,HEADER(300)
  REAL(KIND=DP) :: DTOL,TIME,XPOS,YPOS,ZPOS,ALPH,&
    LAMB,PMAX,VMAX,DT,DY,MOTION,VSHK,LCRIT,LEND,VEL_PS,TCRIT,&
    VSHK_ACT,VDIFF,OBJ
  REAL(KIND=DP), dimension(:), allocatable :: TRIGGER,DATALINE,&
    SHOCKVEL
  REAL(KIND=DP), dimension(:,:), allocatable :: GAUGEPOS,&
    MAXVALUE,AVGVALUE
  LOGICAL :: LOOK
  LOGICAL, dimension(:), allocatable :: SEARCH
  REAL, PARAMETER :: ZERO=0.0D0,HALF=0.5D0,ONE=1.0D0,TWO=2.0D0, &
    THR=3.0D0,FOR=4.0D0,FIV=5.0D0,SIX=6.0D0,SEV=7.0D0,EIG=8.0D0,&
    NIN=9.0D0,TEN=10.0D0,THRTY=30.0D0,&
    PI=3.14159265358979323846264338327 9D0

1030 FORMAT(1x,'Function value =',1x,E23.16)

!*** user-defined settings
  FID = 'hscth'              ! hscth file name (default)
  NY = 80                    ! number of tracers along the charge axis
  NX = 5                     ! number of tracers in the radial dir.
  NTRACERS = NX*NY           ! total number of tracers
  DTOL = 0.02D0              ! reaction threshold to detect shocks
```

```
  VEL_PS = 0.709691D0        ! velocity of pre-programmed burn (cm/mu-s)
  LCRIT = 3.81               ! transition length (cm)
  TCRIT = LCRIT/VEL_PS       ! transition time (mu-sec)
  LEND = LCRIT + TEN         ! farthest tracers to consider

!*** Open file to grab header and number of lines
  OPEN(10,FILE=FID,STATUS='old')
  READ(10,*)
  READ(10,*) HEADER(:)
  READ(10,*)
  EOF = 1
  NLINES = 0
  DO WHILE (EOF.GE.0)
    READ(10,*,IOSTAT=EOF)
    NLINES = NLINES+1
  END DO
  CLOSE(10)
  WRITE(*,*) NLINES,' TIME ENTRIES FOUND FOR'

!** Determine the column ID
  i = 1
  NVARS = 0
  GVARS = 0
  LOOK = .TRUE.
  CID = ZERO*CID
  DO WHILE(LOOK)
    TEXT = HEADER(i)
    j=INDEX(TEXT,".1",.TRUE.)
    k=INDEX(TEXT,".2",.TRUE.)
    IF (j.GT.0) THEN
      NVARS = NVARS+1
      TEXT = TEXT(1:j-1)
      WRITE(*,*) TEXT
      IF (TEXT.EQ."XPOS") THEN
        CID(1) = i
      ELSE IF (TEXT.EQ."YPOS") THEN
        CID(2) = i
      ELSE IF (TEXT.EQ."ZPOS") THEN
        CID(3) = i
      ELSE IF (TEXT.EQ."ALPHA") THEN
        CID(4) = i
      ELSE IF (TEXT.EQ."LAMBDA") THEN
        CID(5) = i
      ELSE IF (TEXT.EQ."PMAX") THEN
        CID(6) = i
      ELSE IF (TEXT.EQ."VMAX") THEN
        CID(7) = i
      END IF
    ELSE IF (k.GT.0) THEN
      LOOK = .FALSE.
    ELSE
      WRITE(*,*) TEXT
      GVARS = GVARS+1
    END IF
    i = i+1
  END DO
  WRITE(*,*) GVARS, ' GLOBAL VARIABLES'
  WRITE(*,*) NVARS, ' TRACER VARIABLES'
  WRITE(*,*) NTRACERS, ' TRACERS TOTAL'
```

```
  WRITE(*,*) '  '
  WRITE(*,*) 'THE VARIABLE COLUMN INDEX IS:'
  WRITE(*,*) CID
  WRITE(*,*) '  '

!*** Initialization
  CMAX = NVARS*NTRACERS+GVARS
  ALLOCATE(DATALINE(CMAX),GAUGEPOS(3,NY),TRIGGER(NY),&
    MAXVALUE(4,NY),AVGVALUE(4,NY),SEARCH(NY),&
    SHOCKVEL(NY))
  DATALINE = ZERO*DATALINE
  GAUGEPOS = ZERO*GAUGEPOS
  TRIGGER  = ZERO*TRIGGER
  AVGVALUE = ZERO*AVGVALUE
  MAXVALUE = ZERO*MAXVALUE
  SHOCKVEL = ZERO*SHOCKVEL
  SEARCH(:) = .TRUE.
  WRITE(*,*) 'INITIALIZATION COMPLETE!'

!*** Open hscth file and discard first 3 header lines
  OPEN(20,FILE=FID,STATUS='old')
  READ(20,*)
  READ(20,*)
  READ(20,*)

  ! outer loop 'i' over time
  DO,i=1,NLINES,1

    ! read line in from hscth file
    READ(20,*,IOSTAT=EOF) DATALINE(:)
    TIME = DATALINE(1)
    WRITE(*,*) "READING TIME ",TIME*1.0D6," MU-SEC"

    ! inner loop 'j' over tracers
    AVGVALUE = ZERO*AVGVALUE
    DO,j=1,NTRACERS,1

      ! values for gauge 'j'
      C_XPOS = NVARS*(j-1)+CID(1)
      C_YPOS = NVARS*(j-1)+CID(2)
      C_ALPH = NVARS*(j-1)+CID(4)
      C_LAMB = NVARS*(j-1)+CID(5)
      C_PMAX = NVARS*(j-1)+CID(6)
      C_VMAX = NVARS*(j-1)+CID(7)

      XPOS = DATALINE(C_XPOS)
      YPOS = DATALINE(C_YPOS)
      ALPH = DATALINE(C_ALPH)
      LAMB = DATALINE(C_LAMB)
      PMAX = DATALINE(C_PMAX)
      VMAX = DATALINE(C_VMAX)

      ! if time zero then record initial gauge position
      ! use values along the center axis only j<=NY
      IF ((i.EQ.1).AND.(j.LE.NY)) THEN
        IF (CID(2).GT.ZERO) THEN
          GAUGEPOS(2,j) = DATALINE(C_YPOS)
        END IF
        MAXVALUE(1,j) = TEN !* initialize distension
```

```
      END IF

      ! average across the diameter
      IF (j.GT.NY) THEN
        k = MOD(j,NY)
        IF (k.EQ.0) THEN
          k = NY
        END IF
      ELSE
        k = j
      END IF
      AVGVALUE(1,k) = AVGVALUE(1,k) + ALPH/NX
      AVGVALUE(2,k) = AVGVALUE(2,k) + LAMB/NX
      AVGVALUE(3,k) = AVGVALUE(3,k) + PMAX/NX
      AVGVALUE(4,k) = AVGVALUE(4,k) + VMAX/NX
    END DO

!=======================================================
!     FIND GLOBAL EXTREMUMS

    DO,k=1,NY,1
      ALPH = AVGVALUE(1,k)
      LAMB = AVGVALUE(2,k)
      PMAX = AVGVALUE(3,k)
      VMAX = AVGVALUE(4,k)

      IF (ALPH.LT.MAXVALUE(1,k)) THEN
        MAXVALUE(1,k) = ALPH
      ENDIF
      IF (LAMB.GT.MAXVALUE(2,k)) THEN
        MAXVALUE(2,k) = LAMB
      ENDIF
      IF (PMAX.GT.MAXVALUE(3,k)) THEN
        MAXVALUE(3,k) = PMAX
      ENDIF
      IF (VMAX.GT.MAXVALUE(4,k)) THEN
        MAXVALUE(4,k) = VMAX
      ENDIF

!=======================================================
!     SHOCK WAVE PASSAGE

      IF (SEARCH(k)) THEN
        IF (MAXVALUE(2,k).GT.DTOL) THEN
          TRIGGER(k) = TIME
          SEARCH(k) = .FALSE.
        END IF
      END IF
    END DO
  END DO
  CLOSE(20)

!=======================================================
!     CENTRAL DIFFERENCE METHOD FOR VELOCITY
  DO,i=2,NY-1,1
    DY = GAUGEPOS(2,i+1)-GAUGEPOS(2,i-1)
    DT = TRIGGER(i+1)-TRIGGER(i-1)
    IF ((DY.EQ.ZERO).OR.(DT.EQ.ZERO)) THEN
      SHOCKVEL(i) = ZERO
```

```
    ELSE
      SHOCKVEL(i) = DY/DT
    ENDIF
  ENDDO
  SHOCKVEL(1) = SHOCKVEL(2)
  SHOCKVEL(NY) = SHOCKVEL(NY-1)

!=========================================================
!     OUTPUT FILES

!*** Output to trajectory file
  OPEN(60,FILE='shock.txt',ACTION='write',STATUS='replace',FORM='formatted')
  WRITE(60,*) &
  "   POS (CM)    ","   TIME (US)   ","   P_SH (GPA)  ",&
  "   UP (KM/SEC) ","   US (KM/SEC) ","   RXN PROGRESS",&
  "   DISTENSION  "
  DO,j=1,NY,1
    TIME = TRIGGER(j)
    YPOS = GAUGEPOS(2,j)
    ALPH = MAXVALUE(1,j)
    LAMB = MAXVALUE(2,j)
    PMAX = MAXVALUE(3,j)
    VMAX = MAXVALUE(4,j)
    VSHK = SHOCKVEL(j)
    WRITE(60,'(7(1pe15.5))') &
      YPOS-LCRIT,TIME*1.0D6-TCRIT,PMAX,VMAX,VSHK*1.0D-5,LAMB,ALPH
  END DO
  CLOSE(60)

!=========================================================
!     COMPARE TO MI DATA

!*** Read in data from file and output velocity difference

OPEN(70,FILE='compare.txt',ACTION='write',STATUS='replace',FORM='formatted')
  WRITE(70,*) &
  "   POS (CM)    ","   VSHK (CTH)  ","   VSHK (MI)   ",&
  "   VDIFF       "

  OBJ = ZERO
  OPEN(30,FILE='mi_vel.dat',STATUS='old')
  READ(30,*)

!*** Compute the objective function
  DO,i=1,NY,1
    READ(30,*) YPOS,VSHK_ACT
    VSHK = SHOCKVEL(i)*1.0D-5
    VDIFF = ABS(VSHK-VSHK_ACT)
    WRITE(70,'(4(1pe15.5))') YPOS,VSHK,VSHK_ACT,VDIFF
    OBJ = OBJ + (ONE-VSHK/VSHK_ACT)**2
  END DO
  OBJ = SQRT(OBJ/27.0D0)
  CLOSE(30)
  CLOSE(70)

!*** Write fitness result to file
  OPEN(80,FILE='inp.out',STATUS='replace',FORM='formatted')
  WRITE(80,1030) OBJ
  CLOSE(80)

END PROGRAM POSTPROC
```

F. PRESENTATION SLIDES

The following slides were presented at an oral defense of the dissertation. The final examination was held on Wednesday, January 20th, 2016, in the auditorium of Chaffee Hall. The content of the slides was limited to a 1-hour presentation, so only the most recent work surrounding the MI experimental results and modeling effort was discussed in detail.

PURDUE ENGINEERING

PURDUE UNIVERSITY ZUCROW LABS ENERGETICS LABORATORY

Analysis and Simulation of Small Scale Microwave Interferometer Experiments on Non-Ideal Explosives

Presenter David E. Kittell
Major Professor Dr. Steven F. Son

School of Mechanical Engineering, Purdue University, West Lafayette, IN, USA
Wednesday, January 20 at 10:00 AM
Chaffee Hall Auditorium

1

Previous Work

- Study of wavelet analysis applied to microwave interferometry (MI)
  - Compared two time-frequency analysis techniques in a recent journal publication by Kittell *et al.* [1]
- Development of a thermodynamically complete equation-of-state (EOS) for hot spot temperature predictions
  - Results to appear in a journal publication by Kittell *et al.* [2]
  - Wrote EOS routines for Sandia National Laboratory CTH hydrocode
- Further details may be found in the dissertation

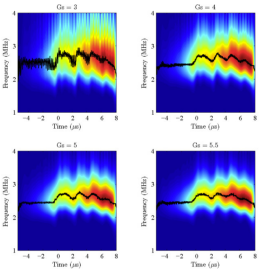

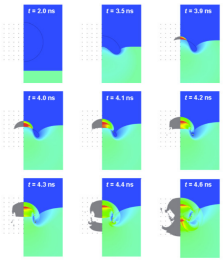

2

Motivation

- Greater understanding of homemade explosives (HMEs)
  - Wide range of sample composition, density, confinement, etc…
  - Lack of detailed experimental data for most HMEs
  - Challenging system to model
- Simulate the threat from improvised explosive devices (IEDs)

Oklahoma City Bombing
April 19, 1995

4800 lb truck bomb
= ammonium nitrate + nitromethane + diesel fuel

New analysis capabilities for investigators…

Toulouse, France
September 21, 2001
- About 200-300 tons of ammonium nitrate detonated at a fertilizer plant (cause unknown)

And accidents too!

3

Background for Explosives Testing

- Explosives are tested to determine their safety and performance
  - Determine a minimum threshold to initiate a detonation
  - Measure detonation velocity, pressure, and TNT equivalent
  - More advanced tests for the performance of explosive devices
- Wide range of HME compositions makes large scale testing prohibitive
  - Stoichiometry, particle size, initial density, confinement, etc…
  - Large scale tests typically require > 100 g of material [3]
  - Some tests require the explosive to be machined or cast
- Small scale tests [3-6] are limited by the large failure diameter of many HMEs
  - Critical to have model support for interpretation of results
  - Scalability of small scale results is largely unknown

4

Background for Microwave Interferometry

- Microwave interferometry (MI) is an established technique to measure shock and detonation velocities
  - Origins from WWII and the dawn of radar
- Reflections occur due to dielectric discontinuities such as a shock wave or a highly ionized reaction front [7-8]

Timeline of Major Publications

Koch (1953)
Cawsey (1958)
Cole (1965)
Alkidas (1974)
Strand (1980)
McCall (1985)
Anicin (1986)
Krall (1993)
Bel'skii (2011)

Frequency bands that have been used

Band	Frequency Range	Wavelength
S	2-4 GHz	decimeter
C	4-8 GHz	
X	8-12 GHz	centimeter
K_u	12-18 GHz	
K	18-27 GHz	
K_a	27-40 GHz	
V	40-75 GHz	millimeter
W	75-110 GHz	

5

Background for Microwave Interferometry

- Reflections from compaction and detonation waves
  - Each displacement in phase by 2π corresponds to a displacement of the moving surface by one-half wavelength [9]

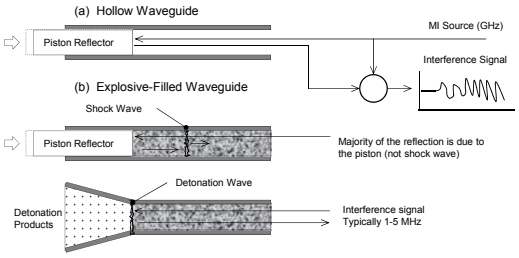

$$v(t) = \frac{\lambda_g}{2} f(t)$$

Example of two-channel MI output

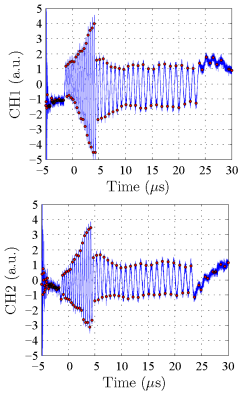

Data analysis may be performed in a variety of ways as shown by Kittell *et al.* [1]

6

Background for Detonation Theory Pt.1

- A Hugoniot is the set of all possible states that matter can obtain across a shock wave from an initial state

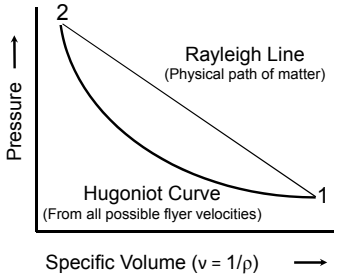

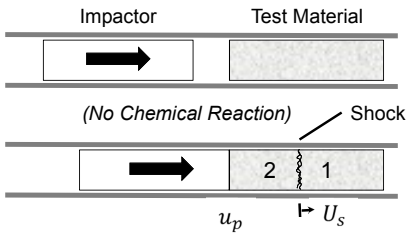

Conservation of Mass	Hugoniot Pressure (State 2)	Hugoniot Energy (State 2)
$1 - \rho_0 v = \frac{u_p}{U_s}$	$p_H = p_0 + \frac{{u_p}^2}{v_0 - v}$	$e_H = e_0 + (v_0 - v)\, p_0 + \frac{1}{2}{u_p}^2$

7

Background for Detonation Theory Pt.2

- Theory of detonation by Chapman (1899) and Jouguet (1905)

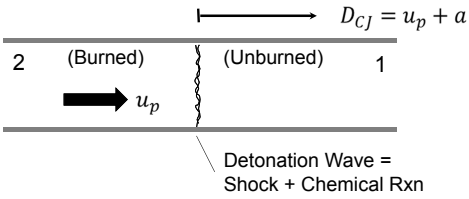

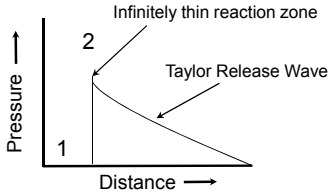

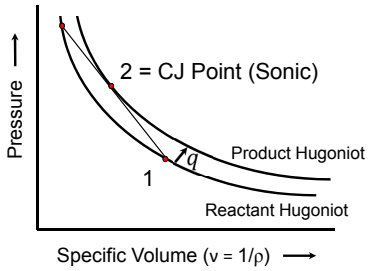

CJ Detonation Calculations

1. Initial conditions
2. Equation-of-state (EOS) for products e.g. BKW and JCZS2i [10,11]
3. Heat of detonation

8

Background for Real Detonation Phenomena

- Radial flow divergence and finite rate chemistry
  - Shock front curvature not considered in CJ theory
  - Subsonic regions cannot propagate energy upstream
  - Kinetics slower than the timescale of a shock wave
- Spectrum of non-ideal behavior
  - Large critical diameters needed to support a detonation wave
  - Thick reaction zones (partially subsonic)
  - Reaction is affected by the confinement
- Transient phenomena
  - Shock-to-detonation transition (SDT)
  - Deflagration-to-detonation transition (DDT)
  - Overdriven detonation (pressure mismatch)
  - Corner turning and dead zone formation
  - Cook off
  - Etc…

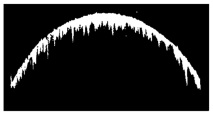

Streak camera imaging for a non-ideal explosive confined by cardboard from Ref. [12]

9

Research Questions

- Can small scale MI tests be used to infer large scale performance?
  - Does the data scale?
  - What mechanisms are relevant to the observed results?
  - Are there any limits for a minimum sample size?
  - What kind of confinement should the experiments have?
- Is it possible to model the small scale MI data with a reactive burn model?
  - Is the MI data useful for model calibration or validation?
  - Are the simulations relevant?
  - Are the physics correct?
  - Is the model robust?

10

Objectives

- Experimental
  - Vary charge diameter, confiner thickness and sound speed to tailor the behavior of overdriven failing detonation waves
  - Investigate a baseline non-ideal explosive that is well characterized with a uniform composition
- Computational
  - Calibrate a reactive burn model based on the theory of ignition and growth
  - Determine if ignition and growth is relevant to the MI tests
  - Minimize the number of free model parameters with physically-based assumptions
  - Explore ways to make the model numerically robust
  - Use the calibrated model to predict additional experiments

11

Materials Used

Ammonium nitrate plus fuel oil (ANFO)

- Performance factors
  - Particle morphology
  - Initial density
  - Equivalence ratio
  - AN pore size
  - wetted surface area
- Typical properties [10]
  - Composition ~6% fuel oil ~94% AN
  - Density range 0.8 to 1.0 g/cm^3
  - Detonation velocity 3.5 to 5.5 km/s
  - Unconfined failure diameter ~8 cm
- Baseline formulation "ANFO KP-1"

Constituent	Weight %
ammonium nitrate	89.94
glass micro-balloons	4.73
diesel fuel (Marathon)	5.33

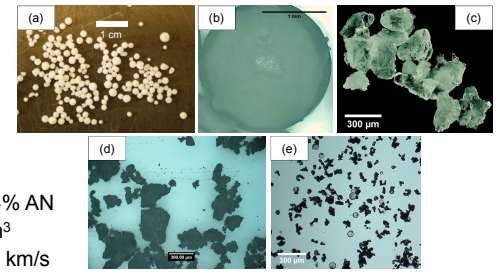

Microscope images of AN particles courtesy of Nick Cummock: (a) Brenntag prills, (b) single prill, (c) Cold-Pack, (d) hand blend, and (e) Kinepak^{TM}

Notes for baseline formulation:

Stoichiometric mixture of Kinepak^{TM} and diesel fuel pressed to 50% TMD

12

Experimental Apparatus

- Example of a 6.52 mm dia. ANFO sample in a 304 SS confiner

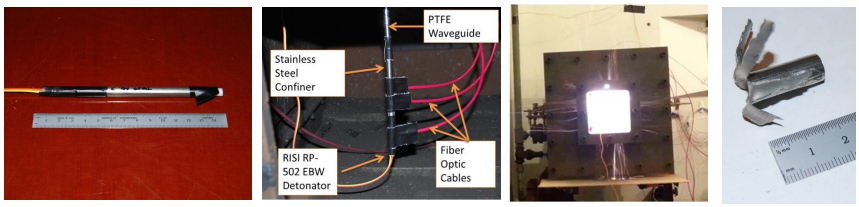

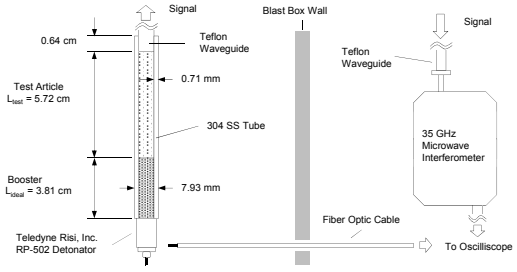

TOP
Sample assembly, instrumentation, and recovery of an ANFO shot

LEFT
Schematic of the experimental apparatus from Kittell *et al.* [1]

13

Sample Measurement

- Example of a 6.52 mm dia. ANFO sample in a 304 SS confiner

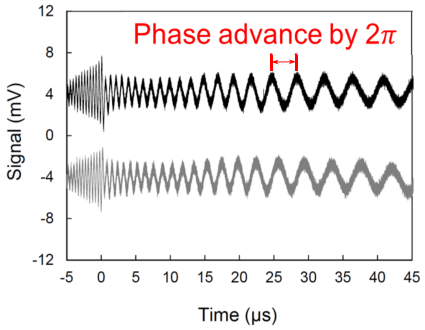

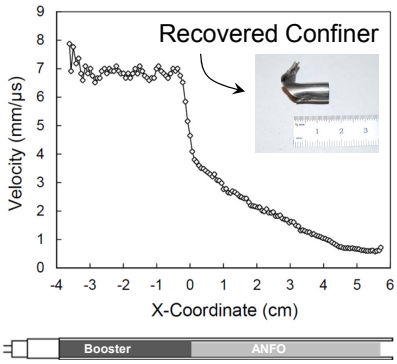

- A simple peak picking analysis was used
  - High quality MI signal output
  - Phase unwrapping and time-frequency analysis techniques may also be used as shown by Kittell *et al.* [1]

14

Explosive Charge Geometries

- Configurations determined from preliminary results
- Test matrix of sixteen shots
  - Density and PRIMASHEET 1000™ booster explosive pressing same for each shot
  - Charges require 1-5 g of test explosive
  - Relatively high sound speed 304 SS (~5 km/s) and low sound speed PVC (~2 km/s) used

Geometry abbreviations used in the presentation

Abbr.	Dia. (mm)	Material	t_w (mm)
THK	11.28	304 SS	32.5
PVC	11.28	304 SS PVC outer layer	0.7 19.1
THN	11.28	304 SS	0.7
SM	6.52	304 SS	0.7

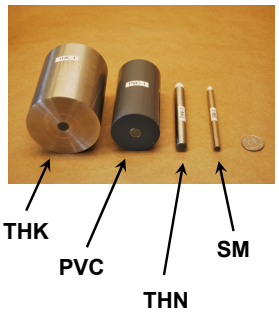

15

Experimental MI Velocity Results

- Position and velocity determined from a peak picking analysis

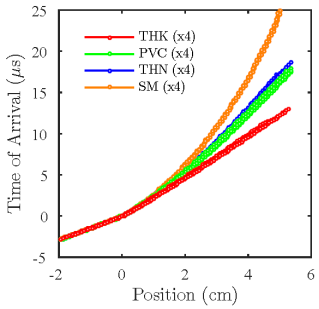

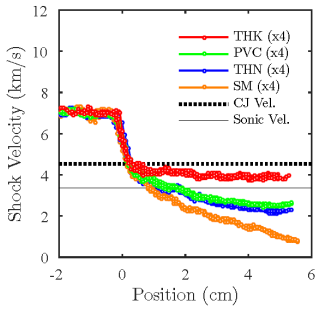

Quantity	Value (km/s)
CJ Vel.	4.522
Sonic Vel.	3.353
Particle Vel.	1.169

Values from CHEETAH [13] thermochemical equilibrium code

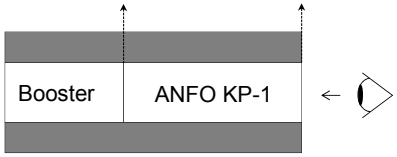

16

Interpretation of MI Velocity Results

- MI data is highly repeatable
  - Tight control of initial density (σ~0.4%)
- All curves correspond to failing overdriven detonation waves
  - Failure rate increases as confinement and diameter decrease
  - THK, PVC, THN probably will fail with a longer run distance
- Inflexion point in velocity (KY point)
  - Proposed by Dr. Kirk Yeager
  - Future work to investigate this point
- Evidence for transition from supersonic to subsonic deflagration
  - PVC and THN similar until 2 cm then deviate near the sonic velocity

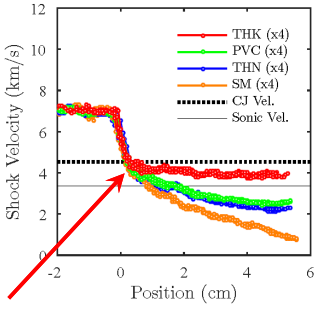

KY Point

A common velocity cut-off might define when the transition from supersonic to subsonic occurs

17

Reactive Burn Models

- Reactive burn models (RBMs) provide the constitutive models necessary to solve transient detonation wave phenomena
  - Solving the inviscid Euler equations of fluid dynamics
  - Neglect thermal effects and material strength [14] (unless more constitutive models are introduced)

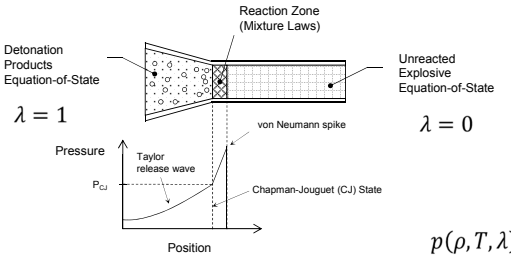

$$\frac{\partial \rho}{\partial t} + \nabla \cdot (\rho \vec{u}) = 0$$

$$\frac{\partial \vec{u}}{\partial t} + (\vec{u} \cdot \nabla)\vec{u} = -\frac{1}{\rho}\nabla p$$

$$\frac{\partial e}{\partial t} + (\vec{u} \cdot \nabla)e + \frac{p}{\rho}(\nabla \cdot \vec{u}) = 0$$

$$p(\rho, T, \lambda) = \lambda\, p_{DP}(\rho, T) + (1 - \lambda)\, p_{UR}(\rho, T)$$

$$e(\rho, T, \lambda) = \lambda\, e_{DP}(\rho, T) + (1 - \lambda)\, e_{UR}(\rho, T)$$

18

Equations-of-State (EOS) Used

- Jones-Wilkins-Lee EOS for detonation products
  - Fitted using a thermochemical equilibrium code [13]
  - Calculated for both ANFO and booster at each initial density

$$p = A\left(1 - \frac{\omega}{R_1 \boldsymbol{V}}\right)e^{-R_1 \boldsymbol{V}} + B\left(1 - \frac{\omega}{R_2 \boldsymbol{V}}\right)e^{-R_2 \boldsymbol{V}} + \frac{\omega e}{v}$$

- Mie-Grüneisen EOS for unreacted ANFO
  - Lack of empirical data for a shock-particle Hugoniot
  - Neglected fuel oil and glass micro-balloons in ANFO KP-1
  - Parameters for crystalline ammonium nitrate obtained from Ref. [15] and extrapolated using a p-α porosity model [16]

$$\left(\frac{\partial p}{\partial e}\right)_v = \Gamma_0 \rho_0 \qquad \Gamma = \frac{v \alpha K_T}{c_v} \qquad U_s = c_0 + s\, u_p + q\, {u_p}^2$$

19

Phenomenological Rate Law

- Theory of Ignition and Growth [17] to describe sub-grid phenomena
- Burn surface topology functions and burning rates
  - Use reaction progress variables to link sub-grid geometry

$$\dot{\lambda} = \sum_j s_j(\lambda)\, r_j(p, \rho, \dots) \qquad \lambda = \frac{V_{DP}}{V}$$

Hole Burning for Spherical Hot Spots

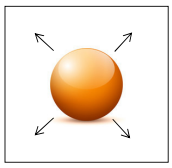

$\lambda \sim R^3$

$s(\lambda) \sim \lambda^{2/3}$

Inward Spherical Grain Burning

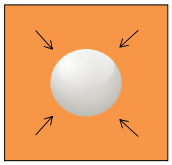

$1\text{-}\lambda \sim R^3$

$s(\lambda) \sim (1\text{-}\lambda)^{2/3}$

Topology functions from Ref. [18]

$s(\lambda)$	Type
$(1-\lambda)$	bulk reaction
$\lambda^{2/3}$	hole burning spherical hot spots
λ^n	Generalized hole burning
$(1-\lambda)^{2/3}$	Inward spherical grain burning
$(1-\lambda)^n$	Generalized grain burning

20

Phenomenological Rate Law

- Assumptions to minimize the number of free parameters
  - Spherical hot spots
  - Late time grain burning
  - Maximum reaction rate at 75% completion
  - Ignition goes with plastic work and pressure squared [17]
  - Weakly pressure-dependent rate law for growth [19-21]

$$\dot{\lambda} = \boxed{I}(1-\lambda)^{2/9}\eta^4 + \boxed{G}(1-\lambda)^{2/9}\lambda^{2/3}p^{0.9}$$

Ignition (I) Growth (G)

where $\eta = {}^{\rho}/_{\rho_0} - 1 - \boxed{a}$

and ignition is set to zero when

$\eta < 0$ or $\lambda > \boxed{\lambda_{ig}}$

4 UNKNOWN PARAMETERS

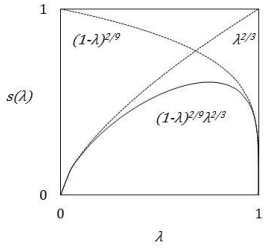

21

CTH Simulation Details

- 2d cylindrical (2dc) and 3d rectangular (3dr) geometries were implemented in the CTH shock physics hydrocode [22]
  - Numerical heterogeneities were included at +/-1% in density
  - Adaptive mesh refinement

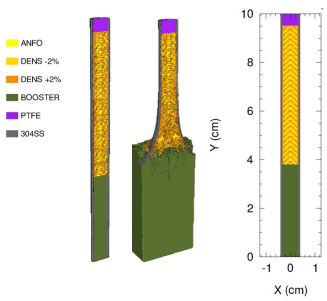

Heterogeneous vs. Homogeneous

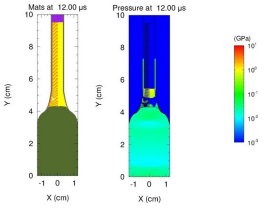

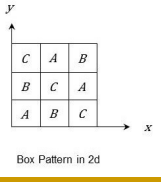

Box Pattern in 2d

- Notes:
  - 1.25 x 1.25 x 10 cm^3
  - 65.1 µm resolution (15.36 zones/mm) is resolved [23]
  - Symmetry and mass removal boundary conditions

IGRB Calibration and Sensitivity

- Custom shock tracking code to extract simulation data
  - Single goodness-of-fit metric
- Efficient Latin hypercube sampling (LHS) technique [24] to sample parameter space
  - Run on the Sandia Cray supercomputers using the DAKOTA code [25]
- Multiple attempts to determine sampling limits for G (highly nonlinear)
- Calibration using the PVC case worked the best
  - Tried SM data without any success
  - IGRB might not be capturing the correct physics for all cases (e.g. subsonic deflagration)

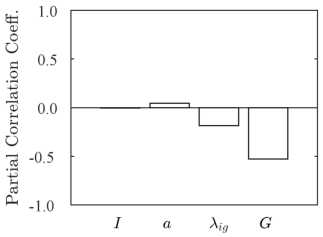

Param.	Low	High	Fit
I	1e5	1e8	1e6
a	0	0.4	0.2
λ_{ig}	0.001	1	0.5
G	0e-4	3e-4	1.5e-4

CTH Simulation Results

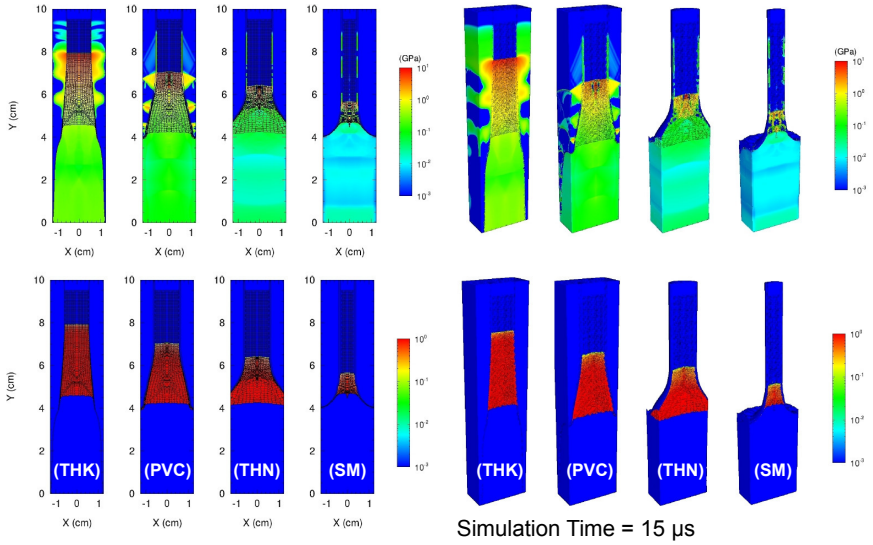

Simulation Time = 15 μs

24

Interpretation of CTH Simulation Results

- IGRB model calibrated to PVC data and used to predict the other cases
  - Incomplete match to SM and THN cases
- Same shock wave velocity determined from 2d and 3d simulations
  - Late time behavior is not identical
- IGRB model fails near the sonic line
  - Mechanism of wave propagation must change going from supersonic to subsonic
  - Suggests a minimum sample size and confinement for MI testing
- Front running pressure waves do not pre-compress the ANFO as suggested by Ref. [26]

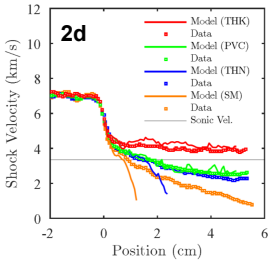

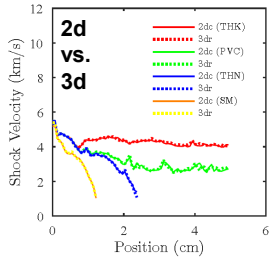

Verification – are the equations solved correctly?
Validation – are the physics correct? (predictive)
Calibration – are the reference data correct?

25

Interpretation of CTH Simulation Results

- Pressure gauges located at 1, 2, 3, and 4 cm into ANFO at 80% dia.

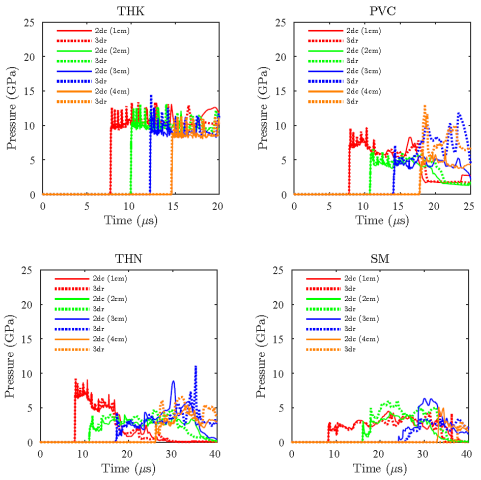

- Time of arrival is identical between 2d and 3d cases
- Shock pressure decreases with distance
- Different types of pressure waves in PVC and THN
  - Pulse shape
  - Initial pressures are similar at 1 cm
- Second reactive wave late in time for THN and SM

Model Predictions for Variable Density

- Density variations with p-α porosity model

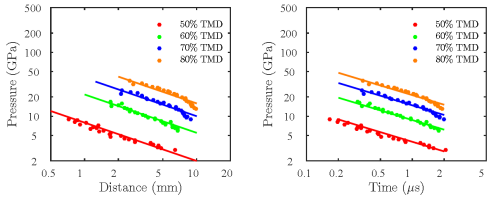

- Pop-plots from 1d calculations (left)
  - Used BCAT code [27]
  - Trend is qualitatively correct i.e. dead-pressing phenomenon [28]

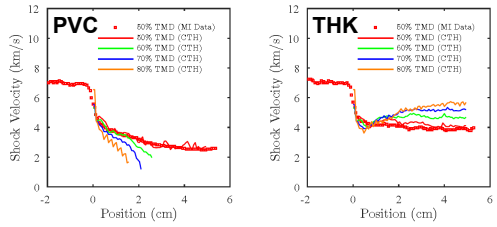

- MI experiments for PVC and THK cases (left)
  - Failure rate increased with density for PVC case
  - Higher velocities at the end of the THK case
  - KY point stayed the same

Model Predictions for a Large Diameter

- Large 50 cm dia. unconfined charge
  - 2d simulation enlarged to 30 x 60 cm^2
  - Numerical heterogeneities are present
- Scale-up over 40x in diameter and over 20,000x in ANFO mass
- Steady velocity achieved 4 cm into the ANFO
  - Shock front curvature and reaction zone thickness may be compared to DSD theory [28]

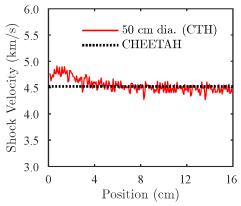

TOP
Detonation velocity compared to CJ calculation over the first 16 cm to show initiation transient

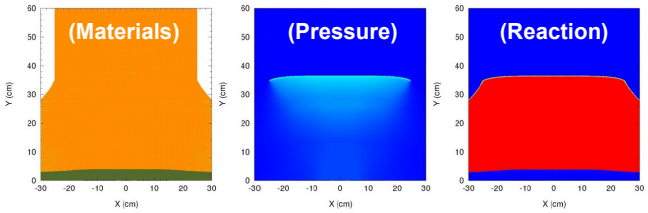

LEFT
Materials, pressure, and reaction at time t = 80 μs in the simulations

28

Conclusions

- Can small scale MI tests be used to infer large scale performance?
  - KY point may correspond to large diameter detonation velocity
  - Factors affecting the location of the KY point are still unknown
  - Shock sensitivity (Pop-plot) may be determined with a calibrated reactive burn model
- Is there a minimum sample size and confinement?
  - Velocities well below the sonic velocity indicate mechanism changes from supersonic to subsonic deflagration
- Is the IGRB model relevant to the MI tests?
  - IGRB model is only relevant for velocities near or above the sonic velocity and thick-walled confinement
- Is the IGRB model predictive?
  - Trends in Pop-plot are qualitatively correct (good)
  - KY inflexion point is invariant when changing initial density (bad)
  - Large diameter detonation wave is planar (bad)

29

Conclusions Cont'd…

- Is the IGRB model numerically robust?
  - Numerical heterogeneities in density may have avoided some of the unstable solutions during calibration
  - Observed non-linear behavior in the coefficient of growth term
- What mechanisms are relevant to the observed results?
  - Initially supersonic reactive wave behavior
  - Thermal effects, multiphase flow, and powder compaction likely dominate the late time response

Journal Publications

D. E. Kittell, L. J. Groven, T. R. Sippel, T. L. Pourpoint, and S. F. Son. Dependence of nano-aluminum and water propellant combustion on pH and rheology. *Combust. Sci. Technol.*, **185**(5):817-834, 2013.

D. E. Kittell, J. O. Mares, and S. F. Son. Using time-frequency analysis to determine time-resolved detonation velocity with microwave interferometry. *Rev. Sci. Instrum.* **86**(4):044705, 2015.

D. E. Kittell and C. D. Yarrington. A physically-based Mie-Grüneisen equation of state to determine hot spot temperature distributions. *Submitted to Combust. Theory Model. (under review)*

D. E. Kittell, N. R. Cummock, and S. F. Son. Analysis and simulation of overdriven failing detonation waves in small diameter ANFO charges using ignition and growth. *To be submitted to J. Appl. Phys. (in progress)*

Conference Publications

D. E. Kittell, T. L. Pourpoint, J. L. Groven, and S. F. Son. Further development of an aluminum and water solid rocket propellant. *47th AIAA/ASME/SAE/ASEE Joint Propulsion Conference and Exhibit*, San Diego, CA, July 31-August 3, 2011: 2011-6137.

C. D. Yarrington, D. E. Kittell, R. R. Wixom, and D. L. Damm. A Mie-Grüneisen EOS with non-constant specific heat. *Journal of Physics: Conference Series, Vol. 500, No. 5, p. 052053*. IOP Publishing, Seattle, WA, July 7-12, 2014.

D. E. Kittell, P. J. Renslow, L. J. Groven, and S. F. Son. Modeling small scale detonation experiments with pressed TATB. *Proc. 15th Int. Det. Symp.*, pp. 1584-1593, San Francisco, CA, July 2014.

D. E. Kittell, J. O. Mares, and S. F. Son. A comparison of wavelet, quadrature, and peak-to-peak methods for determining shock velocity from microwave interferometer data. *Proc. 15th Int. Det. Symp.*, pp. 192-201, San Francisco, CA, July 2014.

Acknowledgement

First and foremost, I would like to thank my advisor Dr. Steven Son and Dr. Lori Groven for their support and guidance. I would also like to thank some of the technical staff at Sandia National Laboratories including Dr. Cole Yarrington, and my manager Dr. Tony Geller for use of the Cray supercomputers through the Student Intern Program. Finally, a big thank-you to everyone at Zucrow Labs who contributed to this project in tangible and intangible ways.

This material is based upon work supported by the U.S. Department of Homeland Security, Science and Technology Directorate, Office of University Programs, under Grant Award No. 2013-ST-061-ED0001.

PURDUE ENGINEERING

PURDUE UNIVERSITY ZUCROW LABS ENERGETICS LABORATORY

Thank You!

Questions?

References

1. D. E. Kittell, J. O. Mares, and S. F. Son. Using time-frequency analysis to determine time-resolved detonation velocity with microwave interferometry. *Rev. Sci. Instrum.* **86**(4):044705, 2015
2. D. E. Kittell and C. D. Yarrington. A physically-based Mie-Grüneisen equation of state to determine hot spot temperature distributions. *Submitted to Combust. Theory Model. (under review)*
3. J. E. Kennedy, C. G. Rumchik, K.-Y. Lee, B. W. Asay, K. A. Thomas, and I. Plaksin. Floret test observations of detonation spreading in insensitive explosives. *Proc. 13th Int. Det. Symp.*, pp. 383-387, Norfolk, VA, July 2006.
4. J. L. Cutting, H. H. Chau, R. L. Hodgin, D. M. Hoffman, F. Garcia, R. S. Lee, E. McGuire, E., A. R. Mitchell, P. F. Pagoria, R. D. Schmidt, R. L. Simpson, P. C. Souers, and R. W. Swansiger. A small-scale screening test for HE performance: application to the new explosive LLM-105. *Proc. 11th Int. Det. Symp.*, pp. 828-835, Snowmass Village, CO, August 1998.
5. L. G. Hill, W. L. Seitz, C. A. Forest, and H. H. Harry. High Explosive Corner Turning Performance and the LANL Mushroom Test. *10th APS Conf. SCCM*, pp. 1-2, Amherst, MA, July 27-August 1, 1997.
6. R. L. Gustavsen, S. A. Sheffield, and R. R. Alcon. Measurements of shock initiation in the tri-amino-tri-nitro-benzene based explosive PBX 9502: Wave forms from embedded gauges and comparison of four different material lots. *J. Appl. Physics*, **99**(11):114907, 2006.
7. A. D. Krall, B. C. Glancy, and H. W. Sandusky. Microwave interferometry of shock waves. I. Unreacting porous media. *J. Appl. Phys.*, **74**(10):6322-6327, 1993.
8. B. C. Glancy, H. W. Sandusky, and A. D. Krall. Microwave interferometry of shock waves. II. Reacting porous media. *J. Appl. Phys.*, **74**(10):6328-6334, 1993.
9. E. G. Johnson. A microwave technique of determining growth to detonation. *AIAA J.*, **3**(11):2109-2111, 1965.
10. C. L. Mader. *Numerical modeling of explosives and propellants*. CRC Press, New York, 1998.
11. M. L. Hobbs, A. L. Brundage, and C. D. Yarrington. JCZS2i: an improved database for EOS calculations at high temperature and pressure. *Proc. 15th Int. Det. Symp.*, pp. 804-813, San Francisco, CA, July 2014.

References

12. J. B. Bdzil, T. D. Aslam, R. A. Catanach, and L. G. Hill. DSD front models: nonideal explosive detonation in ANFO. *Proc. 12th Int. Det. Symp.*, pp. 409-417, San Diego, CA, August 2002.
13. L. Fried and P. Souers. CHEETAH: a next generation thermochemical equilibrium code. Lawrence Livermore National Laboratory Report UCRL-ID-117240, 1994.
14. J. A. Zukas. *Introduction to Hydrocodes*. Elsevier, Amsterdam, 2004.
15. A. N. Dremin, K. K. Shvedov, and O. S. Avdonin. Shock compressibility and temperature of certain explosives in the porous state. *Combust. Explos. Shock*, **6**(4):449-455, 1970.
16. W. Herrmann. Constitutive equation for the dynamic compression of ductile porous materials. *J. Appl. Phys.*, **40**(6):2490-2499, 1969.
17. E. L. Lee and C. M. Tarver. Phenomenological model of shock initiation in heterogeneous explosives. *Phys. Fluids*, **23**(12):2362-2372, 1980.
18. J. Starkenberg and T. M. Dorsey. An assessment pf the performance of the history variable reactive burn explosive initiation model in the CTH code. Technical Report ARL-TR-1667, Army research Laboratory, Aberdeen Proving Ground, MD, 1998.
19. V. P. Sinditskii, V. Y. Egorshev, A. I. Levshenkov, and V. V. Serushkin. Ammonium nitrate: combustion mechanisms and the role of additives. *Propell. Explos. Pyrot.*, **30**(4):269-280, 2005.
20. M. A. Price and A. H. Ghee. Modeling for detonation and energy release from peroxides and non-ideal improvised explosives. *Cent. Eur. J. Ener. Mat.*, **6**(3-4):239-254, 2009.
21. H. R. James, B. D. Lambourn, C. A. Handley, N. J. Whitworth, H. N. Angseesing, P. J. Haskins, M. D. Cook, A. D. Wood, R. I. Briggs, and P. R. Ottley. An investigation of the detonation characteristics of some non-ideal explosive compositions based upon ammonium nitrate. *Proc. 13th Int. Det. Symp.*, pp. 110-120, Norfolk, VA, July 2006.
22. J. M. McGlaun and S. L. Thompson. CTH: a three-dimensional shock wave physics code. *Int. J. Impact Eng.*, **10**(1):351-360, 1990.
23. D. E. Kittell, P. J. Renslow, L. J. Groven, and S. F. Son. Modeling small scale detonation experiments with pressed TATB. *Proc. 15th Int. Det. Symp.*, pp. 1584-1593, San Francisco, CA, July 2014.

References

24. L. P. Swiler and G. D. Wyss. A user's guide to Sandia's latin hypercube sampling software: LHS UNIX library and standalone version. Sandia National Laboratories, Tech. Rep. SAND04-2439.
25. B. M. Adams, W. J. Bohnhoff, K. R. Dalbey, J. P. Eddy, M. S. Eldred, D. M. Gay, K. Haskell, P. D. Hough, and L. P. Swiler. DAKOTA, a multilevel parallel object-oriented framework for design optimization, parameter estimation, uncertainty quantification, and sensitivity analysis: version 5.0 user's manual. Sandia National Laboratories, Tech. Rep. SAND2010-2183, 2009.
26. S. I. Jackson, C. B. Kiyanda, and M. Short. Experimental observations of detonation in ammonium-nitrate-fuel-oil (ANFO) surrounded by a high-sound-speed, shockless, aluminum confiner. *Proc. Combust. Inst.*, **33**(2):2219-2226, 2011.
27. S. Nie, J. Deng, and A. Persson. The dead-pressing phenomenon in an ANFO explosive. *Propell. Explos. Pyrot.*, **18**(2):73-76, 1993.
28. J. B. Bdzil and D. S. Stewart. Modeling two-dimensional detonations with detonation shock dynamics. *Phys. Fluids A-Fluid*, **1**(7):1261-1267, 1989.

Appendix A: Error Analysis

- Random sample variation

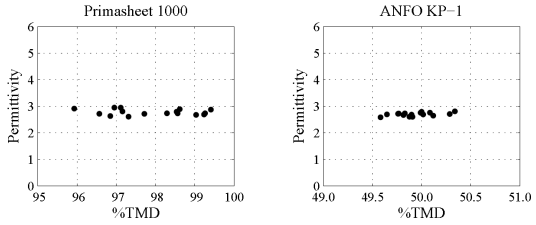

- Measurement errors

Quantity	95% CI	
	Sm. Dia.	Lg. Dia.
Δm (mg)	6.2	6.2
Δd (mm)	0.16	0.11
ΔL (mm)	0.05	0.05
$\Delta\epsilon_{r,TMD}$	0.05	0.05

- Summary of error propagation equations

Explosive	Diameter	Measurement Error			Random Error		
	(mm)	$\Delta\rho_0/\rho_0$	$\Delta\epsilon_r/\epsilon_r$	$\Delta v/v$	$\Delta\rho_0/\rho_0$	$\Delta\epsilon_r/\epsilon_r$	$\Delta v/v$
PS 1000	11.28	2.02%	2.52%	1.36%	2.23%	7.93%	4.27%
	6.52	4.80%	4.53%	2.96%	2.23%	7.93%	5.09%
ANFO KP-1	11.28	2.02%	2.83%	1.53%	0.84%	4.86%	2.63%
	6.52	4.81%	4.64%	3.05%	0.84%	4.86%	3.19%

38

Appendix A: Error Analysis Cont'd…

$$\frac{\Delta W}{W} = \sqrt{\sum_{i=1}^{N}\left(\frac{1}{W}\frac{\partial W}{\partial X_i}\Delta X_i\right)^2},$$

$$\frac{\Delta v}{v} = \sqrt{\left(\frac{\Delta\lambda_g}{\lambda_g}\right)^2 + \left(\frac{\Delta\bar{f}}{\bar{f}}\right)^2},$$

$$\frac{\Delta\lambda_g}{\lambda_g} = \sqrt{\left[\left(\frac{\lambda_g}{\lambda_0}\right)^2\frac{\Delta\epsilon_r}{2}\right]^2 + \left[\left(\frac{\lambda_g}{\lambda_c}\right)^2\frac{\Delta\lambda_c}{\lambda_c}\right]^2}.$$

$$\Delta\epsilon_r = \sqrt{\alpha^2+\beta^2},$$

$$\alpha = 3{\epsilon_r}^{2/3}\left({\epsilon_r}^{1/3}-1\right)\frac{\Delta\rho_0}{\rho_0},$$

$$\beta = {\epsilon_r}^{2/3}\left(\left({\epsilon_r}^{1/3}-1\right)\frac{\rho_{TMD}}{\rho_0}+1\right)^{-2}\frac{\rho_{TMD}}{\rho_0}\Delta\epsilon_{r,TMD},$$

$$\frac{\Delta\rho_0}{\rho_0} = \sqrt{\left(\frac{\Delta m}{m}\right)^2 + \left(\frac{2\Delta d}{d}\right)^2 + \left(\frac{\Delta L}{L}\right)^2}.$$

39

Appendix B: P-α Porosity Model

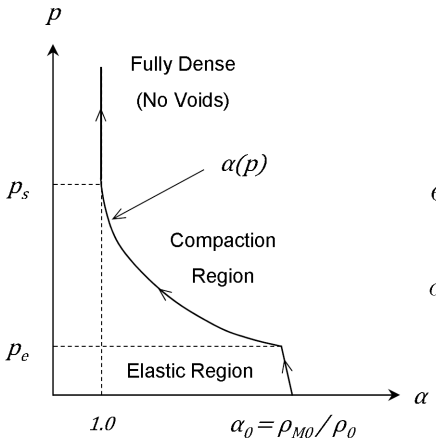

$$\alpha = \frac{\rho_M}{\rho},$$

$$p(\rho, T, \alpha) = p_M(\alpha\rho, T)/\alpha,$$

$$e(\rho, T, \alpha) = e_M(\alpha\rho, T).$$

$$\alpha(p) = 1 + (\alpha_0 - 1)\left(\frac{p_s - p}{p_s - p_e}\right)^2,$$

40

Appendix C: LHS Sampling Scatter Plots

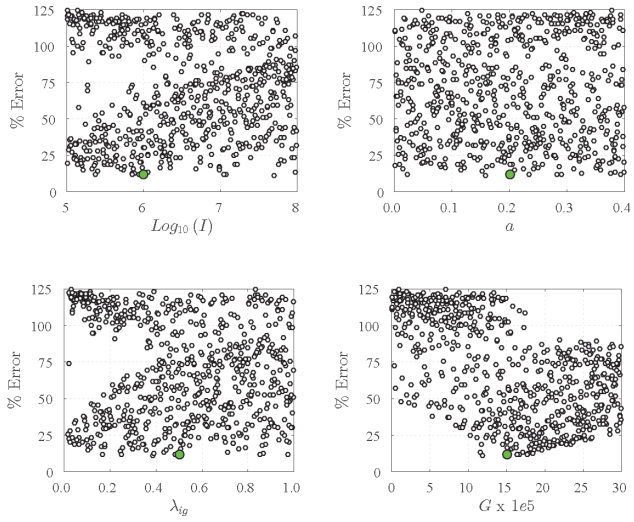

41

VITA

VITA

David Erik Kittell was born November 23, 1987 in Minneapolis, Minnesota to parents Bonnie and George Kittell. He received two Bachelor's degrees in aerospace engineering and mathematics at the University of Minnesota. After graduating with honors, he enrolled in the School of Aeronautics and Astronautics at Purdue University to pursue his graduate career in aerospace propulsion. Upon receiving his Master's degree from Purdue, he re-enrolled in the Ph.D. program through the School of Mechanical Engineering to more closely align himself with the research interests of his advisor, Dr. Steven F. Son in energetic materials. In the near future, he plans to move to Albuquerque, New Mexico to pursue a career at Sandia National Laboratories.